UNIVERSITÀ DEGLI STUDI DI PADOVA

UNIVERSITY OF PADOVA

CENTER OF STUDIES AND ACTIVITIES FOR SPACE
CISAS "G. COLOMBO"

Ph.D School in Space Sciences, Technologies and Measurements - STMS

Astronautics and Satellite Sciences

XXVI cycle

GOCE PRECISE NON-GRAVITATIONAL FORCE MODELING FOR POD APPLICATIONS

Ph.D School Director: Ch.mo Prof. Giampiero Naletto
Supervisor: Ch.mo Prof. Stefano Casotto

Ph.D Student: FRANCESCO GINI

To my parents, Matteo, and Mara.

Ai miei genitori, a Matteo e a Mara.

"The moment you doubt whether you can fly,
you cease forever to be able to do it."

J. M. Barrie

Contents

List of Figures

List of Tables

Introduction

GOCE was launched in 2009 at 250 km altitude to recover Earth's static gravity field. As part of the GOCE-Italy project, we carried out the Precise Orbit Determination (POD) and the determination of ocean tide field model from the GOCE orbital perturbations analysis. In order to be able to observe the orbital perturbations related to the ocean tide field it has been necessary to accurately model all the other force components acting on the spacecraft. Nowadays, with new improved accuracy of Earth gravity fields, thanks to the recent successful and outstanding missions GRACE and GOCE, the largest source of error in the orbit determination is related to the non-gravitational perturbations. These perturbations, mainly caused by the effects of the radiation pressure and the aerodynamics on satellites, are not easy to model, since they directly depend on the satellite geometry and surface properties (e.g., optical and thermal properties) as well as on the environmental properties (e.g., Earth albedo and thermal radiation, atmospheric properties) which are sometimes not well characterized. The work presented in this thesis has, as main objective, the precise modeling of the non-gravitational forces acting on GOCE. A new software ARPA (Aerodynamics and Radiation Pressure Analysis), which takes advantage of the raytracing technique, has been designed and developed to accurately model the non-gravitational perturbations due to the radiation pressure and aerodynamic effects. A sophisticated procedure has been set up, which, starting from the CAD geometry of the satellite and its surface proprieties and by means of a raytracing software, is capable of accurately modeling the interactions between the photons (from the Sun, the Earth or emitted by the spacecraft itself) and the atmospheric molecules with the satellite external surfaces. In particular, ARPA can compute the Solar Radiation Pressure (SRP), Earth Radiation Pressure (ERP), the spacecraft Thermal Re-Radiation (TRR) and the aerodynamic forces and torques acting on any satellite with a high level of accuracy, which are then efficiently integrated and used in the POD software. The adopted methodologies and procedure are presented in this thesis, and the results of the tests on GOCE are illustrated and discussed. The precise orbit determination software, the NAPEOS (NAvigation Package for Earth Observation Satellites) software system, developed and maintained at ESA/ESOC at the Navigation Support Office (HSO-GN), was upgraded to make use of the new ARPA inputs and adopted to perform the tests on GOCE and its orbit determination. The tests were performed on 30 consecutive daily arcs, starting at the beginning of the GOCE science phase on 1st November 2009. The results for the radiation test cases showed a significant reduction of the empirical accelerations (which absorb the eventual mismodeling), especially in the cross-track direction, of

about the 20% for the SRP, 12% for the ERP albedo, 13% for the ERP infrared and 20% for the TRR with respect to the standard NAPEOS force modeling (cannon-ball). For the aerodynamics, an important reduction of the post-fit RMS from 7.6 to 7.3 mm has been observed with the new ARPA model, together with the reduction from 4.6 to 4.2 cm of the distance of the orbits computed with ARPA from the official reduced-dynamics GOCE orbits (Precise Science Orbit — PSO). The obtained results confirm the goodness and the high level of accuracy of the modeling and techniques implemented in ARPA for all the non-gravitational perturbations modeled for GOCE.

Even though the results are presented for the GOCE satellite, the new technique and software are adaptable to satellite of any shape, whether in Earth-bound orbit, or orbiting another planet, or cruising in interplanetary space.

The work presented in this thesis will give an introduction to the ESA GOCE mission in the first chapter. In the second chapter an overview of the relevant literature and of the state of the art of the non-gravitational perturbations modeling will be presented. The third chapter will describe the precise orbit determination theory and procedure. The third chapter describes in detail how the ARPA software has been designed and how the non-gravitational forces have been modeled. This chapter will also show the techniques adopted to efficiently employ of these models in the POD software. The fourth chapter will describe the modifications and upgrade implemented in the POD software to make use of the present modelings. The fifth chapter will present and the results obtained for GOCE for each non-gravitational perturbation, comparing the obtained results with the other available models. Conclusions and future work will be then summarized at the end. An appendix is also included to clarify the reference frames and the significant angular directions considered in ARPA.

Summary

GOCE The Gravity field and steady-state Ocean Circulation Explorer is the first Earth explorer core mission of the European Space Agency (ESA). It was launched on 17 March 2009 from Plesetsk, Russia. The mission is dedicated to high-resolution gravity field extraction and carries, as primary instrument, a three-axis gradiometer for determining the gravity field with an unprecedented accuracy of 1 mGal and the geoid with an accuracy of 1 cm, both at a spatial resolution of 100 km.

Precise Orbit Determination of GOCE has been one task of the GOCE-Italy group — an ESA project endorsement funded by the Italian Space Agency (ASI). One of the research goals of the group at the University of Padova is to accurately model the non-gravitational perturbations acting on the spacecraft, in order not to absorb these force components in the ocean tidal field we want to recover (objective of another work carried out in parallel by our group of research [69]). The work of this thesis is, hence, focused on the precise modeling of the non-gravitational forces acting on GOCE,and in particular the Solar Radiation Pressure (SRP), Earth Radiation Pressure (ERP) for the albedo and infrared components, the satellite Thermal Re-Radiation pressure (TRR), and the aerodynamics. To do so, the ARPA — Aerodynamics and Radiation Pressure Analysis — software has been specifically designed and implemented at the University of Padova to compute these perturbations.

GOCE useful data for POD processing GOCE POD was performed using the following files and information as input:

- GOCE GPS raw observations from the SSTI-A LAGRANGE receiver were obtained in RINEX 2.20 format (file type SST_RIN_1b) through EOLi-SA (Earth Observation Link - Stand Alone[32]), an interactive tool to view and order products from ESA's Earth Observation catalogues;

- official GOCE reduced-dynamics Precise Science Orbit (PSO) solutions were used as a-priori orbits for the smoothing of raw observations during the POD process and as a term of comparison for the estimated orbits. These official orbits are generated at the Astronomical Institute of the University of Bern (AIUB, Bern, Switzerland) with the support of the Institute of Astronomical and Physical Geodesy (IAPG, Technische Universität München, Munich, Germany[14, 101]). The official PSO solutions are

provided with an accuracy of 2 cm and are based on reduced-dynamics solutions using undifferenced GPS observations with the Bernese GPS software package;

- precise GPS orbits, delivered with a 15 min sample interval and 30 s clock solutions were obtained from IGS Final Products center for each day of each GPS week. The accuracy of these products is about 2.5 cm for GPS orbits and about 75 ps for clock solutions;
- GOCE orbits are estimated with respect to the center of mass (CoM) of the satellite, and the position of the GOCE GPS antenna (SSTI-A) and its phase center corrections (ANTEX file[47, 12]) are accurately modeled;
- other auxiliary parameters for GOCE POD processing were retrieved from European Space Operations Centre (ESA/ESOC) ftp website ftp://dgn6.esoc.esa.int/napeos/.

Fully dynamic orbit generation An automatic sequence of programs has been set up in NAPEOS (NAvigation Package for Earth Observation Satellites) software, developed and maintained at ESA/ESOC, in order to perform the GOCE POD. This software package was upgraded to make use of the new ARPA inputs and adopted to perform the tests on GOCE for all the modeled non-gravitational perturbations.

ARPA ARPA — Aerodynamics and Radiation Pressure Analysis — is the software designed and implemented at the University of Padova to compute forces and torques on satellites due to the non-gravitational perturbations: Solar Radiation Pressure (SRP), Earth Radiation Pressure (ERP) for the albedo and infrared components, the satellite Thermal Re-Radiation (TRR), and the aerodynamics.

Figure 1 shows the flowchart for the different ARPA subprograms, with the relative inputs and outputs.

Solar and Earth Radiation Pressure In order to compute the effects of SRP and ERP (albedo and infrared radiation) on the satellite (left hand-side of Figure 1), an accurate spacecraft geometric three-dimensional model (CAD) is necessary. The CAD model realized for GOCE is shown in Figure 2 with its main components. The geometry is the input for the raytracing software which simulates the interaction of the photons coming from the Sun or the Earth with the satellite surfaces, as shown in Figure 3. The commercial software ZEMAX®[21] has been adopted to trace each ray from a fictitious source (simulating the rays from the Sun or the Earth) along its subsequent reflections on the CAD model. The source is located in a grid of positions to simulate all the possible directions of the incoming radiation. For each location of the ray source a raytracing file is created containing all the reflection points of each traced ray. The raytracing files, which contain the geometric information of the rays reflections on the spacecraft, are then read by the ARPA software which, together with the satellite surface optical and thermal properties, computes the physical interaction of the photons with the satellite surfaces,

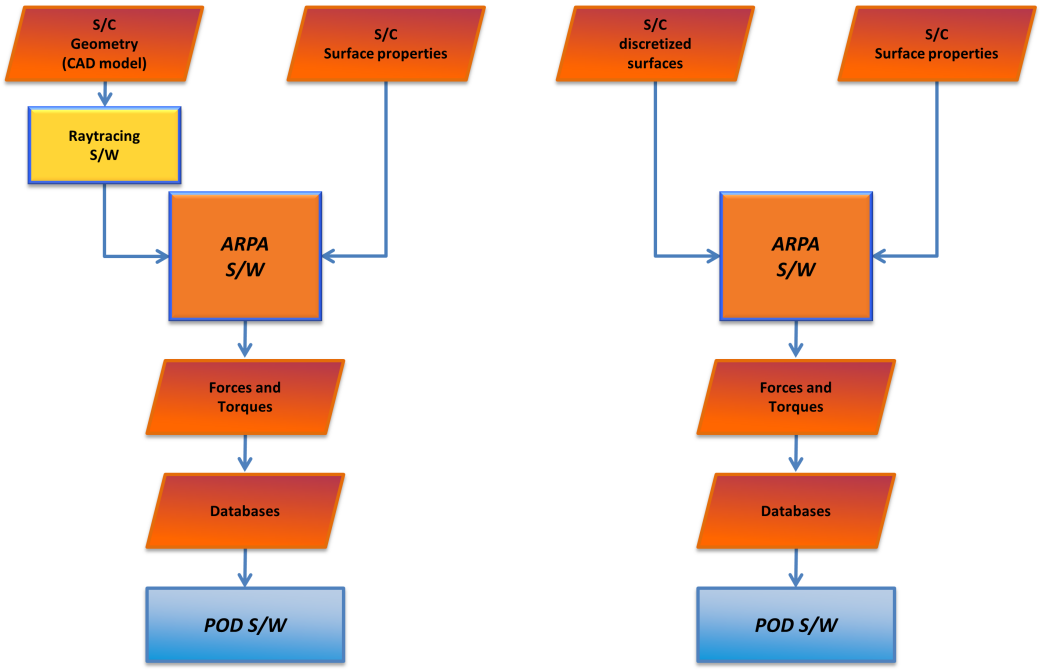

Figure 1: ARPA flowcharts: inputs and outputs of ARPA on the left-hand side for the direct Solar Radiation Pressure (SRP) and for the Earth Radiation Pressure (ERP), on the right-hand side for the satellite Thermal Re-Radiation (TRR) and for the aerodynamics.

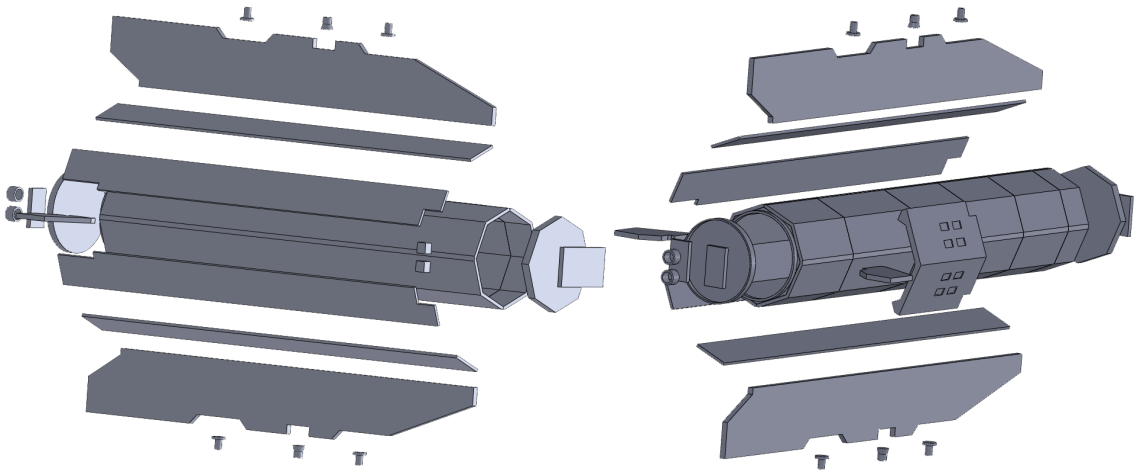

Figure 2: GOCE CAD model, exploded view.
Exploded view of the CAD model of GOCE and its external components.

computing forces and torques for the SRP and ERP components. To compute the force due to the radiation pressure the model described in [106] was applied at each reflection site, considering the specific surface optical and thermal properties and orientation. The

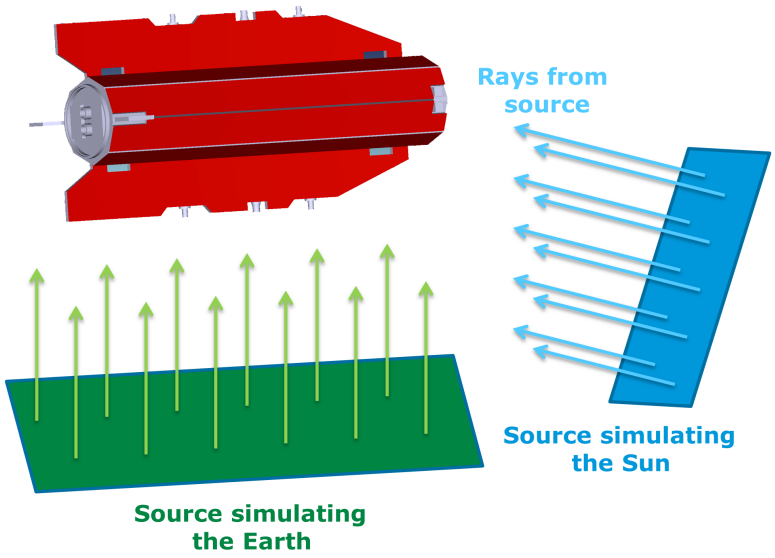

Figure 3: Raytracing procedure over GOCE. Ray sources simulating Sun and Earth are shown.

contribution of each ray is then accumulated to compute the total SRP and ERP force. By means of the raytracer it is possible to compute the radiation pressure forces accurately modeling the auto-shadowing and internal reflections effects. The forces are computed for each possible direction of the incoming solar and Earth (albedo and infrared) radiation and are then converted into coefficients (independent from the solar and Earth radiation flux) and used to create a database which is the input for the POD software.

Satellite Thermal Re-Radiation For the computation of the TRR (right hand-side of Figure 1), instead of a raytracing tool, a file containing the data of the satellite surfaces discretization (external surface mesh) is required to the ARPA software.

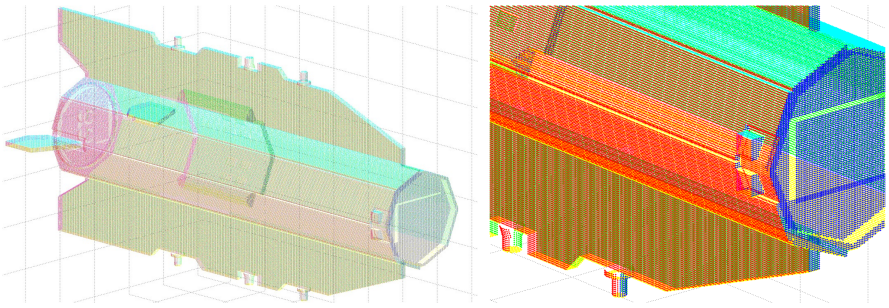

Figure 4: GOCE external surfaces meshed with pixels. Colors are used just to make the mesh clearer. On the left-hand side the entire satellite, and on the right-hand side a detail of the frontal floor.

The external mesh of GOCE shown in Figure 4 was realized. Based on the geometrical

mesh and the thermal properties and temperatures (averages temperature for the eclipsing and non-eclipsing conditions) of the surfaces, ARPA computes the accelerations induced on GOCE by the thermal emission. The force exerted by each surface mesh element on the satellite is computed with the model described in [1]. Lambertian emission[15] obeying to the cosine law was assumed. For the TRR component a database of forces for the eclipsing and non-eclipsing conditions has been created and is the input for the POD software.

Aerodynamics For the computation of the aerodynamics (right hand-side of Figure 1), the same surface mesh shown in Figure 4 is adopted. In this case, based on the geometrical mesh, the surface properties (temperatures, molecular mass of the surfaces) and the atmospheric properties (temperature, density and mean molecular mass of the atmospheric components), ARPA computes the aerodynamic force acting on the spacecraft. The atmospheric drag due to each surface element is computed for each possible direction of the incoming air-flow, based on the formulation of the SESAM model([73]) thermal free-molecular flow ([11, 72]). The contribution of each surface element is then accumulated to compute the total aerodynamic force and torque. The forces are then converted into aerodynamic coefficients (independent from the atmospheric density and satellite speed) and are used to create a database which is the input for the POD software.

Table 1 shows the parameter dependencies for each non-gravitational perturbation as computed with ARPA.

Table 1: Parameters influencing the non-gravitational forces on a spacecraft, as implemented in ARPA.

		SRP	ERP-alb	ERP-IR	TRR	Aero
Radiation/Flow direction	(Az, El)	✓	✓	✓		✓
Solar panels orientation	(ϕ_1, ϕ_2)	✓	✓	✓	✓	✓
Reflectivity (visible band)	ρ_{vis}	✓	✓			
Specularity (visible band)	μ_{vis}	✓	✓			
Reflectivity (IR band)	ρ_{IR}			✓		
Specularity (IR band)	μ_{IR}			✓		
Emissivity (IR band)	ϵ_{IR}				✓	
Surface temperature	T_S				✓	
Atmospheric temperature	T_∞					✓
Atmospheric molecular mass	m_g					✓

ARPA results The NAPEOS software package was upgraded modifying the graphical user interface and the model of forces of the orbital propagator. During the orbit propagation the in-flight conditions (e.g., attitude, solar panels orientation, solar irradiance, eclipse, visible Earth, atmospheric local properties) are used to compute the non-gravitational forces, denormalizing the coefficients contained in the ARPA databases.

The tests were performed on 30 consecutive daily arcs, starting at the beginning of the GOCE science phase on 1st November 2009. GOCE was flying in a drag-free mode during

Table 2: Gravitational, non-gravitational and empirical forces adopted for the GOCE test cases.

Dynamical models	Description	Adopted model
Static gravity field	EIGEN-6C 200x200	[31]
Solid Earth tides	IERS-TN32 71 constituents, 3x3	[62]
Ocean tides	FES2004 106 constituents, 50x50	[59]
Third body perturbation	Lunar gravity	
	Solar gravity	
	Planetary gravity	
	Indirect oblateness perturbation	
Relativistic correction	Correction for General Relativity	[62]
Aerodynamics	Drag force	[16] and ARPA
Thrust	Thrust profile	from telemetry
Radiation Pressure	Solar Radiation Pressure	[62] and ARPA
	Albedo radiation pressure	[4] and ARPA
	Infrared radiation pressure	[4] and ARPA
	Thermal re-radiation pressure	ARPA
Empirical accelerations	CPR along- and cross-track	[88]

the science phase due to its sensible payload. It is, in fact, constantly compensating for along-track non-gravitational accelerations, mainly due to atmospheric drag, by means of a sophisticated close-loop electric propulsion control system. Based on this, two different sets of test cases were designed and carried out:

1. a *Radiative test cases set*, considering the drag-free mode and not considering the satellite aerodynamics, to test the radiation pressure perturbations on GOCE;

2. an *Aerodynamic test cases set*, including the GOCE thrust profile and considering the satellite aerodynamics, to test the aerodynamic perturbations on GOCE.

The model of forces shown in Table 2 has been adopted. For each modeled non-gravitational perturbation only the tested model is switched, maintaining the rest of the setup unaltered. At the same time the number of observations rejected by the data pre-processing (*GnssObs*) and the orbit estimation (*Bahn*) is maintained low (below 1%) in order to obtain comparable solutions.

The *radiative test cases set*, where drag-free mode is considered, is used to test the models of Solar Radiation Pressure (SRP), the Earth Radiation Pressure due to the albedo (ERP albedo) and to the infrared radiation (ERP IR), and the satellite Thermal Re-Radiation (TRR).

The *aerodynamic test cases set*, where the GOCE thrust profile from the telemetry is included in the dynamical model, is used to test the aerodynamics estimating 20 aerodynamic scaling factors C_D's per day to adjust the aerodynamic accelerations computed with the NAPEOS and ARPA models.

ARPA SRP test case A first estimation without Cycle Per Revolution (CPR) empirical accelerations was carried out with NAPEOS in order to compute the daily scaling factors C_R's of the NAPEOS (cannon-ball) and ARPA solar radiation pressure models. These values, used to scale the computed accelerations due to SRP to best fit the GPS observations, were estimated to $C_R = 0.976$ for NAPEOS and $C_R = 1.141$ for ARPA. These values were set up in the dynamical model for the SRP component and kept fixed for all the following tests.

A second estimation including the CPR's (24 per day) was carried out to actually perform the GOCE precise orbit determination to evaluate the behavior of the ARPA SRP model. The CPR's tend to absorb the mismodeling in the dynamical model and the analysis of their amplitude clearly shows the goodness of the model. Both the cannon-ball and ARPA models showed very similar post-fit RMS of the residuals of the GPS carrier-phase (6.2 mm) but significantly different values of the estimated empirical accelerations, as shown in Figure 5. In the along-track direction the ARPA SRP model is capable of slightly

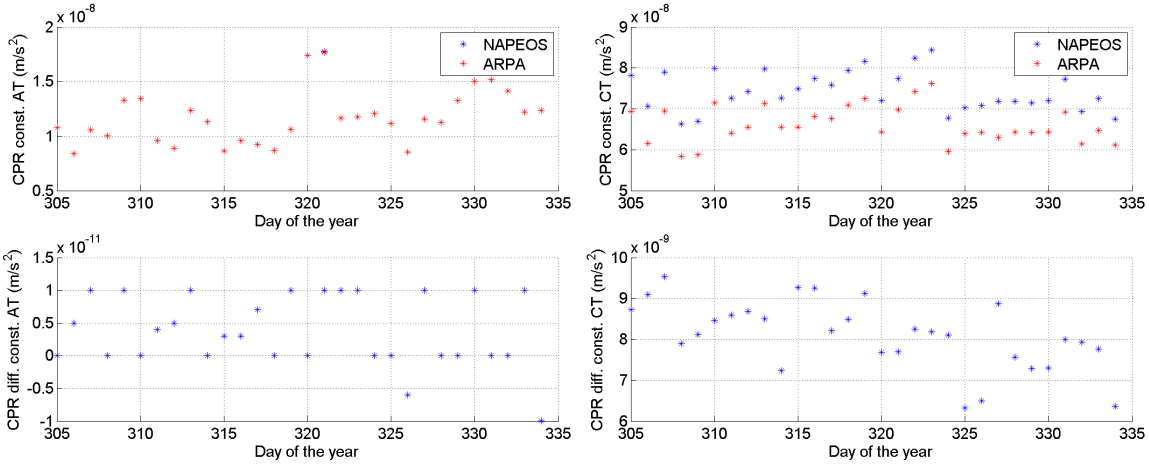

Figure 5: Along- and cross-track CPR's and CPR's difference for the NAPEOS (cannon-ball) and ARPA SRP models. A positive difference means a reduction of the values with the ARPA model.

reducing the empirical accelerations, while in the cross-direction the reduction is significant, with a decrement of about the 20%. This means ARPA is more accurately modeling the SRP perturbation, reducing the mismodeling. Moreover the distance of the orbits computed with ARPA from the reduced-dynamics official PSO's is, in average, lower than 3.9 cm. The very low post-fit RMS, together with the reduction of the 20% in the CPR's and the consistency with the official orbits prove the goodness of the ARPA implemented modeling and technique for the SRP perturbation.

ARPA ERP albedo test case Maintaining constant the SRP scaling factors for the NAPEOS and ARPA models, the ERP albedo model was tested, comparing the cannon-ball solution with the sophisticated ARPA model. Also in this case the albedo scaling factors were kept fixed (to one) and the empirical accelerations were estimated. After the

estimation the post-fit RMS for all the 30 tested daily arcs computed with both the models is at the same level. For what concerns the CPR's, in the along-track direction the ARPA ERP albedo model slightly reduced the empirical accelerations, while in the cross-track direction the reduction is significant, with a decrement of about the 12%, as shown in Figure 6. A mean distance lower than 3.9 *cm* between the PSO's and the orbits computed with the ARPA ERP albedo, together with the low level of the post-fit RMS and the 12% reduction of the cross-track CPR's prove the goodness of the ARPA modeling of the ERP albedo perturbation.

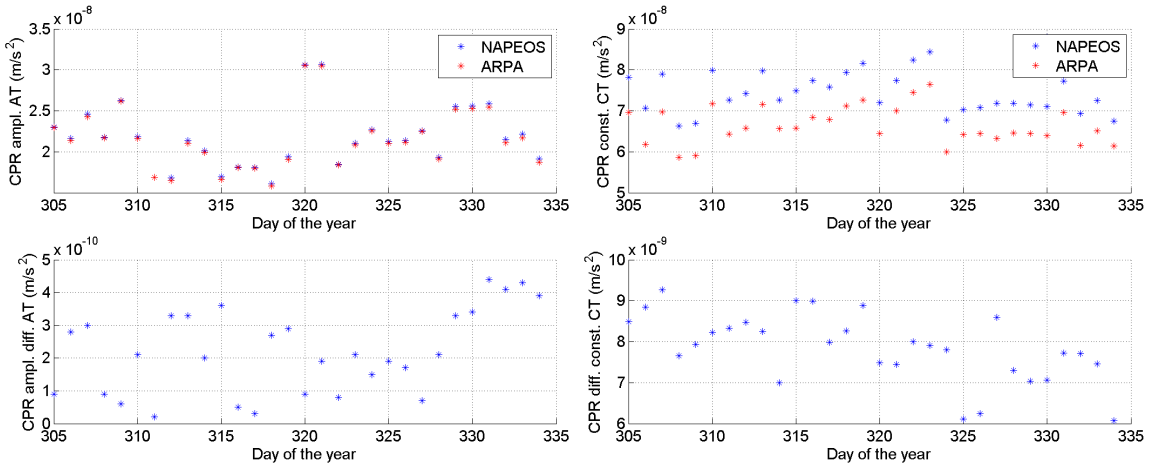

Figure 6: Along- and cross-track CPR's and CPR's difference for the NAPEOS (cannon-ball) and ARPA ERP albedo models. A positive difference means a reduction of the values with the ARPA model.

ARPA ERP infrared test case In a way similar to the ERP albedo procedure the ERP IR NAPEOS and ARPA models were compared. The post-fit RMS showed a decrement of about 0.015 *mm* with the ARPA model and, as shown in Figure 7, a significant reduction of about the 13% in the cross-track empirical accelerations. The distance from the PSO's is again lower than 3.9 *cm*. In this way the obtained results were satisfactory and demonstrated the goodness of the ARPA modeling of the ERP IR perturbation.

ARPA TRR test case NAPEOS does not include the modeling for the satellite thermal re-radiation and hence the ARPA TRR model was tested comparing the results obtained when considering and not considering this model. The solution which included the TRR modeling showed a reduction of the post-fit RMS of about 0.015 *mm* and again a significant reduction of the cross-track empirical accelerations of another 20%, as shown in Figure 8. The distance from the PSO's in maintained at the same level of before. These results proved the goodness of the ARPA modeling of the TRR perturbation.

ARPA aerodynamic test case In this test case the aerodynamic perturbations computed with ARPA are compared with the cannon-ball model computed with the NAPEOS

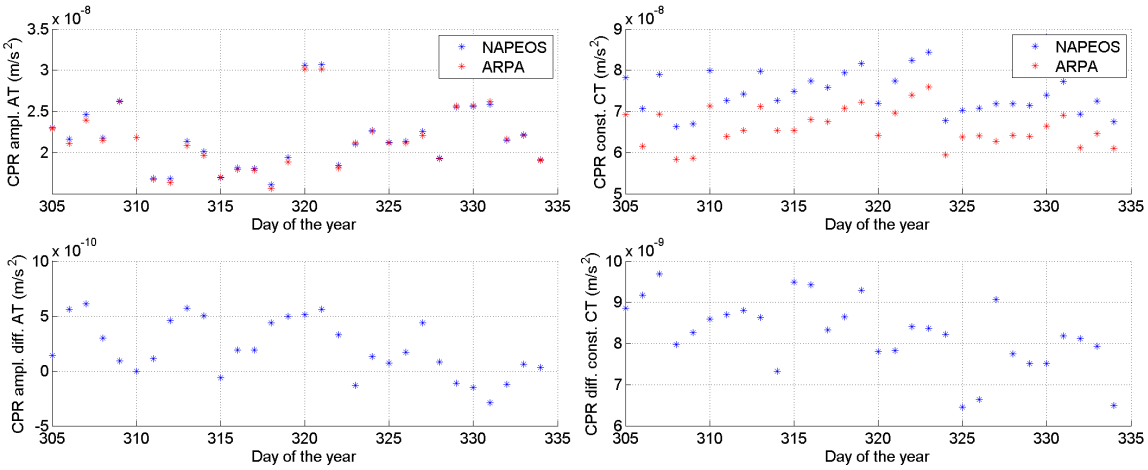

Figure 7: Along- and cross-track constant CPR's and CPR's difference for the NAPEOS (cannon-ball) and ARPA ERP infrared (IR) test cases. A positive difference means a reduction of the values with the ARPA model.

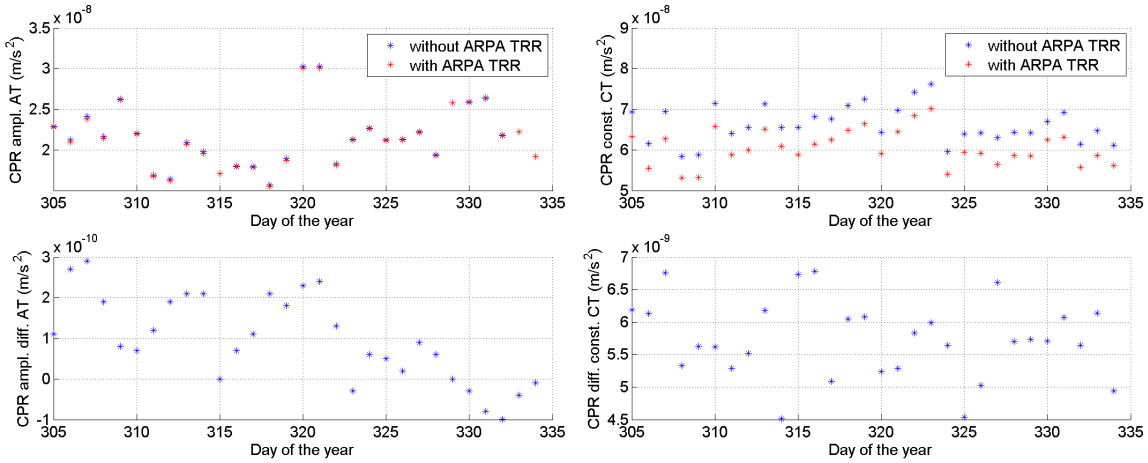

Figure 8: Along- and cross-track constant CPR's and CPR's difference estimated with and without the ARPA TRR model. A positive difference means a reduction of the values with the ARPA model.

standard model. For this test the empirical accelerations were considered in along-track (sine and cosine terms, but no constant term to avoid interference with the drag scaling factors) and cross-track (sine, cosine and constant term) directions. Over the 30 estimated daily arcs the post-fit RMS computed with the NAPEOS aerodynamic model is about 7.787 mm, while the orbits computed with the ARPA aerodynamic model showed an average reduction in the post-fit RMS of about 0.316 mm, as shown in Figure 9. This reduction is observable for the 90% of the tested days and is significant since corresponds to a signal of about 2.2 mm. For some days the improvement in the post-fit RMS reaches the level of about 0.6 mm, corresponding to a signal of about 3 mm. The orbits computed with the

cannon-ball model showed an average distance from the official PSO's of about 4.70 *cm*, while the results obtained with the ARPA aerodynamic model reduced this distance of about 0.42 *cm* (mean value). No appreciable difference between the CPR's estimated with the two aerodynamic models was observed. These results proved the goodness of the ARPA modeling for the aerodynamic perturbation.

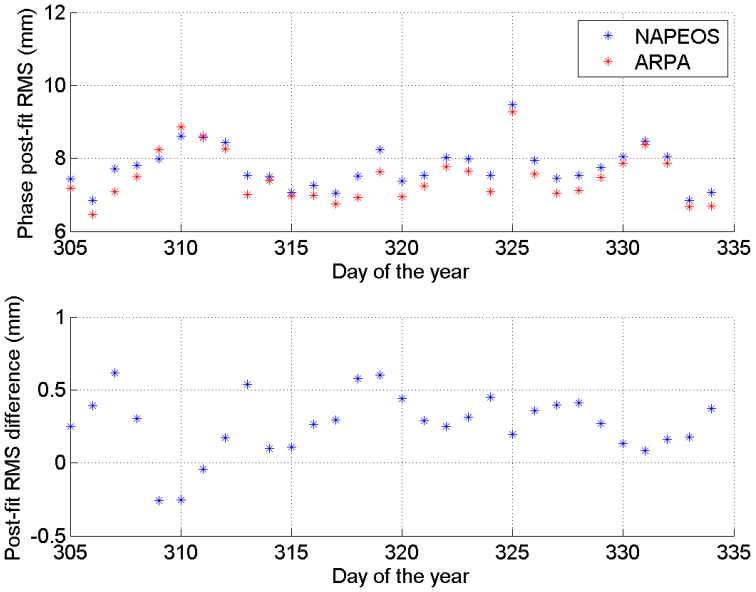

Figure 9: Post-fit RMS of the GPS phase residuals for the NAPEOS (cannon-ball) and ARPA aerodynamic models. A positive difference means a reduction of the values with the ARPA model.

In conclusion A software system (ARPA — Aerodynamics and Radiation Pressure Analysis) has been designed and developed at the University of Padova, capable of computing forces and torques on satellites due to the following non-gravitational perturbations: Solar Radiation Pressure (SRP), Earth Radiation Pressure for the albedo (ERP albedo) and infrared (ERP IR) components, satellite Thermal Re-Radiation (TRR), and aerodynamics. The NAPEOS software system for POD applications, as maintained at ESA/ESOC, was setup and opportunely upgraded to make use of the ARPA non-gravitational forces databases.

The precise orbit determination of GOCE was carried out with NAPEOS for 30 daily arcs starting from the beginning of the science phase on the 1st November 2009 in order to test and validate each ARPA non-gravitational perturbation database. Results obtained with ARPA models were compared to the NAPEOS standard modeling solution (cannon-ball). Two sets of test cases were set up: 1) radiative test cases set (SRP, ERP albedo and IR, and TRR), taking advantage of the GOCE drag-free mode, and 2) aerodynamic test cases set, considering the thrust profile and the aerodynamics of GOCE. Results for the radiative test cases showed a slightly average reduction (0.03 *mm*) of the post-fit RMS of the GPS carrier phase residuals for all the 30 days, and a significant reduction of the

estimated empirical accelerations, mainly in the cross-track direction, of about the 20% with the ARPA SRP model, 12% with the ARPA ERP albedo model, 13% with the ARPA ERP IR model, and 20% with the ARPA TRR model. All the orbits computed with the ARPA models showed consistency with official reduced-dynamics Precise Science Orbits, with a distance from them lower than 4 *cm*. Results for the aerodynamic test case showed an average reduction of the post-fit RMS of about 0.316 *mm* for 90% of the tested days, up to 0.6 *mm* in some cases. The distance of the orbits computed with the ARPA aerodynamics from the PSO's showed an average reduction of about 0.42 *cm* with respect to the cannon-ball solution, showing consistency with the official solutions and improvements with the new ARPA models. These results proved the goodness of the ARPA modeling and techniques adopted for all the considered non-gravitational perturbations.

Even though the results are presented for the GOCE satellite, which was selected as a test bench, the new techniques and software developed in ARPA are adaptable to satellite of any shape, whether in Earth-bound orbit, or orbiting another planet, or cruising in interplanetary space.

Sommario

GOCE Il *Gravity field and steady-state Ocean Circulation Explorer* è la prima delle missione *Earth explorer core mission* dell'Agenzia Spaziale Europea (ESA). È stato lanciato il 17 marzo 2009 da Plesetsk, Russia. La missione è dedicata all'estrazione del campo gravitazionale ad alta risoluzione e trasporta, come strumento primario, un gradiometro a tre assi per determinare il campo di gravità con la precisione senza precedenti di 1 mGal e il geoide con una precisione di 1 cm, entrambi con una risoluzione spaziale di 100 km.

La determinazione orbitale precisa di GOCE è stato un compito del gruppo GOCE-Italy — un progetto di endorsement ESA finanziato dall'Agenzia Spaziale Italiana (ASI). Uno degli obiettivi della ricerca del gruppo all'Università di Padova è quello di modellare accuratamente le perturbazioni non gravitazionali che agiscono sul veicolo spaziale, in modo da non assorbire queste componenti di forza nel campo di marea dell'oceano che vogliamo derivare (obiettivo di un altro lavoro sviluppato in parallelo dal nostro gruppo di ricerca [69]). Il lavoro di questa tesi é, quindi, incentrata sulla modellizzazione precisa delle forze non gravitazionali che agiscono su GOCE, e in particolare la pressione di radiazione solare (SRP), pressione di radiation terrestre (ERP) per le componenti di albedo e di radiazione infrarossa, la pressione indotta sul satellite dalla radiazione termica emessa dal satellite stesso (TRR) e l'aerodinamica. Per fare ciò, il software ARPA — analisi di pressione di radiazione e di aerodinamica — è stato appositamente progettato e sviluppato presso l'Università di Padova per calcolare queste perturbazioni.

Dati GOCE utili al processo di POD La POD di GOCE è stata eseguita usando i seguenti file e dati come input:

- le osservazioni GPS grezze di GOCE dal ricevitore SSTI-A LAGRANGE son state ottenute in formato RINEX 2.20 (file di tipo SST_RIN_1b) tramite EOLi-SA (Earth Observation Link - Stand Alone[32]), uno strumento interattivo per visualizzare e ordinare i prodotti dai cataloghi di ESA per l'Earth Observation.

- le orbite scientifiche precise ed ufficiali a dinamica ridotta (PSO) son state utilizzate come orbite a priori per lisciare le osservazioni grezze durante il processo di POD e come termine di confronto per le orbite stimate. Queste orbite ufficiali sono generate presso l'Astronomical Institute of the University of Bern (AIUB, Bern, Switzerland), con il supporto dell'Institute of Astronomical and Physical Geodesy (IAPG, Technische Universität München, Munich, Germany[14, 101]). Le soluzioni PSO ufficiali sono

fornite con un accuratezza di 2 cm e son basate su soluzioni a dinamica ridotta usando osservazioni GPS alle differenze zero, tramite il pacchetto software GPS Bernese;

- le orbite GPS precise, rilasciate con intervallo di campionamento di 15 minuti e le soluzioni dei clock a 30 secondi, son state ottenute dal centro IGS Final Products per ogni giorno della settimana GPS. L'accuratezza di questi prodotti è 2.5 cm per le orbite GPS e di circa 75 ps per i clock;

- le orbite di GOCE son stimate rispetto al centro di massa (CoM) del satellite, e la posizione dell'antenna GPS (SSTI-A) e delle correzioni del suo centro di fase (ANTEX file[47, 12]) sono modellate accuratamente;

- altri parametri ausiliari per la POD di GOCE son state ottenuti sito ftp dell'European Space Operations Centre (ESA/ESOC) ftp://dgn6.esoc.esa.int/napeos/.

Generazione dell'orbita a dinamica completa Una sequenza di programmi automatizzata è stata settata nel software NAPEOS (NAvigation Package for Earth Observation Satellites), sviluppato e mantenuto in ESA/ESOC, per effettuare la determinazione orbitale precisa di GOCE. In questo pacchetto software è stato implementato l'upgrade per utilizzare gli input di ARPA ed è stato adottato per testate i modelli di perturbazione non gravitazionale su GOCE.

ARPA ARPA — analisi di pressione di radiazione e di aerodinamica — è il software progettato e implementato presso l'Università di Padova per il calcolo delle forze e i momenti agenti sui satelliti e dovuti alle perturbazioni non gravitazionali: pressione di radiazione solare (SRP), pressione di radiation terrestre (ERP) per le componenti di albedo e di radiazione infrarossa, la pressione indotta sul satellite dalla radiazione termica emessa (TRR) e l'aerodinamica.

La Figura 10 mostra il diagramma di flusso dei diversi sottoprogrammi di ARPA, con i relativi input e output.

Pressione di radiazione solare e terrestre Per calcolare gli effetti di SRP e ERP (radiazione di albedo ed infrarossa) sul satellite (lato sinistro di Figura 10), è necessario un modello geometrico tridimensionale del satellite (CAD). Il modello CAD realizzato per GOCE è mostrato in Figura 11 con i suoi componenti. La geometria è l'input per il software di raytracing che simula l'interazione dei fotoni provenienti dal sole e dalla terra con le superfici del satellite, come mostrato in Figura 12. Il software in commercio ZEMAX®[21] è stato utilizzato per seguire il percorso di ogni raggio dalla sua sorgente fittizia (simulando i raggi solari e la radiazione terrestre) lungo le riflessioni successive su modello CAD. La sorgente è posizionata in una griglia di posizioni simulando tutte le direzioni possibili della radiazione incidente. Per ogni posizione della sorgente viene creato un file che contiene tutti i punti di riflessione di ciascun raggio tracciato. I file di raytracing, che contengono le informazioni geometriche delle riflessioni sul satellite, son successivamente letti

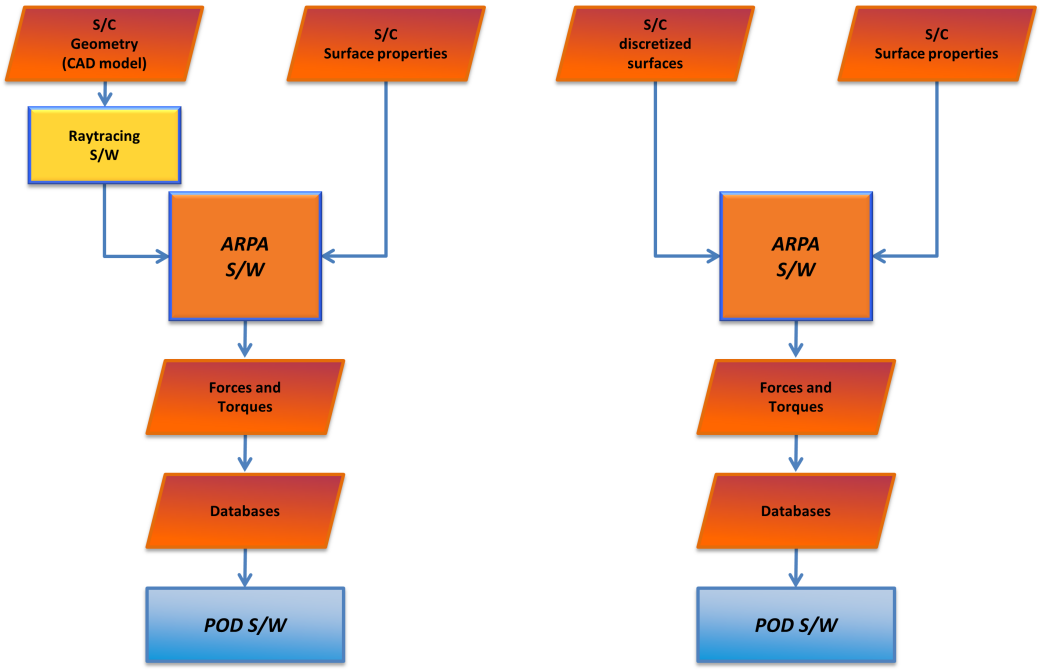

Figure 10: Diagramma di flusso ARPA: input e output di ARPA a sinistra per la pressione di radiazione solare (SRP) e la pressione di radiation terrestre (ERP), a destra per la pressione indotta sul satellite dalla radiazione termica emessa (TRR) e l'aerodinamica.

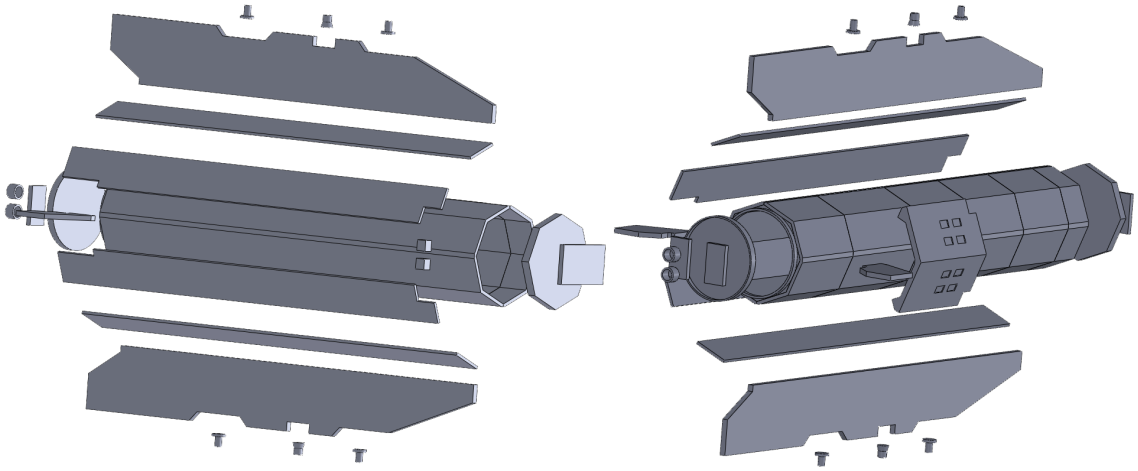

Figure 11: Vista dell'esploso del modello CAD di GOCE e dei suoi componenti esterni.

da ARPA, il quale, assieme alle proprietà ottiche e termiche delle superfici del satellite, calcola l'interazione fisica dei fotoni con le superfici del satellite, calcolando forze e momenti per le componenti di SRP ed ERP. Per calcolare la forza dovuta alla pressione di radiazione il modello descritto in [106] è stato applicato ad ogni punto di riflessione, considerando le

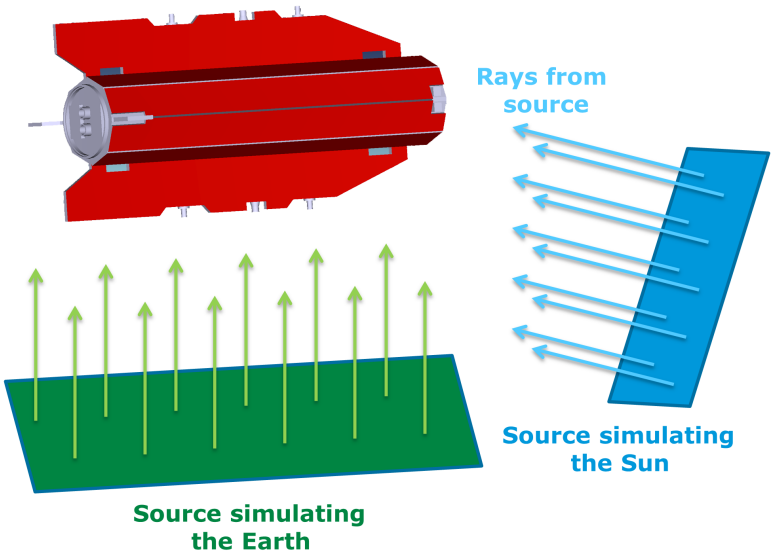

Figure 12: Procedura di raytracing su GOCE. Sono mostrate le sorgenti dei raggi che simulano il sole e la terra.

specifiche proprietà ottiche e termiche e l'orientazione delle superfici. Il contributo di ogni raggio è poi accumulato per calcolare la forza totale di SRP e ERP. Tramite il raytracer è possibile calcolare le forze di pressione di radiazione modellando accuratamente gli effetti di auto-ombreggiatura e di riflessioni interne. Le forze sono calcolate per ogni possibile direzione della radiazione solare e terrestre incidente (albedo ed infrarosso) e sono poi convertite in coefficienti (indipendenti dal flusso di radiazione solare e terrestre) ed usati per creare un database, input per il software di POD.

Riemissione della radiazione termica del satellite Per il calcolo della TRR (lato destro di Figura 10), invece dello strumento di raytracing, è richiesto dal software ARPA un file contente le informazioni della discretizzazione delle superfici esterne del satellite (mesh esterna superficiale).

La mesh esterna di GOCE mostrata in Figura 13 è stata realizzata. Sulla base della mesh geometrica e delle proprietà termiche e delle temperature delle superfici (temperature medie per le condizioni di eclissi e non eclissi) ARPA è in grado di calcolare le accelerazioni indotte su GOCE dall'emissione termica. La forza esercita da ogni elemento della mesh di superficie è calcolata tramite il modello descritto in[1]. Un'emissione di tipo Lambertiana[15] secondo la regola del coseno è stata assunta. Per la componente di TRR è stato creato un database di forze per le condizioni di eclissi e non eclissi, che è l'input per il software di POD.

Aerodinamica Per il calcolo dell'aerodinamica (lato destro di Figura 10), la stessa mesh di superficie di Figura 13 è stata adottata. In questo caso, sulla base della mesh geometrica, le proprietà superficiali (temperature, massa molecolare delle superfici) e le

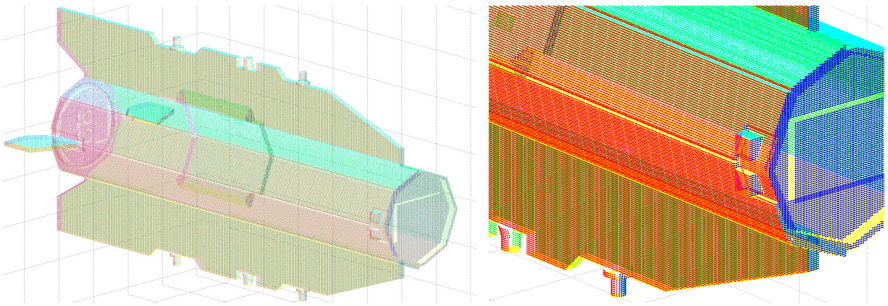

Figure 13: Superfici esterne di GOCE discretizzate in pixel. I colori son utilizzati per render l'immagine più chiara. A sinistra il satellite intero, e a destra un dettaglio della faccia frontale.

proprietà atmosferiche (temperatura, densità, massa molecolare media delle componenti atmosferiche), ARPA è in grado di calcolare la forza aerodinamica agente sul satellite. Il drag atmosferico dato da ogni elemento di superficie è calcolato per ogni possibile direzione del flusso incidente, sulla base della formulazione del modello SESAM ([73]) per il flusso termico in regime particellare ([11, 72]). Il contributo di ogni elemento di superficie è poi accumulato per ottenere la forza e il momento aerodinamici totali. Le forze son poi convertite in coefficienti aerodinamici (indipendenti dalla densità atmosferica e dalla velocità del satellite) e son usati per creare un database che è l'input per il software di POD.

La Tabella 3 mostra le dipendenze dei parametri per ogni perturbazione non gravitazionale, come calcolato con ARPA.

Table 3: Parametri che influenzano le forze non gravitazionali su un satellite, come implementato in ARPA.

		SRP	ERP-alb	ERP-IR	TRR	Aero
Direzioni di radiazione/flusso	(Az, El)	✓	✓	✓		✓
Orientamento pannelli solari	(ϕ_1, ϕ_2)	✓	✓	✓	✓	✓
Riflettività (banda visibile)	ρ_{vis}	✓	✓			
Specularità (banda visibile)	μ_{vis}	✓	✓			
Riflettività (banda IR)	ρ_{IR}			✓		
Specularità (banda IR)	μ_{IR}			✓		
Emissività (banda IR)	ϵ_{IR}				✓	
Temperature superficiale	T_S				✓	
Temperatura atmosferica	T_∞					✓
Massa molecolare atmosferica	m_g					✓

Risultati di ARPA Il pacchetto software NAPEOS è stato integrato modificando il modello di forza del propagatore orbitale e l'interfaccia grafica. Durante la propagazione dell'orbita le condizioni locali in volo (assetto, orientamento dei pannelli solari, irradianza solare, eclissi, terra visibile, proprietà locali dell'atmosfera) son usate per calcolare le forze

Table 4: Forze gravitazionali, non gravitazionali ed empiriche adottate per i test di GOCE.

Dynamical models	Description	Adopted model
Campo gravitazionale statico	EIGEN-6C 200x200	[31]
Maree di terra solida	IERS-TN32 71 costituenti, 3x3	[62]
Maree oceaniche	FES2004 106 costituenti, 50x50	[59]
Perturbazione di terzo corpo	Gravità lunare	
	Gravità solare	
	Gravità planetaria	
	Perturbazione indiretta di schiacciamento	
Correction relativistica	Correzione di relatività generale	[62]
Aerodinamica	Forza di rag	[16] e ARPA
Spinta	Profilo di spinta	da telemetria
Pressione di radiazione	Pressione di radiazione solare	[62] e ARPA
	Pressione di radiazione di albedo	[4] e ARPA
	Pressione di radiazione infrarossa	[4] e ARPA
	Pressione di radiazione termica	ARPA
Accelerazioni empiriche	CPR along- e cross-track	[88]

non gravitazionali, denormalizzando i coefficienti contenuti nei database di ARPA.

I test son stati eseguiti su 30archi giornalieri consecutivi, dall'inizio della fase scientifica di GOCE l'1 Novembre 2009. GOCE volava in modalità drag-free durante la fase scientifica, per via del suo strumento altamente sensibile. GOCE, infatti, compensava costantemente le accelerazioni non gravitazionali nella direzione di volo, principalmente dovute al drag atmosferico, tramite un sofisticato sistema di controllo elettrico della propulsione a ciclo chiuso. Sulla base di questo due diversi set di test son stati definiti and eseguiti:

1. a *Set di test radiativi*, considerando la modalità drag-free and non considerando l'aerodinamica del satellite, al fine di testare le perturbazioni di pressione di radiazione su GOCE;

2. an *Set di test aerodinamici*, includendo il profilo di spinta di GOCE e considerando l'aerodinamica del satellite, al fine di testare le perturbazioni aerodinamiche su GOCE.

Il modello di forza mostrato in Tabella 4 è stato adottato. Per ogni modello di perturbazione non gravitazionale solo il modello testato è cambiato, mantenendo tutto il rest del setup inalterato. Allo stesso tempo il numero di osservazioni scartate dal preprocessamento dei dati (*GnssObs*) e dal processo di stima orbitale (*Bahn*) è mantenuto a un livello basso (sotto l'1%) per ottenere soluzioni comparabili.

I *set di test radiativi*, in cui il modo drag-free è considerato, è utilizzato per testare i modelli di pressione di radiazione solare (SRP), pressione di radiation terrestre per l'albedo (ERP albedo) e la radiazione infrarossa (ERP IR) e la pressione indotta sul satellite dalla radiazione termica emessa (TRR).

I *set di test aerodinamici*, in cui il profilo di spinta dalla telemetria di GOCE è incluso nella dinamica, è utilizzato per testare l'aerodinamica, stimando 20 fattori di scala aerodinamici C_D's al giorno al fine di riscalare le accelerazioni aerodinamiche calcolate con i modelli di NAPEOS e di ARPA.

Test case di ARPA SRP Una prima stima senza i CPR è stata condotta con NAPEOS al fine di calcolare i coefficienti di scala giornalieri C_R per i modelli di NAPEOS (palla di cannone) e di ARPA per la pressione di radiazione solare. Questi valori, utilizzati per riscalare le accelerazioni date dalla SRP per meglio fittare le osservazioni GPS, son state stimate a $C_R = 0.976$ per NAPEOS e $C_R = 1.141$ per ARPA. Questi valori son stati settati nel modello dinamico per la componente di SRP e son mantenuti invariati per tutti i test seguenti.

Un seconda stima è stata condotta considerando i CPR (24 al giorno) per eseguire effettivamente la determinazione orbitale precisa di GOCE, al fine di valutare il comportamento del modello di SRP di ARPA. I CPR tendono ad assorbire i le incorrettezze nel modello di forze e un'analisi della loro ampiezza mostra in maniera evidente la bontà del modello. Sia il modello a palla di cannone che il modello ARPA mostrano risultati molto simili nel post-fit RMS dei residui di fase GPS (6.2 mm), ma differiscono sostanzialmente per i valori delle accelerazioni empiriche stimate, come mostrato in Figura 14.

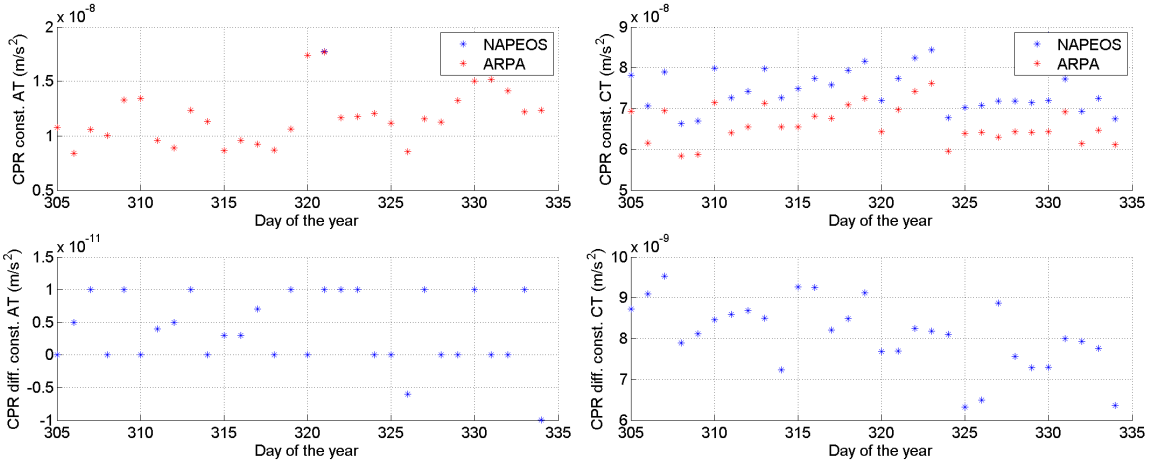

Figure 14: CPR e differenza dei CPR nelle direzioni along- e cross-track per i modelli di SRP di NAPEOS (palla di cannone) e di ARPA. Una differenza positiva rappresenta una diminuzione dei valori con il modello ARPA.

Nella direzione along-track il modello di SRP di ARPA + in grado di ridurre leggermente le accelerazioni empiriche, mentre nella direzione cross-track la riduzione è significativa, con un decremento di circa il 20%. Ciò significa che ARPA modella in maniera più accurata la perturbazione indotta dalla SRP, riducendo gli errori di modellazione. Inoltre la distanza tra le orbite calcolate con ARPA e le PSO è in media inferiore ai 3.9 cm. Il valore di post-fit RMS estremamente basso, assieme alla riduzione del 20% dei CPR e alla coerenza con le

orbite ufficiali prova la bontà della modellazione e delle tecniche implementate in ARPA per la perturbazione di SRP.

Test case di ARPA ERP albedo Mantenendo costanti i fattori di scala di SRP per i modelli di NAPEOS e ARPA, il modello di ERP albedo è stato testato, confrontando la soluzione a palla di cannone con il modello sofisticato di ARPA. Anche in questo caso i fattori di scala di ERP albedo son mantenuti constanti (a uno) e le accelerazioni empiriche sono stimate. Alla fine del processo di stima il post-fit RMS è allo stesso livello per i modelli di NAPEOS e di ARPA per tutti i 30 archi giornalieri testati. Per quanto riguarda i CPR, nella direzione along-track il modello ARPA ERP albedo riduce leggermente le accelerazioni empiriche, mentre nella direzione cross-track la riduzione è significativa, con una diminuzione di circa il 12% come mostrato in Figura 15. Una distanza media dalle PSO inferiore a 3.9 *cm*, assieme al basso livello di post-fit RMS e alla riduzione del 12% dei CPR prova la bontà della modellazione e delle tecniche implementate in ARPA per la perturbazione di ERP per la componente di albedo.

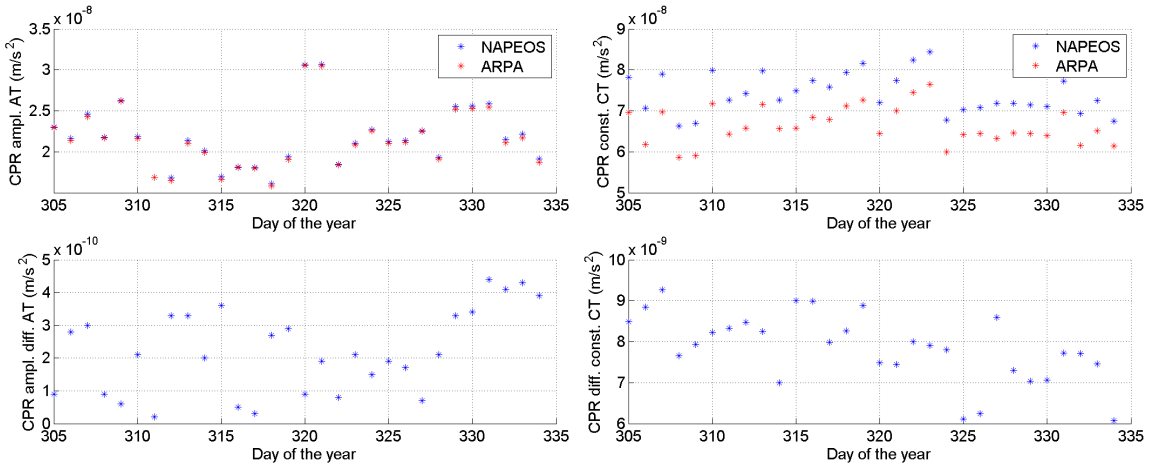

Figure 15: CPR e differenza dei CPR nelle direzioni along- e cross-track per i modelli di ERP albedo di NAPEOS (palla di cannone) e di ARPA. Una differenza positiva rappresenta una diminuzione dei valori con il modello ARPA.

Test case di ARPA ERP IR In maniera simile a quella adottata per l'ERP albedo i modelli di NAPEOS e ARPA per l'ERP IR son stati confrontati. Il post-fit RMS ha mostrato un decremento di circa 0.015 *mm* con il modello ARPA, e come mostrato in Figura 16 una riduzione significativa di circa il 13% delle accelerazioni empiriche nella direzione cross-track. La distanza dalle PSO è ancora inferiore a 3.9 *cm*. In questo modo i risultati ottenuti sono soddisfacenti e dimostrano la bontà del modello di ARPA per le perturbazioni di ERP IR.

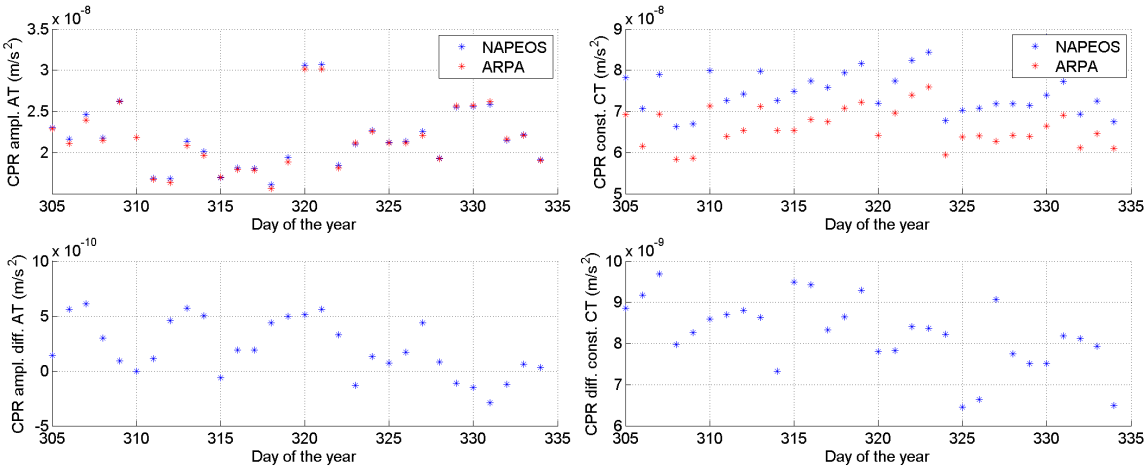

Figure 16: CPR e differenza dei CPR nelle direzioni along- e cross-track per i modelli di ERP IR di NAPEOS (palla di cannone) e di ARPA. Una differenza positiva rappresenta una diminuzione dei valori con il modello ARPA.

Test case di ARPA TRR NAPEOS non include il modello di pressione di radiazione termica del satellite e quindi il modello di ARPA TRR è stato testato confrontando i risultati ottenuti considerando e non considerando il modello. La soluzione che include il modello di TRR ha mostrato una riduzione del post-fit RMS di circa 0.015 mm e ancora una riduzione significativa di circa il 20% delle accelerazioni empiriche nella direzione cross-track, come mostrato in Figura 17. La distanza dalle PSO si mantiene allo stesso livello dei casi precedenti. Questi risultati provano la bontà del modello ARPA per la perturbazione di TRR.

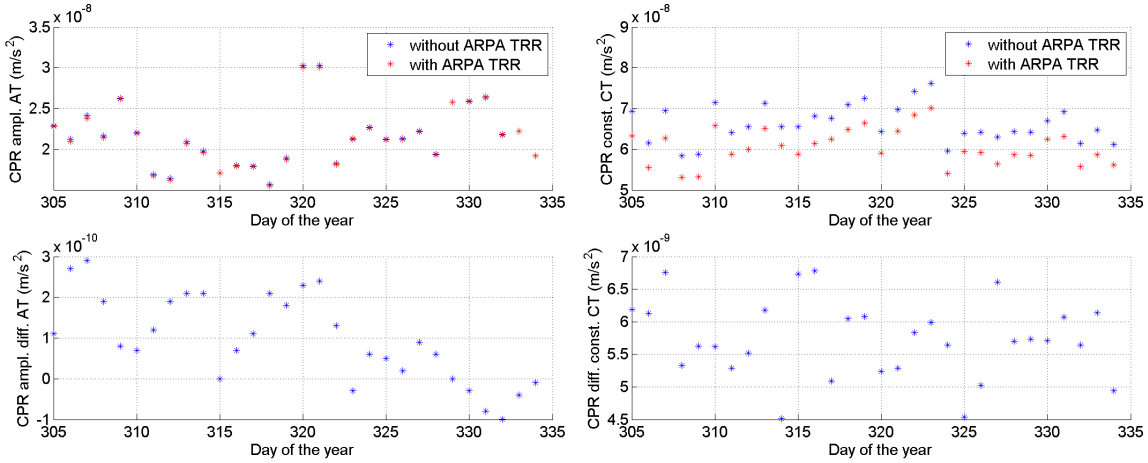

Figure 17: CPR e differenza dei CPR nelle direzioni along- e cross-track stimati con e senza il modello ARPA di TRR. Una differenza positiva rappresenta una diminuzione dei valori con il modello ARPA.

Test case dell'aerodinamica di ARPA In questo test case le perturbazioni aerodinamiche calcolate con ARPA son confrontate con in modello a palla di cannone calcolato con il modello standard di NAPEOS. Per questo test le accelerazioni empiriche son considerate nelle direzioni along-track (termini in seno e coseno, ma non il termine costante per evitare di interferire con i fattori di scala aerodinamici) e cross-track (termini in seno, coseno e costante). Per il periodo dei 30 archi giornalieri stimati il post-fit RMS calcolato con il modello aerodinamico di NAPEOS è di circa 7.787 mm, mentre le orbite calcolate con il modello aerodinamico di ARPA mostra una riduzione media del post-fit RMS di circa 0.316 mm, come mostrato in Figura 18. La diminuzione è osservabile per il 90% dei giorni testati ed è significativa in quanto corrisponde a un segnale di circa 3 mm. Le orbite calcolate con il modello a palla di cannone han mostrato una distanza media dalle POS ufficiali di circa 4.70 cm, mentre i risultati ottenuti con il modello aerodinamico di ARPA ha ridotto questa distanza di circa 0.42 cm (valore medio). Nessuna differenza apprezzabile tra i CPR calcolati con i due modelli atmosferici è stata osservata. Questi risultati provano la bontà del modello ARPA per la perturbazione aerodinamica.

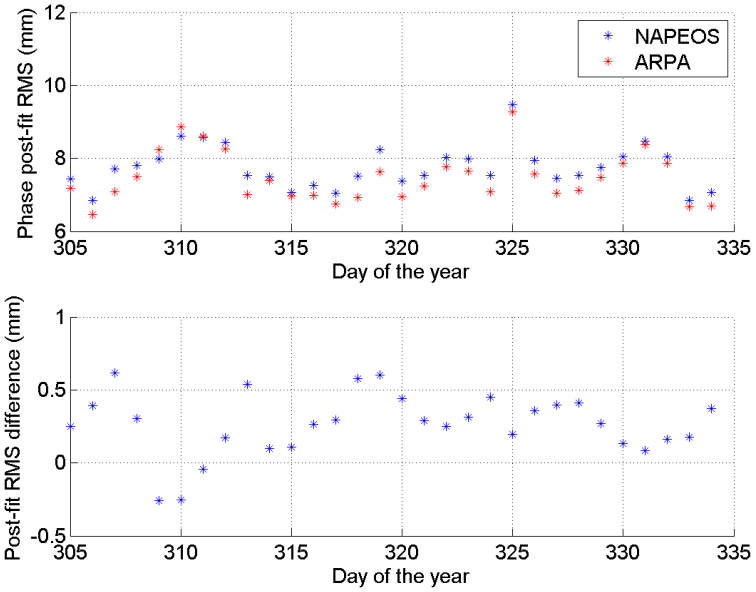

Figure 18: Post-fit RMS dei residui di fase GPS e loro differenza per i modelli di aerodinamica di NAPEOS (palla di cannone) e di ARPA. Una differenza positiva rappresenta una diminuzione dei valori con il modello ARPA.

In conclusione Un sistema software (ARPA — analisi di pressione di radiazione e di aerodinamica) è stato progettato e sviluppato presso l'Università di Padova, in grado di calcolare le forze e i momenti agenti sui satelliti dovuti alle seguenti perturbazioni non gravitazionali: pressione di radiazione solare (SRP), pressione di radiation terrestre per le componenti di albedo (ERP albedo)e di radiazione infrarossa (ERP IR), la pressione indotta sul satellite dalla radiazione termica emessa dal satellite stesso(TRR) e l'aerodinamica. Il

sistema software per applicazioni di POD NAPEOS, mantenuto ad ESA/ESOC, è stato settato e ne è stato eseguito un opportuno upgrade al fine di utilizzare i database di forze non gravitazionali di ARPA.

La determinazione orbitale precisa di GOCE è stata eseguita con NAPEOS per 30 archi giornalieri con inizio coincidente con l'inizio della fase scientifica il 1 Novembre 2009, al fine di testare e validare ogni database di perturbazione non gravitazionale di ARPA. I risultati ottenuti con i modelli ARPA sono confrontati con i modelli standard di NAPEOS (palla di cannone). Due set di test case son stati settati: 1) set di test radiativi (SRP, ERP albedo e IR, e TRR), sfruttando il modo drag-free di GOCE, e 2) set di test aerodinamici, considerando il profilo di spinta e l'aerodinamica di GOCE. I risultati per i test radiativi hanno mostrato una lieve riduzione media (0.03 mm) del post-fit RMS dei residui di fase GPS per tutti i 30 giorni e una riduzione significativa delle accelerazioni empiriche stimate, principalmente nella direzione cross-track, di circa il 20% con il modello ARPA per SRP, 12% con il modello ARPA per ERP albedo, 13% con il modello ARPA per ERP IR, e 20% con il modello ARPA per TRR. Tutte le orbite calcolate con i modelli di ARPA hanno mostrato coerenza con le orbite scientifiche precise ufficiali a dinamica ridotta, con una distanza da esse inferiore ai 4 cm. I risultati del test aerodinamico hanno mostrato una riduzione media del post-fit RMS 0.316 mm per il 90% dei giorni testati, fino a 0.6 mm in certi casi. La distanza delle orbite calcolate con l'aerodinamica di ARPA dalle PSO ha mostrato una diminuzione media di circa 0.42 cm rispetto alla soluzione con la palla di cannone, mostrando coerenza con le soluzioni ufficiali e miglioramenti con i modelli di ARPA. Questi risultati hanno dimostrato la bontà dei modelli e le tecniche di ARPA adottati per tutte le perturbazioni non gravitazionali considerate.

Anche se i risultati sono presentati per il satellite GOCE, che è stato selezionato con banco di prova, le nuove tecniche e software sviluppati in ARPA sono adattabili a satelliti di ogni forma, siano essi in orbita intorno alla Terra, orbitanti altri pianeti o in attraversamento dello spazio interplanetario.

Chapter 1

GOCE mission overview

GOCE (Gravity field and steady-state Ocean Circulation Explorer) was launched on the 17th March 2009 as the first Earth Explorer core mission of the ESA Living Planet Program [48]. GOCE was flying at the very low altitude of about 250 km in a dawn-dusk

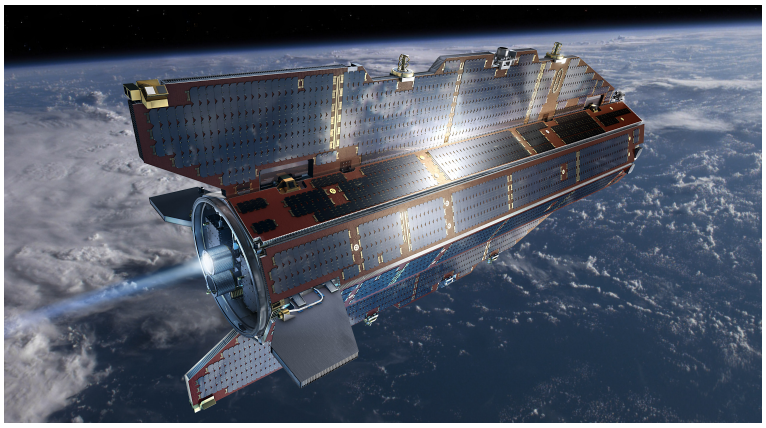

Figure 1.1: Sunny side of GOCE. (ESA at `http://www.esa.int/Our_Activities/Observing_the_Earth/The_Living_Planet_Programme/Earth_Explorers/GOCE/Satellite`)

sun-synchronous and nearly circular orbit, with an inclination of about 96.5 deg with respect to the Earth's equator. In particular the dawn dusk orbit assures a stable power supply from the body-mounted solar panels which are all the time exposed to the direct solar radiation, except for some short eclipses during winter and summer. The orbital plane remains approximately perpendicular towards the Sun direction. Due to its extremely low altitude, where the satellite experienced high aerodynamic braking forces, GOCE was designed with a very slim shape, with a cross-sectional area of 1.1 m^2 and a length of 5.3 m. It was mounting two wings, one at the top and one at the bottom, which were carrying additional solar panels, and two small winglets at its back, which provide additional passive aerodynamic stabilization to the spacecraft. For its peculiar shape and its Italian building site (Torino, at Thales-Alenia Space) GOCE has been unofficially named *a Ferrari in Space*. Its weight at its beginning of life was approximately 1050 kg.

The main purpose of GOCE was to map the static part of the Earth's gravity field with an unprecedented precision of 1 $mGal = 10^{-5}\ m/s^2$ and to model the geoid with an accuracy of 1 cm, with a spatial resolution of 100 km [26].

The scientific payload on-board GOCE was a three-axis Electrostatic Gravity Gradiometer (EGG), for the first time employed in a satellite mission. The EGG consists of three pairs of accelerometers along three spatially orthogonal directions. The accelerometers of a pair are separated by a 50 cm distance. The proof masses are made of platinum-rhodium alloy with a dimension of 4 cm by 4 cm by 1 cm. The proof mass is floating inside the accelerometer cage and is kept at its center by an electrostatic field. When the proof mass experienced a relative motion with respect to the cage (solidly connected to the satellite structure) the electrostatic field reacted in the opposite direction, restoring the previous mass position. From this change in the electrostatic field the experienced acceleration can be derived with extremely high accuracy. Since the accelerations of the proof masses are extremely weak and subject to noise and dissipative forces, the method of differential measurement is used. In fact, the difference of the accelerations experienced by a pair of accelerometers is measured, and this procedure allows to dispose of the other non-gravitational perturbations. In fact what GOCE was studying is the Earth's gravity gradient, measured by the difference of the accelerations experienced by each pair of accelerometers. The *common mode* accelerations measured by the gradiometer were instead due to the external perturbations (e.g., aerodynamics, radiation pressure) which are removed from the gravimetric measurements. The gravity gradient data were the primary scientific product of GOCE [26]. The gradiometer was used to recover the short-wavelength part of the gravity field in the frequency spectrum between 5 mHz and 100 mHz.

The common mode along-track acceleration experienced by the payload represents the external non-gravitational force acting on the spacecraft along that direction, mainly due to atmospheric drag and in a small part to the solar radiation pressure. This information is the input which commands the electric ion propulsion system. The satellite thrusters (two thrusters, one primary and one redundant), positioned at the back of the spacecraft, continuously compensated the along-track accelerations by thrusting the satellite in a close loop. The common mode along-track acceleration is in fact measured and compensated by the thrust, in order to maintaining the *drag-free mode*, extremely important for the gravimetric measurements. The varying thrust level provided by the ion-thruster compensates the in-orbit changing atmospheric drag, mainly related to differences in the atmospheric density. The solar activity significantly affects the atmospheric properties and the drag experienced by GOCE: in fact it has significantly increased from March 2011, causing the average thrust level to jump from about 2.7 mN to about 4 mN, with peaks up to 7.6 mN.

GOCE carried on-board also the SSTI-A/B (Satellite-to-Satellite Tracking Instrument A and B), which are two GPS receivers (A is primary, and B is redundant) which consist of a 12-channel LAGRANGE (Laben GNSS Receiver for Advanced Navigation, Geodesy and Experiments) receiver, working in both the L1 and L2 frequencies, with a sampling rate of 1 Hz. The SSTI instrumentation is used for the satellite orbit determination and for the retrieval of the long- and medium-wavelength components of the gravity field.

Due to its on-board continuously working thruster, GOCE had to carry with *him* all the fuel necessary to overcome the atmospheric drag. But his destiny was definitely sad, since after all the fuel was consumed, the satellite would have dropped in altitude, re-entering the atmosphere.

Figure 1.2: GOCE control team, during the last pass. (ESA at `http://blogs.esa.int/rocketscience/files/2013/11/goce_last_pass.png`)

GOCE ran out of fuel on the 21st October 2013, and its altitude started its progressive drop. The control team in ESOC, which has been working on the spacecraft since its launch, was able to get in contact with GOCE during its last pass in the night of the 12th November 2013, shown in Figure 1.2. GOCE re-entered the Earth's atmosphere near the Falkland Islands in the same night. The last image of the spacecraft is shown in Figure 1.3.

Figure 1.3: GOCE re-entering the atmosphere. (ESA at `http://spaceinimages.esa.int/var/esa/storage/images/esa_multimedia/images/2013/11/goce_reenters_atmosphere/13396346-1-eng-GB/GOCE_reenters_atmosphere.jpg`)

Chapter 2

Non-gravitational forces: literature overview

Since the beginning of the space age the accurate determination of orbits of artificial satellites has been used to improve geophysical [96],[80] and geodetic [49],[100] models of the Earth, including gravitational and non-gravitational force models related to the near-Earth environment. Mission objectives, both for Earth and interplanetary explorations, require increasingly accurate knowledge of the spacecraft position and velocity along the orbit. In the recent past, precision orbit determination (POD) techniques have brought down the 13 cm RMS accuracy of TOPEX/Poseidon in 1994 [96] to the 2-5 cm of GOCE in 2008 [13]. Future POD requirements will require the use of still more accurate modeling of forces to propagate and determine satellite trajectories. The force models commonly implemented in the POD software are highly accurate for what concerns the gravitational components (e.g., the EGM08 Earth gravity field model extends up to spherical harmonic of degree and order 180 considering the geodetic measurements of GOCE [84]), but less accurate in the formulation of the radiation pressure and aerodynamic perturbations acting on satellites, which form the main non-gravitational force components. In the recent years more effort has been done to achieve a better accuracy in the description of the non-gravitational forces on satellites. The importance of having a highly accurate description of these force components is not only related to the accuracy of the scientific data (e.g. GRACE,GOCE) but also for the "space debris campaign" that is at the moment at his primary stage. This will in turn provide useful information for the orbiting bodies dynamics, supporting the activities of orbit determination, propagation and forecast, and for space debris removal procedures. In this chapter an overview of the relevant literature is provided, in relation to the radiation pressure and aerodynamic effects on satellites and how these components are modeled.

2.1 Radiation Pressure models

A close look to the literature about radiation pressure shows that the first widely used solar radiation pressure model was developed for the Block I GPS satellites, by Rockwell International [74]. This model is usually referred to as the *ROCK4* model, and was developed between the end of the 70s and beginning of the 80s. This model, which is considering only the solar radiation pressure component, was developed simulating the interaction of the solar radiation over the GPS satellite. The GPS spacecraft is represented with 13 surfaces, each specified as either a flat plate or as a cylindrical surface [58]. To each of these surfaces information about orientation, area and optical properties (reflectivity and specularity) are provided, in order to compute the final acceleration due to SRP. This was followed by a similar model, the ROCK42 model, developed for the BLOCK II/IIA GPS satellites. For these two models even if the shadowing effects of one surface by another is considered, the secondary and further reflections are not modeled. This model requires the estimation or tuning of two scaling factors for the force components and a constant acceleration along the direction of the solar panels, often referred to as the Y-bias parameter. Both the *ROCK4* and *ROCK42* use the surfaces model to compute the SRP accelerations, then used to build a short Fourier series as a function of the angle between the sun and nadir direction.

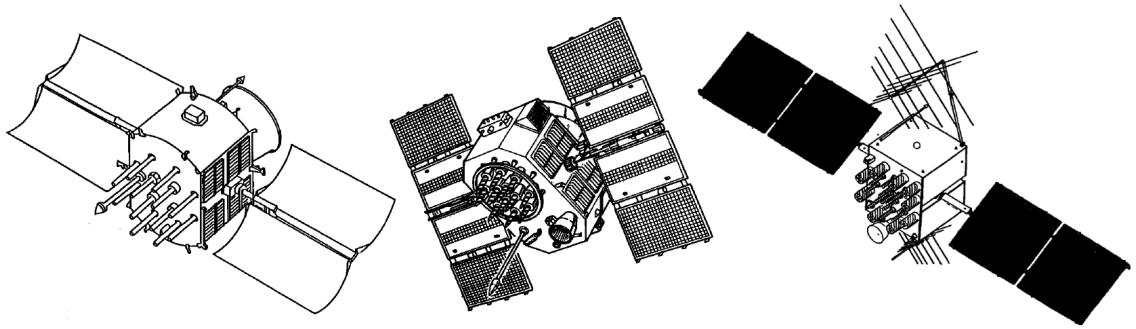

Figure 2.1: From left to right showing: GPS Block I, GPS Block II, GPS Block IIR spacecrafts ([29],Fig. 1a, 1b, 1c).

Although the *ROCK* models satisfied Air Force operational requirements at the time it was delivered, it was necessary to improve it to meet the demands of the late 1980s and the 1990s[29]:

1. the ROCK models are considering only the visible light coming from the Sun. No thermal emission of the spacecraft surfaces is considered, which, on the other hand, has the effect of increasing (+3.9% and +5.0% respectively for Block I and Block II) the total radiation force;

2. several ROCK users reported unmodeled along-track accelerations, apparently produced by a force acting in the direction of the solar panels ($\pm Y$ body-fixed direction). Subsequently, this acceleration was called "Y-bias". Three possible causes of these

effects were identified: 1) the solar panels axis is not perfectly straight or perfectly normal to the bus median plane, 2)the solar sensors are not perfectly align with the designed direction, 3) the heat generated by the bus is preferentially emitted by one side rather the other.

Since the *ROCK* models used only the pseudo-range data for the orbit and parameters estimation, they have an accuracy of about 1 meter [90].

Fliegel, Gallini and Swift[29] included the thermal emission components to the *ROCK* models. The bus and solar panels thermal emission was included to the *ROCK4* model and the *ROCK42* leading to the *T10* and *T20* models respectively. In a second time, when the GPS Block IIR were being built to replace the previous versions, Fliegel and Gallini[30] developed the T30 model, again accounting for the solar and thermal radiation pressure. Likewise the *ROCK* models, each output of T-models can be represented as a short Fourier series, function of the angle between the sun and the nadir directions. The expected error was about 2-3% of the total force, and the corresponding error in orbit prediction was about 3 or 4 meters after 12 hours, almost entirely in-track, giving about 0.5 meters error in pseudorange.

A completely different approach to the radiation pressure modeling has been done by Yoaz E. Bar-Sever and Kenneth M. Russ at the Jet Propulsion Laboratory, California Institute of Technology. As described in [6] and lately in [5], the GPS constellation of Block II and Block IIA satellites was used as a prototype for developing and validating the new approach. It can be described as follow: 1) in a first stage a parameterized model of the solar radiation pressure is developed and, 2) using daily GPS precise ephemerides, produced routinely at JPL for the International GPS Service (IGS), over a period of 9 months, the parameters of the model are adjusted to achieve the best fit. As stated in [6], the resulting model proved to be more accurate than the standard solar pressure model for GPS satellites shown in [29], for the T-models. Even if this model does not consider directly the interaction between the solar radiation and the spacecraft, but is merely oriented to absorb these effects by means of a set of parameters, it leads to the following benefits:

- a cost reduction, due to the replacement of costly pre-launch design phase with cheap post-launch process;

- increased accuracy, due to sensing of actual satellite behavior, as opposed to theoretical behavior;

- increased accuracy, by allowing an infinite fine-tuning process, since with more time, more data are available for the parameters tuning.

In a separate effort, a new solar pressure model for eclipsing GPS satellites was also developed. This empirical technique is hence capable of modeling the actual forces acting on the satellites. Specifically, this model recover the Y-bias acceleration that the ROCK and T-models were not capable of modeling, and this is probably the major contributor to the improvement over the previous models. The model developed in [6] for the GPS Block II

is referred to as *GSPM.II.97* and the models described in [5] are called *GSPM.IIA.04* and *GSPM.IIR.04* respectively for the GPS Block IIA and IIR. In [5] the Bar-Severs Fourier expansion was extended to higher degrees and for the first time applied the empirical approach to the Block IIR satellites. The parameters were then estimated over 10-day orbit arcs using a least-squares procedure and the full covariance information from each 10-day fit.

Another empirical method was developed at the Center for Orbit Determination in Europe (CODE), one of the seven IGS Analysis Centers (ACs), located at the Astronomical Institute, University of Bern (AIUB), Switzerland. This model is based on two previous works [8] and [83]. In these two previous works an empirical model of perturbation due to direct radiation pressure is developed, based on 8 parameters: 6 parameters are the osculating Keplerian elements, while the other two are the *direct radiation pressure* p_0 and the *Y-bias* p_2. These two parameters are estimated for each GPS satellite and each arc of one to three days. This model is referred to as *Extended CODE Orbit Model* (ECOM),
The new and improved solar pressure model for the GPS satellites presented in [89] and [90] is an upgrade of this model. The new orbit parametrization consists of the conventional two parameters plus three additional parameters, a constant and two periodic terms (a cosine and a sine term) in the direction of the Sun ([89]). The performance of the new model is almost an order of magnitude better than the *ROCK* models, while it also allows a reduction of the number of orbit parameters to be estimated, significantly strengthening the GPS solutions. The remaining model error was estimated to be about 50 cm, whereas for the *ROCK* model the error is about 300 cm. The new radiation pressure model also allows a 7-day fit of the GPS orbits at the 7 cm level, solving for only two parameters.

With the advent of geodetic satellites such as TOPEX/Poseidon, GEOSAT, SPOT, and ERS-1 it was required a higher accuracy of the orbital computations to support the scientific data collected [3],[60], [61]. With the at-that-time recent improvements in the gravity field modeling, the accurate modeling of the nonconservative forces became a significant concern. In fact, the TOPEX/Poseidon mission requirements dictated that the mismodeling of the nonconservative forces of solar radiation, Earth albedo and infrared radiation, and spacecraft thermal imbalances produce no more than 6 *cm* radial RMS error over a 10-day period. This required the development of nonconservative force models which were taking into account the satellite's complex geometry, attitude, and surface properties. The new developed "box-wing" satellite model described in [3], [60], and [61] consists in modeling the TOPEX/Poseidon satellite as the combination of the flat plates arranged in the shape of a box, the bus, and a wing, the connected solar array. In this way a model composed of 8 surfaces (2 for the solar panel and 6 for the bus) was built. Optical and thermal properties are associated to each surface and the interaction with the accelerations due the radiation from the Sun, the Earth and thermal emission are computed independently for each surface and summed up. The parameters associated with each flat plate representing the surfaces is then adjusted to to obtain a better representation of the satellite acceleration history. The tuning procedure has been performed in two phases, based on the models :

1. a "micro-model", shown in Figure 2.2 in the center, is built based on finite element

analysis of the spacecraft and is used to generate the accelerations due to radiation in a variety of orbit orientations;

2. a "macro-model", the box-wing model shown in Figure 2.2 on the right, is then used and tuned to reproduce the accelerations observed for the micro-model.

It is stated in [60] and [61] that the tests indicated a straightforward solution for the computation of the solar radiation pressure accelerations, but the modeling necessary for the thermal imbalance was much more complicated due to the satellite's complex attitude control law. In order to compute the accelerations due to radiation pressure on the

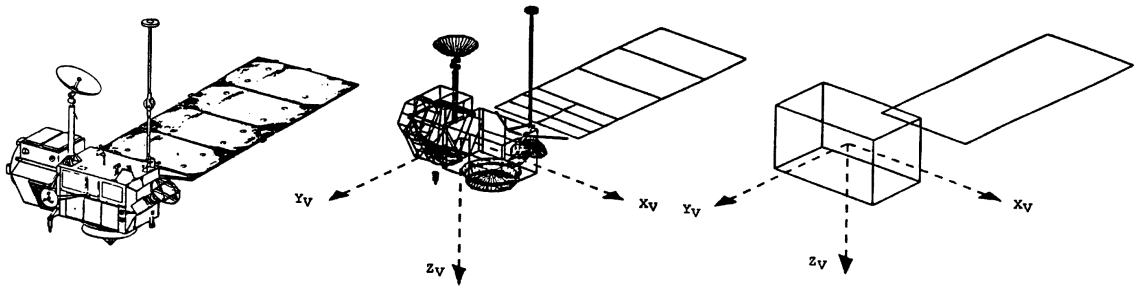

Figure 2.2: From left to right showing: TOPEX/Poseidon spacecraft, micro-model, and box-wing macro-model. ([61],Fig. 1a,b,c).

TOPEX/Poseidon satellite two software systems were used: 1) the Thermal Radiation Analysis System (TRASYS) to compute the fluxes from the Sun and the Earth incident on each surface of the spacecraft, and 2) SINDA to compute the transient orbital thermal history of each surface. Once the radiation fluxes and the temperatures of the surfaces have been defined, they are converted into accelerations. In order to compute the solar radiation pressure acting on the satellite the following value of the solar constant (solar irradiance) was selected

$$G_{\odot} = 1367.7\ W/m^2,$$

based on [103]. This value is than scaled with the actual distance of the spacecraft from the Sun, being the orbit of the Earth around the Sun slightly elliptical (generating a difference of $\pm 3\%$). During recent years a new value of the solar constant has been identified, as shown in [39], with a value of

$$G_{\odot} = 1366.1\ W/m^2.$$

In order to compute the accelerations due to the Earth radiation pressure it was necessary to correctly model the total radiation reflected and emitted by the Earth. In [60] and [61] a brief description of the radiant energy from the Earth is presented. As stated, a fraction of the solar radiation is instantly reflected off the land-water-snow-ice-atmosphere system as shortwave energy and the remainder is absorbed by the Earth. This absorbed energy is later emitted as longwave infrared radiation. For the albedo and infrared Earth radiation modeling the development given in [52] is adopted. In general, this model is based

on a discretization of the Earth into several elemental surface areas, and from each surface element the radiation toward the spacecraft is computed.
For the case of the albedo, the amount of radiation received by a satellite due to an elemental Earth surface, $dA_{\oplus}$, is

$$G_{\oplus-alb} = \frac{a\, G_{\odot}}{\pi\, r^2}\, \cos\theta_{\odot} \cos\gamma\, dA_{\oplus}, \tag{2.1}$$

where $\theta_{\odot}$ is the angle between the unit normal of the elemental Earth surface area and the direction to the Sun, γ is the angle between the Earth surface unit normal and the direction to the satellite, r is the distance from the Earth surface element to the satellite, and a is the albedo coefficient of the surface element. This model assumes that the Earth reflects and emits most of its energy in a diffuse way. In general, the albedo coefficient varies over the entire irradiated portion of the Earth, due to the different reflectivity of the Earth surface. For this modeling a longitudinally averaged model of albedo has been used, as specified in [52]. In this way a simple latitudinal model is used for the albedo, as well as for the Earth emissivity. With an average value of the albedo coefficient $a = 0.34$ the Earth surface reflects, on average, about 465 W/m^2 toward the outer space.

The infrared radiant energy flux density received by the satellite from an elemental Earth surface, $dA_{\oplus}$, is

$$G_{\oplus-IR} = \frac{\varepsilon\, G_{\odot}}{4 * \pi\, r^2}\, \cos\gamma\, dA_{\oplus}, \tag{2.2}$$

where ε is the emissivity of the surface element. With an average emissivity of the Earth of about $\varepsilon = 0.64$, the Earth surface emits, on average, about 232 W/m^2 toward the outer space.

Besides the accelerations induced on the satellite due to the Sun and Earth radiation components, the satellite Thermal Re-Radiation (TRR) is described. As a heated surface produces a thermal force due to its emission of infrared energy, a spacecraft surface with a temperature T will emit a longwave radiation equal to

$$G_{TRR} = \varepsilon\, \sigma\, T^4, \tag{2.3}$$

where σ is the Stefan-Boltzmann constant and ε is the emissivity of the satellite surface. As the temperature of the surface changes throughout the orbit, especially due to eclipsing, the magnitude of the thermal force can change substantially, affecting the spacecraft dynamics.

Another box-wing modeling approach has been developed at the Technische Universit ” at M ” unchen. As described in [82], this model is called *adjustable box-wing* model. It has been demonstrated that the physical models for solar radiation pressure on GPS satellites usually fail to predict the real orbit behavior with sufficient accuracy, mainly due deviations from the nominal attitude, inaccurately known optical properties, or aging of the satellite surfaces. The adjustable box-wing model presented is an intermediate approach between the purely physical/analytical modeling and the empirical models, based on parameters estimation during the spacecraft flight. In fact this model, developed for the GPS satellites of the Block II/IIA and IIR, is based on a modeled box-wing shape, as for shown for TOPEX/Poseidon, but with the difference that the surface optical properties of the

spacecraft are adjusted in order to fit the tracking data. In addition, the so called Y-bias and a parameter related to a rotation angle of the solar panels are estimated. This last parameter, not previously identified for GPS satellites, is a key factor for GPS orbit determination. In this model, shadowing and re-reflections effects are not taken into account. The rotation angles were computed to about 1.5° for GPS Block II/IIA and about 0.5° for GPS Block IIR. In [82] the results of this approach are presented and compared to the CODE empirical model. Using one year of data the estimated parameters and orbits are analyzed. It is stated that the performance of the two models are comparable, when looking at both the orbits overlap and the orbit prediction errors. Nevertheless, the models show important differences between the orbits at the 1-2 cm level and total accelerations. The differences are mainly due to the fundamentally different approaches, being the adjustable box-wing model based on the physical interaction between satellite surfaces and solar radiation, while the CODE is a purely empirical model. Rodriguez-Solano, in his master's thesis [81] carried out at the Technische Universit " at M " unchen, also studied the effects of the Earth radiation pressure on the GPS satellites. In his work he developed and compared models for the Earth radiation and models of the satellite structure that interact with the radiation coming from the Earth. Four different Earth radiation models were constructed and compared:

1. ERM-A: analytical Earth radiation model;
2. ERM-N: numerical Earth radiation model;
3. ERM-LAT: numerical latitude-dependent Earth radiation model;
4. ERM-CERES: numerical Earth radiation model from satellite observations.

These models will in general give the irradiance of the Earth at a certain satellite altitude and relative positions of satellite, Earth and Sun. The ERM-A analytical model is the analytical function that allows the computation of the Earth radiation flux reaching the satellite, based on a constant value for the albedo and a Lambertian reflection of the solar radiation on the Earth surface. The ERM-N numerical model is identical to the previous model, but solved numerically. Both the analytical and numerical models are developed for the reflected radiation (albedo) and the emitted radiation (infrared) components. These two models are anyway very approximative and do not consider the spatial distribution of the reflectivity and emissivity of the Earth. In order to improve the Earth radiation model, data from CERES (Clouds and Earths Radiant Energy System) project [102] were used. These data, as used by Rodriguez-Solano (already processed data of level 3), comes directly as monthly average maps in a spatial grid on latitude and longitude of $2.5° \times 2.5°$. Two sets of monthly maps are provided: one for the albedo component and one for emitted radiation, which are shown in Figure 2.3. By means of a polynomial fit over latitude and time of the year, these discrete maps were transformed into new maps, function of only the latitude (ERM-LAT). The four presented models were compared and the obtained results are shown in Table 2.1.

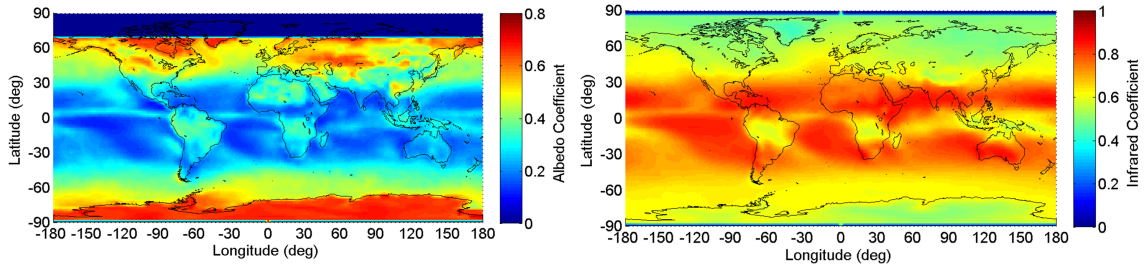

Figure 2.3: CERES January monthly map for albedo (on the left) and infrared (on the right) Earth radiation.

Table 2.1: Albedo Earth radiation models comparison at GPS location [81].

Model	Reflectivity and Emissivity	Mean difference	with respect to
ERM-CERES	CERES data	-	-
ERM-LAT	latitude dependent	0.1%	ERM-CERES
ERM-N	constant	2.1%	ERM-CERES
		2.0%	ERM-LAT
ERM-A	constant	1.6%	ERM-CERES
		1.5%	ERM-LAT
		0.0%	ERM-N

The adjustable box-wing model results were compared with a simple cannon-ball model. The cannon-ball is a simplified model which disregards the real physical dimensions and optical properties of the spacecraft, approximating them with a constant parameter, which is determined numerically from the average dimensions and optical properties of the satellite. The comparison shows averagely lower accelerations for the cannon-ball model with respect to the box-wing model. Moreover with the box-wing models it is clearly observable the change in the satellite attitude with respect to Earth incoming radiation, which leads to higher accuracies for both the albedo and emitted Earth radiation.

Another parameter that has been modeled is the so-called antenna thrust effect. As described in [81] and [107], also the radiation emitted by the GPS satellites antenna is exerting a pressure directly over the antenna. GPS satellites transmit between 70 and 80 watts in L1 and L2 carrier waves, in a constant body-fixed direction. These results in a negative radial acceleration of about $2.4 \times 10^{-10}\ m/s^2$.

A different approach to the description of the non-gravitational perturbations over satellites has been undertaken at the University College London, by the prof. Ziebart and his group. The adopted approach and techniques are presented in [108], [106], [107], [1], [87], and [67]. In [107], a general computer program is described, capable of computing analytical solar radiation pressure models specifically for GLONASS and GPS spacecrafts. In principle the method could be adapted for computing solar radiation pressure models for any spacecraft which have predictable attitude. The required definition of the spacecraft struc-

ture consists of a set of vertices describing the limits of the surface components in the form of regular or irregular planar polygons, and cylindrical shapes to describe curved objects, as Figure 2.4 is showing on the left hand side. The spacecraft components are subdivided into those that remain static in a body fixed reference frame, and those that can move and rotate, such as solar panels and antennas. In addition, the reflectivity and specularity coefficients for each component are defined. The photon flux from the Sun is gridded into an array of rectangular pixels. Each pixel is converted to a ray, traced toward the spacecraft solid model and a test is carried out to determine which surface component is intersected, as shown on the right hand side of Figure 2.4. With this method, the shadowing and auto-reflection effects are modeled with extremely high accuracy. The solar radiation pressure

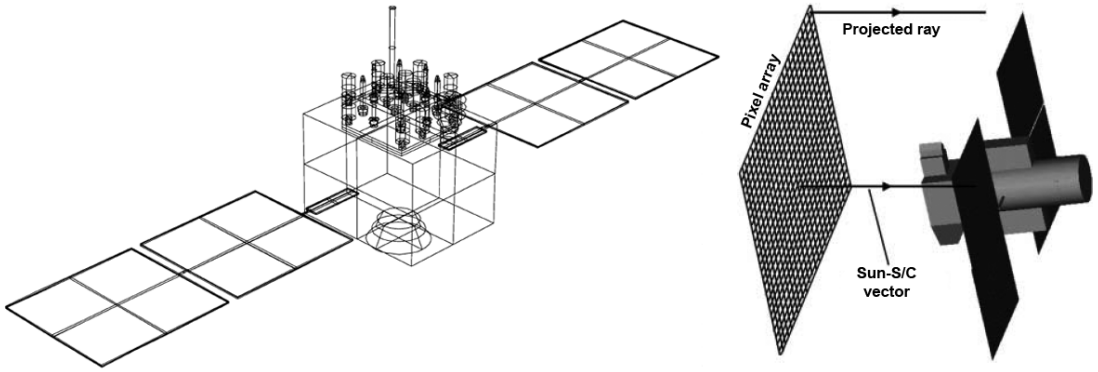

Figure 2.4: Modeling implemented at UCL: spacecraft structure broken down into geometric primitives (on the left, [106] Fig.5) and discretization of the solar radiation source into pixel array (on the right, [108] Fig.2).

acting on the spacecraft is computed for each ray traced from the pixel array toward the satellite. The effects due to all pixels are then summed giving a resultant force vector for the particular Earth-probe-Sun configuration. The pixel array is then rotated around the spacecraft, in order to simulate the possible directions of the incoming solar radiation, and the orientation of the solar panels is meanwhile adjusted to their tracking mode, computing forces and torques on the spacecraft for each orientation. The projection process is repeated for each array location, giving a series of discrete estimates of the response of the satellite to the incident flux. A continuous model (i.e., a Fourier series, spherical harmonics) or a discrete grid is then fitted to the data to give a compact and precise model to apply in the orbit determination process. The technique is described in [108] and [106]. This procedure has been also applied to the GLONASS spacecraft in [67].

A similar technique used to compute the insolation, is also adopted to compute the heat flow from these data. It is then possible to derive the temperatures of the different surfaces of the spacecraft and, integrating over the surface nodes, to compute the forces, again as a function of the satellite attitude. A comparison with the telemetered temperatures was carried out and precisely described in [1]. It is stated that the typically the thermal component of the non-conservative force field is around 5% of the solar radiation

pressure magnitude, but can reach as high as 10% for the GPS Block IIR. It is important to report that the GPS solar panels surface temperature telemetry does indicate that thermal venting is asymmetric and is probably driven by the asymmetric distribution of payload components in the bus. This may contribute to the satellite Y-bias. For the Earth radiation pressure modeling two maps were used: the Earth Radiation Budget Experiment (ERBE) and the Clouds and The Earth's Radiant Energy System (CERES) instruments, used to built monthly averaged maps. The modeling technique acts as a pre-processor to the orbit determination. In the first step a nominal satellite trajectory is used and for each position the number of grid cells visible to the satellite is computed. The radiation from each cell that reaches the satellite is then diminished due to the elevation angle of the satellite and the cell-satellite range. The final acceleration due to Earth radiation is computed for each satellite position. A Fourier series is then fit through the accelerations and the continuous model is then passed to the integrator at each epoch. The UCL group also implemented the antenna thrust effects and upgraded the model of eclipse, as described in [2].

An important activity for the orbit determination, related to interplanetary missions, has been carried out by Benny Rievers and his group at the Center of Applied Space Technology and Microgravity (ZARM) at Bremen, Germany. The work is focused on high precision thermal modeling of complex systems in order to accurately describe the thermal recoil forces, as shown in his works [79], [76], [78], and [77]. The approach adopted is based on a thermal finite elements analysis which can be used to compute thermal maps for different times during a spacecraft mission which are subjected to different illumination conditions and heat loads. For the analysis of the thermal radiation pressure for a complex spacecraft structure, the surfaces have to be divided into a subset of flat quadrilateral surface elements, for which the pressure can be computed individually by means of analytical models. The element resolution has to be high enough to realize a good resemblance of the real surface shapes. An example of this finite element method is shown in Figure 2.5. Based on the geometrical description and the thermal and optical properties of the surfaces, by means of a raytracing tool, the radiation-surface interaction (absorption and reflections) is computed. The resulting individual forces directly lead to the resulting thermal radiation pressure for the whole spacecraft. The thermal recoil force is evaluated in discrete steps on a complete spacecraft orbit.
As described in [77], in orbit determination the thermal recoil forces cannot be neglected. If not considered, the mismodeling can lead to anomalies in the orbit determination, computing the state of the spacecrafts. The analysis carried out by the group at ZARM has been applied so far to the NASA Pioneer 10/11 and ESA Rosetta spacecrafts. The analysis outlines that thermal recoil pressure is not the cause of the Rosetta flyby anomaly but likely resolves the anomalous acceleration observed for the Pioneer 10.

Similar approaches have been adopted to push the orbit accuracy to its limits in order to compute the non-gravitational perturbations. The effects of surface forces for complex spacecraft geometries have been implemented in softwares such as FreeMac [33] and FreeFlow [27], [28], specifically designed and maintained at Delft institute for Earth-Oriented Space research (DEOS) and ESOC. A most recent software package ANGARA

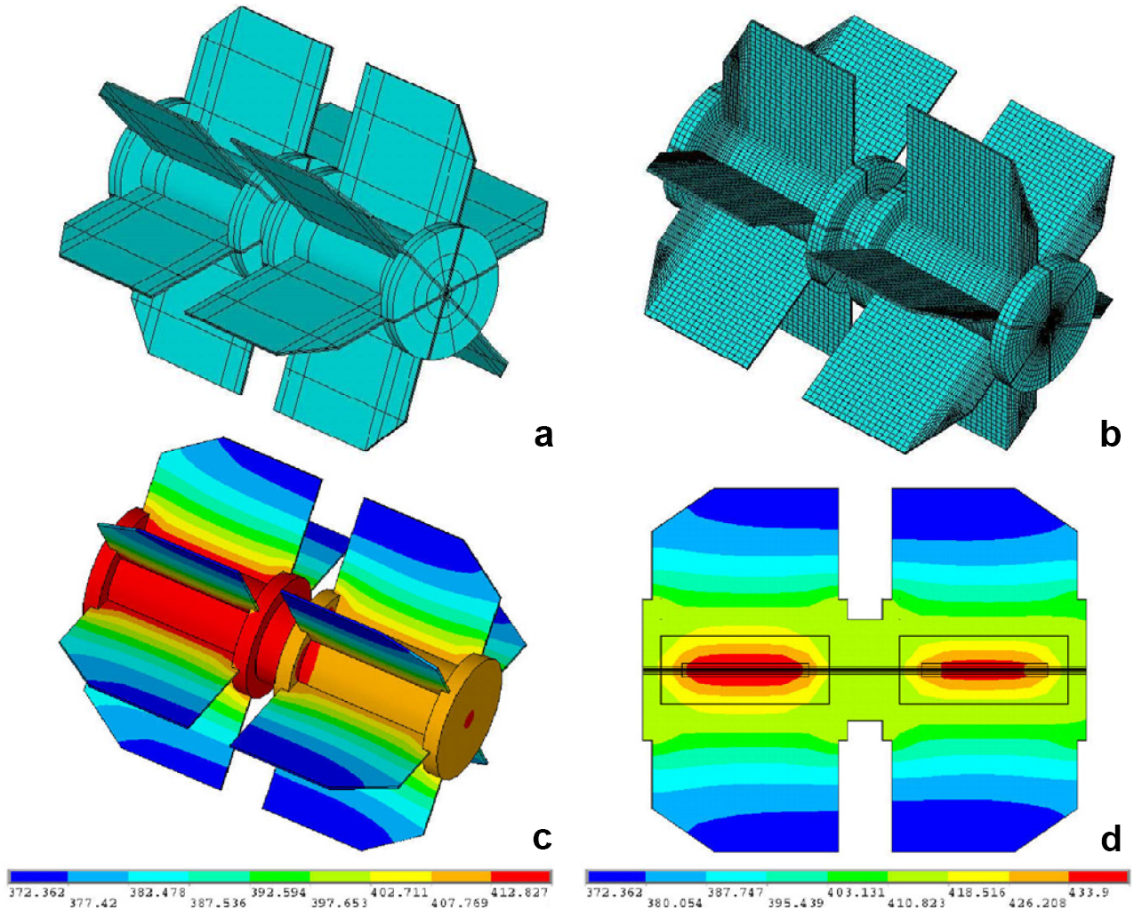

Figure 2.5: Modeling implemented at ZARM: NASA Pioneer 10/11 RTG pre-mesh (a) and mesh (b), and computed RTG temperatures (c and d) ([79] Fig.9 and Fig.13).

(Analysis of Non-Gravitational Accelerations due to Radiation and Aerodynamics [51, 34]) has been developed at ESA/ESOC and has been implemented for the ESA satellites ERS-2 and ENVISAT in the study of Doornbos [22]. These programs use a combination of geometric shadow or flow shielding analysis and integration over elementary surface elements. The ANGARA software package makes use of the Monte-Carlo test particle method to model the forces of radiation pressure and aerodynamics.

2.2 Aerodynamics

Aerodynamic forces acting on satellites are the major component of the non-gravitational perturbations for Low Earth Orbit (LEO) spacecrafts. The satellite aerodynamics derivation is based on the so called *free molecular flow theory*, due to the extremely rarefied atmospheric air-flow and high spacecraft velocities with respect to the atmosphere. The interaction of the atmospheric particles with the outer surfaces of the flying body induces

an acceleration on the satellite which can be described as

$$\mathbf{a}_D = -\frac{1}{2}\,\rho\,\frac{C_D\,A}{m}\,V_{rel}^2\,\hat{\mathbf{V}}_{rel}, \tag{2.4}$$

where ρ is the atmospheric density, C_D is the drag coefficient, A is the cross-sectional area, m is the mass of the spacecraft, and V_{rel} is the velocity of the satellite relative to the Earth co-rotating atmosphere. Equation 2.4 defines the acceleration due to the aerodynamic drag component, which is the component of the aerodynamic force aligned and opposite to the direction of the relative velocity. The in-track force — drag — is the predominant term in the satellite aerodynamics, and this is the component that is predominantly modeled in literature. Considering the three-dimensional aerodynamic force acting on the spacecraft, Equation 2.4 can be rewritten in a more general way as

$$\mathbf{a}_{aero} = -\frac{1}{2}\,\rho\,\frac{\mathbf{C}_{aero}\,A}{m}\,V_{rel}^2, \tag{2.5}$$

where $\mathbf{C}_{aero}$ is a vector which describes the interaction between the airflow and the satellite surfaces taking into account the direction of the resultant aerodynamic force in space — drag, lift and side-slip components. For satellites with accurately known shape and attitude, the largest sources of error are the atmospheric density ρ and the aerodynamic coefficients. In satellite aerodynamics, since it ρ and $\mathbf{C}_D$ are multiplied, it is usually very difficult to separate these two components, in order to correctly model the aerodynamic coefficients of the spacecraft or to derive the atmospheric density. Since the satellite drag component accounts for the majority of the force (at most 98.3% for GOCE), the satellite aerodynamics is usually referred to as "Satellite Drag Theory".

In the realm of spacecraft dynamics and orbit determination, the drag coefficient can be modeled in three different ways:

1. a constant drag coefficient;
2. a fitted drag coefficient;
3. a physical drag coefficient.

Early works which attempted to derive the satellite drag coefficients made use of laboratory measurements on sample objects. Experiments on clean surfaces led to the identification of a fixed drag coefficient of 2.2 for satellites with compact shapes [46, 19, 18]. This constant value has been adopted to derive densities with in-situ measurements and satellite tracking data [98]. The use of a fixed drag coefficient for compact satellites at different altitudes resulted in large biases in the estimated densities, showing its incapability of accurately modeling the interaction between the satellite surfaces and the air-flow. An upgraded model for the drag coefficients is the altitude-dependant, as studied and described in [93, 94, 65], mainly due to the change with altitude of the atmospheric temperature and mean molecular mass, as shown in Figure 2.6. This adopted solution, even if still simplistic, reduces the mean biases in density, well reproducing the atmospheric density variations reducing the errors in the previous density models. However, since the drag coefficients are a function

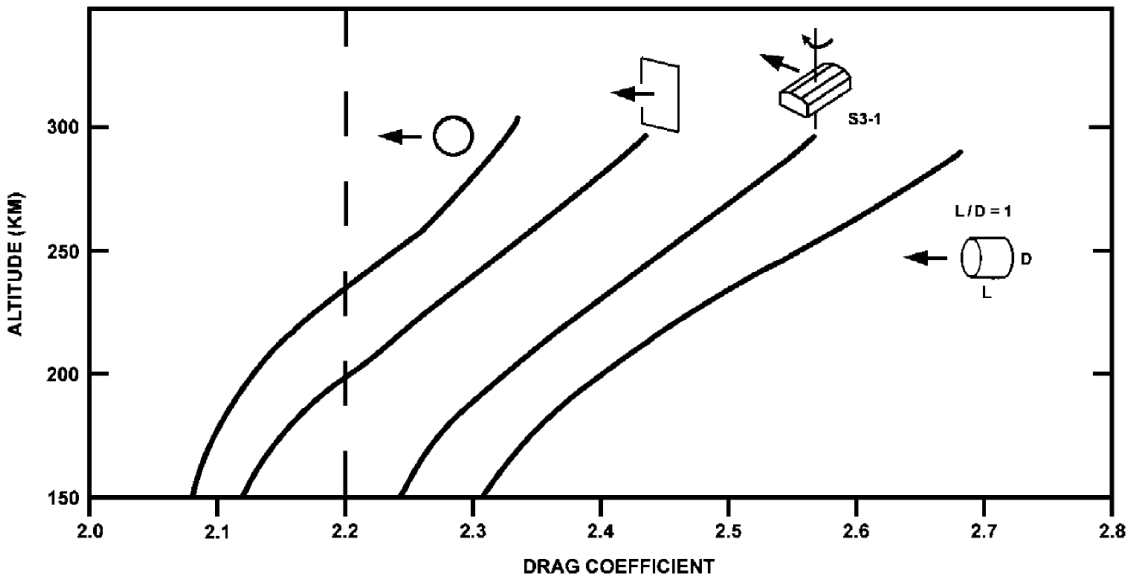

Figure 2.6: Drag coefficients of compact shapes as a function of the altitude. In contrast, the vertical line at 2.2 has been widely used as the drag coefficient for all satellites of compact shape. ([65] Fig.1).

only of the altitude, they do not reproduces the change in density along the orbit, also not modeling its short term variations, causing high uncertainties in the orbit estimation and prediction.

For fitted drag coefficients a different approach is used, and is purely based on their estimation as part of the orbit determination process. Fitted drag coefficients are nevertheless specific to the atmospheric model used and, therefore, carry along its limitations and eventual errors. In addition, due to the estimation process, drag coefficients tend to absorb all the unmodeled perturbations.

In order to better model the interaction of the atmospheric flow with the satellite surfaces different solutions were adopted to compute the physical satellite drag coefficient. A summary of the free-molecular flow theory is presented in [27], which can be applied to the computation of forces and toques due to the atmosphere upon close-earth satellites. In this document the 4 main parameters that affect the total drag acceleration on spacecrafts are identified:

1. incoming atmospheric flow characteristics — incident flow;
2. satellite geometry;
3. satellite surfaces properties;
4. gas-surface interaction.

While the geometry and the surface properties (mainly temperature and material of the outer surfaces) are satellite specific and can be accurately known and modeled, the at-

mospheric flow properties and the gas-surface interaction are the primary source of error for the drag computation. Due to its not perfectly known composition and properties, the atmospheric flow encountered by the satellite is commonly modeled as a distribution function of particles, which is the probability of finding atmospheric particles with certain characteristics at a certain point in the fluid. For the satellite aerodynamic the flow is so rarefied that the free-flow theory can be applied. In other words the movement of the particles is mutually independent. The incident flow can be modeled in different ways (different distribution functions), depending on the considered problem. For most the satellite problems, however, common assumed distribution function is in equilibrium, meaning that the flow has been moving undisturbed for a long enough time and it has a uniform distribution function. When the Mach number of the flow is relatively high the assumption of hypersonic flow can be done. This means that all the particles in the incident flow can be modeled as having a uniform speed $\mathbf{V}_{rel}$. The other significant characteristics of the flow (density, temperature, composition, and molecular mass) can be then obtained from in-situ measurements and/or atmospheric models. An other distinction that is usually done related to the flow properties is between thermal and hyperthermal flow. This distinction, as stated in [92], depends on the ratio (molecular speed ratio) between the mean thermal motion of the atmospheric particles and the relative velocity of the spacecraft with respect to the atmosphere. If the thermal motion is negligible with respect to the relative velocity the flow can be assumed *hyperthermal* and only the surfaces that are directly exposed to the flow contribute to the drag. On the other hand, if the thermal motion is significant, the flow must be assumed *thermal*. In contrast to the hyperthermal case, all the satellite outer surfaces experience impingement due to the random motion of the molecules. In this case the contribution to the drag will be higher for the frontal faces, but also the other faces (mainly the side faces which experience shear stress) will interfere with the flow, increasing the experienced drag.

The difficult task associated to the free-molecular flows is related to how the gas-surface interaction is modeled. A very few and scattered experimental data are available for modeling this interaction ([91]), especially due to the difficulties related to reproducing the extreme atmospheric conditions, and the behavior of the particles and the surface seems to be much more complicated than predicted by the models that are currently in use. Different interaction models have been developed in the past and they can be summarized in:

- *specular reflection*: with this model the particles hitting a surface are simply mirror-like reflected, disregarding the eventual surface roughness. This model is usually applied together with other reflections models;

- *diffuse reflection*: in this case the reflection of the incoming particles is completely diffuse, following the "cosine law". The fundamental concept of this model is that an impinging atmospheric particle enters the surface structure, arrives at a thermodynamical equilibrium and then, after some time, it is re-emitted in a purely random direction with a velocity that depends on the satellite surface temperature. This reflection model is very frequently used, because it has been observed that even

mirror-finished surfaces does not produce significant specular reflections;

- *Maxwellian model*: this model derives from the previous ones, where a fraction (σ) of the incoming molecules is reflected diffusely and the remanent fraction ($1 - \sigma$) is immediately reflected specularly. The parameter of the model σ is a number between 0 and 1 which represents the fraction of molecules reflected diffusely;

- *model of Schaaf and Chambre*: this model, presented in [85], is a modification of the Maxwellian model. This model does not attempt to describe the flow of the particles, but only tries to fit the experimental data available. In this model two parameters are introduced, in order to better describe the effects of the pressure and shear stress on the satellite surfaces, computing them with a different participation of specular reflection. This introduction of a second parameter with respect to the Maxwellian model allows fitting experimental data with more accuracy. In [27] the model is illustrated and the equations to compute aerodynamic forces due to momentum transfer in normal and shear directions are presented in the formulation adopted by [85, 54, 55].

- *model of Schamberg*: this model, developed by Schamberg in 1959 and described in [43], makes use of three parameters, where the third additional parameter controls the diffusion level of the flow, the energy accommodation with the satellite surfaces, and the angle of reflection. The significant characteristics of the Schamberg model are: 1) the incident flow is supposed to be hyperthermal; 2) reflected molecules depart in a conical beam with aperture defined by the first parameter ϕ; 3) the velocity of the reflected molecules is uniform, and is a function of the incident flow velocity and the second parameter α, called thermal accommodation coefficient; 4) the direction of the reflected particles depend on the direction on the incident flow and on the third parameter ν. These reflection laws were chosen to describe experimental results, accurately matching the observations done before early 60s. For more recent data, which have higher resolution, the observations are not matched anymore with the same high accuracy, and several reflection laws of this form have to superimposed to match the experimental data.

Due to how they were developed, the model of Schaaf and Chambre and the model of Schamberg can be considered as hybrids between purely fitted and physical drag coefficients. A graphical description of the models can be observed in Figure 2.7. Closed-form solutions of the drag coefficients for simple shapes such as flat plates, spheres, cylinders, and conical frustums were derived in [85, 86], and applied to simple shape satellites.

Another important reflection model for the free molecular flow is the *Nocilla model*, developed and described in [68, 41]. Test cases and free molecular flow theory is also greatly described with experiments in [42]. In this model normal and tangential momentum transfer from atmospheric molecules to surfaces are computed and thermal accommodation is introduced.

Based on the presented models different softwares were implemented and tested, in order to derive the drag coefficients of satellites. The software developed by the end of the

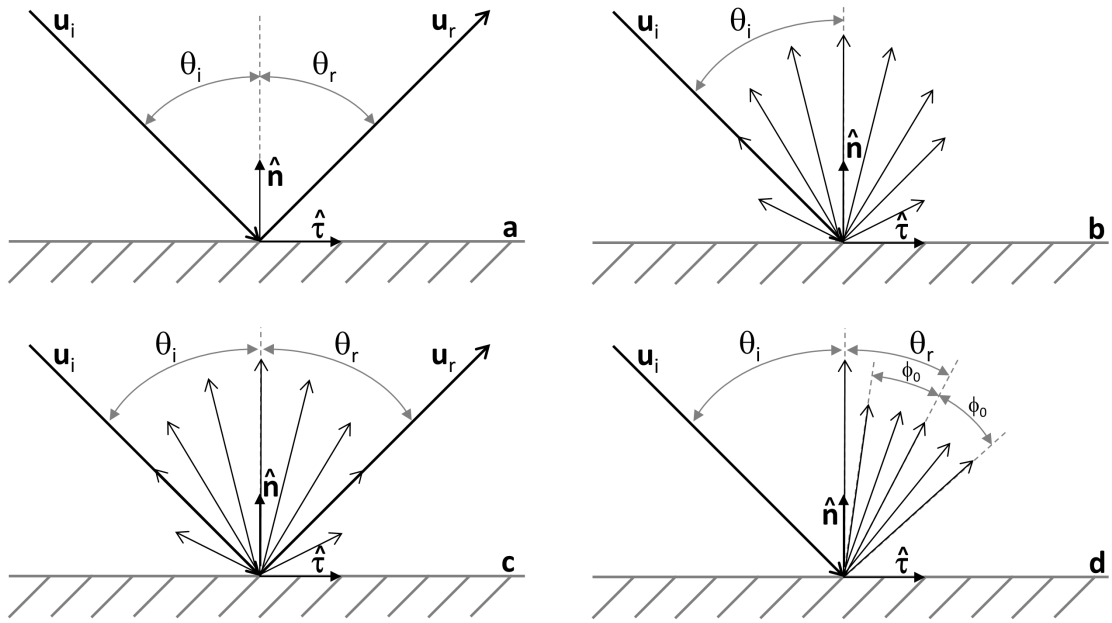

Figure 2.7: Reflection models for free molecular flow: a) diffuse reflection, b) specular reflection, c) Maxwellian model and model of Schaaf and Chambre, d) model of Schamberg.

80s, used at the European Space Agency at ESOC is *FREEFLW* [27, 28]. *FREEFLW* is based on the single-impingement hypothesis, meaning that only the first reflection of the air particles over the satellite surfaces is considered. This software is capable of computing aerodynamic forces and torques on simple shape satellites. The program accepts as input the primitive geometries which compound the spacecraft (e.g., flat surfaces, cylinders), then, by means of a shadow algorithms, identifies the surfaces and portion of surfaces directly exposed to the airflow. *FREEFLW* uses an integral method, that is the momentum exchange equations provided by the reflection models are integrated on the exposed primitive geometries, leading to the computation of aerodynamic forces and toques. This software relies on the model of Schaaf and Chambre and the model of Schamberg, but other reflection models can be implemented. In addition *FREEFLW* can also compute radiation pressure perturbations using the Maxwell model as photon-surface interaction law.

Another software developed for computing the satellite aerodynamics is *RAMSES* — a Rarefied Aerodynamics Modelling System for Earth Satellites — developed at the Hypersonic Technology G ” ottingen, Lindau/Harz, Germany as a contract for ESA/ESOC [56, 57, 51]. *RAMSES* consists of several subsystems which provide satellite geometry generation as primitive shapes, a free molecular integral and Monte Carlo method, based on either the model of Maxwell or of Schaaf and Chambre or Nocilla, a bridging method for the transitional regime and postprocessing of the results. The Monte Carlo method allows the computation of aerodynamic forces also for multiple collisions inside a main control volume. The particles path is followed by the software from their introduction in a control

volume, during their subsequent reflections on the satellite surfaces and then they are lost when they exit the control volume.

A previous work related to skin-force modeling for satellites has been carried out by the Matra Espace, Toulouse, France [50], under an ESA contract. This software, by means of Monte-Carlo raytracing, is capable of computing forces and torques due to aerodynamics, direct solar radiation pressure and Earth radiation pressure (albedo and IR). Fritsche and Klinkrad [36, 35] developed the *ANGARA* system — Analysis of Non-Gravitational Accelerations due to Radiation and Aerodynamics —, which also makes use of the Test Particle Monte Carlo (TPMC). Doornbos [22, 24]used the *ANGARA* system to model drag coefficients for the ERS-2 and ENVISAT satellites.

Graziano[38] in his dissertation did a comparative study of all the computational tools available for modeling spacecraft aerodynamics. In his proposed Spacecraft Engineering, Design, and Analysis Tools (SEDAT) system, he used a hybrid of the Ray-Tracing Panel (RTP) and the Test Particle Monte Carlo methods for aerodynamic analysis.

Mehta [63, 64] adopted the Direct Simulation Monte Carlo (DSMC) method, developed by Bird [9, 10, 11], is a computational technique for the simulation of dilute gas flows at the molecular level and is, to date, the basic numerical method in the kinetic theory of gases and rarefied gas dynamics. In his work Mehta presents innovative and state-of-the-art technique of developing parameterized drag coefficient models which is presented and validated using the GRACE satellite.

One of the most recent research activities related to the satellite aerodynamic modeling has been carried out by Pilinski and his group at ASTRA and at the University of Colorado, Boulder (Colorado) [71, 72, 73]. Their work is mainly focused on the determination of the energy accommodation coefficient, which is formally defined as the fraction of kinetic energy lost by the molecules incident on the spacecraft surfaces upon reemission. Accurately modeling the energy accommodation coefficient it is possible to compute the total amount of momentum exchanged between the airflow and the satellite, and therefore the satellite drag coefficient. What is innovative in their work is the sophistication of the "lattice theory", or theory of the substrate, based on Goodman's theory [37]. In other words, depending on the atmospheric components and on the satellite orbit, the incoming air particles do not always directly impact on the satellite surfaces but can interact with a thin substrate of air which is covering the spacecraft. The main component that has a direct impact on the accommodation coefficient is the amount of atomic oxygen that is covering the satellite surfaces. It has been observed that discrepancies between laboratory data and real cases, such as LEO satellites or reentering bodies, can be related to the fact that the the amount of atomic oxygen in the thermosphere adsorbs onto the satellite surfaces. In this way the incoming molecules, instead of interacting with a metallic lattice or glass surface of a solar panel, collide with the lighter adsorbate species, resulting in a more inelastic collision. Atomic oxygen adsorption has been confirmed by observation from pressure gauges and is the primary reason for the altitude dependence of the drag coefficient. Since the models derived by ASTRA are based both on physical derivations and fitted data, these are called semi-empirical models. The most recent and complete work that was also adopted in the

aerodynamic work of this thesis is the so called Semi-Empirical Satellite Accommodation Model — SESAM[73].

Chapter 3

Fundamentals of Statistical Orbit Determination

3.1 Introduction

Statistical Orbit Determination is the set of techniques that allows the estimate of the orbital parameters of a spacecraft or a celestial body during its motion around the Earth or more generally in the Solar System.

Since the knowledge of the true state (position and velocity, and other parameters) of the considered body will never be absolute, statistical techniques are necessary. In particular, the least squares approach is used to minimize the differences between observations and a model of them, computed through a set of parameters that form the *dynamic* and *kinematic* models and propagated in time through a set of differential equations, the equations of motion. This requires a parametrization of the problem and depends on the physics of the problem itself.

The classical orbit determination problem is characterized by the assumption that the bodies move under the influence of a central force. For the satellite orbit determination problem the minimal set of parameters required is the position and velocity vectors at some given epoch. This minimal set can then be expanded to include dynamic and measurement model parameters, which may be needed to improve the orbit determination and prediction accuracy. Indicating the general state vector at a time t as $\mathbf{X}(t)$, the general orbit determination problem can be posed as follow.

If at an initial epoch, t_0, the state $\mathbf{X}_0$ of a body following a ballistic trajectory is given and if the equations of motion are known, these can be integrated to determine the state of the body at any time. However, in real conditions, the initial state is never known exactly. Moreover, certain physical constants as well as the mathematical models of the forces acting on the body are known only with a certain level of approximation. Such errors will cause the propagated trajectory of the body to deviate from the real one. Consequently, in order to determine the position and velocity of a satellite at some time $t \neq t_0$, it must be tracked from tracking stations (ground stations) or satellites (e.g. GNSS constellation)

whose position is precisely known, as shown in Figure 3.1. With the observations of the spacecraft motion, a better estimate of its trajectory can be determined. The estimate of the trajectory is not exact since the observations and the models are intrinsically affected by both random and systematic errors.

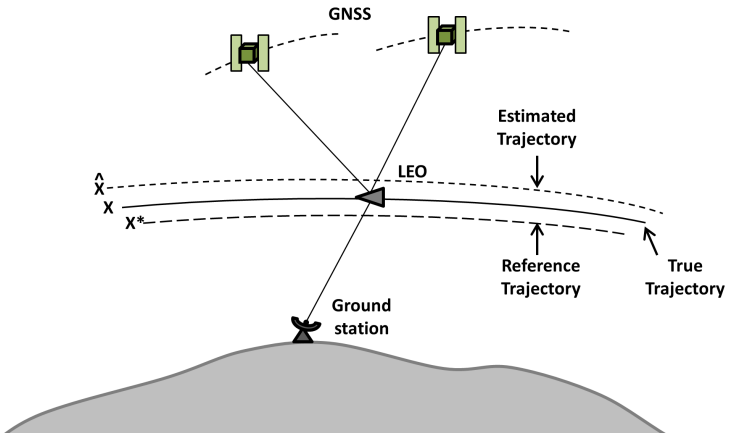

Figure 3.1: Low Earth orbit satellite tracking, by means of ground stations and GNSS satellites.

The problem of determining the best estimate of the state of a body, whose initial state is unknown, from observations and models affected by errors, is referred to as the problem of state estimation. Once the best estimate of the initial state vector and model parameters are determined, the state vector and other parameters can be determined for different epochs.

The estimated values can differ from the true values due to the following effects:

- inaccuracies in the estimated state vector caused by errors in the orbit determination process, such as:
  1. approximations involved in the method of orbit improvement and in the mathematical model;
  2. errors in the observations;
  3. errors in the computational procedure used in the solution process;
- errors in the numerical integration procedure caused by errors in the dynamical model and computer truncation and roundoff errors.

To obtain a better orbit estimate, a sufficient number of observations must be available covering the time span of interest.

In general, rather than being directly observable, the observations are non-linear functions of the state vector parameters. Also the differential equations of motion are strongly non linear and this leads to the conclusion that multiple solutions for the estimation problem can be found, but only one is the optimal.

The most common method of orbit determination is the *least-squares* approach. The goal is to minimize the *observation residuals*, the difference between the true measurements and their computed values. There are essentially two ways to update the state vector:

- the *sequential* or *recursive* estimation, if a new estimate is obtained after each observation;
- the *batch* estimation, If all the measurements are collected and then processed to obtain an estimate of the state vector at a specified initial epoch (*batch epoch*).

Generally speaking, a sequential estimator (e.g. Kalman filter) is more sensitive to the goodness of the individual points and converges faster to the right solution (if properly tuned) than a batch algorithm. This is usually used for real-time applications. The batch estimation is slower since different iterations are usually required before it converges, but leads to solutions with higher accuracy. The method adopted in this thesis is the batch estimation as developed and applied to satellite precise orbit determination by Tapley, [97].

This thesis has the objective of developing a new methodology for modeling the non-gravitational forces on Earth orbiting satellites, in order to decrease the level of approximation usually adopted for these models. As approach for test and validate the new method, the least square batch estimation procedure is adopted.

3.2 Linearization of the orbit determination process

In the general orbit determination problem, both the dynamics and the measurements involve significant nonlinear relationships. For the general case, the governing relations involve the nonlinear expression

$$\dot{\mathbf{X}} = \mathbf{F}(\mathbf{X}, t)\,, \qquad \mathbf{X}(t_k) \equiv \mathbf{X}_k\,, \tag{3.1}$$

$$\mathbf{Y}_i = \mathbf{G}(\mathbf{X}_i, t_i) + \boldsymbol{\varepsilon}_i\,, \qquad i = 1, ..., l\,, \tag{3.2}$$

where $\mathbf{X}_k$ is the unknown n-dimensional state vector at the time t_k, and $\mathbf{Y}_i$ for $i = 1, ..., l$, is a p-dimensional set of observations that are to be used to obtain a best estimate of the unknown value of $\mathbf{X}_k$ (i.e. $\hat{\mathbf{X}}_k$). In general, $p < n$ and $m = p \times l \gg n$.

The formulation represented by Equation 3.1 and 3.2 is characterized by:

- the inability to observe the state directly;
- nonlinear relations between the observations and the state;
- fewer observations at any time epoch than there are state vector components ($p < n$);
- errors in the observations represented by $\boldsymbol{\varepsilon}_i$.

As previously said, the equations of motion $\mathbf{F}(\mathbf{X}, t)$ of a satellite and the model of observation $\mathbf{G}(\mathbf{X}_i, t_i)$ are usually non-linear. If the state vector and the observation vector can be related in a linear manner, then the linear estimation theory can be applied to the orbit determination problem.

In order to linearize the problem it is necessary that a reasonable reference trajectory $\mathbf{X}^*$ is available, and that the true trajectory$\mathbf{X}$ and the reference trajectory remain sufficiently close throughout the time interval of interest. Under these conditions the trajectory for the actual motion can be expanded in a Taylor's series about the reference trajectory at

each point in time. If this expansion is truncated after the first order, then the deviation in the state from the reference trajectory can be described by a set of linear differential equations with time-dependent coefficients. In a similar manner it is possible to linearize the observation deviation and the state deviation. In this way, the nonlinear orbit determination problem in which the complete state vector is to be estimated can be replaced by a linear orbit determination problem in which the deviation from some reference solution is to be determined.

To carry out this linearization procedure, let the $n \times 1$ state deviation vector, $\mathbf{x}$, and the $p \times 1$ observation deviation vector, $\mathbf{y}$, be defined as follows:

$$\begin{aligned} \mathbf{x}(t) &= \mathbf{X}(t) - \mathbf{X}^*(t)\,, \\ \mathbf{y}(t) &= \mathbf{Y}(t) - \mathbf{Y}^*(t)\,. \end{aligned} \tag{3.3}$$

It follow that

$$\dot{\mathbf{x}}(t) = \dot{\mathbf{X}}(t) - \dot{\mathbf{X}}^*(t)\,. \tag{3.4}$$

Expanding Equation 3.1 and 3.2 in a Taylor's series about the reference trajectory leads to

$$\begin{aligned} \dot{\mathbf{X}}(t) &= \mathbf{F}(\mathbf{X}, t) = \mathbf{F}(\mathbf{X}^*, t) + \left[\frac{\partial \mathbf{F}(t)}{\partial \mathbf{X}(t)}\right]^* \mathbf{x}(t) + \dots\,, \\ \mathbf{Y}_i(t) &= \mathbf{G}(\mathbf{X}_i, t_i) + \boldsymbol{\varepsilon}_i = \mathbf{G}(\mathbf{X}_i^*, t_i) + \left[\frac{\partial \mathbf{G}}{\partial \mathbf{X}}\right]_i^* \mathbf{x}_i + \dots + \boldsymbol{\varepsilon}_i\,, \end{aligned} \tag{3.5}$$

where the star indicates that the partial derivative matrix is evaluated on the reference solution, $\mathbf{X}^*(t)$, which is obtained by integrating Equation 3.1 with the specified initial conditions, $\mathbf{X}^*(t_0)$. If the terms of order higher than the first in Equation 3.5 are neglected, and if the condition $\dot{\mathbf{X}}^* = \mathbf{F}(\mathbf{X}^*, t)$ and $\mathbf{Y}_i^* = \mathbf{G}(\mathbf{X}_i^*, t_i)$ are used, Equation 3.5 can be written as

$$\begin{aligned} \dot{\mathbf{x}}(t) &= \mathbf{A}(t)\mathbf{x}(t)\,, \\ \mathbf{y}_i &= \tilde{\mathbf{H}}_i \mathbf{x}_i + \boldsymbol{\varepsilon}_i\,, \qquad i = 1, ..., l\,, \end{aligned} \tag{3.6}$$

where

$$\mathbf{A}(t) = \left[\frac{\partial \mathbf{F}(t)}{\partial \mathbf{X}(t)}\right]^*, \qquad \tilde{\mathbf{H}}_i = \left[\frac{\partial \mathbf{G}}{\partial \mathbf{X}}\right]_i^*. \tag{3.7}$$

In conclusion, the original nonlinear estimation problem is replaced with a linear estimation problem described by Equation 3.6, where

$$\begin{aligned} \mathbf{x}(t) &= \mathbf{X}(t) - \mathbf{X}^*(t)\,, \\ \mathbf{x}_i &= \mathbf{X}(t_i) - \mathbf{X}^*(t_i)\,, \\ \mathbf{y}_i &= \mathbf{Y}_i - \mathbf{G}(\mathbf{X}_i^*, t_i)\,. \end{aligned}$$

Since this thesis is focused on the implementation of the non-gravitational forces acting on the satellite it is fundamental to remark the following: the newly implemented method should provide

1. the acceleration $\dot{\mathbf{X}}^*$ in order to propagate the state vector;

2. the partial derivatives of the equations of motion with respect to the state vector $\left[\frac{\partial \mathbf{F}(t)}{\partial[\mathbf{r},\mathbf{v}]}\right]^*$, to propagate the state transition matrix;

3. the partial derivatives of the equations of motion with respect to the parameters if the model $\left[\frac{\partial \mathbf{F}(t)}{\partial \boldsymbol{\beta}}\right]^*$, again to propagate the state transition matrix.

3.2.1 The state transition matrix

The first of Equation 3.6 represents a system of linear differential equations with time-dependents coefficients. The symbol $[]^*$ indicates that the values of $\mathbf{X}$ are derived from a particular solution to the equations $\dot{\mathbf{X}} = \mathbf{F}(\mathbf{X}, t)$ which is generated with the initial conditions $\mathbf{X}(t_0) = \mathbf{X}_0^*$. The general solution for this system, $\dot{\mathbf{x}}(t) = \mathbf{A}(t)\mathbf{x}(t)$, can be expressed as

$$\mathbf{x}(t) = \boldsymbol{\Phi}(t, t_k)\mathbf{x}_k \,, \tag{3.8}$$

where $\mathbf{x}_k$ is the value of $\mathbf{x}$ at t_k, that is, $\mathbf{x}_k = \mathbf{x}(t_k)$. The matrix $\boldsymbol{\Phi}(t_i, t_k)$ is called the *state transition matrix*. The state transition matrix has the following useful properties:

$$\begin{aligned} \boldsymbol{\Phi}(t_i, t_i) &= \mathbf{I} \,, \\ \boldsymbol{\Phi}(t_i, t_k) &= \boldsymbol{\Phi}(t_i, t_j)\boldsymbol{\Phi}(t_j, t_k) \,, \\ \boldsymbol{\Phi}(t_i, t_k) &= \boldsymbol{\Phi}^{-1}(t_k, t_i) \,. \end{aligned} \tag{3.9}$$

The differential equation for $\boldsymbol{\Phi}(t_i, t_k)$ can be obtained by differentiating Equation 3.8 (noting that $\mathbf{x}_k$ is a constant). This yields

$$\dot{\mathbf{x}}(t) = \dot{\boldsymbol{\Phi}}(t, t_k)\mathbf{x}_k \,. \tag{3.10}$$

Substituting Equation 3.10 into the first of Equation 3.6 and using Equation 3.8 yields

$$\dot{\boldsymbol{\Phi}}(t, t_k)\mathbf{x}_k = \mathbf{A}(t)\boldsymbol{\Phi}(t, t_k)\mathbf{x}_k \,. \tag{3.11}$$

Since this condition must be satisfied for all $\mathbf{x}_k$, it follows that

$$\dot{\boldsymbol{\Phi}}(t, t_k) = \mathbf{A}(t)\boldsymbol{\Phi}(t, t_k) \,, \tag{3.12}$$

with initial conditions

$$\boldsymbol{\Phi}(t_k, t_k) = \mathbf{I} \,. \tag{3.13}$$

Under certain conditions on $\mathbf{A}(t)$, the state transition matrix may be inverted analytically.

3.2.2 Solution for the state transition matrix

A linear differential equation of the type $\dot{\mathbf{x}}(t) = \mathbf{A}(t)\mathbf{x}(t)$ or $\dot{\mathbf{\Phi}}(t, t_0) = \mathbf{A}(t)\mathbf{\Phi}(t, t_0)$ has an infinite number of solutions in terms of arbitrary constants. However, when initial conditions, $\mathbf{x}(t_0)$ and $\mathbf{\Phi}(t_0, t_0)$, are specified and the elements of $\mathbf{A}(t)$ are continuous functions of time, the solution becomes unique.

The solution for $\mathbf{\Phi}(t, t_0)$ is facilitated by noting that the individual columns of the differential equation for $\dot{\mathbf{\Phi}}(t, t_0)$ are uncoupled and independent. To illustrate this, consider the following case where the state vector is given by

$$\mathbf{X}(t) = [\mathbf{r}, \mathbf{v}, \boldsymbol{\beta}]^T \,. \tag{3.14}$$

$\mathbf{X}$ is the state vector containing six position and velocity elements and $\boldsymbol{\beta}$, an m-vector, represents all constants parameters that are to be solved for. Hence, $\mathbf{X}$ is a vector of dimension $n = m + 6$. Equation 3.12 can be written in terms of the individual elements of the state transition matrix as follows:

$$\dot{\mathbf{\Phi}}(t, t_0) = \begin{bmatrix} \dot{\Phi}_{11} & \dot{\Phi}_{12} & \dot{\Phi}_{13} \\ \dot{\Phi}_{21} & \dot{\Phi}_{22} & \dot{\Phi}_{23} \\ \dot{\Phi}_{31} & \dot{\Phi}_{32} & \dot{\Phi}_{33} \end{bmatrix} = \begin{bmatrix} A_{11} & A_{12} & A_{13} \\ A_{21} & A_{22} & A_{23} \\ A_{31} & A_{32} & A_{33} \end{bmatrix} \begin{bmatrix} \Phi_{11} & \Phi_{12} & \Phi_{13} \\ \Phi_{21} & \Phi_{22} & \Phi_{23} \\ \Phi_{31} & \Phi_{32} & \Phi_{33} \end{bmatrix} , \tag{3.15}$$

subject to the following initial conditions at t_0

$$\begin{bmatrix} \Phi_{11} & \Phi_{12} & \Phi_{13} \\ \Phi_{21} & \Phi_{22} & \Phi_{23} \\ \Phi_{31} & \Phi_{32} & \Phi_{33} \end{bmatrix} = \begin{bmatrix} \mathbf{I} & \mathbf{0} & \mathbf{0} \\ \mathbf{0} & \mathbf{I} & \mathbf{0} \\ \mathbf{0} & \mathbf{0} & \mathbf{I} \end{bmatrix} = \mathbf{I} \,. \tag{3.16}$$

Recall that the A_{ij} are known quantities obtained by evaluating

$$A_{ij}(t) = \left[\frac{\partial \mathbf{F}_i(t)}{\partial \mathbf{X}_j(t)} \right]^* , \tag{3.17}$$

on the reference trajectory. From Equation 3.15 it can be observed that the columns of $\dot{\mathbf{\Phi}}(t, t_0)$ are independent. Hence, it can be solved for $\mathbf{\Phi}(t, t_0)$ by integrating independently two 3×1 vector differential equations. For any practical orbit determination application, the solution for $\mathbf{\Phi}(t, t_0)$ will be obtained via numerical integration. Hence, we can supply a vector of derivative values for the differential equation of the nominal state vector and $\dot{\mathbf{\Phi}}(t, t_0)$ to the numerical integration routine. For this one-dimensional case we would supply the integrator with the following vector at each time point:

$$\begin{bmatrix} \dot{\mathbf{r}} & \dot{\mathbf{v}} & \dot{\Phi}_{11} & \dot{\Phi}_{21} & \dot{\Phi}_{31} & \dot{\Phi}_{12} & \dot{\Phi}_{22} & \dot{\Phi}_{32} & \dot{\Phi}_{13} & \dot{\Phi}_{23} & \dot{\Phi}_{33} \end{bmatrix}^T . \tag{3.18}$$

The first two elements would provide the reference orbit, $\mathbf{X}^*(t)$, and the next nine would yield the elements of $\mathbf{\Phi}(t, t_0)$. The reference orbit is used to evaluate $\mathbf{A}(t)$, which is needed to evaluate $\dot{\mathbf{\Phi}}(t, t_0)$ in Equation 3.15.

3.2.3 Relating the observations to an epoch state

Using Equation 3.8, the second of Equation 3.6 may be written in terms of the state at t_k as

$$\begin{aligned} \mathbf{y}_1 &= \tilde{\mathbf{H}}_1\mathbf{\Phi}(t_1,t_k)\mathbf{x}_k + \boldsymbol{\varepsilon}_1\,, \\ \mathbf{y}_2 &= \tilde{\mathbf{H}}_2\mathbf{\Phi}(t_2,t_k)\mathbf{x}_k + \boldsymbol{\varepsilon}_2\,, \\ &\vdots \\ \mathbf{y}_l &= \tilde{\mathbf{H}}_l\mathbf{\Phi}(t_l,t_k)\mathbf{x}_k + \boldsymbol{\varepsilon}_l\,. \end{aligned} \tag{3.19}$$

Equation 3.19 now contain $m = p \times l$ observations and only n unknown components of the state. If $\boldsymbol{\varepsilon}_i$ (with $i = 1, ..., l$) is zero, any linearly independent n of Equation 3.19 can be used to determine $\mathbf{x}_k$.

If the following definitions are used

$$\mathbf{y} = \begin{bmatrix} \mathbf{y}_1 \\ \vdots \\ \mathbf{y}_l \end{bmatrix}, \qquad \mathbf{H} = \begin{bmatrix} \tilde{\mathbf{H}}_1\mathbf{\Phi}(t_1,t_k) \\ \vdots \\ \tilde{\mathbf{H}}_l\mathbf{\Phi}(t_l,t_k) \end{bmatrix}, \qquad \boldsymbol{\varepsilon} = \begin{bmatrix} \boldsymbol{\varepsilon}_1 \\ \vdots \\ \boldsymbol{\varepsilon}_l \end{bmatrix}, \tag{3.20}$$

and if the subscript on $\mathbf{x}_k$ is dropped for convenience, then Equation 3.19 can be expressed as follows:

$$\mathbf{y} = \mathbf{H}\mathbf{x} + \boldsymbol{\varepsilon}\,, \tag{3.21}$$

where $\mathbf{y}$ is an $m \times 1$ vector, $\mathbf{x}$ is an $n \times 1$ vector, $\boldsymbol{\varepsilon}$ is an $m \times 1$ vector, $\mathbf{H}$ is an $m \times n$ mapping matrix, where $m = p \times l$ is the total number of observations. If p or l is sufficiently large, the essential condition $m > n$ is satisfied.

3.3 Least squares estimate

The least squares solution selects the estimate of $\mathbf{x}$ as that value that minimizes the sum of the squares of the calculated observation residuals. That is, $\mathbf{x}$ is selected to minimize the following *performance index*:

$$J(\mathbf{x}) = \frac{1}{2}\boldsymbol{\varepsilon}^T\boldsymbol{\varepsilon}\,. \tag{3.22}$$

The sum of the squares of the calculated observation errors is a logical choice for the performance index. A criterion defined, for example, by the sum of calculated observation errors could be identically zero with very large observation errors having plus and minus signs that cancel each other. Whether the observation error is positive or negative, its square will be positive and the performance index defined by Equation 3.22 can vanish only if each of the observation errors is identically zero. If $\boldsymbol{\varepsilon}$, as defined by Equation 3.21, is substituted into Equation 3.22, the following expression is obtained:

$$J(\mathbf{x}) = \frac{1}{2}\boldsymbol{\varepsilon}^T\boldsymbol{\varepsilon} = \sum_{i=1}^{l}\frac{1}{2}\boldsymbol{\varepsilon}_i^T\boldsymbol{\varepsilon}_i = \frac{1}{2}(\mathbf{y}-\mathbf{H}\mathbf{x})^T(\mathbf{y}-\mathbf{H}\mathbf{x})\,. \tag{3.23}$$

Note that Equation 3.23 is a quadratic function of $\mathbf{x}$, and as a consequence the expression will have a unique minima when

$$\frac{\partial J}{\partial \mathbf{x}} = \mathbf{0}\,, \qquad \text{and} \qquad \delta\mathbf{x}^T \frac{\partial^2 J}{\partial \mathbf{x}^2}\delta\mathbf{x} > \mathbf{0}\,, \tag{3.24}$$

for all $\delta\mathbf{x} \neq 0$. The second condition implies that the symmetric matrix $\frac{\partial^2 J}{\partial \mathbf{x}^2}$ is positive definite.

Carrying out the first operation on Equation 3.23 yields

$$\frac{\partial J}{\partial \mathbf{x}} = \mathbf{0} = -(\mathbf{y} - \mathbf{H}\mathbf{x})^T\mathbf{H} = -\mathbf{H}^T(\mathbf{y} - \mathbf{H}\mathbf{x})\,. \tag{3.25}$$

The value of $\mathbf{x}$ that satisfies Equation 3.25 will be the best estimate of $\mathbf{x}$, which we will call $\hat{\mathbf{x}}$. Hence,

$$(\mathbf{H}^T\mathbf{H})\hat{\mathbf{x}} = \mathbf{H}^T\mathbf{y}\,. \tag{3.26}$$

Also

$$\frac{\partial^2 J}{\partial \mathbf{x}^2} = \mathbf{H}^T\mathbf{H}\,, \tag{3.27}$$

which will be positive definite if $\mathbf{H}$ is full rank.

Three major shortcomings of the simple least square solution are:

1. each observation error is weighted equally even though the accuracy of observations may differ;
2. the observation errors may be correlated (not independent), and the simple least squares solution makes no allowance for this;
3. the method does not consider that the errors are samples from a random process and makes no attempt to utilize any statistical information.

3.3.1 Weighted least squares solution

Given a vector sequence of observations $\mathbf{y}_1$, $\mathbf{y}_2$, ..., $\mathbf{y}_l$ related through the state transition matrix to the state at some epoch time, $\mathbf{x}_k$, and an associated weighting matrix, $\mathbf{w}_i$, for each of the observations vectors, one can write

$$\begin{aligned} \mathbf{y}_1 &= \mathbf{H}_1\mathbf{x}_k + \boldsymbol{\varepsilon}_1\,, & \mathbf{w}_1;\\ \mathbf{y}_2 &= \mathbf{H}_2\mathbf{x}_k + \boldsymbol{\varepsilon}_2\,, & \mathbf{w}_2;\\ &\vdots & \\ \mathbf{y}_l &= \mathbf{H}_l\mathbf{x}_k + \boldsymbol{\varepsilon}_l\,, & \mathbf{w}_l; \end{aligned} \tag{3.28}$$

where $\mathbf{H}_i$ is the matrix $\tilde{\mathbf{H}}_i$ propagated at the time t_i:

$$\mathbf{H}_i = \tilde{\mathbf{H}}_i\boldsymbol{\Phi}(t_i, t_k)\,. \tag{3.29}$$

In Equation 3.28 the weighting matrices, $\mathbf{w}_i$, are assumed to be diagonal with their elements normalized to a range between zero and one. Observations weighted with a one would be

given the highest possible weight and those weighted with zero would be neglected. The following definitions can be used

$$\mathbf{y} = \begin{bmatrix} \mathbf{y}_1 \\ \mathbf{y}_2 \\ \vdots \\ \mathbf{y}_l \end{bmatrix}, \qquad \mathbf{H} = \begin{bmatrix} \mathbf{H}_1 \\ \mathbf{H}_2 \\ \vdots \\ \mathbf{H}_l \end{bmatrix}, \qquad \boldsymbol{\varepsilon} = \begin{bmatrix} \boldsymbol{\varepsilon}_1 \\ \boldsymbol{\varepsilon}_2 \\ \vdots \\ \boldsymbol{\varepsilon}_l \end{bmatrix}, \qquad \mathbf{W} = \begin{bmatrix} \mathbf{w}_1 & 0 & ... & 0 \\ 0 & \mathbf{w}_2 & ... & 0 \\ \vdots & \vdots & ... & \vdots \\ 0 & 0 & ... & \mathbf{w}_l \end{bmatrix}. \tag{3.30}$$

Each observation $\mathbf{y}_i$ is assumed to be a p-vector and $\mathbf{x}_k$ is a n-vector. Equation 3.28 now can be expressed as

$$\mathbf{y} = \mathbf{H}\mathbf{x}_k + \boldsymbol{\varepsilon}\,, \qquad \mathbf{W}\,. \tag{3.31}$$

The weighted least square problem can then be posed as follows: given the linear observation state relationship expressed by Equation 3.31, find the estimate of $\mathbf{x}_k$ to minimize the weighted sum of the squares of the calculated observation errors.

The performance index is

$$J(\mathbf{x}_k) = \frac{1}{2}\boldsymbol{\varepsilon}^T\mathbf{W}\boldsymbol{\varepsilon} = \sum_{i=1}^{l}\frac{1}{2}\boldsymbol{\varepsilon}_i^T\mathbf{W}\boldsymbol{\varepsilon}_i\,. \tag{3.32}$$

Using Equation 3.31, $J(\mathbf{x}_k)$ can be expressed as

$$J(\mathbf{x}_k) = \frac{1}{2}(\mathbf{y} - \mathbf{H}\mathbf{x}_k)^T\mathbf{W}(\mathbf{y} - \mathbf{H}\mathbf{x}_k)\,. \tag{3.33}$$

A necessary condition for a minimum of $J(\mathbf{x}_k)$ is that its first derivative with respect to $\mathbf{x}_k$ vanishes

$$\frac{\partial J}{\partial \mathbf{x}_k} = \mathbf{0} = -(\mathbf{y} - \mathbf{H}\mathbf{x}_k)^T\mathbf{W}\mathbf{H} = -\mathbf{H}^T\mathbf{W}(\mathbf{y} - \mathbf{H}\mathbf{x}_k)\,. \tag{3.34}$$

This expression can be rearranged to obtain the normal equations in the least squares formulation as

$$(\mathbf{H}^T\mathbf{W}\mathbf{H})\mathbf{x}_k = \mathbf{H}^T\mathbf{W}\mathbf{y}\,. \tag{3.35}$$

If the normal matrix $\mathbf{H}^T\mathbf{W}\mathbf{H}$ is positive definite, it will have an inverse and the solution to Equation 3.35 is

$$\hat{\mathbf{x}}_k = (\mathbf{H}^T\mathbf{W}\mathbf{H})^{-1}\mathbf{H}^T\mathbf{W}\mathbf{y}\,. \tag{3.36}$$

The value of $\hat{\mathbf{x}}_k$ given by Equation 3.36 is the weighted least squares estimate and is the estimate that minimizes the sum of squares of the weighted observation errors. Note that Equation 3.36 can be expressed as

$$\hat{\mathbf{x}}_k = \mathbf{P}_k\mathbf{H}^T\mathbf{W}\mathbf{y}\,, \tag{3.37}$$

where

$$\mathbf{P}_k = (\mathbf{H}^T\mathbf{W}\mathbf{H})^{-1}\,. \tag{3.38}$$

The $n \times n$ matrix $\mathbf{P}_k$ is symmetric. Furthermore, if it exists, it must be positive definite, since it is computed as the inverse of the positive definite matrix, $\mathbf{H}^T\mathbf{W}\mathbf{H}$. The parameter

observability is related to the rank of this matrix. If all parameters in $\mathbf{x}_k$ are observable (i.e., can be uniquely determined with the observation set $\mathbf{y}$), then $\mathbf{P}_k$ will be full rank and $\mathbf{P}_k$ will have an inverse. The number of independent observations must be greater than or equal to the number of parameters being estimated if $\mathbf{P}_k$ is to be invertible. Furthermore, $\mathbf{P}_k$ is related to the accuracy of the estimate, $\hat{\mathbf{x}}_k$. In general, the larger the magnitude of the elements of the matrix, $\mathbf{P}_k$, the less accurate the estimate.

If an a priori value, $\bar{\mathbf{x}}_k$, is available for $\mathbf{x}_k$ and an associated weighting matrix, $\bar{\mathbf{W}}_k$, is given, the weighted least square estimate for $\mathbf{x}_k$ can be obtained by choosing for $\hat{\mathbf{x}}_k$ the value of $\mathbf{x}_k$, which minimizes the performance index

$$J(\mathbf{x}_k) = \frac{1}{2}(\mathbf{y} - \mathbf{H}\mathbf{x}_k)^T\mathbf{W}(\mathbf{y} - \mathbf{H}\mathbf{x}_k) + \frac{1}{2}(\bar{\mathbf{x}}_k - \mathbf{x}_k)^T\bar{\mathbf{W}}_k(\bar{\mathbf{x}}_k - \mathbf{x}_k)\,. \tag{3.39}$$

This results in

$$\hat{\mathbf{x}}_k = (\mathbf{H}^T\mathbf{W}\mathbf{H} + \bar{\mathbf{W}}_k)^{-1}\left(\mathbf{H}^T\mathbf{W}\mathbf{y} + \bar{\mathbf{W}}_k\bar{\mathbf{x}}_k\right)\,, \tag{3.40}$$

where $\bar{\mathbf{x}}_k$ represents an a priori estimate of $\mathbf{x}_k$ and $\bar{\mathbf{W}}_k$ represents a weighting matrix for the a priori estimate of $\mathbf{x}_k$.

3.3.2 The minimum variance estimate

The least squares and weighted least squares methods do not include any information on the statistical characteristics of the measurement errors or the a priori errors in the values of the parameters to be estimated. The minimum variance approach is one method for removing this limitation. The minimum variance criterion is used widely in developing solutions to estimation problems because of the simplicity in its use. It has the advantage that the complete statistical description of the random errors in the problem is not required. Rather, only the first and second moments of the probability density function of the observation errors are required. This information is expressed in the mean and covariance matrix associated with the random error.

If it is assumed that the observation error $\boldsymbol{\varepsilon}_i$ is random with zero mean and specified covariance, the state estimation problem can be formulated as follows.

Given the system of state-propagation equations and observation state equations

$$\mathbf{x}_i = \boldsymbol{\Phi}(t_i, t_k)\mathbf{x}_k\,, \tag{3.41}$$

$$\mathbf{y}_i = \tilde{\mathbf{H}}_i\mathbf{x}_i + \boldsymbol{\varepsilon}_i\,, \qquad i = 1, ..., l\,, \tag{3.42}$$

find the linear, unbiased, minimum variance estimate, $\hat{\mathbf{x}}_k$, of the state $\mathbf{x}_k$.

Using the state transition matrix and the definitions of Equation 3.28, it is possible to reduce Equation 3.41 to the following form

$$\mathbf{y} = \mathbf{H}\mathbf{x}_k + \boldsymbol{\varepsilon}\,, \tag{3.43}$$

where

$$E[\boldsymbol{\varepsilon}] = \begin{bmatrix} E[\boldsymbol{\varepsilon}_1] \\ E[\boldsymbol{\varepsilon}_2] \\ \vdots \\ E[\boldsymbol{\varepsilon}_l] \end{bmatrix} = \begin{bmatrix} \mathbf{0} \\ \mathbf{0} \\ \vdots \\ \mathbf{0} \end{bmatrix}, \qquad E[\boldsymbol{\varepsilon}\boldsymbol{\varepsilon}^T] = \begin{bmatrix} \mathbf{R}_{11} & \mathbf{R}_{12} & ... & \mathbf{R}_{1l} \\ \mathbf{R}_{12}^T & \mathbf{R}_{22} & ... & \mathbf{R}_{2l} \\ \vdots & ... & ... & \vdots \\ \mathbf{R}_{1l}^T & ... & ... & \mathbf{R}_{ll} \end{bmatrix} = \mathbf{R}\,.$$

Generally, $\mathbf{R}_{11} = \mathbf{R}_{22} = ... = \mathbf{R}_{ll}$ and $\mathbf{R}_{ij} = \mathbf{0}$ $(i \neq j)$, but this is not a necessary restriction. $\mathbf{R}_{ij} \neq \mathbf{0}$ $(i \neq j)$ corresponds to the more general case of time-correlated observation errors.

From the problem statement, the estimate is to be the best linear, unbiased, minimum variance estimate. The consequences of each of these requirements are addressed in the following steps.

1. *Linear*: the requirement of a linear estimate implies that the estimate is to be made up of a linear combination of the observations:

$$\mathbf{x}_k = \mathbf{M}\mathbf{y}\,. \tag{3.44}$$

   The $n \times m$ matrix $\mathbf{M}$ is unspecified and is to be selected to obtain the best estimate.

2. *Unbiased*: if the estimate is unbiased, then by definition

$$E[\hat{\mathbf{x}}] = \mathbf{x}\,. \tag{3.45}$$

   Substituting Equation 3.44 and 3.41 into Equation 3.45 leads to the following requirement

$$E[\hat{\mathbf{x}}_k] = E[\mathbf{M}\mathbf{y}] = E[\mathbf{M}\mathbf{H}\mathbf{x}_k + \mathbf{M}\boldsymbol{\varepsilon}] = \mathbf{x}_k\,. \tag{3.46}$$

   But, since $E[\boldsymbol{\varepsilon}] = \mathbf{0}$, this reduces to

$$\mathbf{M}\mathbf{H}\mathbf{x}_k = \mathbf{x}_k\,, \tag{3.47}$$

   from which the following constraint on $\mathbf{M}$ is obtained

$$\mathbf{M}\mathbf{H} = \mathbf{I}\,. \tag{3.48}$$

   That is, if the estimate is to be unbiased, the linear mapping matrix $\mathbf{M}$ must satisfy Equation 3.48. This condition requires the rows of $\mathbf{M}$ to be orthogonal to the columns of $\mathbf{H}$.

3. *Minimum Variance*: if the estimate is unbiased, then the estimation error covariance matrix can be expressed as

$$\mathbf{P}_k = E\{[(\hat{\mathbf{x}}_k - \mathbf{x}_k) - E(\hat{\mathbf{x}}_k - \mathbf{x}_k)][(\hat{\mathbf{x}}_k - \mathbf{x}_k) - E(\hat{\mathbf{x}}_k - \mathbf{x}_k)]^T\} = E[(\hat{\mathbf{x}}_k - \mathbf{x}_k)(\hat{\mathbf{x}}_k - \mathbf{x}_k)^T]\,. \tag{3.49}$$

The strategy is to minimize the last expression satisfying the two constraints 1) and 2) at the same time. It can be shown (see [97]) that this leads to the following formulas:

$$\mathbf{P}_k = \left(\mathbf{H}^T\mathbf{R}^{-1}\mathbf{H}\right)^{-1}, \tag{3.50}$$

$$\hat{\mathbf{x}}_k = \left(\mathbf{H}^T\mathbf{R}^{-1}\mathbf{H}\right)^{-1}\mathbf{H}^T\mathbf{R}^{-1}\mathbf{y}\,. \tag{3.51}$$

Note that computation of the estimate, $\hat{\mathbf{x}}_k$, requires inverting the $n \times n$ normal matrix $\mathbf{H}^T\mathbf{R}^{-1}\mathbf{H}$. For a large dimension system the computation of this inverse may be difficult. For this reason, alternative techniques have been employed (Cholesky decomposition, Householder transformations and Given's rotations, see [97] [75]). The solution given by Equation 3.51 will agree with the weighted least square solution if the weighting matrix, $\mathbf{W}$, used in the least square approach is equal to the inverse of the observation noise covariance matrix; that is if $\mathbf{W} = \mathbf{R}^{-1}$.

3.3.3 Propagation of the estimate and covariance matrix

If an estimate at a time t_j is obtained by using Equation 3.51, the estimate may be mapped to any later time by using the state transition matrix $\mathbf{\Phi}$

$$\bar{\mathbf{x}}_k = \mathbf{\Phi}\left(t_k, t_j\right)\hat{\mathbf{x}}_j\,, \tag{3.52}$$

where $\bar{\mathbf{x}}_k$ is the best estimate of $\mathbf{x}_k$ at time $t_k > t_j$ based on the observations collected up to t_j. The expression for propagating the covariance matrix $\bar{\mathbf{P}}_k$ is the following:

$$\bar{\mathbf{P}}_k = \mathbf{\Phi}\left(t_k, t_j\right)\mathbf{P}_j\mathbf{\Phi}^T\left(t_k, t_j\right)\,, \tag{3.53}$$

where $\mathbf{P}_j = E[(\hat{\mathbf{x}}_j - \mathbf{x}_j)(\hat{\mathbf{x}}_j - \mathbf{x}_j)^T|\mathbf{y}_1, ..., \mathbf{y}_j]$ is the covariance matrix at time t_j provided the observations up to t_j.

3.3.4 Minimum variance estimate with a priori information

If an estimate $\hat{\mathbf{x}}_j$ and the associated covariance matrix $\mathbf{P}_j$ are obtained at a time t_j, and an additional observation or observation sequence is obtained at time t_k, the estimate and the observation can be combined in a straightforward manner to obtain the new estimate $\hat{\mathbf{x}}_k$. The problem can be stated as follows: given the propagated estimates of the state vector $\bar{\mathbf{x}}_k$ and the covariance matrix $\bar{\mathbf{P}}_k$ and a new observation $\mathbf{y}_k$ at time t_k

$$\mathbf{y}_k = \tilde{\mathbf{H}}_k\mathbf{x}_k + \boldsymbol{\varepsilon}_k, \tag{3.54}$$

where $E\left[\boldsymbol{\varepsilon}_k\right] = \mathbf{0}$, $E[\boldsymbol{\varepsilon}_k\boldsymbol{\varepsilon}_j^T] = \mathbf{R}_k\delta_{kj}$, and $E[(\mathbf{x}_j - \hat{\mathbf{x}}_j)\boldsymbol{\varepsilon}_k^T] = \mathbf{0}$, find the linear, minimum variance, unbiased estimate of $\mathbf{x}_k$.

The solution to this problem can be obtained easily in the case that $\bar{\mathbf{x}}_k$ can be interpreted as an observation. In this case, we can prove [97] that the new optimal estimate is:

$$\hat{\mathbf{x}}_k = (\mathbf{H}_k^T\mathbf{R}_k^{-1}\mathbf{H}_k + \overline{\mathbf{P}}_k^{-1})^{-1}(\mathbf{H}_k^T\mathbf{R}_k^{-1}\mathbf{y}_k + \overline{\mathbf{P}}_k^{-1}\bar{\mathbf{x}}_k)\,, \tag{3.55}$$

and the associated covariance is:

$$\mathbf{P}_k = E[(\hat{\mathbf{x}}_k - E[\hat{\mathbf{x}}_k])(\hat{\mathbf{x}}_k - E[\hat{\mathbf{x}}_k])^T] = (\mathbf{H}_k^T \mathbf{R}_k^{-1} \mathbf{H}_k + \overline{\mathbf{P}}_k^{-1})^{-1}. \tag{3.56}$$

It has to be pointed out that:

- the array $\mathbf{y}_k$ can be a single observation or it may include a batch of observations mapped to t_k;
- the a-priori estimate $\bar{\mathbf{x}}_k$ may represent the estimate based on a priori initial conditions or the estimate based upon a set of previously reduced observations;
- the $n \times n$ normal matrix of Equation 3.55 must be inverted and if the dimension n is large, this inversion can lead to computational problems.

The algorithm that uses Equation 3.55 and 3.56 is called **batch processor** or **batch filter**. An in depth discussion on the algorithm can be found in Tapley, [97].

3.4 Computational algorithm for the batch processor

Given a set of initial conditions $\mathbf{X}^*(t_0)$, an a priori estimate $\bar{\mathbf{x}}_0$ and the associated error covariance matrix, $\bar{\mathbf{P}}_0$, the computational algorithm for the batch processor generally uses the normal equation form for $\hat{\mathbf{x}}_0$. Writing Equation 3.40 in normal equations form for a batch of observations and recognizing that $\mathbf{W} = \mathbf{R}^{-1}$ and $\bar{\mathbf{W}} = \bar{\mathbf{P}}_0^{-1}$ yields

$$(\mathbf{H}^T \mathbf{R}^{-1} \mathbf{H} + \bar{\mathbf{P}}_0^{-1}) \hat{\mathbf{x}}_0 = \mathbf{H}^T \mathbf{R}^{-1} \mathbf{y} + \bar{\mathbf{P}}_0^{-1} \bar{\mathbf{x}}_0 \,. \tag{3.57}$$

Here t_0 is an arbitrary epoch and all quantities in Equation 3.57 are assumed to have been mapped to this epoch using the appropriate state transition matrices as illustrated in Equations 3.28 and 3.30.

If $\mathbf{R}$ is a block diagonal matrix, that is the observations are uncorrelated in time although correlations between the observations at any given time may exist, these matrices simply may be accumulated as follows:

$$\mathbf{H}^T \mathbf{R}^{-1} \mathbf{H} = \sum_{i=1}^{l} [\tilde{\mathbf{H}}_i \mathbf{\Phi}(t_i, t_0)]^T \mathbf{R}_i^{-1} \tilde{\mathbf{H}}_i \mathbf{\Phi}(t_i, t_0) \,, \tag{3.58}$$

$$\mathbf{H}^T \mathbf{R}^{-1} \mathbf{y} = \sum_{i=1}^{l} [\tilde{\mathbf{H}}_i \mathbf{\Phi}(t_i, t_0)]^T \mathbf{R}_i^{-1} \mathbf{y}_i \,. \tag{3.59}$$

In general $\mathbf{X}^*(t_0)$ would be chosen so that $\bar{\mathbf{x}}_0 = \mathbf{0}$, and $\bar{\mathbf{P}}_0$ would reflect the relative accuracy of the elements of the initial conditions vector $\mathbf{X}^*(t_0)$. In theory $\bar{\mathbf{x}}_0$ and $\bar{\mathbf{P}}_0$ represent information and should be treated as data that are merged with the observation data, as indicated by Equation 3.57. Consequently, the value of $\mathbf{X}_0^* + \bar{\mathbf{x}}_0$ should be held constant for the beginning of each iteration. Since the initial condition vector $\mathbf{X}_0^*$ is augmented by

the value of $\hat{\mathbf{x}}_0$ after each iteration, that is, $(\mathbf{X}_0^*)_n = (\mathbf{X}_0^*)_{n-1} + (\hat{\mathbf{x}}_0)_{n-1}$, holding $\mathbf{X}_0^* + \bar{\mathbf{x}}_0$ constant results in the following expression for $(\bar{\mathbf{x}}_0)_n$

$$(\bar{\mathbf{x}}_0)_n = (\bar{\mathbf{x}}_0)_{n-1} - (\hat{\mathbf{x}}_0)_{n-1} \,. \tag{3.60}$$

Recall that the state transition matrix is obtained by integrating

$$\dot{\mathbf{\Phi}}(t, t_k) = \mathbf{A}(t)\mathbf{\Phi}(t, t_k) \,, \tag{3.61}$$

subject to the initial conditions $\mathbf{\Phi}(t_k, t_k) = \mathbf{I}$ along with the nonlinear equations, $\dot{\mathbf{X}}^* = \mathbf{F}(\mathbf{X}^*, t)$, which define the nominal trajectory, $\dot{\mathbf{X}}^*(t)$. The matrix $\mathbf{A}(t)$ is evaluated on the reference trajectory,

$$\mathbf{A}(t) = \frac{\partial \mathbf{F}(\mathbf{X}^*, t)}{\partial \mathbf{X}} \,, \tag{3.62}$$

where $\mathbf{F}(\mathbf{X}^*, t)$ is the time derivative of the state vector in the differential equations governing the time evolution of the system. The observation-state mapping matrix is given by

$$\tilde{\mathbf{H}}_i = \frac{\partial \mathbf{G}(\mathbf{X}_i^*, t_i)}{\partial \mathbf{X}} \,, \tag{3.63}$$

where $\mathbf{G}(\mathbf{X}_i^*, t_i)$ are the observation-state relationships evaluated on the nominal or reference trajectory.

Notice that the solution for $\hat{\mathbf{x}}_0$ involved inversion of the information matrix, $\mathbf{\Lambda}_0$, where

$$\mathbf{\Lambda}_0 = \mathbf{H}^T \mathbf{R}^{-1} \mathbf{H} + \bar{\mathbf{P}}_0^{-1} \,. \tag{3.64}$$

Generally the normal equations would not be solved by a direct inversion of $\mathbf{\Lambda}_0$ but rather would be solved by an indirect but more accurate technique, such as the Cholesky decomposition. The sequence of operations required to implement the batch estimation process is outlined in Figure 3.2, where we assume that there are no observations at t_0. If observations exist at t_0, set $\mathbf{\Lambda} = \bar{\mathbf{P}}_0^{-1} + \mathbf{H}_0^T \mathbf{R}_0^{-1} \mathbf{H}_0$ and $\mathbf{N} = \mathbf{H}_0^T \mathbf{R}_0^{-1} \mathbf{y}_0$ in the initialization. As previously stated, the entire sequence of computations are repeated until the estimation process has converged. If there are observations at t_0, the state transition matrix for processing these observations is the identity matrix.

This procedure yields a minimum value of the performance index

$$J(\mathbf{x}) = (\hat{\mathbf{x}}_0 - \bar{\mathbf{x}}_0)^T \bar{\mathbf{P}}_0^{-1} + \sum_{i=1}^{l} \hat{\boldsymbol{\varepsilon}}_i^T \mathbf{R}_i^{-1} \hat{\boldsymbol{\varepsilon}}_i \,, \tag{3.65}$$

where

$$\hat{\boldsymbol{\varepsilon}}_i = \mathbf{y}_i - \mathbf{H}_i \hat{\mathbf{x}}_0 \,, \tag{3.66}$$

and $\hat{\boldsymbol{\varepsilon}}_i$ is the best estimate of the observation error.

In practice, $\bar{\mathbf{P}}_0$ is generally not a realistic representation of the accuracy of $\bar{\mathbf{x}}_0$ and it is used only to better condition to estimation error covariance matrix, $\mathbf{P}$. In this case, $\bar{\mathbf{x}}_0$ usually is set to zero for each iteration and $\bar{\mathbf{P}}_0$ is chosen to be a diagonal matrix with

large diagonal values. Hence, the first term in Equation 3.65 will be very small and the tracking data residuals will determine the value of $J(\mathbf{x})$. The rms (root mean square) of the observation residuals generally is computed and may be used as a measure of convergence; when the rms no larger changes the solution is assumed to be converged. The rms is computed from

$$rms = \left\{ \frac{\sum_{i=1}^{l} \hat{\boldsymbol{\varepsilon}}_i^T \mathbf{R}_i^{-1} \hat{\boldsymbol{\varepsilon}}_i}{m} \right\}^{\frac{1}{2}} , \tag{3.67}$$

where $\hat{\boldsymbol{\varepsilon}}_i$ is a p-vector and $m = l \times p$. Hence, m is the total number of observations. The Equation 3.67 is referred to as the weighted rms. If the rms is computed without including the weighting matrix, $\mathbf{R}_i^{-1}$, it may be referred to as the unweighted rms or just the rms.

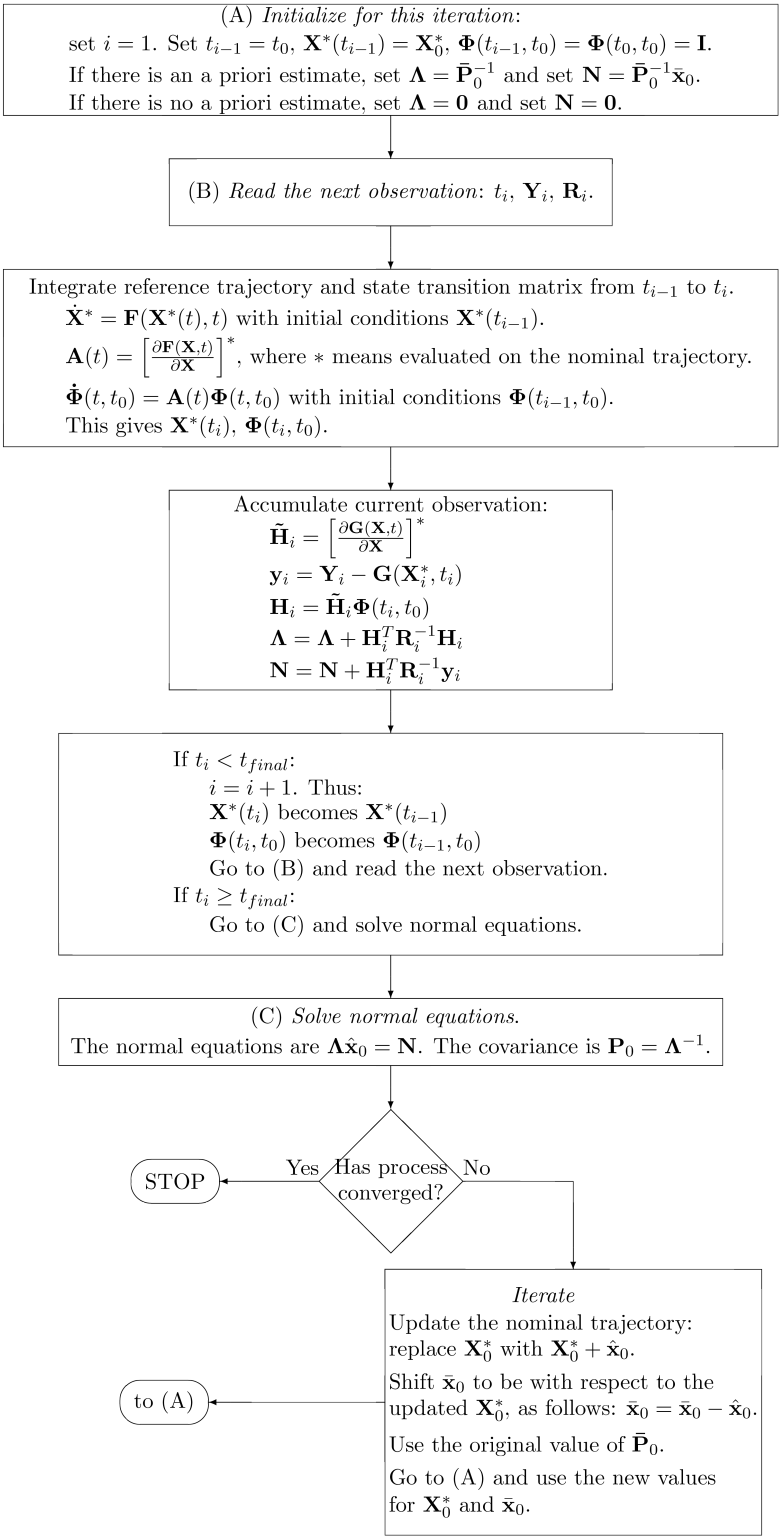

Figure 3.2: Batch processing algorithm flow chart.

Chapter 4

ARPA

ARPA — Aerodynamics and Radiation Pressure Analysis — is the software designed and implemented at the University of Padova to compute forces and torques on satellites due to the non-gravitational perturbations: Solar Radiation Pressure (SRP), Earth Radiation Pressure (ERP) for the albedo and infrared components, the satellite Thermal Re-Radiation (TRR), and the aerodynamics.

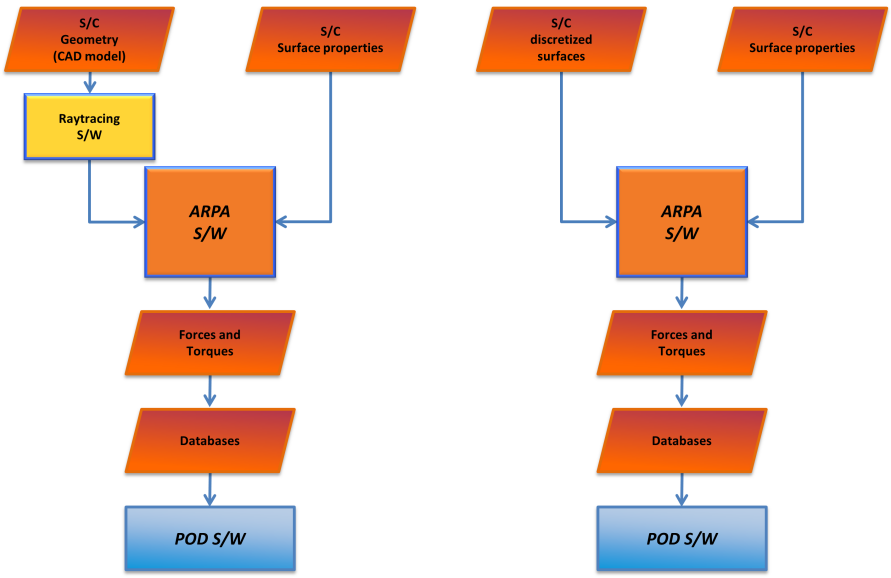

Figure 4.1: ARPA flowcharts: inputs and outputs of ARPA on the left-hand side for the direct Solar Radiation Pressure (SRP) and for the Earth Radiation Pressure (ERP), on the right-hand side for the satellite Thermal Re-Radiation (TRR) and for the aerodynamics.

Figure 4.1 shows the flowchart for the different ARPA subprograms, with the relative inputs and outputs. In order to compute the effects of SRP and ERP on the satellite (left hand-side of Figure 4.1), an accurate spacecraft geometric three-dimensional model (CAD) is necessary. The CAD model is the input for the raytracing software which simulates the

interaction of the photons coming from the Sun or the Earth with the satellite surfaces. The raytracing software creates files which contain the geometric information of the rays reflections on the spacecraft. These files are then read by the ARPA software which, together with the satellite surface properties, computes the physical interaction of the photons with the satellite surfaces, computing forces and torques for the SRP and ERP components. The forces are then converted into coefficients and are used to create a database which will be the input for the Precise Orbit Determination (POD) software. On the other hand, for the computation of the TRR and the aerodynamics (right hand-side of Figure 4.1), the main difference is that the raytracing software is no more needed but, instead, a file containing the data of the satellite surfaces discretization (external surfaces mesh) is required to the ARPA software.

The inputs, outputs and adopted softwares will be described in this chapter, and the ARPA software design and models will be presented.

4.1 ARPA input file generation

4.1.1 CAD geometry generation

An accurate 3D model of the satellite is required in order to simulate the photons or the atmospheric particles impinging on the surfaces, to compute forces and torques on the body. The satellite CAD model is the input for the raytracing software, and starting from its external faces, the surface discretization (surface mesh) is built. Computer-Aided Design (CAD) softwares as Solidworks® [20] and AutoCAD® [44] were adopted to realize the CAD model of GOCE and the test-case shapes.

For the realization of the GOCE CAD model, shown in Figure4.2, the satellite specifics were retrieved from the technical report [17], and the main components were modeled as shown in Figures 4.3 and 4.4. Only the outer surfaces were modeled, since photons and

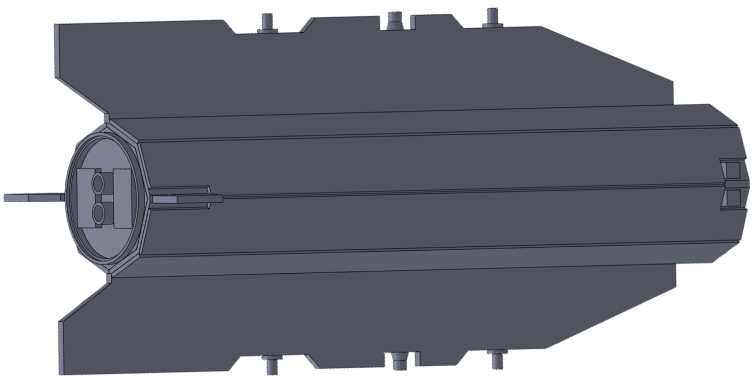

Figure 4.2: GOCE 3D CAD model adopted for the non-gravitational forces computation with ARPA.

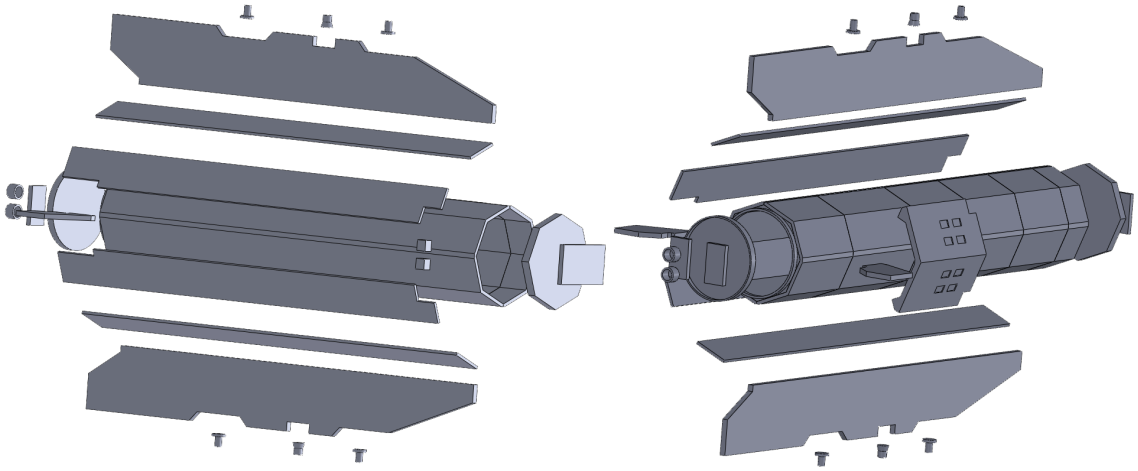

Figure 4.3: Exploded view of the CAD model of GOCE and its external components.

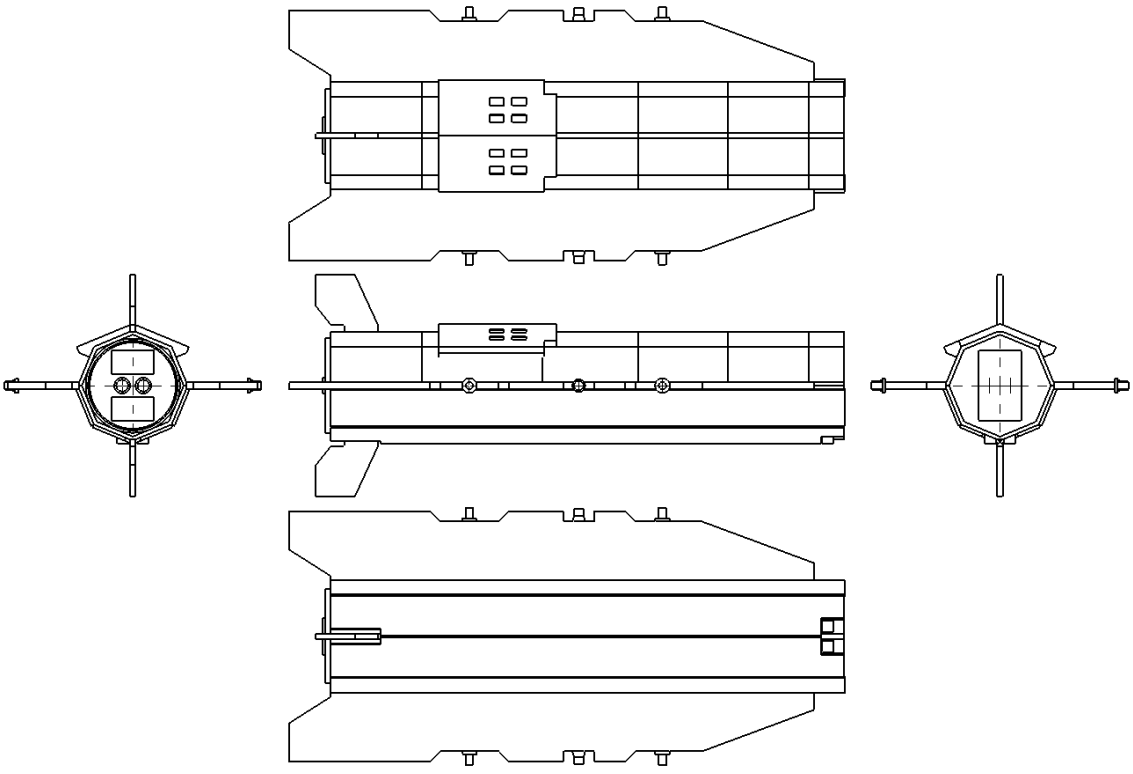

Figure 4.4: Orthogonal projection of the CAD model of GOCE.

atmospheric particles interact only on these faces. In addition, only the main external surfaces and components were modeled. Due to their complexity and time-consuming features, the small components (e.g., external wires, bolts), which would slightly affect the

final result, were neglected. The higher number of details is modeled, the higher accuracy of the final result will be attained, but, at the same time, higher times for the modeling and for the computation will be required. Hence a compromise between modeling/computational time and accuracy of the final geometry was selected, still maintaining a high level of accuracy of the model.

4.1.2 Surface properties database definition

It is necessary to define the different properties of the satellite surfaces in order to convert the geometric information coming from the raytracing software and the surface mesh into a physical interaction of photons and atmospheric molecules with these surfaces. It was hence necessary to design and build a database containing the required properties and parameters of the considered surfaces. The properties were retrieved for each surface from the thermal technical reports [105] and [7]and are reported in Table 4.1. The first set

Table 4.1: Surface properties required as input for ARPA.

Surface						Temperatures		Optical and thermal properties				
ID	Obj	Obj ID	Face ID	Type	Material	T_{NoEcl}	T_{Ecl}	α_{BOL}	α_{EOL}	ϵ	μ_{opt}	μ_{IR}

of parameters identified as "Surface" is the bridge between the geometrical and physical information. In fact all the impinged surfaces contained in the raytracing files and in the surface mesh are identified with specific number ID's. These ID's are collected in the surface properties database, and are directly linked with the corresponding properties, which are used to computed the effects of the non-gravitational perturbations. In particular:

- **ID** is a progressive number, in order to distinguish each surface;
- **Obj** is the name of the object, as named in the raytracing software;
- **Obj ID** is the progressive number associated to each object, as in the raytracing software;
- **Face ID** is the progressive number associated to each face of an object, as in the raytracing software. Each object is in fact subdivided into different faces;
- **Type** provides additional information about the face, to avoid eventual confusion in the surface identification;
- **Material** describes the material which forms or covers the surface.

The two following sets cluster the physical parameters, and will be further discussed in the following sections. The second set of parameters identified as "Temperatures" gathers together the following:

- $\mathbf{T_{NoEcl}}$ is the mean temperature of the surface when the satellite is not in eclipse;
- $\mathbf{T_{Ecl}}$ is the mean temperature of the surface when the satellite is in eclipse.

The third set of parameters, the "Optical and thermal properties" consists of:

- $\boldsymbol{\alpha_{BOL}}$ is the coefficient of absorption of the surface at the satellite Beginning Of Life (BOL), specific for the optical band;
- $\boldsymbol{\alpha_{EOL}}$ is the coefficient of absorption of the surface at the satellite End Of Life (EOL), specific for the optical band;
- $\boldsymbol{\epsilon}$ is the emissivity of the surface, specific for the infrared band (thermal band);
- $\boldsymbol{\mu_{opt}}$ is the reflectivity of the surface, specific for the optical band;
- $\boldsymbol{\mu_{IR}}$ is the reflectivity of the surface, specific for the infrared band.

The main surfaces indexed in the database are illustrated in Figure 4.5.

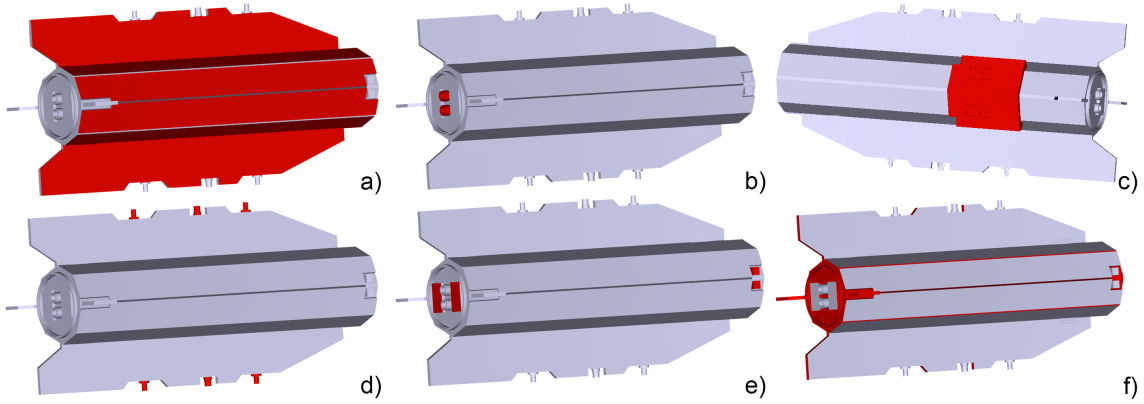

Figure 4.5: Main GOCE surfaces indexed in the database, highlighted in red. In order, a) solar panels, b) ion thrusters, c) radiator, d) GPS and S-band antennas, e) on-board instrumentation, f) other structures.

4.1.3 Raytracing application

This is the fundamental step to describe with high accuracy the geometric interaction between the photons with the satellite surfaces. By means of the raytracing technique it is in fact possible to follow the complete path of each ray, representing a photon from the Sun or the Earth, from its source along its subsequent reflections on the satellite, until it is lost (no further reflections on the satellite take place). This technique, since very efficient and accurate, has been adopted to describe the geometric interactions in order to finally compute forces and torques for the non-gravitational components of direct solar radiation pressure and Earth radiation pressure.

The raytracing tool that was adopted for ARPA is the commercial software ZEMAX® [21]. ZEMAX® is the industry standard optical system design software, capable of combining sequential lens design, analysis, optimization, tolerancing, physical optics, non-sequential optical system design, polarization, thin-film modeling and mechanical CAD

Import/Export. Its main purpose is hence to design and optimize optical paths, and is usually adopted in the design of complex lens systems such as telescopes and satellite on-board cameras. Of course, the purpose of this software in relation to the current work is extremely different from its designed scopes, and this approach is totally innovative. The software behavior has been evaluated for this new application with simple test cases, like the ones shown in Figure 4.6 and more complex shapes, in order to validate its applicability to simulate the rays from a source over complex CAD models, such as satellites. The

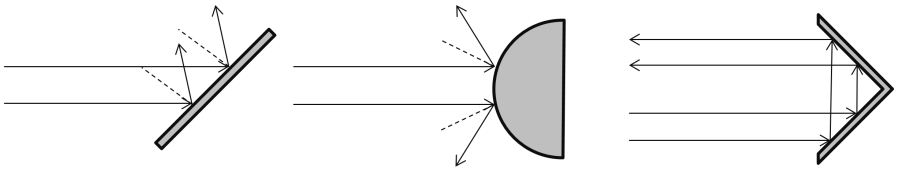

Figure 4.6: Simple test case shapes adopted to test the applicability of the raytracer.

results of the raytracer such as reflection points, direction cosines of the rays before and after reflections over the test-case shapes were compared to the analytic solutions. These tests were all successful with high level of accuracy (errors smaller than 0.01%).

The software ZEMAX® has been setup in the "non-sequential mode" in order to import the CAD geometries in the standard ACIS text (SAT) or stereolithography (STL) formats. Once the CAD geometry has been imported, the surfaces are automatically identified. At this point all the faces should be manually checked and eventually the surface ID's should be reassigned, in order to match the structure shown in Table 4.1. One or more sources of parallel rays are then set up in order to generate the rays. Both the ray sources and the geometry are located and tilted in order to achieve the correct illumination conditions, corresponding to the real conditions. All the rays from the sources are then traced toward the geometry and the reflections are written into binary ZEMAX output files. The most significant data that are exported are:

- **Ray ID** is the progressive number associated to each ray;
- **Refl ID** is the progressive number associated to each ray, corresponding to the number of reflections the ray had before the current one;
- **Obj** is the name associated of the object;
- **Obj ID** is the progressive number associated to each object;
- **Face ID** is the progressive number associated to each face of an object;
- $(\mathbf{X}, \mathbf{Y}, \mathbf{Z})$ is the vector containing the coordinates of point of reflection of the ray on the object, expressed in the ZEMAX reference frame;
- $(\mathbf{L}, \mathbf{M}, \mathbf{N})$ is the director cosines vector of the ray before the reflection on the object, expressed in the ZEMAX reference frame;

- $(\mathbf{N_x}, \mathbf{N_y}, \mathbf{N_z})$ is the director cosines vector of the local outward normal to the object surface, at the point of reflection, expressed in the ZEMAX reference frame;

Note that Obj, Obj ID, and Face ID are the same as the parameters in the surface properties database. This is the method adopted in ARPA to associate the geometrical information from the raytracer with the physical information from the surface properties database.

In order to simplify the positioning and orientation of the geometries and the ray source the GOCE body-fixed reference frame has been set coincident with ZEMAX reference frame. Figure 4.7 shows the GOCE CAD model and some of the traced rays in ZEMAX.

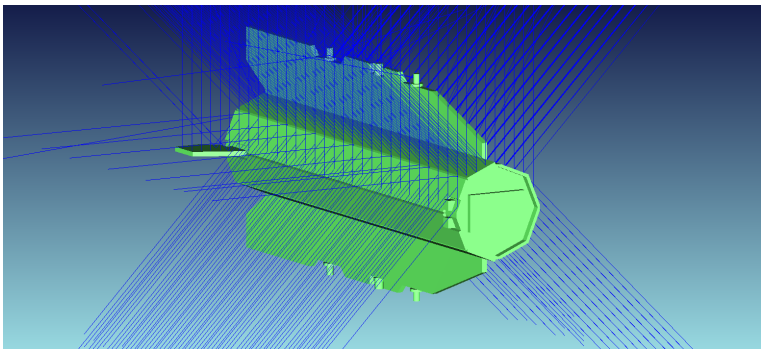

Figure 4.7: GOCE CAD model in the ZEMAX raytracing software. Rays come from the top.

In order to compute forces and torques on the spacecraft due to the different position of the Sun or the Earth with respect to the satellite reference frame, the following solution was adopted:

1. a planar ray source is positioned in the desired location and oriented toward the satellite geometry. The ray source has dimensions and distance from the geometry designed in order to completely cover all the surfaces with rays;

2. the rays are traced toward the geometry and multiple reflections are considered, up to 10 subsequent reflections. Reflection mode is purely specular, and no ray splitting due to surface diffusivity is considered (the reason will be explained in the following sections). The emitted rays are orthogonal to the plane of their source;

3. a file containing the reflections information is created and saved. The ray source is then moved to the following position and the procedure starts again until all the required positions have been simulated.

This procedure is also illustrated in Figure 4.8.

4.1.4 Outer surfaces discretization

As can be observed in Figure 4.1 on the right-hand side, in order to compute forces and torques due to satellite Thermal Re-Radiation (TRR) and aerodynamics, an accurate

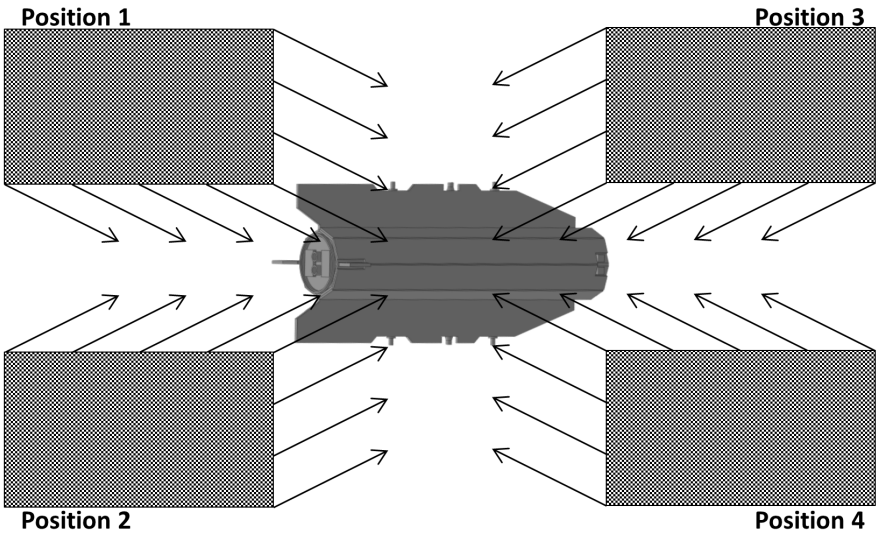

Figure 4.8: Procedure adopted to simulate all the possible positions of Sun and Earth with respect to the satellite reference frame. The ray source is positioned in subsequent locations and rays are traced toward the satellite geometry.

surface discretization is necessary. It was hence necessary to subdivide each external surface of the satellite CAD model into rectangular pixels. A two-dimensional mesh of quads (rectangles) was created for each surface of the geometry and to each rectangular mesh element (pixel) the following parameters were assigned:

- **Obj ID** is the progressive number associated to each object, on which the pixel is located;
- **Face ID** is the progressive number associated to each face of an object, on which the pixel is located;
- $\mathbf{A_{pixel}}$ is the area of the pixel;
- $(\mathbf{X}, \mathbf{Y}, \mathbf{Z})$ is the vector containing the coordinates of the barycenter of the pixel, in the body-fixed reference frame;
- $(\mathbf{N_x}, \mathbf{N_y}, \mathbf{N_z})$ is the director cosines vector of the local outward normal, in the body-fixed reference frame.

Figure 4.9 shows the surface mesh on the surfaces of GOCE.

4.2 Solar Radiation Pressure

4.2.1 Mathematical model adopted in ARPA

Radiation pressure is the pressure exerted by the electromagnetic radiation upon any surface that is absorbing or reflecting the photons. In this case the direct Solar Radiation

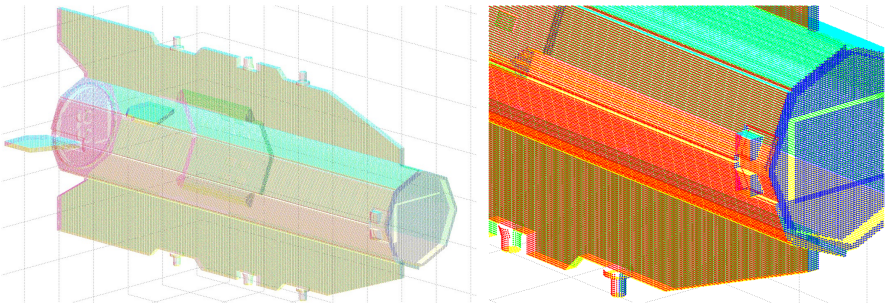

Figure 4.9: GOCE external surfaces meshed with pixels. Colors are used just to make the mesh clearer. On the left-hand side the entire satellite, and on the right-hand side a detail of the frontal floor.

Pressure (SRP) is exerted by the photons coming from the Sun upon the surfaces of satellite orbiting the Earth. The interaction between the photons and the surfaces generate a momentum exchange between the two which exerts a pressure and hence a non-gravitational perturbing force on the spacecraft. Even if the resulting acceleration due to SRP is very small ($10^{-8}\ m/s^2$) this effect must be taken into account in order to accurately compute the satellite orbit. Einstein's special theory of relativity, the energy-momentum relation, defines the relationship between total energy E, the intrinsic (rest) mass m_0, and the momentum p for any object by means of the relativistic equation

$$E^2 = (p\,c)^2 + \left(m_0\,c^2\right)^2 \tag{4.1}$$

where c is the speed of light in vacuum. For a photon $m_0 = 0$ and hence $E = c\,p$. Einstein, taking advantage of the Max Planck's theories, proposed the corpuscular theory of light, where the energy of each photon is proportional to its frequency ν such that $E = h\,\nu$, where h is Planck's constant. Substituting this relation into Equation 4.1 yields

$$p = \frac{h\,\nu}{c}. \tag{4.2}$$

Thus, a photon's momentum is proportional to its frequency and, if such a photon is absorbed or reflected by a surface, an exchange of momentum between the photon and the hit body takes place. Consider now the momentum exchange due to $n(\nu)$ photons, which is the average number of solar photons with frequency ν, striking the unit area of a surface per second (Δt) at 1 Astronomical Unit (AU) distance from the Sun

$$p = \frac{n(\nu) h\,\nu}{c}\Delta t. \tag{4.3}$$

Deriving with respect to time yields

$$\frac{\mathrm{d}p_{n(\nu)}}{\mathrm{d}t} = \frac{n(\nu)\,h\,\nu}{c}, \tag{4.4}$$

which corresponds to the change of momentum per unit area per unit time. Equation 4.4 is the force per unit area (pressure) acting on the surface caused by the photons with

frequency ν. Integrating over the whole solar electromagnetic spectrum, it is possible to calculate the total pressure exerted on a surface at $1AU$ due to the direct solar radiation pressure,

$$P_{\odot} = \int_{Sun} \left(\frac{h}{c}\right) n(\nu)\nu \, \mathrm{d}\nu = \frac{E_{\odot}}{c}, \tag{4.5}$$

where $E_{\odot}$ is the solar irradiance, usually referred to as solar constant measured in W/m^2. Different values have been identified $E_{\odot}$, such as 1367 W/m^2 [66], but most recently it has been measured to be about 1361 W/m^2 based on regular readings from NASA's Solar Radiation and Climate Experiment (SORCE) satellite [53]. The solar constant is not properly constant, since it varies both in time and in space. It is in fact a function of the solar activity, which determines slight variations and oscillations of its value during an 11-year sunspot cycle. Different models are used to determine and adjust this value (i.e. daily Zurich sunspot number R_Z model, MgII index model, R_Z-MgII-10.7 cm radio flux index model [39]). Furthermore the constant given at $1AU$ should be scaled if radiation pressure is needed at different distances from the Sun. Given the values of the irradiance $E_{\odot} = 1361\ W/m^2$ and $c = 299792458\ m/s$ the solar radiation pressure on a surface at 1 AU is

$$P_{\odot} = \frac{E_{\odot}}{c} \simeq 4.54 \times 10^{-6}\ \frac{N}{m^2}$$

The solar radiation pressure effects mainly depends on the following three parameters:

1. the value of the solar irradiance $E_{\odot}$, which depends on the actual distance of the satellite surface from the Sun and on the solar activity;
2. the orientation of the surface with respect to the incoming radiation. The orientation of each surface is a function of the attitude of the satellite and the orientation of its moving parts (e.g., solar panels, antennas);
3. the optical properties of the surfaces of the satellite, which define the amount of solar radiation that is absorbed or reflected.

To analyze the effects of the radiation pressure on the satellites two fundamental assumptions are made:

1. a negligible component of the radiation from the Sun or the Earth that is hitting the satellite is transmitted through the surfaces. The radiation is hence either absorbed or reflected (specularly or diffusively);
2. for the diffuse radiation component the surface acts as a perfect Lambertian body, hence the surface's luminance is isotropic, and the luminous intensity obeys Lambert's cosine law.

Hence the radiation is either absorbed or reflected by the spacecraft and the transmissivity (fraction of radiation transmitted) is set to zero. Based on these hypotheses, two sets of parameters are defined, as already said in the optical and thermal properties Section 4.1.2: one set for the optical band and one for the infrared band.

For a satellite surface, in the optical band:

- α is the coefficient of absorption, which represents the ratio between the amount of radiation absorbed and the amount of radiation hitting the surface;
- ρ_{opt} is the reflectivity, which represents the ratio between the amount of radiation reflected and the amount of radiation hitting the surface;
- μ_{opt} is the specularity, which represents the ratio between the amount of radiation specularly reflected and the amount of radiation reflected by the surface.

On the other hand, for a satellite surface, in the infrared band:

- ϵ is the emissivity, which represents the ratio between the amount of radiation absorbed and the amount of radiation hitting the surface;
- ρ_{IR} is the reflectivity in the infrared band;
- μ_{IR} is the specularity in the infrared band.

From the hypothesis of no transmissivity τ, it is possible to derive the following relations

$$\begin{aligned} \alpha + \rho_{opt} + \tau_{opt} = 1 \quad &\rightarrow \quad \rho_{opt} = 1 - \alpha \\ \epsilon + \rho_{IR} + \tau_{IR} = 1 \quad &\rightarrow \quad \rho_{IR} = 1 - \epsilon \end{aligned}$$

Figure 4.10 shows the three modeled types of interaction between the photons and the satellite surfaces. The radiation can be a) absorbed, b) specularly reflected, or c) diffusively reflected by the surface. Each of these three types of interaction generate a different momentum exchange between the radiation and the spacecraft, and the cumulative effect generate the total perturbing acceleration due solar radiation pressure on the satellite.

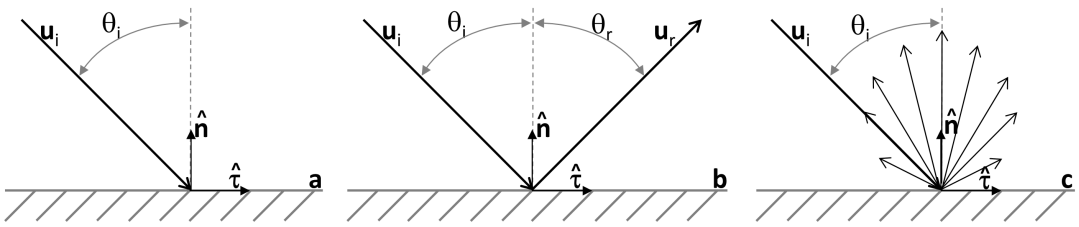

Figure 4.10: Photons-surface interaction types: a) absorbed, b) specularly reflected, and c) diffusively reflected radiation on a surface.

The reflection model assumed in this work to compute the effects of the solar and Earth radiation pressure is the Maxwellian reflection model. With this model it is assumed that part of the radiation is absorbed, part is specularly reflected and part is diffusively reflected, as shown in Figure 4.10. For a generic surface with the optical and thermal properties previously described, the following quantities can hence be defined:

- ρ is the fraction of incident radiation that is reflected;

- $1-\rho$ is the fraction of incident radiation that is absorbed;
- $\rho\,\mu$ is the fraction of incident radiation that is reflected specularly;
- $\rho\,(1-\mu)$ is the fraction of incident radiation that is reflected diffusely.

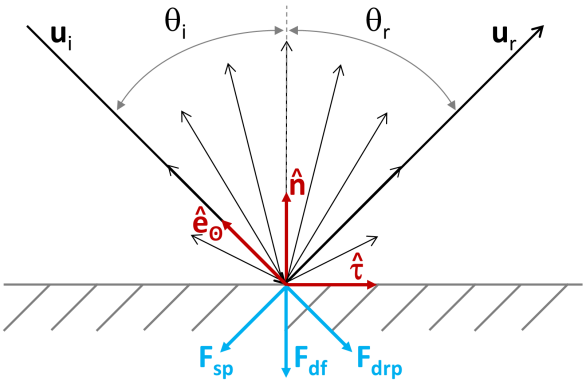

Figure 4.11: Forces due to solar radiation pressure for a both absorbing and reflecting surface. Reflection is both specular and diffuse.

As can be observed in Figure 4.11, the force $\mathbf{F}_{drp}$ due to the total incident radiation is directed along the S/C-Sun direction $\hat{\mathbf{e}}_\odot$, but pointing away from the Sun, $\mathbf{F}_{sp}$ due to the specularly reflected radiation is the recoil force acting along the direction of the specularly reflected rays, and $\mathbf{F}_{df}$ is the recoil force due to the diffusely reflected radiation acting along the normal to the surface $\hat{\mathbf{n}}$, again pointing in the opposite direction. The force magnitudes due to these components are

$$F_{drp} = \frac{E_\odot A}{c}\cos\theta, \tag{4.6a}$$

$$F_{sp} = \rho\,\mu\frac{E_\odot A}{c}\cos\theta, \tag{4.6b}$$

$$F_{df} = \frac{2}{3}\rho\,(1-\mu)\frac{E_\odot A}{c}\cos\theta, \tag{4.6c}$$

where A is the area of the irradiated surface, and θ is angle between the incident radiation and the local normal to the surface. This yields the following normal $\hat{\mathbf{n}}$ and shear $\boldsymbol{\tau}$ components

$$\mathbf{F}_n = -\frac{E_\odot A}{c}\cos\theta\left[(1+\rho\,\mu)\cos\theta + \frac{2}{3}\rho(1-\mu)\right]\hat{\mathbf{n}} \tag{4.7a}$$

$$\mathbf{F}_\tau = \frac{E_\odot A}{c}\cos\theta(1-\rho\,\mu)\sin\theta\,\hat{\boldsymbol{\tau}} \tag{4.7b}$$

From the computational point of view, since the raytracer directly provides the direction of the incoming radiation $\hat{\mathbf{e}}_\odot$ and local outward normal to the surface $\hat{\mathbf{n}}$, it is faster and

easier to compute the force contributions due to the absorbed and reflected radiation as

$$\mathbf{F}_{abs} = -\frac{E_{\odot}A}{c}\cos\theta\,(1-\rho)\,\hat{\mathbf{e}}_{\odot} \tag{4.8a}$$

$$\mathbf{F}_{sr} = -\frac{E_{\odot}A}{c}\cos^2\theta\,2\mu\,\rho\,\hat{\mathbf{n}} \tag{4.8b}$$

$$\mathbf{F}_{dr} = -\frac{E_{\odot}A}{c}\cos\theta\left(\rho(1-\mu)\,\hat{\mathbf{e}}_{\odot} + \frac{2}{3}\rho(1-\mu)\cos\theta\,\hat{\mathbf{n}}\right), \tag{4.8c}$$

where $\mathbf{F}_{abs}$ is the force component due to the radiation that is absorbed, $\mathbf{F}_{sr}$ is the force component due to the radiation that is specularly reflected, and $\mathbf{F}_{dr}$ is the force component due to the radiation that is diffusively reflected. Equations 4.8 are also adopted in [106]. Equations 4.8 can be rewritten in the normal $\hat{\mathbf{n}}$ and S/C-Sun $\hat{\mathbf{e}}_{\odot}$ components as

$$\mathbf{F}_{n} = -\frac{E_{\odot}A}{c}\cos^2\theta\left(\frac{2}{3}\,\rho + \frac{4}{3}\,\rho\,\mu\right)\hat{\mathbf{n}}, \tag{4.9a}$$

$$\mathbf{F}_{e_{\odot}} = -\frac{E_{\odot}A}{c}\cos\theta\,(1-\rho\,\mu)\,\hat{\mathbf{e}}_{\odot}, \tag{4.9b}$$

which are the equations implemented in ARPA to compute the forces due to the direct solar radiation pressure on a surface.

4.2.2 Implementation in ARPA

It was already described in Section 4.1.3 how the raytracing procedure was designed and implemented. This section will describe in detail how the geometrical information from the raytracing files are converted into a physical interaction between the photons and the satellite surfaces. Recalling the raytracing section, the adopted approach consists of:

1. a ray source is positioned in front of the simulated geometry, discretized into a grid of pixels;

2. from each pixel a ray is traced toward the geometry, and its paths due to specular reflections are followed;

3. the necessary reflection information is saved to a file, then imported into ARPA.

In ARPA the first step is to associate to each pixel of the ray source the value of force due to the direct solar radiation pressure. In Equations 4.9 A is the area of the irradiated surface, while $A\cos\theta$ is the surface projected area in the direction of the incoming radiation. Each pixel represents in fact a part of the total projected area, since the rays are orthogonal to the source, hence, knowing the pixel area (which depends on the resolution of the discretized source) it is possible to rewrite Equations 4.9 as the following

$$\mathbf{F}_{n} = -F_{pixel}\,\cos\theta\left(\frac{2}{3}\,\rho + \frac{4}{3}\,\rho\,\mu\right)\hat{\mathbf{n}}, \tag{4.10a}$$

$$\mathbf{F}_{e_{\odot}} = -F_{pixel}\,(1-\rho\,\mu)\,\hat{\mathbf{e}}_{\odot}, \tag{4.10b}$$

where

$$F_{pixel} = \frac{E_{\odot} A_{pixel}}{c} = \frac{E_{\odot} A}{c} \cos\theta, \tag{4.11}$$

which is the force associated to each pixel due to the direct solar radiation pressure. For each point of reflection Equations 4.10 are applied, retrieving the geometrical components from the raytracing file

$$\begin{aligned} \hat{\mathbf{n}} &= [N_x,\ N_y,\ N_z]^T, \\ \hat{\mathbf{e}}_{\odot} &= [L,\ M,\ N]^T, \\ \cos\theta &= \hat{\mathbf{n}} \cdot \hat{\mathbf{e}}_{\odot}, \end{aligned}$$

and the optical and thermal properties of the reflecting surface from the surface properties database. At the reflection point the "Obj ID" and "Face ID" are known, and can hence be associated to the necessary surface properties ρ and μ. Equations 4.12 can hence be applied to compute the force over one surface due to the solar radiation pressure at the first reflection. Multiple reflections are also modeled by ARPA. In the work of this thesis it was assumed that the effects of the second and further reflections due to the diffusive component is small with respect to the specularly reflected component of the radiation, and hence can be neglected. This is done because the diffuse reflection takes place in a Lambertian way, which therefore results in a distribution in space of the total energy of the reflecting rays, while the component of radiation that is specularly reflected maintains a high level of energy and hence the reflected radiation can give an extra contribution to the total force due to SRP. Neglecting the diffuse radiation and subtracting the absorbed radiation component, the force per pixel associated to each specularly reflected ray after the first reflection is

$$F_{pixel\text{ - }1^{st}\,refl} = \frac{E_{\odot} \cdot A_{pixel}}{c}\ (\rho\,\mu)\,. \tag{4.12}$$

After the first reflection the path is followed until the tenth reflection (whether it happens) and the force due to the subsequent reflections is computed. Since only the specular component of radiation is modeled after each reflection, the raytracer is set up in order to follow only the specular paths. There is to say that it would be anyway possible to compute the multiple reflections also for the diffuse components, for example by splitting each ray in multiple ones after each reflection, but this would exponentially increase both the raytracing and the ARPA computational times, slightly contributing to the final result. For these reasons the multiple reflections were modeled only for the specular components. In general the force per pixel associated to each specularly reflected ray after the n-th reflection is

$$F_{pixel\text{ - }n^{th}\,refl} = \frac{E_{\odot} \cdot A_{pixel}}{c} \prod_{j=1}^{n} (\rho_j\,\mu_j)\,, \tag{4.13}$$

where ρ_j and μ_j are the surface properties of the surface hit at the j-th reflection. Substituting Equation 4.13 into Equations 4.10 it is possible to compute the force due SRP of a single ray at each reflection on the satellite surfaces. It is then possible to accumulate

the contribution of each j-th reflection in the $\hat{\mathbf{n}}$ and $\hat{\mathbf{e}}_{\odot}$ directions, to compute the total radiation pressure per pixel, as

$$\mathbf{F}_{pixel} = \sum_{j=1}^{n} \mathbf{F}_{pixel-j} = \sum_{j=1}^{n} \left(\mathbf{F}_{n\ pixel-j} + \mathbf{F}_{e_{\odot}\ pixel-j} \right). \tag{4.14}$$

Accumulating the contribution of each pixel yields the total force due to the solar radiation pressure

$$\mathbf{F} = \sum_{i=1}^{m} \sum_{j=1}^{n_i} \mathbf{F}_{ij}, \tag{4.15}$$

for each i-th pixel and each j-th reflection, where m is the total number of pixels and n_i is the total number of reflections per each i-the pixel.

Considering a body-fixed reference frame centered in the Center of Mass (CoM) of the satellite, as shown in Figure 4.12, it is possible to compute the torque applied to the center of mass of the satellite due to the solar radiation pressure as

$$\mathbf{T_{CoM}} = \sum_{i=1}^{m} \sum_{j=1}^{n_i} \mathbf{d}_j \times \mathbf{F}_{ij}, \tag{4.16}$$

where $\mathbf{d}_j$ is the position vector of the j-th point of reflection of the i-th ray with respect to the center of mass.

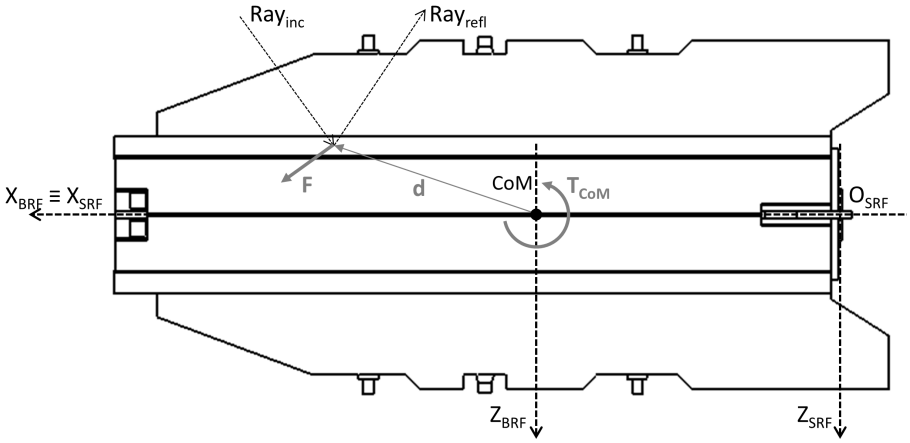

Figure 4.12: SRP force and torque about the Center of Mass (CoM) due to one ray hitting the spacecraft. Body-fixed Reference Frame (BRF) and Satellite-fixed Reference Frame (SRF) are also shown.

4.2.3 SRP Coefficients and Database creation

The most important characteristic of a database containing the forces and torques due to the non-gravitational perturbations is its general validity. In fact it is fundamental that the previously described forces derived for particular conditions (e.g., particular solar

Table 4.2: Parameters influencing the resultant SRP force on a spacecraft. See Appendix A for the definition of the geometric parameters.

Parameter	Parameter type	Parameter explanation
$E_\odot$	Environmental parameter	solar constant
ρ	Satellite parameter	surface reflectivity
μ	Satellite parameter	surface specularity
Az	Geometric parameter	Azimuth of the incoming radiation direction in SRF
El	Geometric parameter	Elevation of the incoming radiation direction in the SRF
ϕ_1	Geometric parameter	1st Degree of Freedom of the solar panels
ϕ_2	Geometric parameter	2nd Degree of Freedom of the solar panels

irradiance, spacecraft attitude) are manipulated in order to be easily and quickly adjusted to the in-flight conditions of the spacecraft during the POD process. This is a fundamental step to achieve a fast and efficient computation of the non-gravitational forces during the POD.

The first step is to identify which parameters affect the forces and torques on the spacecraft and need to be adjusted during the POD process. Before proceeding further, there is to highlight the fact that the adopted POD software system NAPEOS, as maintained at the ESA/ESOC Navigation Support Office (ESA/ESOC HSO-GN) do not propagate the satellite attitude, and hence, even if the torques are computed they are excluded from the following analysis. Table 4.2 shows the parameters that influence the resultant SRP force on a spacecraft. In order to achieve the general validity of the computed forces, the effect of these parameters should be analyzed.

The first parameter $E_\odot$ is the solar constant, which, as already stated, depends on the solar activity and the distance from the Sun. In Equations 4.9 and 4.10 the fraction $E_\odot/c$ is a multiplier, and it hence be collected after the summation of the force contribution of each pixel, as the modified version of Equation 4.15

$$\mathbf{F} = \frac{E_\odot}{c} \sum_{i=1}^{m} \sum_{j=1}^{n_i} \mathbf{F}'_{ij}, \tag{4.17}$$

where $\mathbf{F}'_{ij}$ is the force of each pixel at each reflection normalized by the factor $E_\odot/c$. It is hence possible normalize Equation 4.17 by the factor $E_\odot/c$, computing the adimensional force coefficients as

$$\mathbf{C_F} = \mathbf{F}\ \frac{c}{E_\odot\ A_{ref}}, \tag{4.18}$$

where A_{ref} is an arbitrary reference area adopted to adimensionalize the coefficients. In this way it is possible to dispose of the dependency of the SRP compute force from the solar irradiance $E_\odot$.

The second parameter is the surface reflectivity ρ. ρ is specific for each satellite surface and, as already described, corresponds to $1-\alpha$ or $1-\epsilon$, depending on the bandwidth considered. Each surface of the satellite is subjected to degradation of its surface properties with time, and hence the reflectivity is not constant along the all mission. This change of the optical and thermal properties with respect to time lead to a change in the interaction of

the photons with the surfaces, hence leading to different SRP forces. The optical reflectivity of the different surface materials for the GOCE satellite are shown in Figure 4.13. In Figure

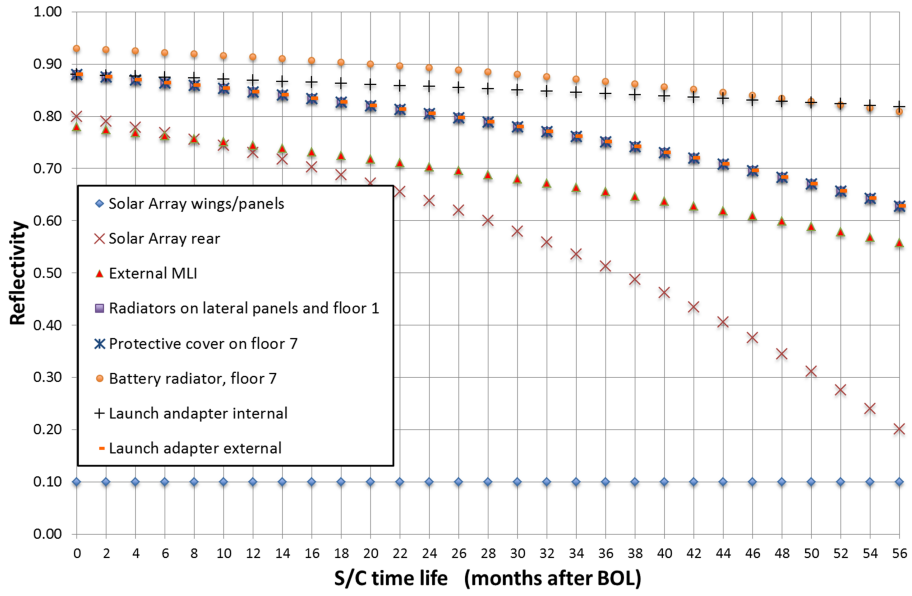

Figure 4.13: GOCE optical reflectivity degradation in time.

4.13 it is possible to observe the reflectivity of the surfaces that tends to decrease for almost all the surfaces. The only exception is the reflectivity of the solar arrays, which is constant in time. Figure 4.14 shows the coefficients force due to SRP as computed for GOCE for different angles of the incoming solar radiation in the BRF. For GOCE it was computed by

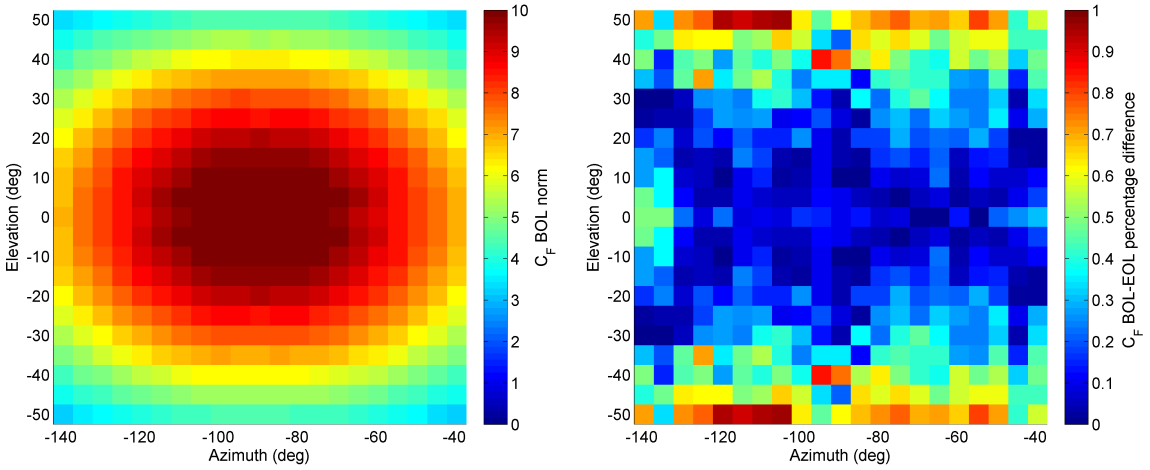

Figure 4.14: GOCE coefficient norm. On the left hand-side the coefficients computed at the BOL, and on the right hand-side the percentage difference of the coefficients from BOL to EOL, due to the optical properties degradation.

a software that analytically propagates the orbit, that the incoming solar radiation will be in the range of $Az = [-140\ -40]\ deg$ and $El = [-50\ -50]\ deg$ in the body-fixed reference frame. As it is observable, the difference is very small in terms of force amplitude (below 1%) and force direction (maximum deflection below 0.6 deg) for all the considered conditions. This is due to the fact that the satellite surfaces mostly exposed to the direct solar radiation are the solar arrays, which have no degradation with time. Hence the difference over time is very limited, and at the EOL (about 4.5 years after March 2009) the effect over the force due to SRP is very small. Assuming the conditions of degradation after about 2 years from BOL, it is possible to neglect the optical properties degradation effect committing an error lower than 0.5% in amplitude and 0.3 deg in direction. In this way it is possible to dispose of the dependency of the SRP computed force from the degradation of the reflectivity in the visual band.

Since no specific information related to the surface specularity were identified, the parameter μ was assumed constant, and can be then excluded from the dependencies as well. There is anyway to clarify that, if specific information is provided, yearly or monthly databases can be easily computed taking into account the actual optical/thermal and specular surface properties degradation, modeling in this way also the dependency of the SRP forces from time.

The four additional parameters Az, El, ϕ_1, and ϕ_2, defined as geometrical parameters (see Appendix A), are significantly affecting the force due to SRP. In general, for a satellite with one or more solar panels, 1) a change in the direction of the incoming radiation with respect to the body-fixed reference frame (BRF) or 2) a rotation of the solar panels with respect to the satellite bus will result in a different resulting SRP force, both in magnitude and direction. For this reason it is not possible to exclude these parameters from the dependencies and hence Az, El, ϕ_1, and ϕ_2 will be the four inputs for the SRP database. Anyway for what concerns GOCE, since it has no rotating solar panels but only body-mounted cells, ϕ_1, and ϕ_2 are not necessary.

In conclusion, the parameters from which the computed SRP forces depend from are the geometrical parameters Az, El, ϕ_1, and ϕ_2, described in Table 4.2. In this way it was possible to develop a database of coefficients of SRP force (see Equation 4.18) as a function of the geometrical parameters.

4.2.4 Test Cases results

In order to test and validate the procedure adopted to compute the force over a satellite due to the SRP two main test cases were carried out: 1) test on a tilted flat plate and 2) test on perfect sphere. The force due to SRP was computed by using the raytracing method and the implemented ARPA software and the obtain results were compared to the analytic solutions. Furthermore the comparison was carried out to identify the necessary resolution of the discrete ray source and hence the necessary number of rays, in order to limit the errors derived from the geometrical interaction of the simulated rays with the CAD modeled bodies.

Table 4.3: Flat plate test case results. Raytracing and analytical solutions are compared, for two different ray-source resolutions and different sets of optical properties.

Optical Properties	Raytracing solution (N) 1 cm^2 resolution	Raytracing solution (N) 1 mm^2 resolution	Analytical solution (N)
$\rho = 0$ $\mu = 0$	$F_x = 0$ $F_y = 0$ $F_z = 3.989129 \times 10^{-06}$ $\lvert\mathbf{F}\rvert = 3.989129 \times 10^{-06}$	$F_x = 0$ $F_y = 0$ $F_z = 3.962671 \times 10^{-06}$ $\lvert\mathbf{F}\rvert = 3.962671 \times 10^{-06}$	$F_x = 0$ $F_y = 0$ $F_z = 3.931588 \times 10^{-06}$ $\lvert\mathbf{F}\rvert = 3.931588 \times 10^{-06}$
Approximation	1.4635 %	0.7906 %	–
$\rho = 0.5$ $\mu = 0.5$	$F_x = 1.151562 \times 10^{-06}$ $F_y = 0$ $F_z = 4.986411 \times 10^{-06}$ $\lvert\mathbf{F}\rvert = 5.117655 \times 10^{-06}$	$F_x = 1.130806 \times 10^{-06}$ $F_y = 0$ $F_z = 4.945764 \times 10^{-06}$ $\lvert\mathbf{F}\rvert = 5.073392 \times 10^{-06}$	$F_x = 1.134952 \times 10^{-06}$ $F_y = 0$ $F_z = 4.914486 \times 10^{-06}$ $\lvert\mathbf{F}\rvert = 5.043837 \times 10^{-06}$
Approximation	1.4635 %	0.5860 %	–
$\rho = 1$ $\mu = 0$	$F_x = 1.151562 \times 10^{-06}$ $F_y = 0$ $F_z = 5.983693 \times 10^{-06}$ $\lvert\mathbf{F}\rvert = 6.093495 \times 10^{-06}$	$F_x = 1.130806 \times 10^{-06}$ $F_y = 0$ $F_z = 5.936432 \times 10^{-06}$ $\lvert\mathbf{F}\rvert = 6.043174 \times 10^{-06}$	$F_x = 1.134952 \times 10^{-06}$ $F_y = 0$ $F_z = 5.897383 \times 10^{-06}$ $\lvert\mathbf{F}\rvert = 6.005601 \times 10^{-06}$
Approximation	1.4635 %	0.6256 %	–

The first test case was carried for a flat plate, with a 1 m^2 square shape, whose outward normal is tilted of 30 deg with respect to the direction of the incoming radiation, as shown in Figure 4.15 on the left-hand side. Table 4.3 sums up the obtained results for what concerns the force due to SRP, for different optical properties of the surface and different resolutions. As can be observed in Table 4.3 the accuracy of the adopted raytracing method

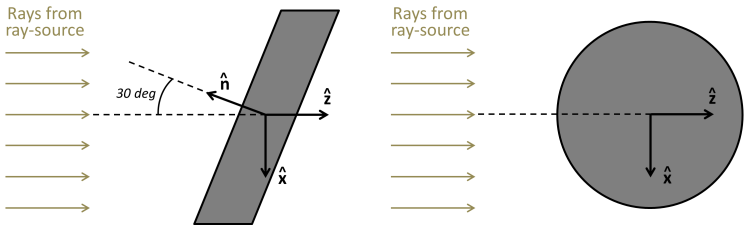

Figure 4.15: Flat plate and perfect sphere test cases. Direction of the incoming radiation, tilted plate/sphere and reference system adopted for the force computation are shown.

is clearly a function of the resolution of the raytracing source. As shown, with a resolution of 1 cm^2 the error is lower than 1.5% for all the three optical properties sets. For the higher resolution of 1 mm^2 the approximation with respect to the analytical solution decreases to values between 0.5% and 0.8%. These results proved the validity and the correct design of the raytracing technique and of the ARPA software, relatively to the SRP computation. It is clear that the achievable accuracy of the raytracing method directly depends on the resolution of the ray-source and hence on the number of traced rays. From this particular test it can also be deduced that it is not directly the absolute dimension of the pixels that determines the accuracy of the results but it is the their relative dimension with respect to

the object dimensions. In other words, the accuracy of the test on a flat plate of 1 m^2 with a ray-source discretization of 1 mm^2 is the same that can be achieved on a flat plate of 100 m^2 with a ray-source discretization of 1 cm^2 (the number of rays is in fact the same). Maintaining instead the same dimensions of the object and increasing the resolution of the ray-source (and hence the number of rays) the achievable accuracy increases as well.

It can be hence concluded that the achievable accuracy of the raytracing application depends on the relative dimensions of the ray-source pixels with respect to the dimensions of the projected area of the tested object. Of course a larger number of rays would lead to higher accuracy, but also the required computational time and memory would increase. A compromise between accuracy, time and required computational power will hence be necessary.

The second test case was carried on a perfect sphere with a diameter of 1 m, as shown in Figure 4.15 on the right-hand side. The test was performed in order to test the raytracing approach accuracy over rounded shapes. As for the flat plate the raytracing technique is tested with two different ray-source resolutions and different optical properties sets. Results are shown in Table 4.4. The results obtained for the perfect sphere show that the approx-

Table 4.4: Perfect sphere test case results. Raytracing and analytical solutions are compared, for two different ray-source resolutions and different sets of optical properties.

Optical Properties	Raytracing solution (N) 1 cm^2 resolution	Raytracing solution (N) 1 mm^2 resolution	Analytical solution (N)
$\rho = 0$ $\mu = 0$	$F_x = 0$ $F_y = 0$ $F_z = 3.561479 \times 10^{-06}$ $\lvert\mathbf{F}\rvert = 3.561479 \times 10^{-06}$	$F_x = 0$ $F_y = 0$ $F_z = 3.565333 \times 10^{-06}$ $\lvert\mathbf{F}\rvert = 3.565333 \times 10^{-06}$	$F_x = 0$ $F_y = 0$ $F_z = 3.565556 \times 10^{-06}$ $\lvert\mathbf{F}\rvert = 3.565556 \times 10^{-06}$
Approximation	1.143×10^{-01} %	6.254×10^{-03} %	–
$\rho = 0.5$ $\mu = 0.5$	$F_x = 2.887296 \times 10^{-15}$ $F_y = 1.560249 \times 10^{-14}$ $F_z = 3.859614 \times 10^{-06}$ $\lvert\mathbf{F}\rvert = 3.859614 \times 10^{-06}$	$F_x = 2.886942 \times 10^{-17}$ $F_y = 1.560028 \times 10^{-16}$ $F_z = 3.862519 \times 10^{-06}$ $\lvert\mathbf{F}\rvert = 3.862519 \times 10^{-06}$	$F_x = 0$ $F_y = 0$ $F_z = 3.862686 \times 10^{-06}$ $\lvert\mathbf{F}\rvert = 3.862686 \times 10^{-06}$
Approximation	7.953×10^{-02} %	4.323×10^{-03} %	–
$\rho = 1$ $\mu = 0$	$F_x = 2.887296 \times 10^{-15}$ $F_y = 1.560249 \times 10^{-14}$ $F_z = 4.749983 \times 10^{-06}$ $\lvert\mathbf{F}\rvert = 4.749983 \times 10^{-06}$	$F_x = 2.886942 \times 10^{-17}$ $F_y = 1.560028 \times 10^{-16}$ $F_z = 4.753852 \times 10^{-06}$ $\lvert\mathbf{F}\rvert = 4.753852 \times 10^{-06}$	$F_x = 0$ $F_y = 0$ $F_z = 4.754075 \times 10^{-06}$ $\lvert\mathbf{F}\rvert = 4.754075 \times 10^{-06}$
Approximation	8.607×10^{-02} %	4.691×10^{-03} %	–

imation over the rounded shape is very small for the considered resolutions and optical properties compared to the flat plate.

From the higher accuracy achieved with the sphere test case with respect to the flat plate a further investigation has been carried out. The difference in the results has been identified in the following: due to the finite resolution of the ray-source, the raytracing technique is not capable of perfectly modeling the edges of the plate, leading to an approximation of

the sampled body surface. This effect is shown in Figure 4.16. Due to the effects at the

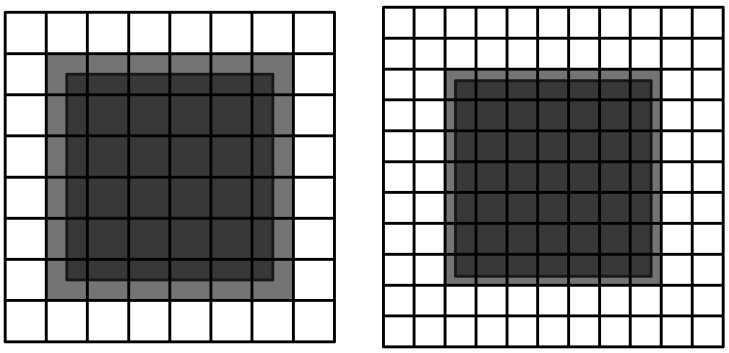

Figure 4.16: Analysis of the effects of the ray-source discretization on the flat plate sampled area.

edges the effective area of the plate is slightly overestimated, leading to higher force values. The effect on the edges of the sphere is instead smooth, due to the high angle between the direction of the rays and the local outward normal to the surface. Since the sphere is symmetric the effects normal to the ray direction get canceled.

In conclusion, as expected, the accuracy of the achievable results is directly proportional to the resolution (relative dimensions) of the ray-source and the number of rays. A compromise should be hence be specifically identified for each tested object, based on its absolute dimensions and the dimensions of its modeled surface features, in order to achieve a sufficient number of reflected rays on each surface without overloading the computational time. With higher computational power it would be easy to increase the number of simulated rays, hence increasing the accuracy of the results and the resolution of the directional grid (the grid of the directions of the rays).

4.3 Earth Radiation Pressure — Albedo and Infrared

4.3.1 Mathematical model adopted in ARPA

Earth Radiation Pressure (ERP) is the pressure exerted by the electromagnetic radiation coming from the Earth and impinging any absorbing or reflecting satellite surface. The Earth radiation can be divided in two components:

1. the albedo radiation, which is the solar radiation reflected by the Earth atmosphere and surface. Therefore the albedo radiation component has a spectral content very similar to the one of the solar radiation, centered in the visible wavelengths;

2. the infrared (IR) radiation, which is instead the thermal radiation emitted by the Earth, centered in the IR wavelengths.

A simple sketch of the solar and Earth radiation is shown in Figure 4.17.

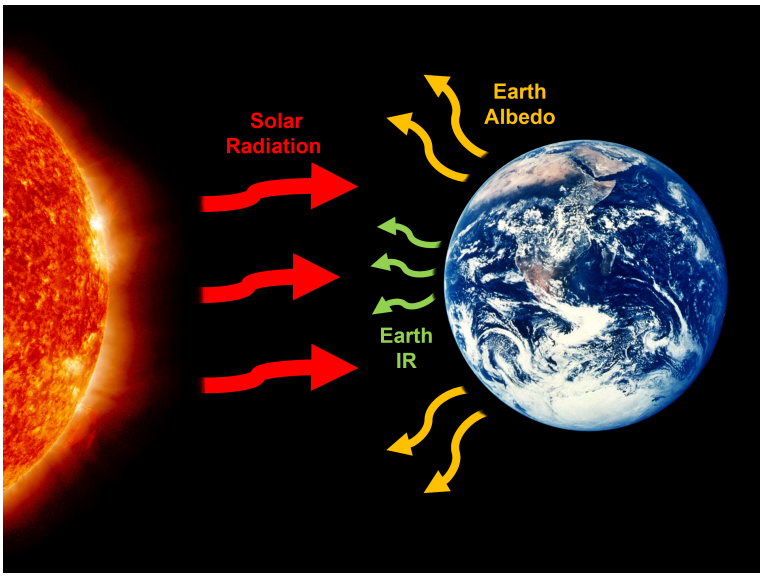

Figure 4.17: Solar and Earth radiation with the reflected (albedo) and emitted (infrared) components.

Since the surface properties of the spacecrafts are specified for the two different spectra, the effects of the IR ERP and of the albedo ERP should be distinguished in the computation. Similarly to the SRP, the ERP can be computed as:

$$P_{\oplus_A} = \frac{E_{\oplus_A}}{c}, \tag{4.19}$$

and

$$P_{\oplus_{IR}} = \frac{E_{\oplus_{IR}}}{c}, \tag{4.20}$$

where $E_{\oplus_A}$ and $E_{\oplus_{IR}}$ are the Earth irradiance respectively in the optical and infrared spectrum. Both $E_{\oplus_A}$ and $E_{\oplus_{IR}}$ are a function of the local Earth surface properties, such as local atmospheric conditions (e.g., clouds or clear sky) or surface covering (e.g., water, forests, snow). These characteristics determine the local reflectivity and emissivity if the Earth. Different models have been derive to describe this local properties, function of the latitude or function of latitude, longitude and time, such as the grid of cells reported in Figure 2.3 for the CERES model. The formulation to derive forces and torques due to Earth radiation pressure is completely identical to the one described for the Solar radiation pressure, with the only difference of taking into account the irradiance and the surface properties for the albedo and the infrared components.

4.3.2 Implementation in ARPA

Also the technique adopted in ARPA to model the ERP is identical to the one adopted for the SRP and described in the Section 4.2, taking into account the irradiance and the surface properties for the albedo and the infrared components.

Table 4.5: Parameters influencing the resultant ERP force on a spacecraft.

Parameter	Parameter type	Parameter explanation
$E_\oplus$	Environmental parameter	Earth irradiance
ρ	Satellite parameter	surface reflectivity
μ	Satellite parameter	surface specularity
Az	Geometric parameter	Azimuth of the incoming radiation direction in SRF
El	Geometric parameter	Elevation of the incoming radiation direction in the SRF
ϕ_1	Geometric parameter	1st Degree of Freedom of the solar panels
ϕ_2	Geometric parameter	2nd Degree of Freedom of the solar panels

Again the interaction of each ray (from each pixel) of the ray-source is modeled and accumulated to compute the total force and torque on the spacecraft, considering the subsequent multiple reflections as described for the SRP.

4.3.3 ERP Coefficients and Database creation

It is again necessary to identify which parameters affect the forces due to ERP on the spacecraft and need to be adjusted during the POD process. Table 4.5 shows the parameters that influence the resultant ERP force on a spacecraft. As for the SRP, in order to achieve the general validity of the computed forces, the effect of these parameters should be analyzed. If not explicitly stated, the adopted procedure is valid for both the albedo and infrared components (considering the correct surface properties and irradiance).

The first parameter $E_\oplus$ is the Earth irradiance, which depends on the solar radiation, the distance between the Earth and the Sun, and the Earth surface properties (reflectivity and emissivity). For the SRP it was shown in Equations 4.9 and 4.10 that the fraction $E_\odot/c$ is a multiplier. The same model applied to ERP leads to the fraction $E_\oplus/c$ as multiplier. It can hence be collected after the summation of the force contribution of each pixel, as

$$\mathbf{F} = \frac{E_\oplus}{c} \sum_{i=1}^{m} \sum_{j=1}^{n_i} \mathbf{F}'_{ij}, \tag{4.21}$$

where $\mathbf{F}'_{ij}$ is the force of each pixel at each reflection normalized by the factor $E_\oplus/c$. It is hence possible normalize Equation 4.21 by the factor $E_\oplus/c$, computing the adimensional force coefficients as

$$\mathbf{C_F} = \mathbf{F}\ \frac{c}{E_\oplus\ A_{ref}}, \tag{4.22}$$

where A_{ref} is an arbitrary reference area adopted to adimensionalize the coefficients. In this way it is possible to dispose of the dependency of the ERP computed force from the Earth irradiance $E_\oplus$, for both the albedo and infrared components.

The second parameter is the surface reflectivity ρ. In this case it is necessary to distinguish between the infrared and albedo components.

- The infrared reflectivity ρ_{IR} directly depends on the infrared emissivity ϵ, as $\rho_{IR} = 1-\epsilon$. From the GOCE technical documentation the values of emissivity for the satellite

surfaces were retrieved but no information about its degradation was provided. The emissivity provided was hence adopted for the surfaces assuming no degradation of the property in the infrared band. In this way ρ_{IR} can be assumed constant and can hence be excluded from the dependencies.

– The optical reflectivity ρ_{opt} is instead a function of the coefficient of absorption α in the optical band, as $\rho_{opt} = 1 - \alpha$. For this parameter the technical documentation provides sufficient information about the properties degradation as previously shown in Figure 4.13. Figure 4.18 shows the coefficients force due to ERP albedo component as computed for GOCE for different angles of the incoming Earth radiation in the BRF at Beginning Of Life (BOL) and End Of Life (EOL). As it is observable, the difference is small in terms of force amplitude for the majority of the directions considered (the one significant for the Earth radiation). The coefficients computed for values of azimuth around +90 *deg* and low elevation (when the radiation is incoming from the opposite side of the solar panels, where the radiator is located) the difference between BOL and EOL is significant. This is due to the fact that the optical properties of the shadow side (+Y) of the spacecraft degrade faster than for the rest of the satellite. This non-symmetric degradation profile leads to an unbalanced change in the force vector, which changes its amplitude (as shown in Figure 4.18) and its direction, up to 10 *deg*. In this case the difference from BOL and EOL is significant and cannot be neglected. It is hence not possible to dispose of the dependency of the ERP computed force from the degradation of the reflectivity in the visual band. In order to limit the number of input parameters for the database limiting the error in the ERP albedo coefficients it was chosen to build monthly or bimonthly databases throughout the entire life of the satellite. The average monthly or bimonthly optical properties were selected leading to 54 monthly databases with an error below 0.5% (±0.25%), and 27 bimonthly databases with an error below 1% (±0.5%) in the force coefficients.

No specific information related to the surface specularity were identified, and the parameter μ was assumed constant, and can be then excluded from the dependencies.

The four additional parameters Az, El, ϕ_1, and ϕ_2, defined as geometrical parameters (see Appendix A), are significantly affecting the force due to ERP for both the albedo and infrared components. Again, for GOCE the solar panels degrees of freedom are not applicable.

In conclusion, the parameters from which the computed ERP forces depend from are the geometrical parameters Az, El, ϕ_1, and ϕ_2, described in Table 4.5, as for the SRP. For what concerns the ERP albedo component the optical properties degradation has been modeled by means of monthly or bimonthly databases. In this way it was possible to develop one database of coefficients of ERP infrared force and 54 monthly and 27 bimonthly databases of coefficients of ERP albedo force, functions only of the geometrical parameters.

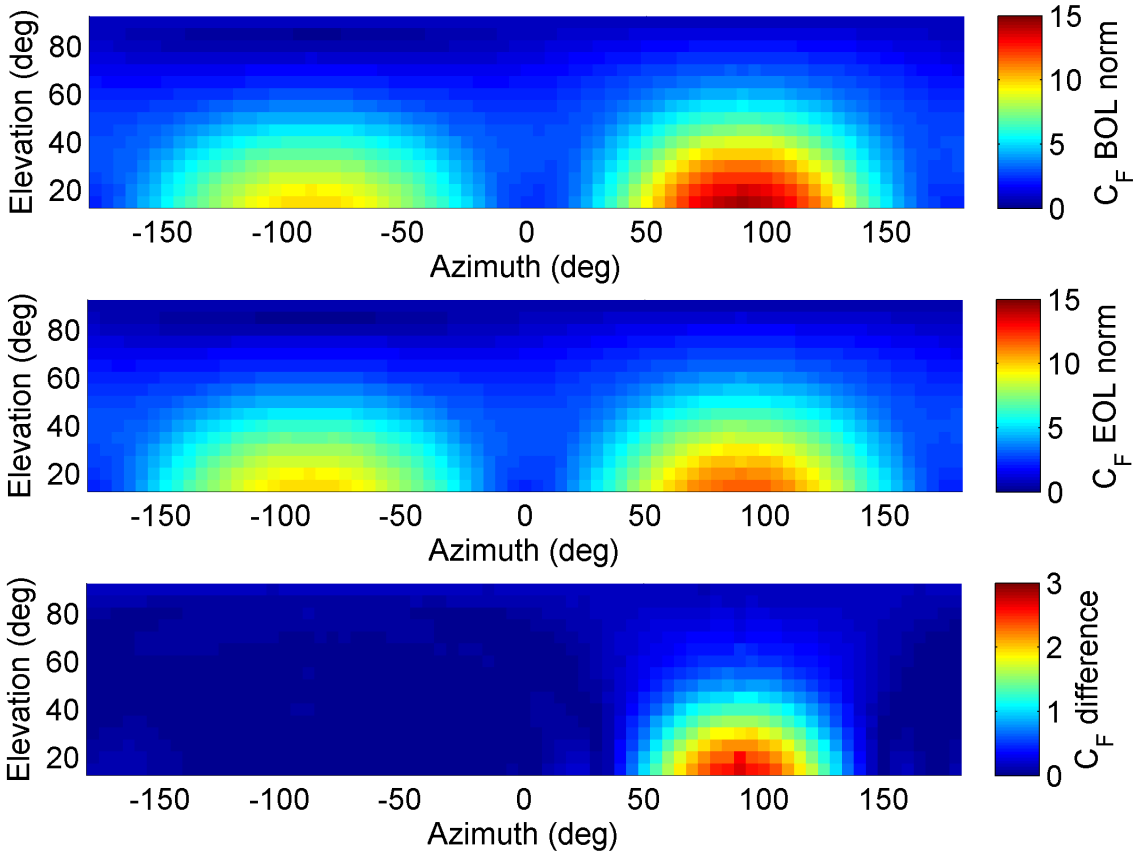

Figure 4.18: GOCE coefficient norm. At the top the coefficients computed at the BOL, at the center the coefficients computed at the EOL, and at the bottom the difference between the two, due to the optical properties degradation.

4.3.4 Test Cases result

Since the raytracing technique adopted for modeling the Earth radiation pressure is the same as for the solar radiation pressure no additional test cases were carried out, the only difference being the irradiance and the thermal surface properties for the ERP IR.

4.4 Thermal Re-Radiation Pressure

4.4.1 Mathematical model adopted in ARPA

The spacecraft Thermal Re-Radiation pressure (TRR) is the pressure exerted by the electromagnetic radiation emitted by a satellite surface. Based on the Stefan-Boltzmann law, every surface of area A with emissivity ϵ and a temperature T_s (with $T_s > 0\ K$) radiates toward the outer space a total power

$$P = A\,\epsilon\,\sigma\,T_s^4. \tag{4.23}$$

In order to determine which is the pressure exerted by this emitted power on the surface it is necessary to model the emitted radiation direction. If the body is treated as a diffuse radiator (which is a reasonable approximation for many surfaces [45], Lamberts Law can be applied [15]. Lamberts law states that for a diffuse radiator the energy flux E_P (measured in W/m^2) going through a point P varies as the cosine of the angle θ between that direction and the normal vector $\mathbf{n}$ of the surface element Q, and inversely with the square of the distance r between the source and the point, as

$$E_P = \frac{I \cos\theta}{r^2}, \tag{4.24}$$

where I is defined as the energy flux per unit solid angle, per unit area of emitting surface projected normal to the direction in which the energy is traveling, and this is constant in Lambertian emission. The mathematical derivation of the integral of Equation 4.24 in the outer semi-space can be found in [1], and leads to the corresponding recoil force applied to the body, per unit area of the surface

$$\mathbf{F}_{TRR} = -\frac{2}{3\,c}\int_A \epsilon\,\sigma\,T_s^4\,dA\,\mathbf{n}, \tag{4.25}$$

which is aligned with the outer normal to the surface, but pointing oppositely.

4.4.2 Implementation in ARPA

As can be observed from Equation 4.25 the main parameters that determine the TRR are:

1. the surface emissivity ϵ,
2. the surface temperature T,
3. the surface area A.

The surface emissivity was previously described in Section 4.1.2, while the surface temperature will be described in detail in the following section in the database creation. For what concerns the surface area (area A and its outer normal $\mathbf{n}$) it is necessary to accurately describe the outer surfaces of the spacecraft. For this reason a discretization of the outer surfaces, as shown in Section 4.1.4, was realized. In this way it is possible to solve Equation 4.25 numerically, summing up the contribution of each i-th pixel to the TRR force as follow

$$\mathbf{F}_{TRR} = -\frac{2}{3\,c}\sum_{i=1}^{m} \epsilon_i\,\sigma\,T_{s_i}^4\,A_i\,\mathbf{n}_i, \tag{4.26}$$

where m is the total number of pixels. In this way, based on the area of each pixel A_i, its normal $\mathbf{n}_i$, its thermal property ϵ_i, and its temperature T_i it is possible to compute the force $\mathbf{F}_{TRR}$. Similarly it is possible to compute the total torque exerted by the thermal emission

$$\mathbf{T}_{TRR} = -\frac{2}{3\,c}\sum_{i=1}^{m} \epsilon_i\,\sigma\,T_{s_i}^4\,A_i\,\mathbf{d}_i \times \mathbf{n_i}, \tag{4.27}$$

Table 4.6: Parameters influencing the resultant TRR force on a spacecraft

Parameter	Parameter type	Parameter explanation
T_s	Satellite parameter	surface temperature
ϵ	Satellite parameter	surface emissivity
ϕ_1	Geometric parameter	1st Degree of Freedom of the solar panels
ϕ_2	Geometric parameter	2nd Degree of Freedom of the solar panels

where $\mathbf{d}_i$ is the position vector of the i-th pixel on the surface with respect to the satellite center of mass.

4.4.3 TRR Database creation

The parameters that affect the TRR force components are shown in Table 4.6. For what concerns the temperature of the surfaces of the spacecraft the GOCE telemetry data[1] and the data from the thermal technical report [104] were analyzed. The temperature profile of the solar panels mounted on the wings and on the central (CP) and outer (OP) panels of GOCE can be observed in Figures 4.19 and 4.20. Also the other surfaces on the front(+X), back(-X) and shadow(+Y) sides of the satellite were analyzed. As observable in both the Figures 4.19 and 4.20 the temperature of each surface during the year is usually constrained to a narrow range of temperatures, while sometimes they are subjected to a temperature drop due to the satellite entering in eclipse. The eclipse condition is shown in Figure 4.21. Due to the sun-synchronous dawn dusk orbit the satellite is usually exposed to the direct solar radiation while for certain periods of time (during summer and winter) the satellite during the orbits enters in eclipse. This is observable from the temperature profile, where the satellite temperatures are higher and almost constant when there are no eclipses (hot case) while for other periods the temperatures quickly drop due to the eclipses (cold case). From the analysis of the temperature profiles, in order to create a database of forces which applicable to all the orbits of GOCE, the followings were assumed:

- when the satellite is fully exposed to the direct solar radiation each surface is at its non-eclipse equilibrium temperature (hot case);
- when the satellite is in complete eclipse each surface is at its eclipse equilibrium temperature (cold case);
- when the satellite is passing from non-eclipse to eclipse and viceversa, the temperature of each surface changes as a function of the fraction of Sun visible from the spacecraft.

In this way, identifying the non-eclipse and eclipse equilibrium temperatures of each satellite panel, it is possible to apply Equation 4.26 to compute the TRR force in case of no eclipse and in case of eclipse. Based on the telemetry data it was possible to identify the hot and

[1]These data were kindly provided by ESA/ESOC GOCE control team. A special thank for the support goes to the GOCE System Operation Manager C. Steiger and to the GOCE System Operation Engineer C.E. Ghisi.

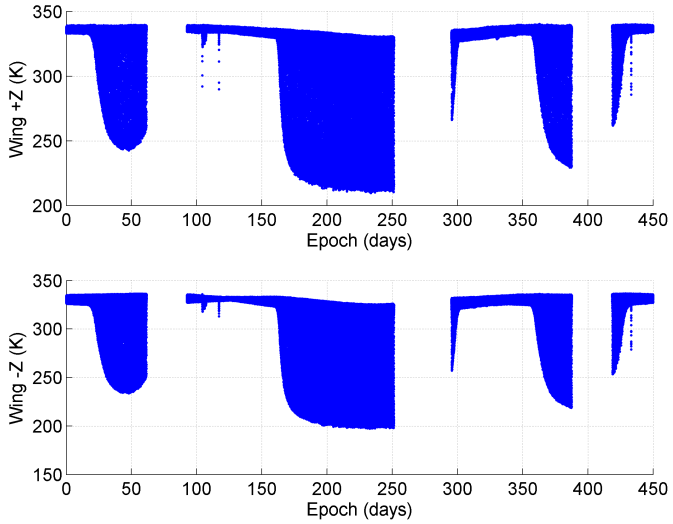

Figure 4.19: Temperatures profile of the GOCE wing-mounted solar panels.

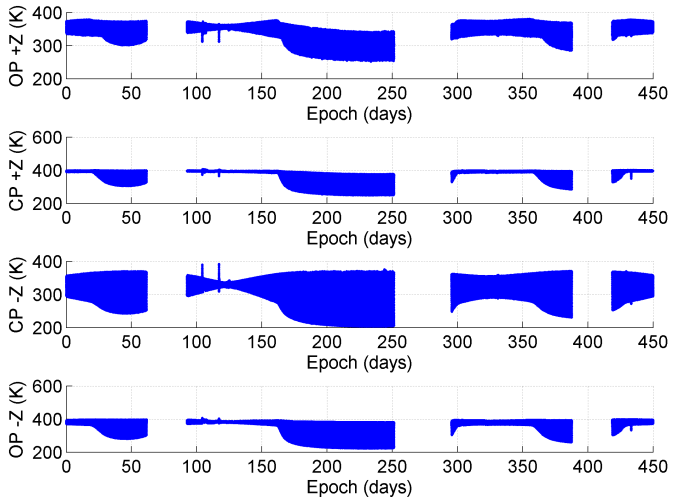

Figure 4.20: Temperatures profile of the GOCE body-mounted solar panels, showing the outer panels (OP) and central panels (CP) of the satellite.

cold cases temperatures averaging respectively the non-eclipse and eclipse temperatures of each satellite surface. The hot and cold temperatures for the solar panels are reported in Table 4.7. Even if the standard deviation obtained with this approach is relatively high, it will be shown in the results that the method is capable of accurately modeling the perturbation introduced by the TRR. This approach was chosen in order to maintain the general validity of the database designed limiting as most as possible the approximation

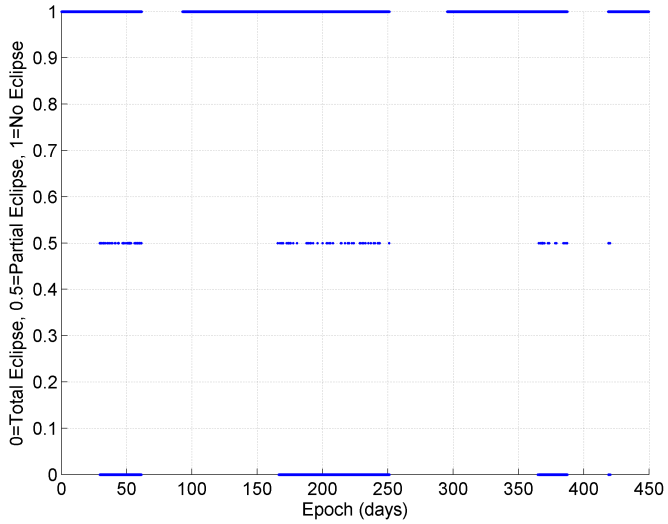

Figure 4.21: GOCE eclipse condition. 0 corresponds to total eclipse, 0.5 to partial eclipse, 1 to no-eclipse conditions of the spacecraft.

Table 4.7: Hot and cold temperatures and their standard deviation for the GOCE solar panels.

Solar Panel	Hot temp. (K)	STD Hot temp. (K)	Cold temp. (K)	STD Cold temp. (K)
Wing +Z	329.94	16.27	249.47	29.93
Wing -Z	324.42	17.68	240.05	31.48
Outer Panel +Z	344.57	21.45	296.51	27.11
Outer Panel -Z	372.56	20.48	281.61	34.05
Center Panel +Z	383.97	34.99	302.66	25.33
Center Panel -Z	321.40	24.86	252.58	35.86

introduced.

For what concerns the surface emissivity ϵ the solution is the same adopted for the Earth radiation pressure in the infrared band. From the GOCE technical documentation the values of emissivity for the satellite surfaces were retrieved but no information about its degradation was provided. The emissivity provided was hence adopted for the surfaces assuming no degradation of the property in the infrared band.

The two additional parameters ϕ_1, and ϕ_2, defined as geometrical parameters (see Appendix A), are significantly affecting the force due to TRR due tot he rotation of the solar panels. A rotation of the solar panels will result in a change of the direction of the TRR force, due to the change in direction of the surfaces thermal emission. Again, for GOCE the solar panels degrees of freedom are not applicable.

In conclusion, the parameters from which the computed TRR forces depend from are the condition of eclipse, which defines the surface temperatures, and the geometrical parameters ϕ_1, and ϕ_2. For each orientation of the solar panels two forces (magnitude and direction

for the eclipse and non-eclipse condition) are computed as

$$\mathbf{F}_{TRR-ecl} = = -\frac{2\,\sigma}{3\,c}\sum_{i=1}^{m}\epsilon_i\,T_{ecl_i}^4\sum_{j=1}^{m_i}A_j\,\mathbf{n}_j, \tag{4.28a}$$

$$\mathbf{F}_{TRR-NOecl} = = -\frac{2\,\sigma}{3\,c}\sum_{i=1}^{m}\epsilon_i\,T_{NOecl_i}^4\sum_{j=1}^{m_i}A_j\,\mathbf{n}_j, \tag{4.28b}$$

where i is the i-th panel of the satellite with temperature T_{ecl_i} or T_{NOecl_i} and emissivity ϵ_i, each panel discretized with m_i pixels. j corresponds to j-th pixel of the i-th panel with area A_j and outward normal $\mathbf{n}_j$. In this way it was possible to develop one database of two TRR forces (eclipse and non-eclipse) functions only of the solar panels orientation. For GOCE this turns out to be only one database which contains only the eclipse and non-eclipse TRR forces.

4.4.4 Test Cases results

In order to test and validate the procedure adopted to compute the force over a satellite due to the TRR two main test cases were carried out: 1) test on flat plate and 2) test on perfect sphere, as shown in Figure 4.22.

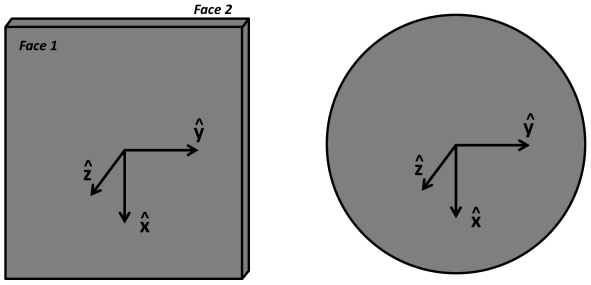

Figure 4.22: Flat plate and perfect sphere test cases. Flat plate is assumed with a negligible thickness and with different temperatures of the faces. The sphere is instead assumed with isotropic emissivity and temperature distribution.

The results for the flat plate are shown in Table 4.8 and for the sphere in Table 4.9. As it is observable from the test cases for both the flat plate and the sphere the solution implemented in ARPA is capable of accurately describing the force due to TRR on flat and curved surfaces. Again, to higher resolutions of the surface mesh correspond higher accuracy of the force modeling. It will be hence necessary, as for the SRP and ERP, to achieve the compromise between accuracy and computational power and time.

Table 4.8: Flat plate test case results. ARPA and analytical solutions are compared. $T_1 = 0\ deg$ and $T_2 = 100\ deg$ and $A = 1\ m^2$.

Emissivity	ARPA solution (N) $1\ cm^2$ resolution	ARPA solution (N) $1\ mm^2$ resolution	Analytical solution (N)
$\epsilon = 0.5$	$F_x = 0$ $F_y = 0$ $F_z = 8.7431 \times 10^{-07}$ $\|\mathbf{F}\| = 8.7431 \times 10^{-07}$	$F_x = 0$ $F_y = 0$ $F_z = 8.7177 \times 10^{-07}$ $\|\mathbf{F}\| = 8.7177 \times 10^{-07}$	$F_x = 0$ $F_y = 0$ $F_z = 8.7080 \times 10^{-07}$ $\|\mathbf{F}\| = 8.7080 \times 10^{-07}$
Approximation	0.4031 %	0.1114 %	–
$\epsilon = 1$	$F_x = 0$ $F_y = 0$ $F_z = 1.7486 \times 10^{-06}$ $\|\mathbf{F}\| = 1.7486 \times 10^{-06}$	$F_x = 0$ $F_y = 0$ $F_z = 1.7435 \times 10^{-06}$ $\|\mathbf{F}\| = 1.7435 \times 10^{-06}$	$F_x = 0$ $F_y = 0$ $F_z = 1.7416 \times 10^{-06}$ $\|\mathbf{F}\| = 1.7416 \times 10^{-06}$
Approximation	0.4031 %	0.1114 %	–

Table 4.9: Perfect sphere test case results. ARPA and analytical solutions are compared. $T = 100\ deg$ and diameter $D = 1\ m$.

Emissivity	ARPA solution (N) $1\ cm^2$ resolution	ARPA solution (N) $1\ mm^2$ resolution	Analytical solution (N)
$\epsilon = 0.5$	$F_x = 2.3164 \times 10^{-10}$ $F_y = 1.9478 \times 10^{-10}$ $F_z = 1.5471 \times 10^{-10}$ $\|\mathbf{F}\| = 3.3990 \times 10^{-10}$	$F_x = 1.4173 \times 10^{-11}$ $F_y = 1.1421 \times 10^{-11}$ $F_z = 2.1547 \times 10^{-11}$ $\|\mathbf{F}\| = 2.8206 \times 10^{-11}$	$F_x = 0$ $F_y = 0$ $F_z = 0$ $\|\mathbf{F}\| = 0$
Approximation	3.3990×10^{-10}	2.8206×10^{-11}	–
$\epsilon = 1$	$F_x = 4.6328 \times 10^{-10}$ $F_y = 3.8956 \times 10^{-10}$ $F_z = 3.0942 \times 10^{-10}$ $\|\mathbf{F}\| = 6.7980 \times 10^{-10}$	$F_x = 2.8346 \times 10^{-11}$ $F_y = 2.2842 \times 10^{-11}$ $F_z = 4.3094 \times 10^{-11}$ $\|\mathbf{F}\| = 5.6412 \times 10^{-11}$	$F_x = 0$ $F_y = 0$ $F_z = 0$ $\|\mathbf{F}\| = 0$
Approximation	6.7980×10^{-10}	5.6412×10^{-11}	–

4.5 Aerodynamics

4.5.1 Mathematical model adopted in ARPA

At altitudes above 120-150 km the atmospheric density is sufficiently low that conventional continuum assumptions are no longer valid [92]. The parameter which defines the characteristics of the interaction between the airflow and the satellite is called Knudsen number Kn, which is defined a

$$Kn = \frac{\lambda}{L}, \tag{4.29}$$

where λ is the mean molecular free path of the air particles which compone the atmosphere and L is the characteristic length of the spacecraft, usually its length. When this parameter is below the value of 0.01 the airflow can be considered as a continuum and the continuum regime is applied (Navier-Stokes equations). When the Knudsen number is between 0.01 and 10 the transition regime is applied, and when it is higher than 10 the flow assumes the free-molecular flow regime. The satellite aerodynamics is usually based on this last regime. In free-molecular flow regime the air particles can be treated independently, and if an air particle hits the surface of a spacecraft, it will travel a significantly long path before it collides again with the satellite or with another particle (from here the name "free-molecular"). Based on [92], $\lambda = 1400\ m$ was identified for an average altitude of GOCE of about 260 km, and, since the satellite length is about $L = 5.26\,m$ the Knudsen number was computed to be $Kn = 266$, clearly identifying the free molecular flow regime for the computation of the GOCE aerodynamics.

In order to model the satellite aerodynamics for GOCE the hyperthermal simplification has not been introduced. Recalling from the theory ([92]) the distinction between thermal and hyperthermal flow depends on the molecular speed ratio, which is the ratio between the mean thermal motion of the atmospheric particles and the relative velocity of the spacecraft with respect to the atmosphere which are shown in Equation (4.30) and (4.31):

$$V_{mp} = \sqrt{\frac{2\,k_B\,T_\infty}{m_g}}, \tag{4.30}$$

$$V_{rel} = \left\| \mathbf{V}_{S/C} - \mathbf{V}_{atm} \right\|, \tag{4.31}$$

where k_B is the Boltzmann constant, T_∞ is the atmospheric temperature, m_g is the atmospheric mean molecular mass, $\mathbf{V}_{S/C}$ is the inertial velocity vector of the spacecraft, and $\mathbf{V}_{atm}$ is the inertial velocity of the atmosphere, assumed co-rotating with the Earth.

The most probable speed ratio can hence be computed as

$$s = \frac{V_{rel}}{V_{mp}}. \tag{4.32}$$

For the average conditions of GOCE ($T_\infty = 800\ K$, $m_g = 3.19 \times 10^{-26}\ kg/mol$, and $V_{rel} = 7810\ m/s$), the average most probable speed is $V_{mp} = 834\ m/s$ and the speed ratio is $s = 9.37$, value that does not allow the hyperthermal simplification. It is in fact

observable that the thermal motion (thermal agitation) represented by the most probable speed is note negligible (10.7%) with respect to the satellite relative velocity: the thermal flow theory should hence be adopted.

In order to compute the aerodynamic of a satellite it is necessary to compute first the kinetic temperature of the incident flow as

$$T_{k,i} = \frac{m_g \, V_{rel}^2}{3 \, k_B}. \tag{4.33}$$

The accommodation coefficient represents the average fraction of energy lost by the molecules impinging the surfaces, and is formally defined as [85]

$$\alpha_{acc} = \frac{T_{k,i} - T_{k,r}}{T_{k,i} - T_{wall}}, \tag{4.34}$$

where $T_{k,r}$ is the kinetic temperature of the reflected flow and T_{wall} is the surface temperature of the spacecraft. The derivation of the accommodation coefficients will be discussed later. From (4.34) it is possible to derive the the kinetic temperature of the reflected flow as

$$T_{k,r} = T_{k,i} \, (1 - \alpha_{acc}) \, + \, \alpha_{acc} \, T_{wall}. \tag{4.35}$$

Based on [11], it is hence possible to write the aerodynamic pressure p and the shear stress τ on a surface of the spacecraft as

$$\begin{aligned} \frac{p}{p_\infty} &= \left(\frac{s \sin\alpha}{\sqrt{\pi}} + \frac{1}{2} \sqrt{\frac{T_{k,r}}{T_\infty}} \right) e^{-(s \sin\alpha)^2} \\ &+ \left(\frac{1}{2} (s \sin\alpha)^2 + \frac{1}{2} \sqrt{\pi} \sqrt{\frac{T_{k,r}}{T_\infty}} s \sin\alpha \right) (1 + erf \, (s \sin\alpha)) \end{aligned} \tag{4.36}$$

$$\frac{\tau}{p_\infty} = \frac{s \cos\alpha}{\sqrt{\pi}} e^{-(s \sin\alpha)^2} + \sqrt{\pi} \, s \sin\alpha \, (1 + erf \, (s \sin\alpha)) \, . \tag{4.37}$$

Equations (4.36) and (4.37) show respectively the component of pressure normal to the surface (pressure) and along the surface (shear stress). p_∞ is the atmospheric pressure of the undisturbed flow that is hitting the satellite surfaces,α is the angle of attack of the flow on the surface, defined as at the top corner of Figure 4.23, and erf is the Gauss error function, defined as

$$erf \, (x) = \frac{2}{\sqrt{\pi}} \int_0^x e^{-t^2} \mathrm{d}t. \tag{4.38}$$

Figure 4.23 shows also the pressure and shear stress, normalized by the atmospheric pressure, as a function of the angle of attack. For this plot the accommodation coefficient was chosen equal to 0.99, and the spacecraft wall temperature equal to 300 K, while the other parameters were set up equal to the GOCE average conditions. It is interesting to observe the component of shear stress when the angle of attack is below 0 deg. This means that when the surface is not directly exposed to the airflow it is still experiencing a braking effect of the air, contributing to the total aerodynamic drag. In the specific case of GOCE

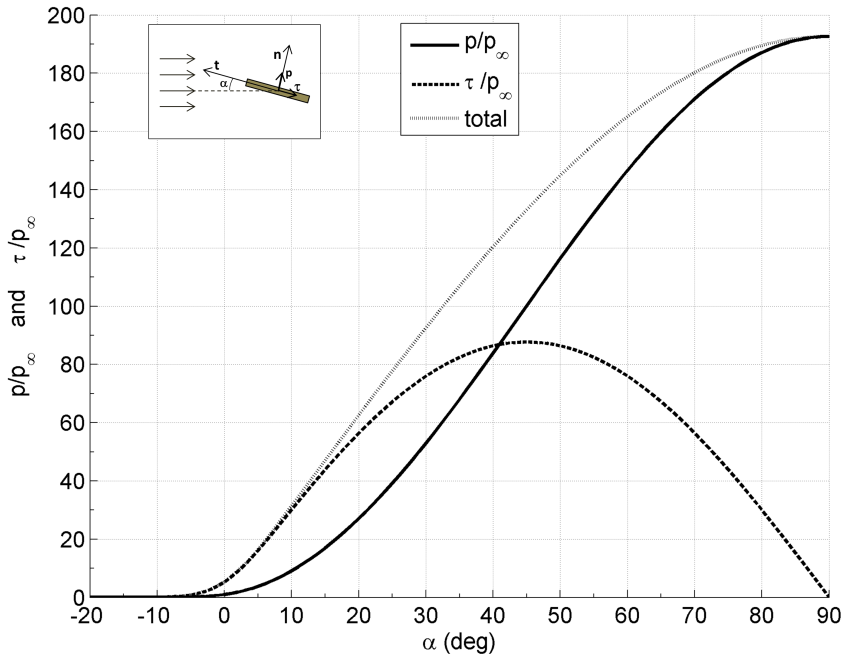

Figure 4.23: Aerodynamic pressure p and shear stress τ on a flat plate, normalized by the atmospheric pressure p_∞, as a function of the angle of attack α of the incoming airflow.

the lateral panels and wing significantly contribute to the total aerodynamic acceleration experienced by the satellite and cannot be neglected. In fact for this satellite, which has a very small frontal area of about 1 m^2, the total lateral area is close to 25 m^2 and shear stress on these surfaces cannot be neglected. For increasing angles of attack both the components of shear stress and pressure increases and after the 40 *deg* the pressure component becomes predominant, while the shear stress, after reaching its maximum at 45 *deg*, progressively decreases. In the end, with the surface exposed normally to the flow the component of pressure is maximum and the shear stress goes to zero, exerting the maximum aerodynamic force on the body.

Figure 4.24 shows the aerodynamic coefficients for a flat plate. As it is possible to observe, for increasing values of the angle of attack the drag of the flat plate increases, reaching its maximum when the plate is orthogonal to the incoming flow. The lift instead increases until its maximum at about $\alpha = 40\,deg$ and then decreases again to zero. This is the condition of stall. It is interesting to observe that for low speed ratios the aerodynamic interaction with the surfaces is stronger, leading to higher drag and lift coefficients. The higher the speed ratio is the lower drag and lift coefficient the satellite would experience. This does not mean that the satellite would experience lower aerodynamic acceleration, since, if the speed ratio is higher due to higher relative velocity, the final drag force would be in the end higher. Recalling Equation (2.4) the drag acceleration is in fact directly proportional to V_{rel}^2. Instead, if the speed ratio increases due to lower atmospheric temperature T_∞ or higher mean molecular mass m_g (see Equation (4.30)) also the resulting drag acceleration

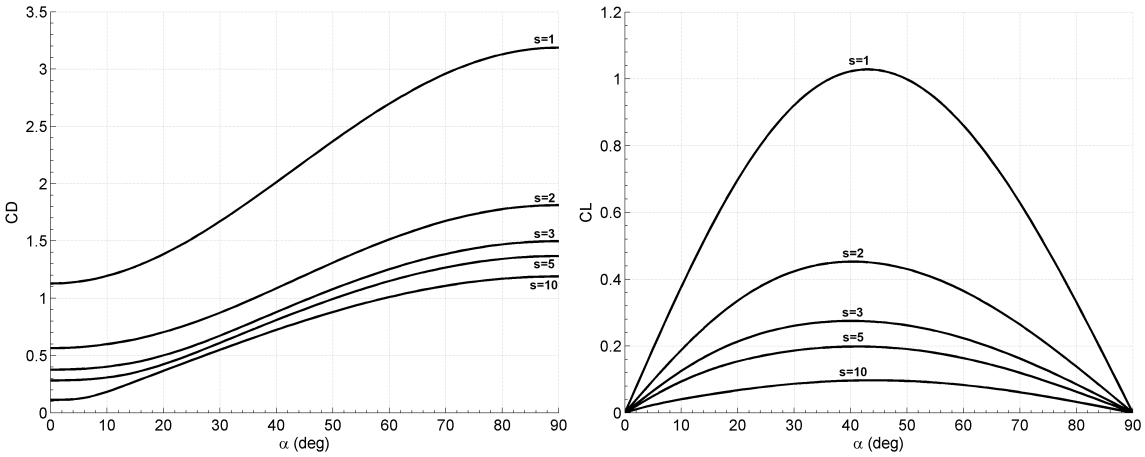

Figure 4.24: Aerodynamic drag coefficient (C_D, on the left) and lift coefficient (C_L, on the right) for a flat plate as a function of the angle of attack α of the incoming airflow.

experienced by the satellite will be lower. In other words lower atmospheric temperature T_∞ and higher mean molecular mass m_g, keeping constant all the other parameters, will reduce the satellite drag.

As already said, the main difficulty in modeling the satellite aerodynamics is related to the modeling of the interaction of the airflow with the satellite surfaces, and in particular to the the momentum and energy exchange that takes place during this interaction. Based on Equation (4.35) the kinetic temperature of the reflected particles is directly dependant on the kinetic temperature of the incoming particles and the satellite surface temperature via the accommodation coefficient α_{acc}. Based on the Bird theory of Equations (4.36) and (4.37), the definition of the satellite aerodynamics directly depends on the modeling the energy accommodation coefficient. Based on the most recent literature ([63, 64, 71, 72, 73]) three most significant models for the energy accommodation coefficient were selected and analyzed.

1. the accommodation coefficient used by Sutton [95];

2. the semi-empirical Energy Accommodation Coefficient Model developed by Pilinski [71], based on the lattice theory, which will be unofficially called *EACM* model for simplicity, as quoted in [63];

3. the Semi-Empirical Satellite energy Accommodation coefficient Model (SESAM) also developed by Pilinski [73], which is an evolution of the EACM model.

For Sutton the accommodation coefficient of the spacecraft can be assumed constant and equal to $\alpha_{acc} = 0.93$, which corresponds to quasi-fully accommodated reflected flow. The assumption of a constant accommodation coefficient, even if suitable for the force database creation, is physically too simplistic and does not accurately represents the airflow-surface

interaction. For this reason it has not been adopted for the database computation, even if it has been implemented in ARPA.

The EACM model instead defines the accommodation coefficient as a function of the surface substrate of atomic oxygen, applying a modification to the Goodman's theory [37]. This model defines the accommodation coefficient directly in the form of the Langmuir formula

$$\alpha_{acc} = \frac{K\,P}{1\,+\,K\,P}, \tag{4.39}$$

where K is the Langmuir fitting parameter, a constant equal to $K = 7.5 \times 10^{-17}$ and $P = n_O\,T_\infty$, where n_O is the number density of the atomic oxygen. This model, based on Langmuir's adsorption isotherm, is a semi-empirical model which combines the theory that gas-surface interactions in low Earth orbit are driven by adsorption of atomic oxygen, with observations of satellite accommodation coefficients.

The SESAM model instead defines the accommodation coefficient as a weighted average of the two gas-surface interaction types: the interaction between the airflow and the satellite surface and the interaction between the airflow and the adsorbate (the thin substrate of atomic oxygen covering the surface). The accommodation coefficient can be written as

$$\alpha_{acc} = (1-\theta)\,\alpha_s\,+\,\theta\,\alpha_{ads}, \tag{4.40}$$

where θ represents the fraction of sites in the surface occupied by adsorbate, α_{ads} is the average accommodation coefficient experienced by incoming molecules colliding with the adsorbate and α_s is the average accommodation coefficient for collisions with the surface material. The gas-substrate interaction can be simply approximated by a lattice interaction model such as that of Goodman [37], as

$$\alpha_s = \frac{K_s\,\mu_s}{(1\,+\,\mu_s)^2}, \tag{4.41}$$

where K_s is the substrate coefficient, and μ_s is the mass ratio of the incoming molecule m_g to the molecules of the surface lattice m_s. The effective fractional coverage of atomic oxygen is defined as

$$\theta = \frac{K_L\,P_O}{1\,+\,K_L\,P_O}, \tag{4.42}$$

where K_L is the Langmuir parameter [73], and P_O is the partial pressure of the atomic oxygen, defined as

$$P_O = \frac{1}{2}\,\rho_O\,V_{rel}^2\,\left(\frac{2s^2+1}{\sqrt{\pi}s^3}\,e^{-s^2}\,\frac{4s^4+4s^2+1}{2s^4}\,erf\,(s)\right), \tag{4.43}$$

where ρ_O is the density of the atomic oxygen. It is practical for the further applications to recall the definion

$$\rho_O = n_O\,m_O$$

where n_O is the number density of atomic oxygen and m_O is the atomic oxygen mass, equal to $2.657e-26\ kg$. Adsorption experiments involving adsorption at the gas-liquid interface provide further support for an α_{ads} value of unity when the impinging molecule is close in mass to the adsorbed molecule [73].

4.5.2 Implementation in ARPA

By means of Equations 4.36 and 4.37 it is possible to compute the aerodynamic pressure and shear stress on a surface. Recalling the thermal flow theory adopted in this work, each satellite surface, even if not directly exposed to the airflow, experiences the interaction with the atmospheric particles due to their thermal vibration, contributing to the total aerodynamic effects on the spacecraft. For this reason the surface mesh discretization described in Section 4.1.4 has been adopted to compute the aerodynamic forces and torques.

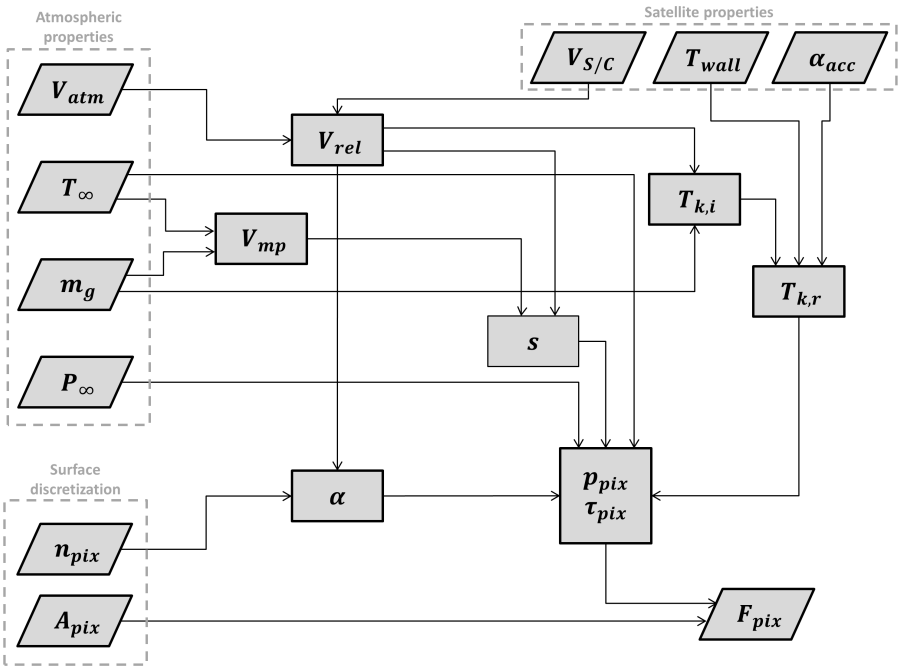

Figure 4.25: Block diagram of the implemented process in ARPA to compute the aerodynamic force over a surface element (pixel).

Figure 4.25 shows the process adopted in ARPA to compute the aerodynamic forces. Given the atmospheric properties (i.e, atmospheric inertial speed $\mathbf{V}_{atm}$, temperature T_∞, mean molecular mass m_g, and pressure p_∞), the satellite properties (i.e., spacecraft inertial speed $\mathbf{V}_{S/C}$, surface temperature T_{wall}, and accommodation coefficient α_{acc}), and the surface discretization pixel properties (pixel outward normal $\mathbf{n}_{pix}$, and pixel area A_{pix}) it is possible to compute the contribution of each pixel of the surface with the atmospheric airflow, deriving the aerodynamic force for each pixel. What is important to notice is that, for each pixel, the angle of attack α of the incoming airflow with the considered pixel is computed and the pixel area A_{pix} is used to convert pressure and shear stress into the aerodynamic force. Afterwards the contribution of each pixel is accumulated leading to the

aerodynamic force, as

$$\mathbf{F}_{aero} = p_\infty \sum_{i=1}^{m} A_{pix_i} \left(p_{pix_i} \, \mathbf{n}_{pix_i} \; + \; \tau_{pix_i} \, \boldsymbol{\tau}_{pix_i} \right), \tag{4.44}$$

and aerodynamic torque

$$\mathbf{F}_{aero} = p_\infty \sum_{i=1}^{m} A_{pix_i} \, \mathbf{d}_i \times \left(p_{pix_i} \, \mathbf{n}_{pix_i} \; + \; \tau_{pix_i} \, \boldsymbol{\tau}_{pix_i} \right), \tag{4.45}$$

where $\mathbf{d}_i$ is the position vector of the i-th pixel on the surface with respect to the satellite center of mass. With a surface discretization it possible hence possible to compute the aerodynamic force and torque on a body with any shape.

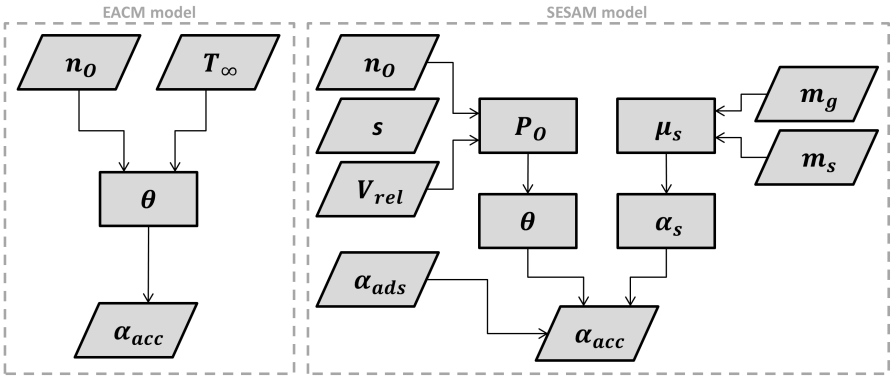

Figure 4.26: Block diagram of accommodation coefficient for the EACM and SESAM models.

Figure 4.26 shows the implementation of the EACM and SESAM model for the computation of the accommodation coefficients. The EACM model allows the computation of the accommodation coefficient from the atmospheric properties (i.e., number density of atomic oxygen n_O and atmospheric temperature T_∞), while the SESAM model requires more parameters to describe the atmosphere (n_O and the mean molecular mass m_g), the satellite-atmospheric properties (i.e.,speed ratio s, relative velocity V_{rel} and accommodation coefficient of the adsorbate α_{ads}), and the satellite properties (i.e., mean molecular mass of the satellite surfaces m_s).

4.5.3 Aerodynamic Coefficients and Database creation

Again, in order to achieve the general validity of the database of aerodynamic forces, it is necessary to identify which parameters affect the forces on the spacecraft and need to be adjusted during the POD process. Table 4.10 shows the parameters that influence the resultant aerodynamic force on a spacecraft.

In Table 4.10 the first parameter ρ_∞ is shown instead of the atmospheric pressure p_∞. From a technical point of view, it does not make any difference to consider one of the two

Table 4.10: Parameters influencing the resultant aerodynamic force on a spacecraft.

Parameter	Parameter type	Parameter explanation
ρ_∞	Environmental parameter	Atmospheric density
T_∞	Environmental parameter	Atmospheric temperature
m_g	Environmental parameter	Atmospheric mean molecular mass
n_O	Environmental parameter	Number density of atomic oxygen
V_{rel}	Sat-Env. parameter	S/C relative velocity with respect to atmosphere
T_{wall}	Satellite parameter	Satellite surfaces temperature
Az	Geometric parameter	Azimuth of the incoming airflow direction in SRF
El	Geometric parameter	Elevation of the incoming irflow direction in the SRF
ϕ_1	Geometric parameter	1st Degree of Freedom of the solar panels
ϕ_2	Geometric parameter	2nd Degree of Freedom of the solar panels

parameters, since, together with T_∞ and m_g, their are directly proportional based on the ideal gas law

$$p_\infty = k_B \frac{\rho_\infty \, T_\infty}{m_g}, \tag{4.46}$$

where k_B is the Boltzmann constant. ρ_∞ was selected for simplicity since it directly computed by the the MSIS-E-90 ([40]) and NRLMSISE-00 ([70]) atmospheric models. By computing the aerodynamic coefficients

$$\mathbf{C_F} = \frac{\mathbf{F}}{\frac{1}{2}\,\rho_\infty \, V_{rel}^2 \, A_{ref}}, \tag{4.47}$$

where A_{ref} is an arbitrary reference area, and substituting Equation 4.46 into Equation 4.44, it is possible to dispose of the dependency of the aerodynamic coefficients from the atmospheric density, leading to the simplified aerodynamic coefficients

$$\mathbf{C_F} = \frac{k_B \frac{T_\infty}{m_g} \sum_{i=1}^{m} A_{pix_i} \left(p_{pix_i} \, \mathbf{n}_{pix_i} \; + \; \tau_{pix_i} \, \boldsymbol{\tau}_{pix_i} \right)}{\frac{1}{2}\, V_{rel}^2 \, A_{ref}}. \tag{4.48}$$

For what concerns the relative velocity of the spacecraft with respect to the atmosphere V_{rel} it was necessary to identify the maximum excursion of this parameter for GOCE. The orbit of GOCE during the designed science phase is almost perfectly circular (orbital eccentricity $e = 0.0027$) and the atmosphere is assumed co-rotating with the Earth. By means of a numerical simulation the relative velocity has been computed, and its maximum magnitude has been computed to be about $V_{rel_{MAX}} \approx 7.7826 \; km/s$ and its minimum about $V_{rel_{MIN}} \approx 7.8383 \; km/s$, as shown in Figure 4.27. Maintaining constant all the other parameters at their average conditions, the aerodynamic coefficients were computed for the maximum and minimum values of V_{rel}, and the results are shown in Table 4.11. It is observable that this change of V_{rel} only leads to a change of about 0.23% in the magnitude of $\mathbf{C_F}$ and in a negligible deflection of the direction of the force (about $3 \times 10^{-4} \; deg$). The dependance of the aerodynamic coefficients from the variation of the relative velocity can be neglected and V_{rel} can be excluded. Its average value $V_{rel_{AVG}} \approx 7.8105 \; km/s$ will be assumed for the coefficients computation.

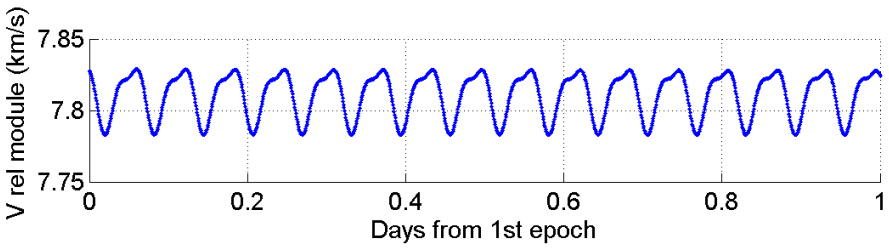

Figure 4.27: Relative velocity of GOCE with respect to the Earth co-rotating atmosphere.

Table 4.11: Aerodynamic coefficients for minimum and maximum values of V_{rel}.

Aerodynamic coefficients	$V_{rel_{MIN}}$	$V_{rel_{MAX}}$
C_{F_x}	-3.5462	-3.5346
C_{F_y}	-0.0017	-0.0017
C_{F_z}	-0.0003	-0.0003

The satellite surfaces temperature T_{wall} determines, together with the accommodation coefficient and the kinetic temperature of the incoming flow, the kinetic temperature of the reflected flow. Again, the temperature excursion of all the surfaces has been identified and the aerodynamic coefficients were computed for the hot case (non-eclipse condition) and cold case (eclipse condition). As can be observed in Figure 4.28, for all the three reported models, the difference between the aerodynamic coefficients computed for the eclipse and non-eclipse conditions is very small. As can be observed in Table 4.12 the change from hot case to cold case leads to negligible variations of the force magnitude (at most 0.1% with the SESAM model) and direction (at most 0.1 *deg* with the SESAM model), and the dependance of the aerodynamic coefficients from the temperature of the satellite surfaces can be hence excluded. The average conditions of temperature have been assumed for the satellite surfaces for the computation of the aerodynamic forces.

For what concerns the three remaining environmental parameters, the atmospheric temperature T_∞, mean molecular mass m_g and number density of atomic oxygen n_O, another simulation was performed in order to identify all the possible conditions of these parameters. The simulation was run over the entire expected satellite life (from March 2009 to December 2013), for the expected science-phase altitudes (from 230 *km* to 270 *km* including margins) for the latitude and longitudes, using the NRLMSISE-00 as atmospheric model and the solar activity files provided by ESA/ESOC and integrated in NAPEOS. Table 4.13

Table 4.12: Aerodynamic coefficients magnitude variation and deflection for minimum and maximum values of T_{wall}.

Aerodynamic coefficients	$\mathbf{C}_F$ amplitude diff.	$\mathbf{C}_F$ deflection
SESAM model	0.11%	0.10 *deg*
EACM model	0.06%	0.05 *deg*
SUTTON model	0.03%	0.03 *deg*

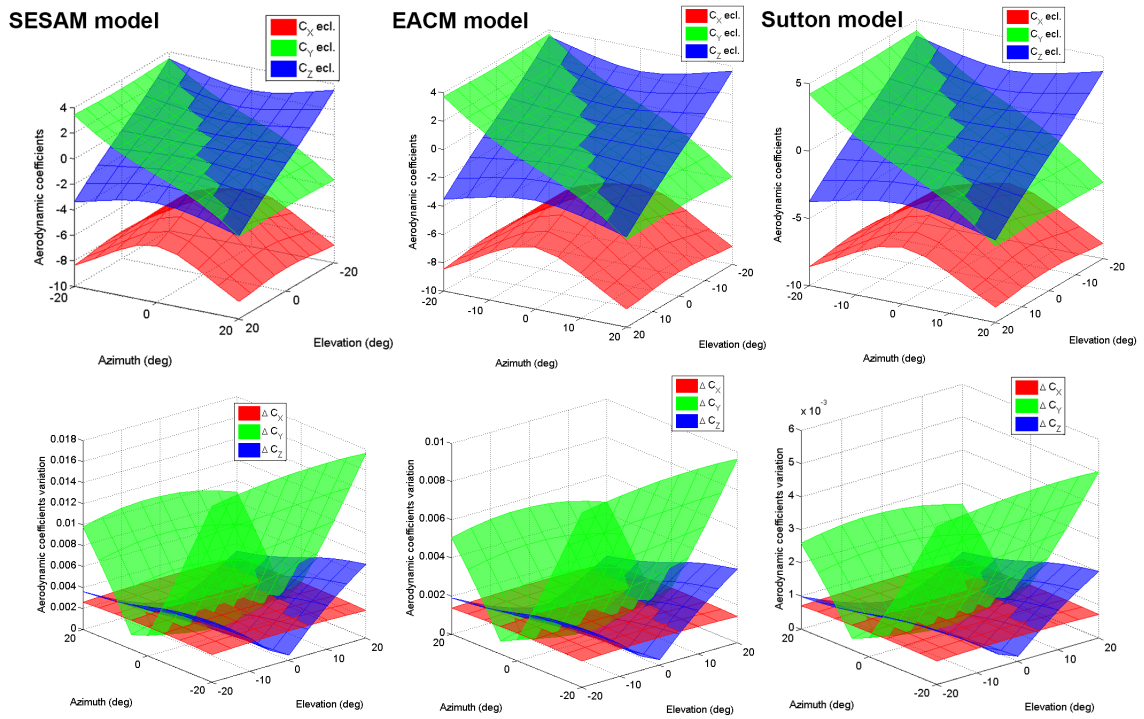

Figure 4.28: Effects of T_{wall} on the aerodynamic coefficients computed with different accommodation coefficients models. At the top, the coefficients for the condition of eclipse, and, at the bottom, the difference between coefficients in eclipse and non-eclipse. Non-eclipse coefficients are not shown, due to their small distance from the eclipse ones.

shows the range of variation computed for T_∞, m_g, and n_O. It was observed that the three atmospheric parameters considered are correlated and should be hence treated together. Figure 4.29 shows the correlation of the three atmospheric parameters. The Person correlation index ρ_{xy} has been computed to evaluate the correlation and the following values were identified:

- $\rho_{m_g - T_\infty} \approx 0.75$, which represents a strong correlation;
- $\rho_{n_O - T_\infty} \approx 0.48$, which represents a moderate correlation.

The three parameters were hence analyzed all together to observe their effect on the aerodynamic coefficients. For the reasons previously stated (the model is simplistic not considering

Table 4.13: Maximum and minimum values for the atmospheric temperature T_∞, mean molecular mass m_g and number density of atomic oxygen n_O computed for the simulation period and conditions.

Atmospheric parameter	min. value	max. value
T_∞	$543\ K$	$1279\ K$
m_g	$2.61 \times 10^{-26}\ kg/mol$	$4.23 \times 10^{-26}\ kg/mol$
n_O	$2.63 \times 10^{14}\ cm^{-3}$	$3.26 \times 10^{15}\ cm^{-3}$

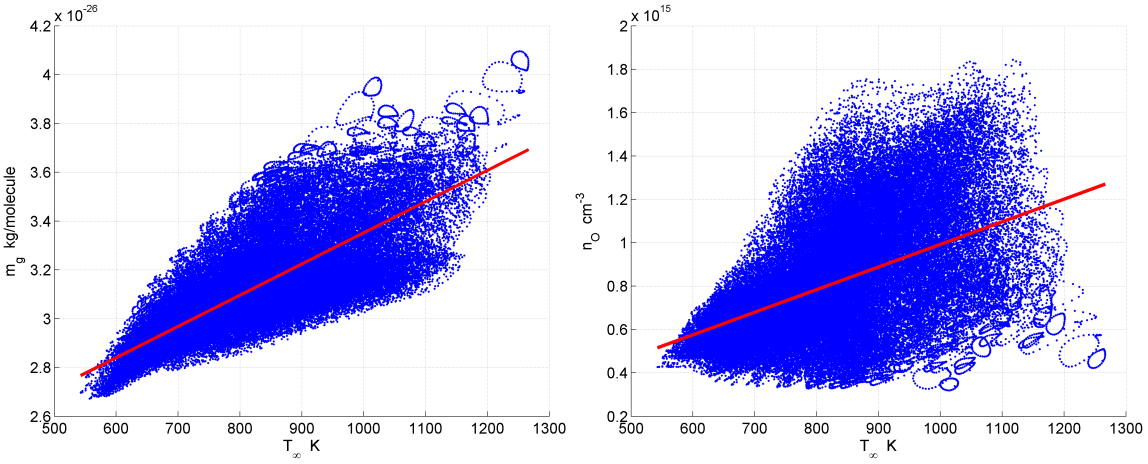

Figure 4.29: Correlation between the atmospheric temperature T_∞, mean molecular mass m_g and number density of atomic oxygen n_O.

Table 4.14: GOCE drag coefficients maximum and minimum values computed by with the EACM and SESAM models. T_∞, m_g, and n_O identify the conditions for which the drag coefficient is maximum and minimum.

	C_D		T_∞	m_g	n_O
EACM	$C_{D_{MIN}}$	3.448	543 K	2.89×10^{-26} kg/mol	1.13×10^{15} cm^{-3}
	$C_{D_{MAX}}$	3.853	1279 K	4.00×10^{-26} kg/mol	4.20×10^{14} cm^{-3}
	ΔC_D	10.9%			
SESAM	$C_{D_{MIN}}$	3.337	543 K	2.89×10^{-26} kg/mol	1.13×10^{15} cm^{-3}
	$C_{D_{MAX}}$	3.724	1279 K	4.00×10^{-26} kg/mol	4.20×10^{14} cm^{-3}
	ΔC_D	11.1%			

the effects of the atomic oxygen in the aerodynamics) the SUTTON model was excluded from the analysis. For each computed combination of T_∞, m_g, and n_O the drag coefficient C_D of GOCE was computed for both the EACM and SESAM models and the results are reported in Table 4.14. As observable for both the EACM and SESAM models the maximum variability of the GOCE drag coefficient is about 11%, which is not negligible. To test the effective dependance of the aerodynamic coefficients from the number density of atomic oxygen the following additional test was carried out. While maintaining T_∞ and m_g constant, n_O was set up to its maximum and minimum values and the accommodation (α_{acc}) and drag (C_D) coefficients were computed. It was observed that the maximum variation of both α_{acc} and C_D takes place for the average conditions of T_∞ and m_g and for the maximum and minimum values of n_O. Table 4.15 sums up the obtained results. It is possible to observe that a change in n_O from its minimum to its maximum value determine a change of more than 5% in both the accommodation coefficient and the drag coefficient of GOCE when using th EACM model. Its effect is instead extremely limited when using the SESAM model, where both the change in the accommodation coefficient and the drag coefficient are negligible. It is in fact observable that the accommodation coefficients computed with

Table 4.15: GOCE drag coefficients and accommodation coefficients maximum and minimum values computed by with the EACM and SESAM models. T_∞, m_g are set at their average values, while the maximum and minimum values of n_O are shown.

	C_D		α_{acc}		T_∞	m_g	n_O
EACM	$C_{D_{MIN}}$	3.596	$\alpha_{acc_{MIN}}$	0.94264	833 K	3.21×10^{-26} kg/mol	2.63×10^{14} cm^{-3}
	$C_{D_{MAX}}$	3.790	$\alpha_{acc_{MAX}}$	0.99512	833 K	3.21×10^{-26} kg/mol	3.26×10^{15} cm^{-3}
	ΔC_D	5.24%	$\Delta\alpha_{acc}$	5.42%			
SESAM	$C_{D_{MIN}}$	3.562	$\alpha_{acc_{MIN}}$	0.99947	833 K	3.21×10^{-26} kg/mol	2.63×10^{14} cm^{-3}
	$C_{D_{MAX}}$	3.566	$\alpha_{acc_{MAX}}$	0.99996	833 K	3.21×10^{-26} kg/mol	3.26×10^{15} cm^{-3}
	ΔC_D	0.11%	$\Delta\alpha_{acc}$	0.05%			

the SESAM model are extremely close to the unity, meaning that the lattice substrate is almost completely saturated with atomic oxygen. Therefore a change in the quantity of atomic oxygen does not lead to a significant change in the accommodation coefficient and on the resultant aerodynamic forces. In this way, by using the SESAM model, it possible to assume the average value of atomic oxygen and to dispose of the dependance from this parameter. This is an additional reason for which the SESAM model was adopted.

As for the radiation pressure, the geometrical parameters Az, El, ϕ_1, and ϕ_2, which define the direction of the incoming airflow and the orientation of the solar panels, determine a significant change in the aerodynamic forces and should hence be considered for the database.

In conclusion, the parameters from which the computed aerodynamic forces depend from are the geometrical parameters Az, El, ϕ_1, and ϕ_2. When considering the EACM model the atmospheric parameters T_∞, m_g, and n_O shall be considered, while when considering the SESAM model only the atmospheric parameters T_∞ and m_g are sufficient to the describe the satellite-atmosphere interactions.

Since the SESAM model is an evolution of the EACM model, and it has been largely tested and adjusted by means of many observations [73], since it also requires few parameters with respect to the EACM model, and since it is more suitable for modeling the aerodynamics of GOCE[2], the SESAM model was selected to build the database of aerodynamic forces on GOCE.

4.5.4 Test Cases results

In order to test and validate the procedure adopted to compute the force over a satellite due to the aerodynamics two main test cases were carried out: 1) test on flat plate and 2) test on cylinder. The force due to the aerodynamics was computed by using the previously described method implemented in the ARPA software (by means of the outer surfaces discretization) and the obtain results were compared to the analytic solutions.

The test case were carried out for a flat plate with a 1 m^2 square shape and a cylinder of 1 m diameter and 2 m length. The tests were carried out simulating the airflow from the directions $Az = [-90\,,\,+90]$ deg and $El = [-90\,,\,+90]$ deg, when the the flat plate and

[2]Marcin Pilinski, PhD, Research Scientist at ASTRA (Boulder): personal communication, February 2013

cylinder base are normal to the flow for $Az = 0\ deg$ and $El = 0\ deg$. Figure 4.30 shows

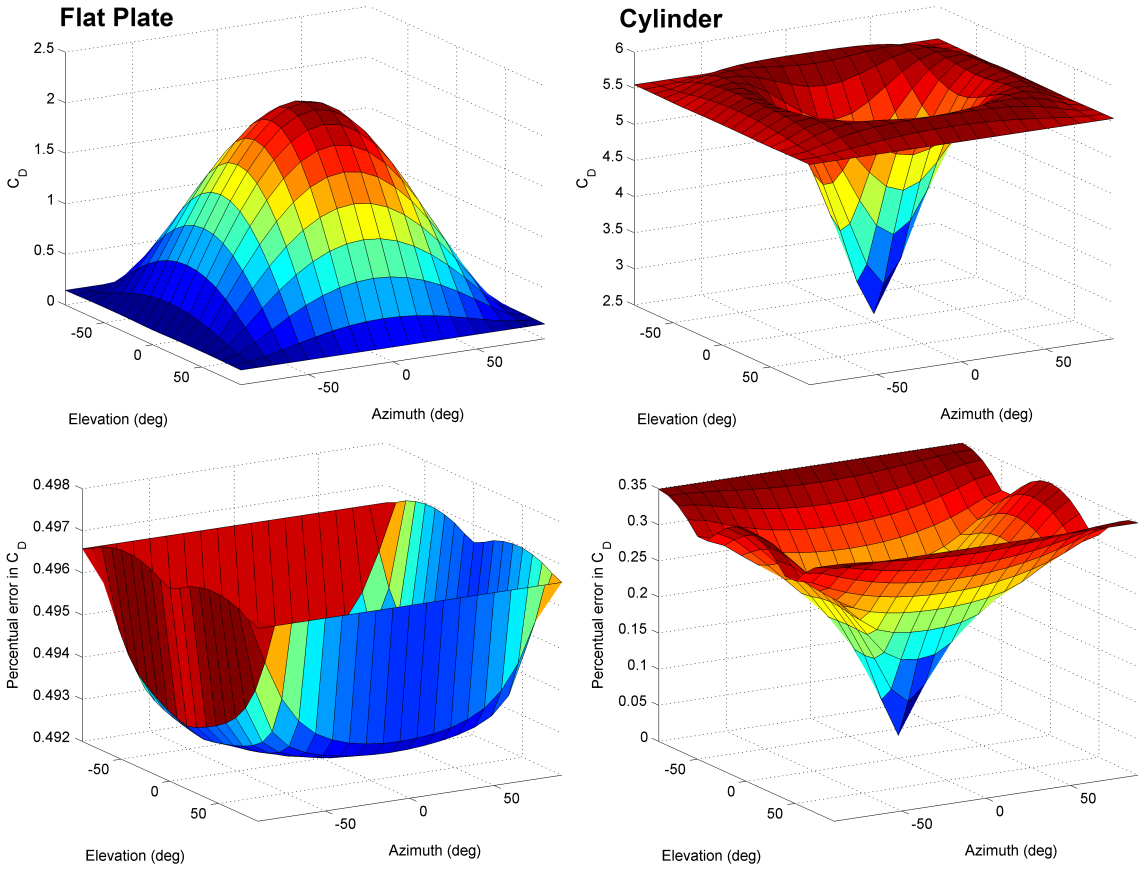

Figure 4.30: Test cases results for the aerodynamics. On the left-hand side, at the top, the drag coefficient computed for the flat plate and at the bottom the percentage difference on the ARPA implemented with respect to the analytical solution. On the right-hand side the drag coefficients and the comparison with the analytical solution for the cylinder.

the results obtained for the two test cases. On the left-hand side, at the top, the drag coefficient computed for the flat plate and at the bottom the percentage difference on the ARPA implemented with respect to the analytical solution. Similarly the results for the cylinder are reported on the right-hand side of the figure. As it is observable from both the test cases the implementation in ARPA is very accurate, limiting the level of mismodeling to about the 0.5% for the flat plate and to 0.35% for the cylinder. It was observed that for both the cases the error is directly related to the resolution of the superficial mesh adopted for modeling the outer surfaces of the analyzed shapes. In this cases each surface pixel element has an area of 1 cm^2. Again, as already observed for the radiation force cases, higher resolutions lead to higher accuracies, but a compromise between resolution (number of surface elements) and computational power should be maintained. Also in this case the dimensions of the surface elements have to adapted to the absolute dimensions of the simulated object and to its superficial features. Anyway, these two simple test cases

confirm the correctness and the accuracy of the strategy adopted in ARPA, confirming its applicability to more complicated shapes, such as GOCE and other satellites.

Chapter 5

Implementation of ARPA in POD software

In order to use the sophisticated databases and strategies developed with ARPA during the POD process, it has been necessary to opportunely modify and upgrade NAPEOS. The NAPEOS software system has been modified in two parts. The first modification is related to the Graphical User Interface (GUI). NAPEOS GUI, written in Tcl/Tk scripting language, has been integrated in order to set the path of the ARPA databases and being able to load them in the NAPEOS database. The second modification has been done to the model of forces of NAPEOS, where the loaded databases are used to compute the in-flight non-gravitational accelerations during the orbit propagation. In addition the scaling factors C_R and C_D, respectively for the radiation and aerodynamic accelerations, are estimated to scale the modeled accelerations. This chapter describes in detail the procedure implemented to compute the ARPA non-gravitational accelerations from the input databases. For all the non gravitational forces considered in the NAPEOS dynamics the following standard procedure is adopted:

1. at the beginning of the POD process the correct databases are loaded and the indexed force coefficients are kept in the memory until the end of the process;

2. based on in-flight conditions the correct coefficients are retrieved from the databases and used to compute the accelerations and the partial derivatives, fed to the propagator;

3. at the end of the POD process the memory is freed deallocating the loaded databases.

This procedure is repeated at each step of integration of the orbit. All the forces and force coefficients in the ARPA databases are computed in a body-fixed reference frame and should be rotate into an inertial (J2000) reference system for the NAPEOS propagator. Due to their relatively small dimensions (only some kilobytes for GOCE) and their indexed nature, the databases are quickly loaded and the correct coefficients are immediately retrieved.

5.1 Solar Radiation Pressure

The procedure implemented in NAPEOS to compute the solar radiation pressure accelerations with ARPA is shown in Figure 5.1. Starting from the ephemeris of the Sun and of the spacecraft in an Earth centered reference frame (ECEF or ECI) and knowing the attitude of the satellite, it is possible to compute the solar radiation pressure $P_{\odot}$ at the satellite location (function mainly of the S/C-Sun distance), the direction of the incoming solar radiation (Az, El) (see Figure A.1), and the orientation of the solar panels (ϕ_1, ϕ_2) (oriented to minimize the angle between their normal and the S/C-Sun direction, see Figure A.2). The direction of the solar radiation and the orientation of the solar panels are used to retrieve the correct SRP force coefficients $\mathbf{C}_F$ from the SRP database for this particular configuration (interpolating the coefficients, if necessary). The reference area A_{ref} used to compute the coefficients is also retrieved. With $P_{\odot}$ and A_{ref} and the satellite mass the SRP coefficients $\mathbf{C}_F$ are denormalized to compute the SRP acceleration $\mathbf{a}$ and the partial derivatives of this acceleration with respect to the state vector $d\mathbf{a}/d\mathbf{x}$ and with respect to the scaling parameter (C_R) $d\mathbf{a}/dp$. The SRP acceleration is then adjusted by the scaling parameter C_R computing the scaled acceleration $\mathbf{a}_{sc}$. The SRP acceleration $\mathbf{a}_{sc}$ and the partial derivatives are fed to the NAPEOS propagator.

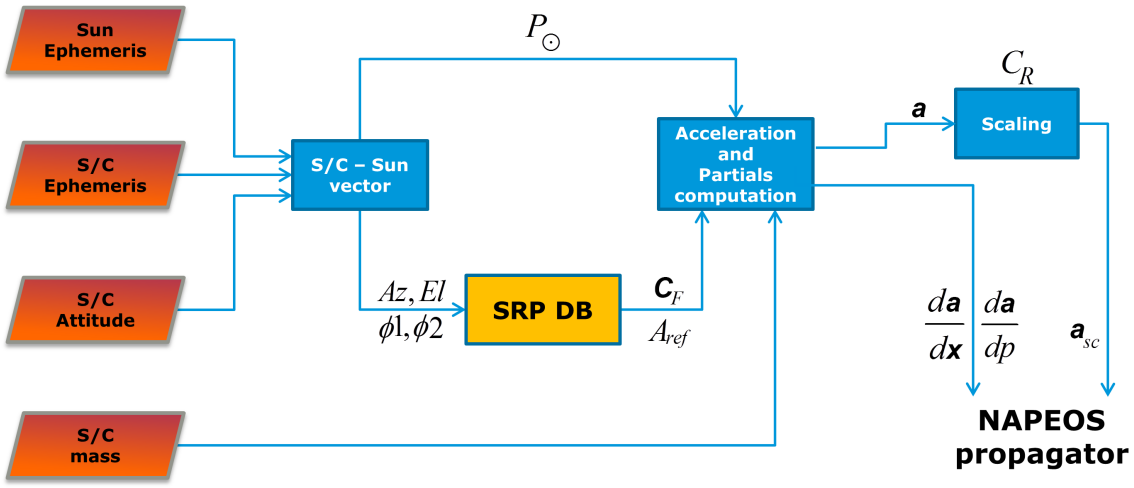

Figure 5.1: ARPA SRP model block diagram, as implemented in NAPEOS.

5.2 Earth Radiation Pressure: albedo and infrared

The procedure implemented to compute the Earth radiation pressure accelerations due to albedo and IR radiation with ARPA is shown in Figure 5.2. Again, starting from the ephemeris of the Sun (only for the albedo) and of the spacecraft in an Earth centered reference frame and knowing the attitude of the satellite, and the Earth radiation maps, it is possible to compute the Earth radiation pressure for the albedo $P_{\oplus_{alb}}$ and the IR $P_{\oplus_{IR}}$

at the satellite location, the direction of the incoming Earth radiation (Az, El), and the orientation of the solar panels. The direction of the Earth radiation and the orientation of the solar panels are used to retrieve the correct ERP force coefficients $\mathbf{C}_F$ from the ERP albedo and ERP IR databases. The reference area A_{ref} used to compute the coefficients is also retrieved. With $P_{\oplus}$ and A_{ref} and the satellite mass the ERP coefficients $\mathbf{C}_F$ are denormalized to compute the ERP acceleration and the partial derivatives of this acceleration with respect to the scaling parameter (C_R) $d\mathbf{a}/dp$ (the effects of the partial derivatives with respect to the state vector are negligible). The ERP acceleration is then adjusted by the scaling parameter C_R computing the scaled acceleration $\mathbf{a}_{sc}$. The ERP acceleration $\mathbf{a}_{sc}$ and the partial derivatives are fed to the NAPEOS propagator.

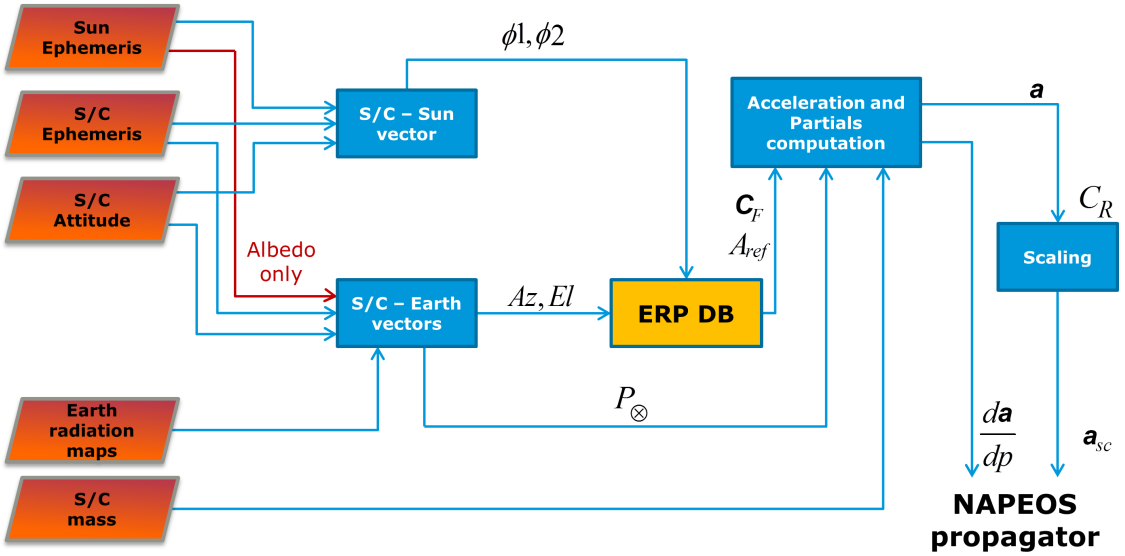

Figure 5.2: ARPA ERP model (albedo and IR) block diagram, as implemented in NAPEOS.

5.3 Thermal Re-Radiation Pressure

The procedure implemented to compute the satellite thermal re-radiation pressure accelerations requires less steps than the SRP and ERP computation, as shown in Figure 5.3. From the ephemeris of the Sun and of the spacecraft in an Earth centered reference frame and knowing the attitude of the satellite, it is possible to compute the orientation of the solar panels and fraction of visible Sun, which indicate the condition of eclipse. With the solar panels orientation the correct forces due to TRR are retrieved from the TRR database and, together with the Sun fraction and the satellite mass the acceleration due to TRR is directly fed to the NAPEOS propagator, without scaling. Since no scaling parameters are necessary to the TRR, no partial derivatives computation is required.

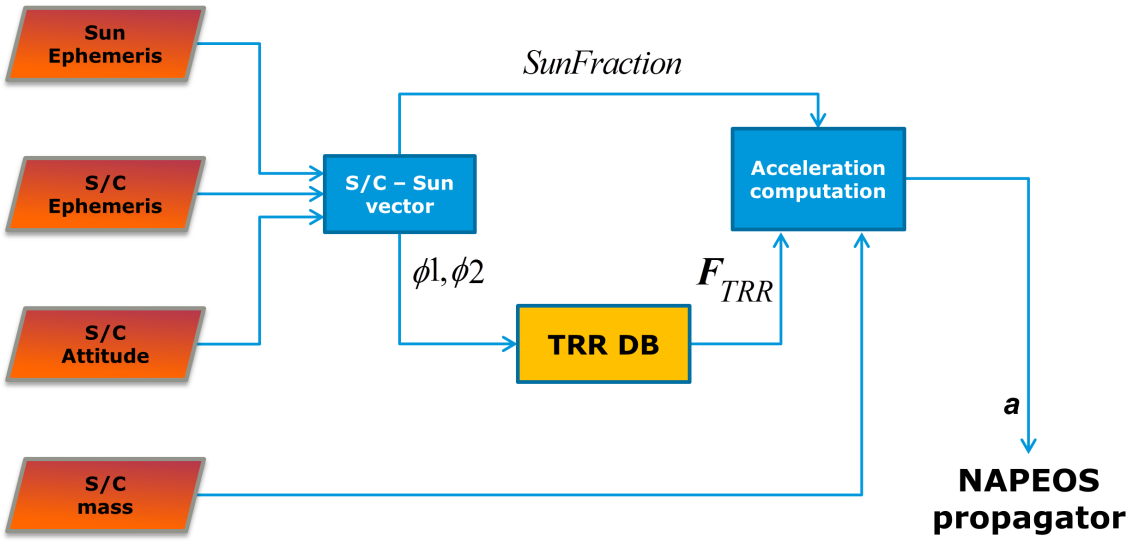

Figure 5.3: ARPA TRR model block diagram, as implemented in NAPEOS.

5.4 Aerodynamics

The procedure implemented in NAPEOS to compute the aerodynamic accelerations with ARPA is more complicated, as shown in Figure 5.4. Again, starting from the ephemeris of the Sun and of the spacecraft in an Earth centered reference and knowing the attitude of the satellite, it is possible to compute the orientation of the solar panels (ϕ_1, ϕ_2). From the spacecraft state vector, its attitude and an atmospheric model it possible to compute the direction of the incoming flow (Az, El), the local atmospheric properties that are the inputs to the ARPA database (atmospheric temperature T_∞ and mean molecular mass m_g). The satellite velocity relative to the atmosphere V_{rel} and the atmospheric density rho_∞ are also computed. From the aerodynamic database the correct coefficients $\mathbf{C}_F$ and the reference area A_{ref} are retrieved, and with these and the satellite mass the coefficients are then denormalized to compute the aerodynamic acceleration and the partial derivatives of this acceleration with respect to the state vector $d\mathbf{a}/d\mathbf{x}$ and with respect to the scaling parameter (C_D) $d\mathbf{a}/dp$. The acceleration is then adjusted by the scaling parameter C_D computing the scaled acceleration $\mathbf{a}_{sc}$. The aerodynamic acceleration $\mathbf{a}_{sc}$ and the partial derivatives are finally fed to the NAPEOS propagator.

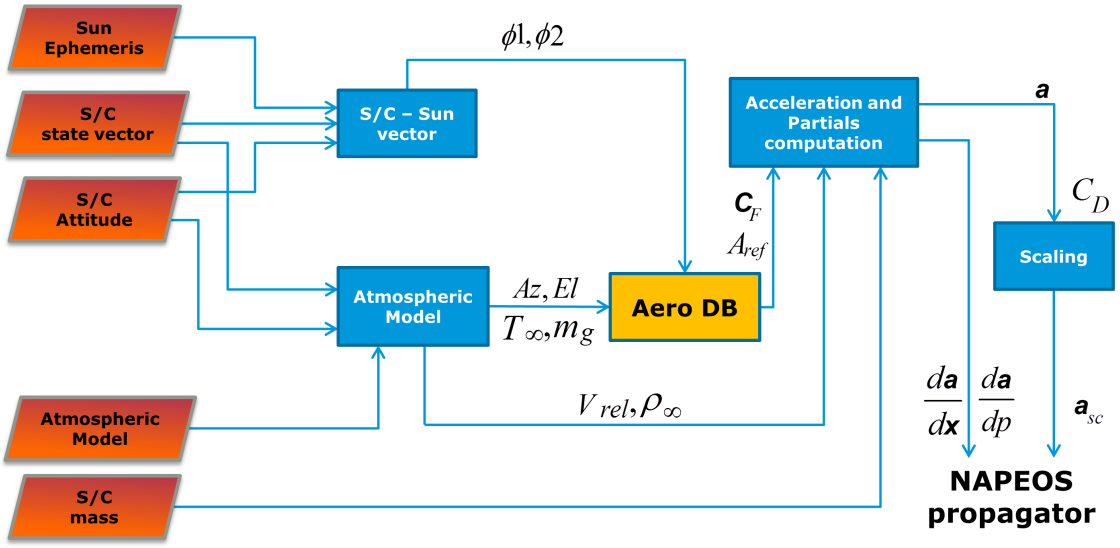

Figure 5.4: ARPA aerodynamic model block diagram, as implemented in NAPEOS.

Chapter 6

Test cases and results

6.1 Test Cases definition

In order to test, calibrate and validate the developed ARPA databases and the upgrades implemented in the ESA/ESOC NAPEOS software system, test cases were carried out for each non-gravitational perturbation component.

GOCE was flying in a drag-free mode during the science phase due to its sensible payload. It is, in fact, constantly compensating for along-track non-gravitational accelerations, mainly due to atmospheric drag, by means of a sophisticated close-loop electric propulsion control system. When the along-track pair of accelerometers experiences a common-mode acceleration, an input is sent to the Drag-Free and Attitude Control system (DFAC) which automatically compensate it by regulating the thrust. For the purpose of this thesis, this mode is extremely useful to test the implemented GOCE aerodynamics, since the thrust profile is a direct measurement of the along-track non-gravitational perturbations. Based on this fact two different sets of test cases were designed and carried out:

1. a *Radiative test case*, considering the drag-free mode and not considering the satellite aerodynamics, to test the radiation pressure perturbations on GOCE;

2. an *Aerodynamic test case*, including the GOCE thrust profile and considering the satellite aerodynamics, to test the aerodynamic perturbations on GOCE;

The tests were performed on 30 consecutive daily arcs, starting at the beginning of the GOCE science phase on 1st November 2009. Each modeled non-gravitational perturbation component has been set-up and tested singularly. In the POD process carried out with NAPEOS, empirical accelerations in the radial (r), along-track (a) and cross-track (c) directions can be included in the force model to compensate the model omission errors. The empirical accelerations consist of a combination of two periodic terms, each a function of the satellite argument of latitude u, and a constant one, as follows:

$$\begin{aligned} \Delta\mathbf{a}_r &= (a_{r0} + a_{rc}\cos u + a_{rs}\sin u)\,\hat{\mathbf{u}}_r \\ \Delta\mathbf{a}_a &= (a_{a0} + a_{ac}\cos u + a_{as}\sin u)\,\hat{\mathbf{u}}_a \\ \Delta\mathbf{a}_c &= (a_{c0} + a_{cc}\cos u + a_{cs}\sin u)\,\hat{\mathbf{u}}_c. \end{aligned} \tag{6.1}$$

Table 6.1: Model of forces adopted for the GOCE test cases.

Dynamical models	Description	Adopted model
Static gravity field	EIGEN-6C 200x200	[31]
Solid Earth tides	IERS-TN32 71 constituents, 3x3	[62]
Ocean tides	FES2004 106 constituents, 50x50	[59]
Third body perturbation	Lunar gravity	
	Solar gravity	
	Planetary gravity	
	Indirect oblateness perturbation	
Relativistic correction	Correction for General Relativity	[62]
Aerodynamics	Drag force	[16] and ARPA
Thrust	Thrust profile	from telemetry
Radiation Pressure	Solar Radiation Pressure	[62] and ARPA
	Albedo radiation pressure	[4] and ARPA
	Infrared radiation pressure	[4] and ARPA
	Thermal re-radiation pressure	ARPA
Empirical accelerations	CPR along- and cross-track	[88]

The nine parameters appearing in these equations (the constant terms a_{r0}, a_{a0}, a_{c0}, the cosine terms a_{rc}, a_{ac}, a_{cc}, and the sine terms a_{rs}, a_{as}, a_{cs}) are called CPR's because the period of these accelerations is one cycle per revolution. For the following test cases the along-track and cross-track parameters are estimated over hourly intervals, which establishes a densely-parameterized, fully-dynamic POD approach. Table 6.1 shows the force models adopted for the test cases. The non-gravitational force components will be in detail discussed for each specific test case.

6.2 NAPEOS POD sequence

GOCE POD was performed using as the main input data the GOCE GPS phase observables (RINEX files in 2.20 format, downloaded with EOLI-SA — Earth Observation Link - Stand Alone [32]), International GNSS Service (IGS [25]) final GPS orbits and clock solutions, and the official reduced-dynamics Precise Science Orbits (PSO [13, 99]).

Figure 6.1 shows the sequence of NAPEOS programs set up for the GOCE POD and adopted for the test cases. The sequence starts with the IGS 30s clock files (GPS clocks) that are converted to NAPEOS transmitter clock bias files (.tcb) for the 24 hours of the analyzed day (*ClockUpd/GOCE*). The satellite positions from the official reduced-dynamics PSO's are then converted to NTDF (NAPEOS Tracking Data Format) (*Tracksim/ORBIT-FIT*) that are then used to generate the best-fitting orbit for the analyzed day (*Bahn/ORBIT-FIT*). With this step the state vector and all the necessary parameters (the radiation pressure coefficient (C_R), the aerodynamic coefficient (C_D) and the Cycle Per Revolution (CPR) in along-track and cross-track directions, for the constant, sine and cosine terms)

are estimated and an a-priori orbit with the set up force model is generated. The IGS orbit file of the analyzed day is then merged with the first epoch of the IGS file of the next day (*CmdLine/COPY-IGS*) because the IGS time interval ranges from 00:00:00 to 23:45:00, and it is necessary to include the first epoch of the next day to be able to use the observations for the whole day, without loosing 15 min of data per day. The generated IGS sp3 orbit is then merged with the computed a-priori orbit to obtain a combined sp3 file with a 60 s sampling (*OrbUpd/ORBIT-FIT*). The rinex files available for the processed day are collected in an RTDC file (RINEX Tracking Data Catalogue) (*BuildCat/GOCE*), which are then pre-processed to initialize the receiver clocks (*GnssObs/GOCE-RAW*). A raw orbit is then computed at meter level using only GPS undifferenced pseudorange as observation, and estimating the GOCE clocks (*Bahn/GOCE-RAW*). In this step the pre-computed satellite state vector, C_R, C_D and CPR's are used to initialize the estimation process. The resulting raw orbit is then merged with the IGS sp3 orbits (*OrbUpd/GOCE-RAW*). The available observations are then pre-processed using as input the RTDC catalogue and the combined IGS and raw a-priori orbits (*GnssObs/GOCE*). At this time the effective orbit estimation is performed at millimeter level using both the GPS undifferenced carrier phase and pseudorange observations, taking as input the a-priori raw orbit and the initialized parameters and clocks (*Bahn/GOCE*). The temporary data no more necessary are then removed (*CmdLine/REMOVE-IGS*).

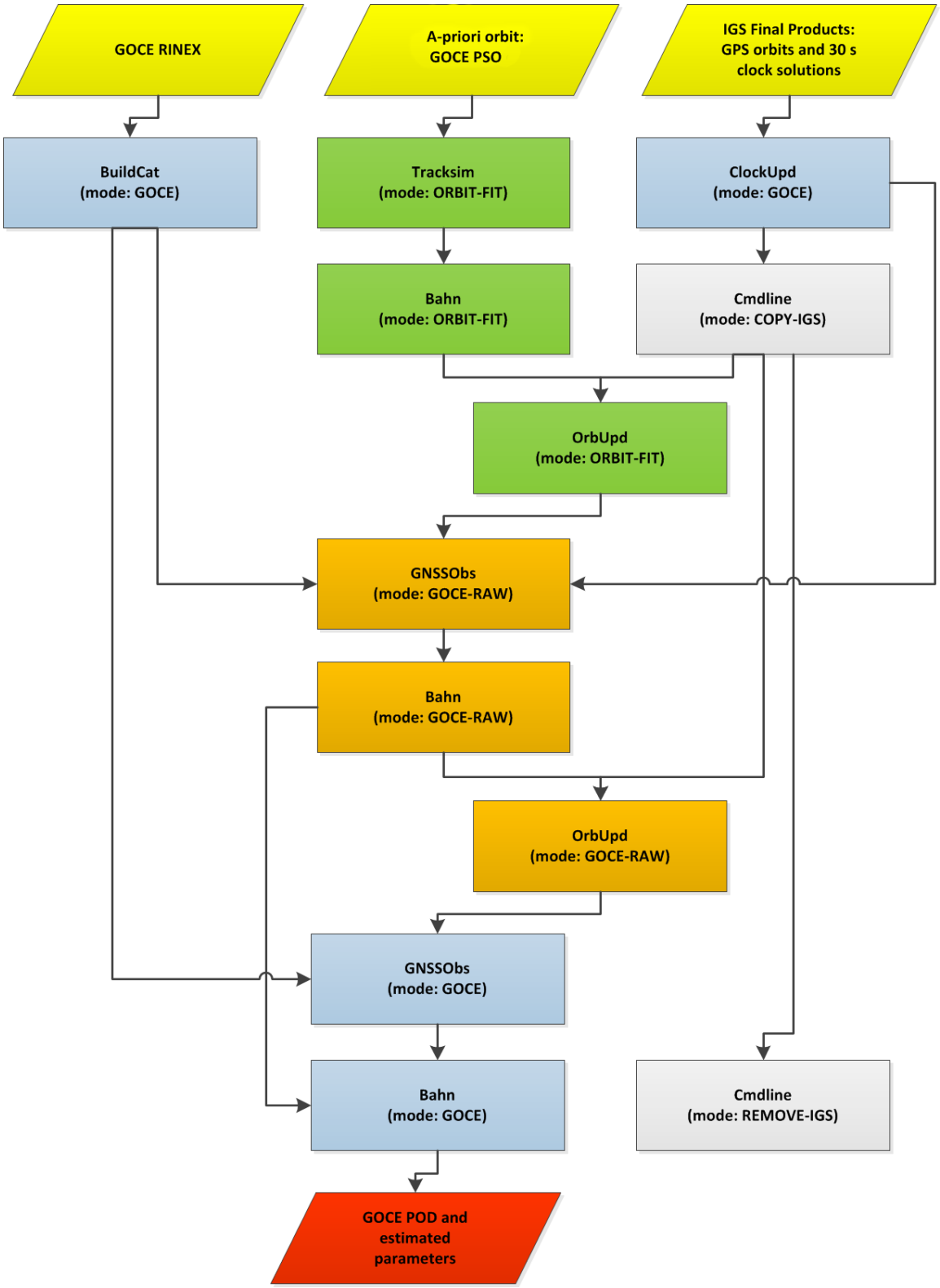

Figure 6.1: General sequence of NAPEOS programs used for GOCE POD process.

Table 6.2: Non-gravitational force models adopted for the GOCE solar radiation pressure calibration. NAPEOS and ARPA SRP coefficients are estimated.

Force source	Description	Parameter	Model
SRP	Solar rad. press.	daily C_R estimated	NAPEOS & ARPA
ERP	Albedo rad. press.	fixed $C_{R_{Alb}}$	NAPEOS
	Infrared rad. press.	fixed $C_{R_{IR}}$	NAPEOS
TRR	Thermal re-rad. press.	not considered	—
Emp. acc.	CPR's	not considered	—

6.3 Radiative test case

This set of test cases has been adopted to test the databases and implemented routines for what concerns the perturbations on GOCE due to Sun, Earth (albedo and IR) and spacecraft thermal radiation. For all these tests the drag-free mode has been considered. In this way it was not necessary to take into account in the dynamical model the forces deriving from the satellite aerodynamics and thrust, since they are reciprocally counteracting. All the tests were performed by comparing the new models developed with ARPA and the standard solution adopted by NAPEOS. For each modeled non-gravitational perturbation only the tested model is switched, while the rest of the setup is maintained unaltered. In the same way the number of observations rejected by the data pre-processing (*GnssObs*) and the orbit estimation (*Bahn*) is maintained low (below 1%) in order to obtain comparable solutions.

6.3.1 Solar Radiation Pressure

A first test was performed in order to calibrate the SRP models, determining the solar radiation pressure scaling factors C_R for both the NAPEOS and ARPA models. Since it is extremely difficult to achieve the perfect modeling of this perturbation (due for example of uncertainties and mismodeling of the satellite optical properties, geometry and attitude) a scaling factor C_R is estimated daily in order to adjust the models.

This first test was carried out over a period of 30 days, while estimating daily orbital arcs by means of a fully dynamic approach. As shown in Table 6.2 the SRP coefficients are estimated considering a constant Earth radiation pressure ($C_{R_{Alb}} = 1$ and $C_{R_{IR}} = 1$) and no TRR and empirical accelerations. The empirical accelerations tend to absorb all the mismodeling and would interfere with the C_R's estimation, which is the objective of this test, and are hence not considered.

Figure 6.2 shows the estimated solar radiation pressure coefficients, for the NAPEOS and ARPA SRP models. As it is observable, the coefficients estimated with ARPA are slightly higher then the ones obtained with the NAPEOS model. Over the 30 daily arcs period the average of the solar radiation pressure scaling factors is $C_R = 0.976$ for the NAPEOS model and $C_R = 1.141$ for the ARPA model. This means that during the estimation process, in order to best fit the available observations, it is necessary to slightly decrease the effects

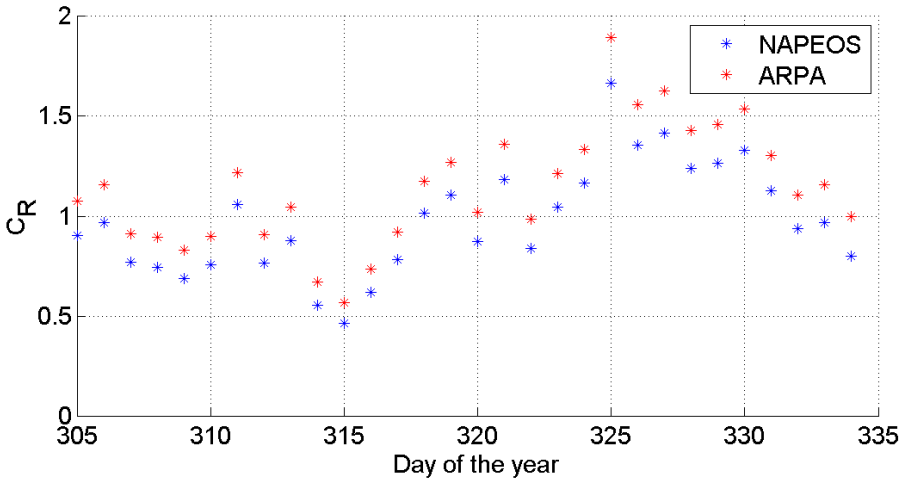

Figure 6.2: Estimated SRP coefficients, obtained by means of a fully dynamic approach.

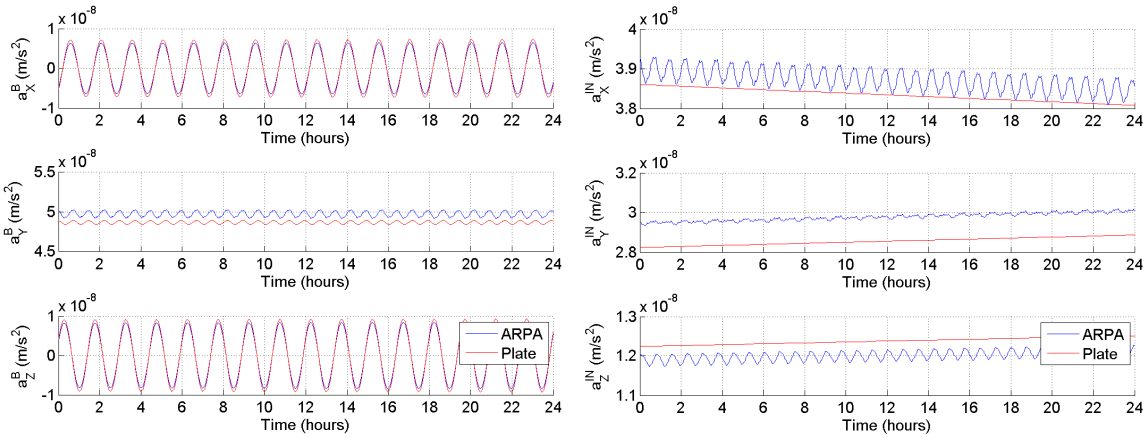

Figure 6.3: Solar radiation pressure accelerations obtained with the NAPEOS model (flat plate) and the ARPA model, in the body-fixed (left-hand side) and inertial (right-hand side) reference frames.

of the SRP for the NAPEOS model (a decrement of 2.4%) and slightly increase the effects of the SRP for the ARPA model (an increment of 14.1%). The values of $C_R = 0.976$ and $C_R = 1.141$ were set up in NAPEOS as fixed parameters for all the further tests. With both the models the post-fit RMS is about 250 cm and the observations rejection is below 0.4% (about 100 observations out of 28000).

Figure 6.3 shows the accelerations computed for the SRP after scaling each model with the estimated C_R's. As can be observed, the accelerations in the body-fixed reference frame are quite similar for the along-track ($+X$) and radial ($-Z$) directions but differ in the cross-track ($-Y$) component. The solar radiation pressure is mainly directed in the cross-track direction due to the sunsynchronous dawn-dusk orbit of GOCE. With the ARPA model the SRP acceleration along this direction is slightly higher (2.4%) than with the NAPEOS

Table 6.3: Non-gravitational force models adopted for the GOCE solar radiation pressure test cases. NAPEOS and ARPA SRP models are compared.

Force source	Description	Parameter	Model
SRP	Solar rad. press.	fixed C_R	NAPEOS & ARPA
ERP	Albedo rad. press.	fixed $C_{R_{Alb}}$	NAPEOS
	Infrared rad. press.	fixed $C_{R_{IR}}$	NAPEOS
TRR	Thermal re-rad. press.	not considered	—
Emp. acc.	CPR constant along-track	estimated hourly	NAPEOS
	CPR constant cross-track	estimated hourly	NAPEOS
	CPR cosine along-track	estimated hourly	NAPEOS
	CPR cosine cross-track	estimated hourly	NAPEOS
	CPR sine along-track	estimated hourly	NAPEOS
	CPR sine cross-track	estimated hourly	NAPEOS

model.

For the second test the previously estimated values of $C_R = 0.976$ and $C_R = 1.141$ were applied. For this test the non-gravitational dynamical model described in Table 6.3 was set up. In this case the solar radiation pressure was set fixed and the empirical accelerations in the along- and cross-track directions were estimated to absorb the mismodeling and to obtain an orbit with a low post-fit RMS, at a millimeter level. This test was carried out to effectively test the new ARPA SRP model, comparing it to the standard NAPEOS solution.

The post-fit RMS is shown in Figure 6.4. As can be observed, the resulting post-fit RMS obtained with both the SRP models is almost the same, about 6.212 mm. The difference between these two models is not appreciable from the post-fit RMS since the major part of the mismodeling is absorbed by the estimated CPR's. The difference is hence observable in Figure 6.5, where the CPR's in the along- and cross-track are reported. As shown, in the along-track direction the ARPA SRP model is capable of slightly reducing the empirical accelerations, while in the cross-direction the reduction is significant. The decrement in the cross-track direction is about the 20%, meaning that the ARPA SRP model is better modeling the non-gravitational perturbation. The empirical accelerations, which, as said, absorb the majority of the mismodeling, are significantly reduced and ARPA is hence accurately modeling the SRP perturbation. Moreover, due to the sunsynchronous orbit of GOCE, the radiation from the Sun is all the time striking the same side of the satellite, which low changes in its direction in the body-fixed reference frame. In this particular condition the NAPEOS standard solution for the SRP, the flat plate solution, is already accurately modeling the perturbation. Hence, a 20% reduction of the CPR's in the cross-track direction is indeed significant and proves the goodness of the ARPA implemented modeling and technique for the SRP perturbation.

Figure 6.6 shows the results of the comparison between the reduced-dynamics official PSO solutions and the orbits obtained with the NAPEOS and ARPA SRP models. Both the PSO-NAPEOS and PSO-ARPA orbit distances are at the centimeter level, with an

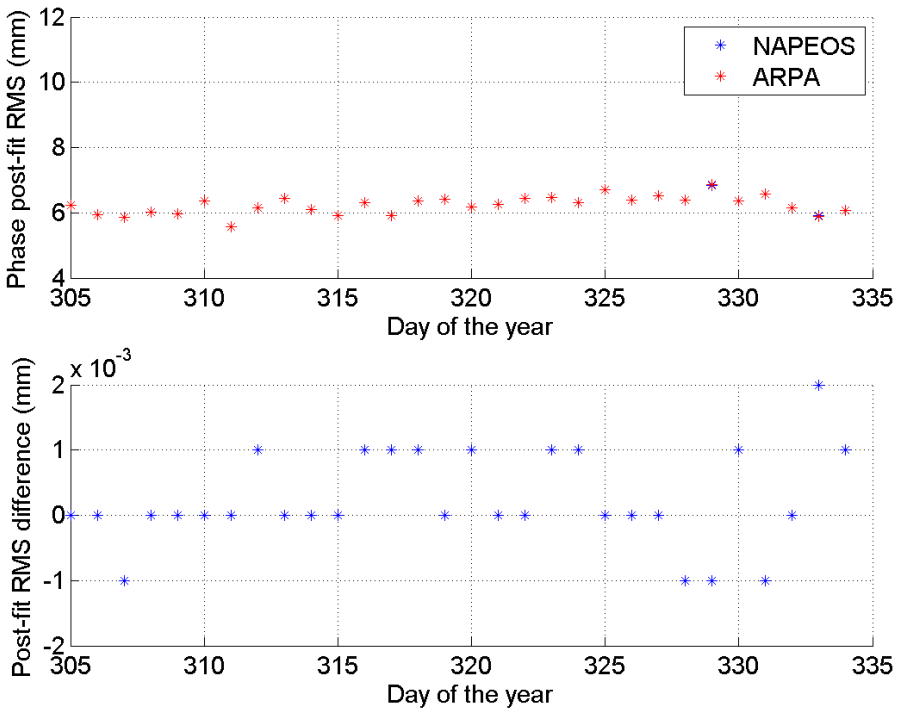

Figure 6.4: Post-fit RMS for the NAPEOS and ARPA SRP test cases.

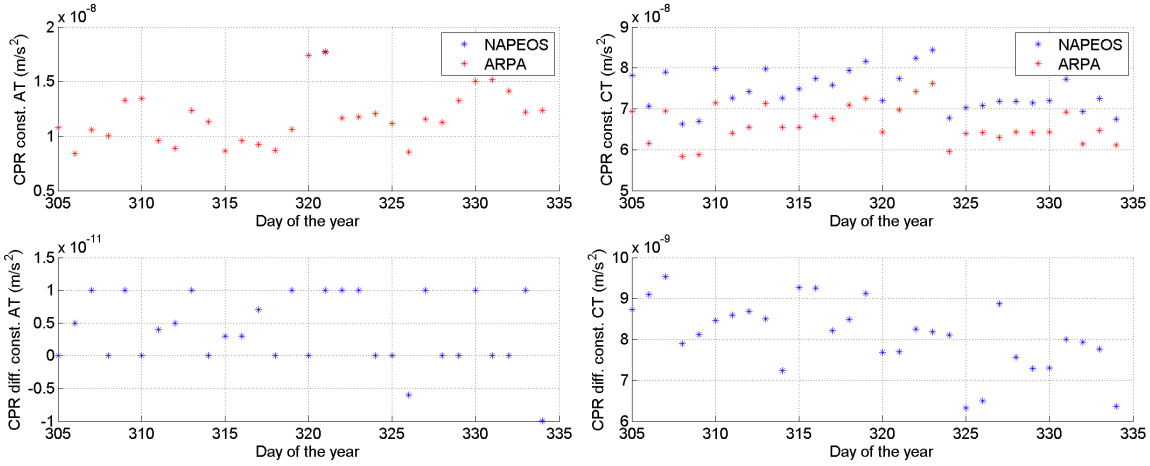

Figure 6.5: Along- and cross-track constant CPR's and CPR's difference for the NAPEOS and ARPA SRP test cases. A positive difference means a reduction of the values with the ARPA model.

average of about 3.9 *cm*. Both the computed orbits show good consistency with the PSO solutions.

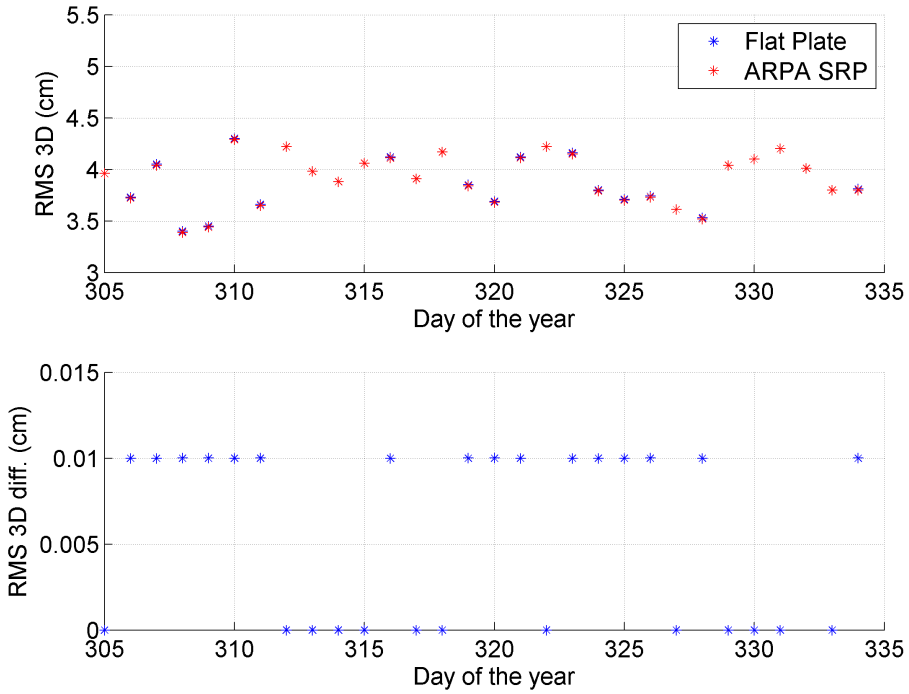

Figure 6.6: Comparison between the reduced-dynamics official PSO solutions and the orbits obtained with the NAPEOS and ARPA SRP models. A positive difference means a reduction of the values with the ARPA model.

Table 6.4:]
Non-gravitational force models adopted for the GOCE Earth albedo radiation pressure test cases. NAPEOS and ARPA ERP-Alb models are compared.

Force source	Description	Parameter	Model
SRP	Solar rad. press.	fixed C_R	ARPA
ERP	Albedo rad. press.	fixed $C_{R_{Alb}}$	NAPEOS & ARPA
	Infrared rad. press.	fixed $C_{R_{IR}}$	NAPEOS
TRR	Thermal re-rad. press.	not considered	—
Emp. acc.	CPR constant along-track	estimated hourly	NAPEOS
	CPR constant cross-track	estimated hourly	NAPEOS
	CPR cosine along-track	estimated hourly	NAPEOS
	CPR cosine cross-track	estimated hourly	NAPEOS
	CPR sine along-track	estimated hourly	NAPEOS
	CPR sine cross-track	estimated hourly	NAPEOS

6.3.2 Earth Radiation Pressure: Albedo

For this test a comparison between the NAPEOS standard model for the albedo ERP (flat plate) was compared with the ARPA albedo ERP model. For this test the non-gravitational dynamical model described in Table 6.4 was set up. In this case the solar radiation pressure was set fixed ($C_R = 1.141$) with the ARPA model, and the Earth radiation pressure for the infrared component was computed with the NAPEOS model. The albedo ERP was computed once with the NAPEOS model and once with the ARPA model and the solutions were compared. Also in this case no satellite thermal re-radiation was considered and the empirical accelerations in the along- and cross-track directions were again estimated to absorb the mismodeling and to obtain an orbit with post-fit RMS at a millimeter level.

The albedo Earth radiation pressure was computed with the three available Earth radiation maps:

1. the latitude-dependent Earth radiation maps ([4, 88]);
2. the ANGARA Earth radiation maps ([22]);
3. the CERES Earth radiation maps ([81]).

All the three maps are suitable also for the infrared ERP modeling and will be used again in the next section. The first of the three maps assumes the albedo and infrared properties of the Earth as a function only of the latitude, neglecting their local and longitudinal variations. The other two maps model the Earth surface as a discrete set of cells of 2.5×2.5 *deg*, and for each cell they provide monthly albedo and emissivity coefficients. During the POD process, while propagating the orbit of the satellite, at each step of integration the total radiation reaching the spacecraft is computed. For the latitude-dependent map

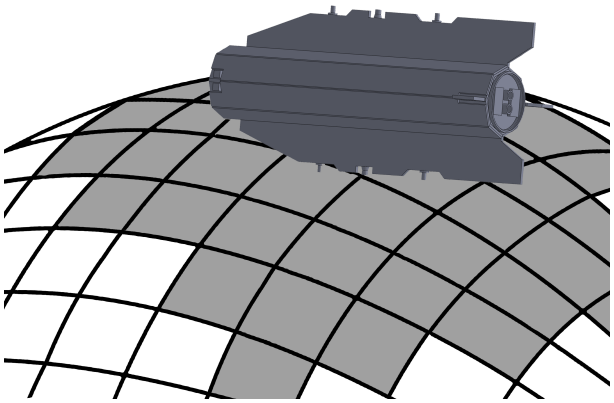

Figure 6.7: Earth surface discretization for albedo and infrared Earth radiation. Surface cells visible from the spacecraft are highlighted.

the radiation is computed by numerically integrating the radiation function over the Earth surface visible from the satellite. For the other two maps the radiation from each cell visible from the spacecraft and reaching the satellite is summed up, as shown in Figure 6.7.

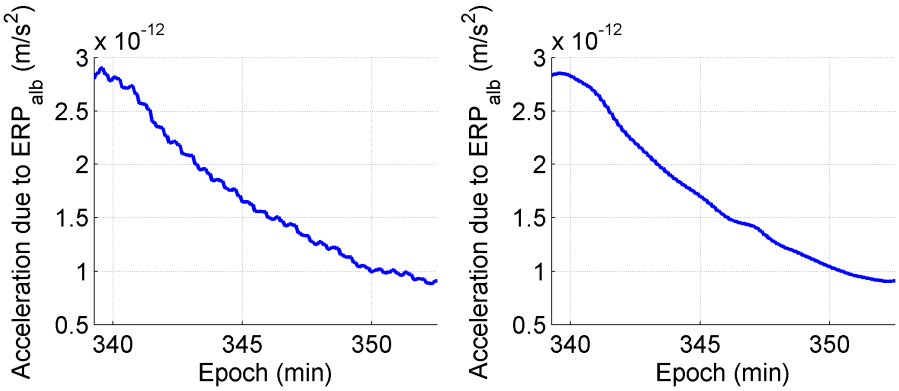

Figure 6.8: Effects of Earth surface discretization for albedo radiation on the acceleration on the spacecraft. On the left-hand side the acceleration computed with the standard maps resolution ($2.5 \times 2.5\ deg$) and on the right-hand side the same result computed with four times the previous resolution ($1.25 \times 1.25\ deg$).

Before proceeding further a clarification is necessary. GOCE was flying at an extremely low altitude ($250\ km$) and when computing the accelerations due to the Earth radiation pressure it was observed that it is significantly sensible to the resolution of the Earth cell-maps. As observable in Figure 6.8 on the left-hand side, the acceleration due to the albedo Earth radiation pressure is subjected to periodical oscillations and irregularities, due to the too low resolution of the map. The cells dimensions (about $280 \times 280\ km^2$ at the equator) are too big with respect to the satellite altitude and lead to oscillations in the acceleration when the spacecraft is flying from one cell to another. Increasing the resolution by four

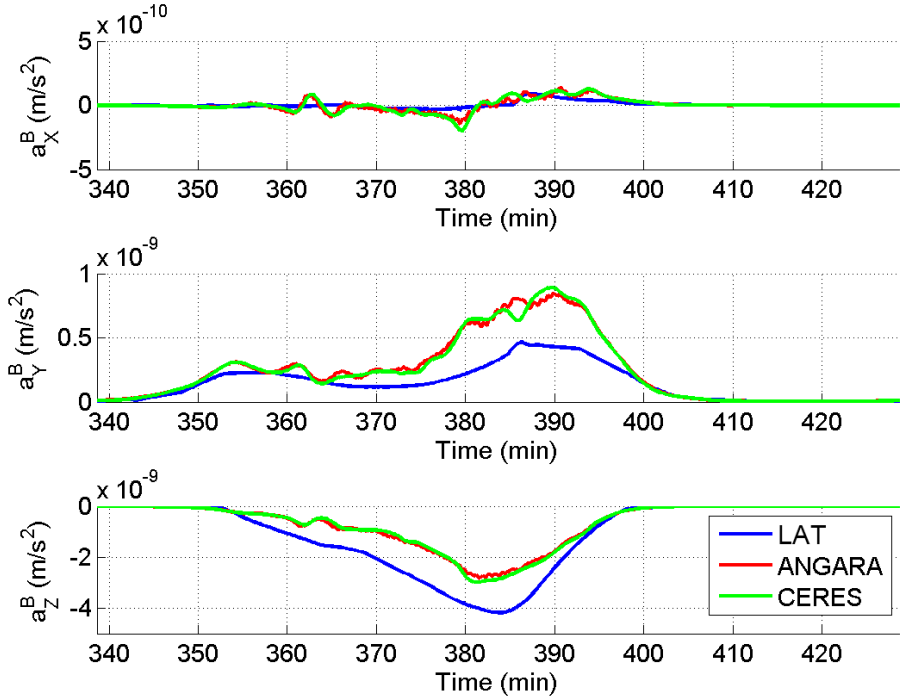

Figure 6.9: Albedo Earth radiation pressure accelerations of GOCE for one orbit, computed with the ARPA model with different Earth radiation models, in the body-fixed reference frame.

times leads to cells dimensions significantly lower (about 140 $\times$ 140 km^2 at the equator) which lead to accelerations that are smoother, as shown in Figure 6.8 on the right-hand side, which more realistically model the Earth radiation environment. Improvement in the post-fit RMS was observed for both the albedo and infrared ERP components when using the higher resolutions for the ANGARA and CERES maps.

Figure 6.9 shows the accelerations computed with the ARPA ERP albedo model using the three Earth radiation models. As observable the main component of the acceleration is in the radial direction ($-Z$). The perturbations computed with the latitude-dependent model yield a higher acceleration in the radial direction due to the higher value of radiation reaching the satellite this model computes.

The results obtained with the latitude-dependent Earth radiation maps are shown in Figure 6.10 for what concerns the post-fit RMS. In this case the ARPA ERP albedo model is slightly reducing the post-fit RMS.

The improvement introduced with the ARPA ERP albedo model with the latitude maps is more observable in Figure 6.11, where the CPR's in the along- (amplitude term[1]) and cross-track (constant term) are reported. As shown, in the along-track direction the ARPA ERP albedo model is capable of slightly reducing the empirical accelerations, while in the cross-direction the reduction is significant. The decrement in the cross-track direction is about the 12%, meaning that the ARPA ERP albedo model is improving the solution.

[1]Recalling Equation 6.1 term, $a_{ampl} = \sqrt{a_{ac}^2 + a_{ac}^2}$.

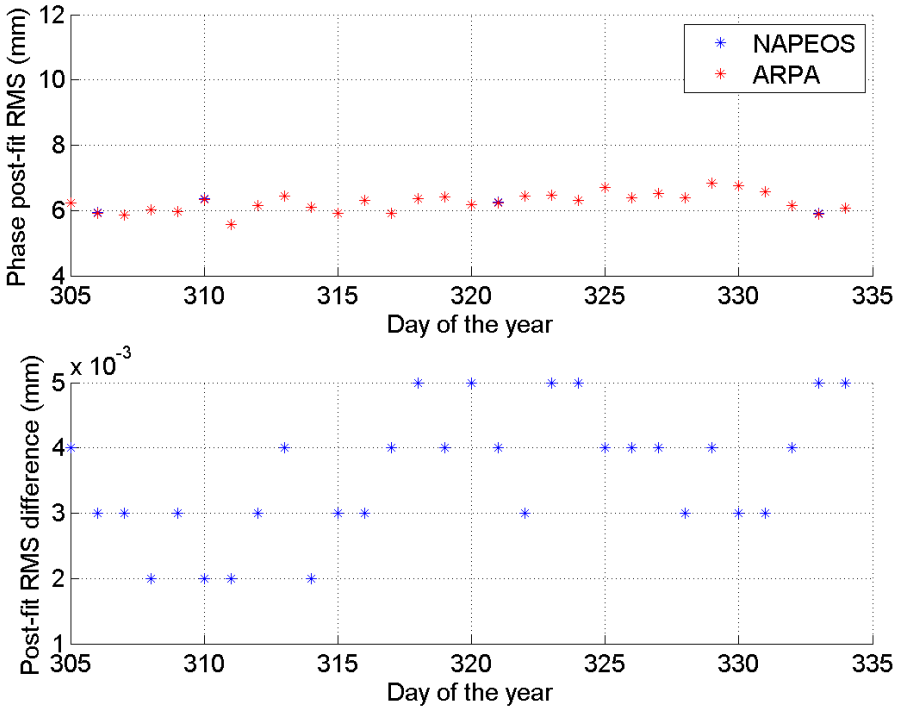

Figure 6.10: Post-fit RMS for the NAPEOS and ARPA ERP albedo test cases.

The empirical accelerations are hence significantly reduced and it can be concluded that ARPA is accurately modeling the ERP albedo perturbation, with respect to the standard NAPEOS solution. The 12% reduction of the CPR's in the cross-track direction is indeed significant and proves the goodness of the ARPA implemented modeling and technique for the ERP albedo perturbation.

Figure 6.12 shows the results of the comparison between the reduced-dynamics official PSO solutions and the orbits obtained with the NAPEOS and the ARPA ERP albedo models. Both the PSO-NAPEOS and PSO-ARPA orbit distances are at the centimeter level, with an average of about 3.9 *cm*. Both the computed orbits show good consistency with the PSO solutions. Due to the low level of the ERP albedo accelerations affecting the satellite dynamics and the absorption of the empirical accelerations, the difference between the ARPA and NAPEOS orbits is small. The distance of ARPA ERP albedo solutions from the PSO solutions is anyway slightly lower than the NAPEOS orbit distances for the 60% of the daily arcs.

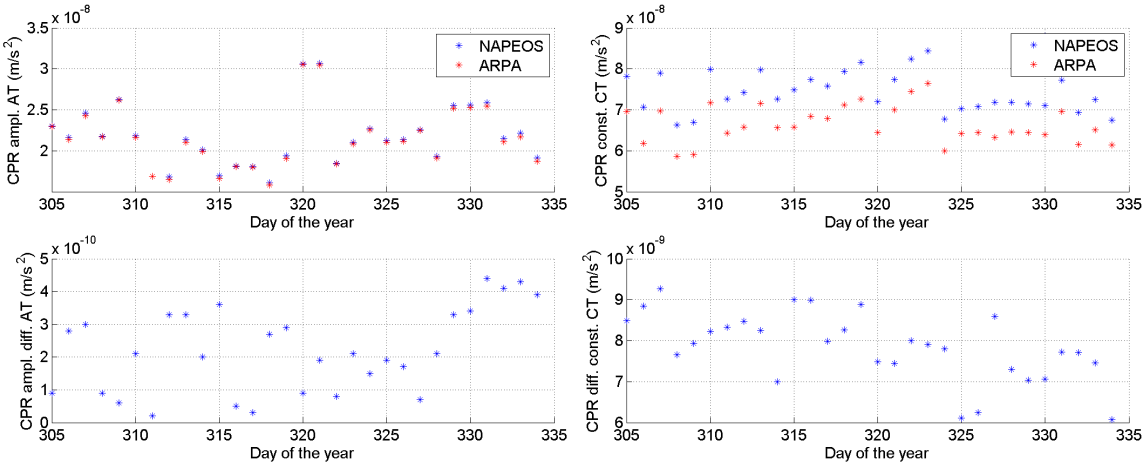

Figure 6.11: Along-track amplitude and cross-track constant CPR's and CPR's difference for the NAPEOS and ARPA ERP albedo test cases. A positive difference means a reduction of the values with the ARPA model.

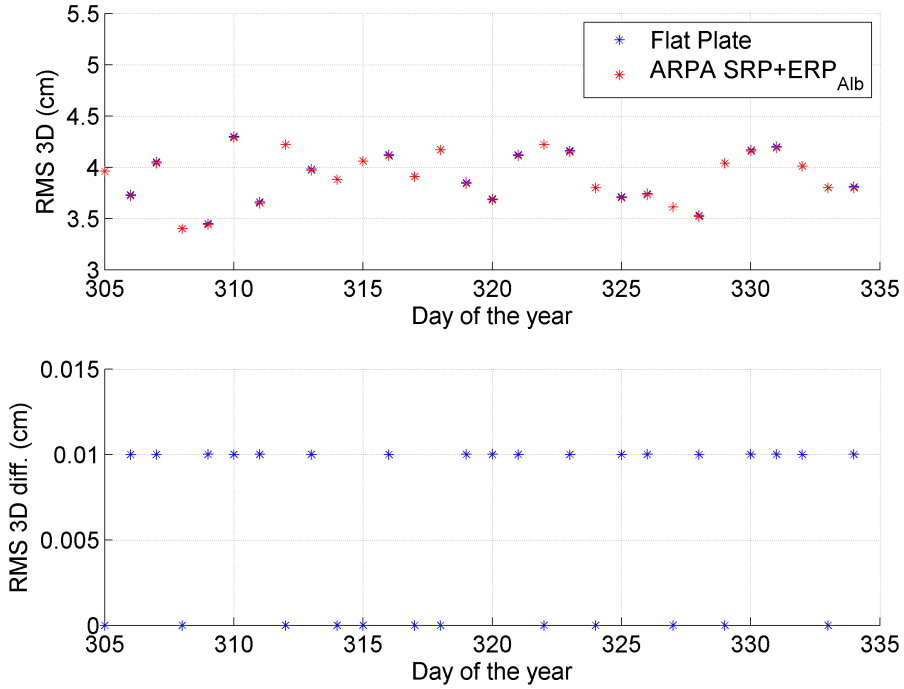

Figure 6.12: Comparison between the reduced-dynamics official PSO solutions and the orbits obtained with the NAPEOS and ARPA ERP albedo models. A positive difference means a reduction of the values with the ARPA model.

Table 6.5: Non-gravitational force models adopted for the GOCE Earth infrared radiation pressure test cases. NAPEOS and ARPA ERP-IR models are compared.

Force source	Description	Parameter	Model
SRP	Solar rad. press.	fixed C_R	ARPA
ERP	Albedo rad. press.	fixed $C_{R_{Alb}}$	NAPEOS
	Infrared rad. press.	fixed $C_{R_{IR}}$	NAPEOS & ARPA
TRR	Thermal re-rad. press.	not considered	—
Emp. acc.	CPR constant along-track	estimated hourly	NAPEOS
	CPR constant cross-track	estimated hourly	NAPEOS
	CPR cosine along-track	estimated hourly	NAPEOS
	CPR cosine cross-track	estimated hourly	NAPEOS
	CPR sine along-track	estimated hourly	NAPEOS
	CPR sine cross-track	estimated hourly	NAPEOS

6.3.3 Earth Radiation Pressure: Infrared

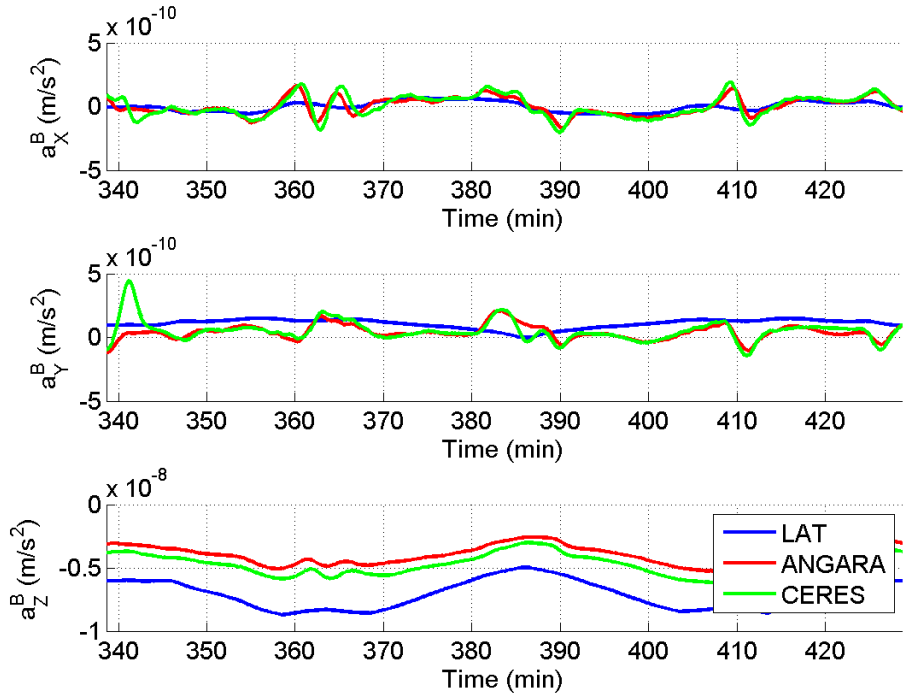

Figure 6.13: Infrared Earth radiation pressure accelerations of GOCE for one orbit, computed with the ARPA model with different Earth radiation models, in the body-fixed reference frame.

For this test a comparison between the NAPEOS standard model (flat plate) for the infrared ERP was compared with the ARPA model. For this test the non-gravitational dynamical model described in Table 6.5 was set up.

Figure 6.13 shows the accelerations computed with the ARPA ERP IR model using the

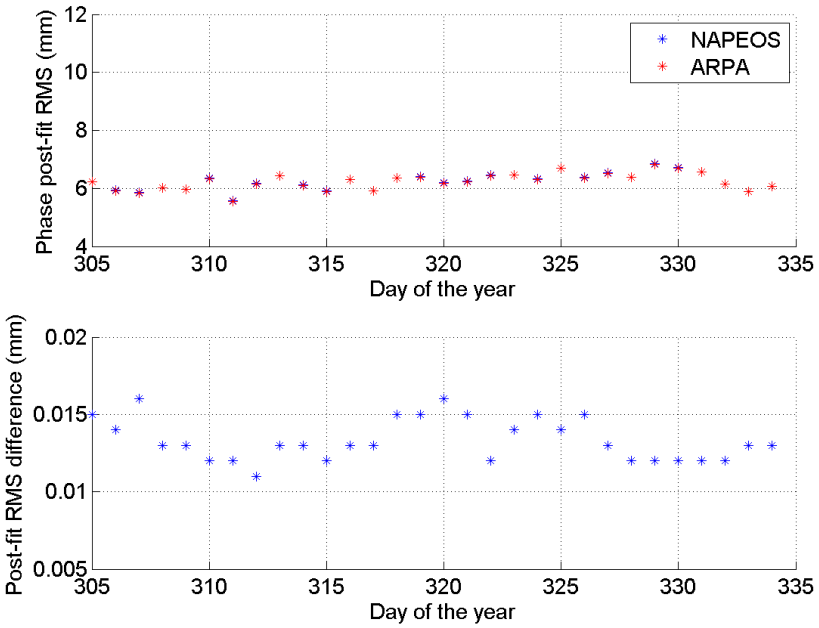

Figure 6.14: Post-fit RMS for the NAPEOS and ARPA ERP IR test cases.

three Earth radiation models, previously described. As observable, as for the albedo, the main component of the acceleration is in the radial direction ($-Z$ direction), while the along the other two directions the effects of the ERP are at least one order of magnitude lower. In the radial direction the acceleration is almost constant. As for the albedo, the accelerations computed with the latitude-dependent model result higher in the radial direction than the other two models due to the higher value of radiation reaching the satellite that this model computes.

The results obtained with the latitude-dependent Earth radiation maps are shown in Figure 6.14 for what concerns the post-fit RMS. Again the ARPA ERP IR model is slightly reducing the post-fit RMS.

The improvement introduced with the ARPA ERP IR model with the latitude maps is, once again, more observable in Figure 6.15, where the CPR's in the along- (amplitude term) and cross-track (constant term) are reported. As shown, in the along-track direction the ARPA ERP IR model is capable of averagely reducing the empirical accelerations, while in the cross-direction the reduction is significant, similarly to the ARPA ERP albedo model. The decrement is the cross-track direction is about the 13%, meaning that the ARPA ERP IR model is improving the solution. The empirical accelerations are hence significantly reduced and it can be concluded that ARPA is also accurately modeling the ERP IR perturbation, better than the standard NAPEOS solution. The 13% reduction of the CPR's in the cross-track direction is indeed significant and proves the goodness of the ARPA implemented modeling and technique for the ERP IR perturbation.

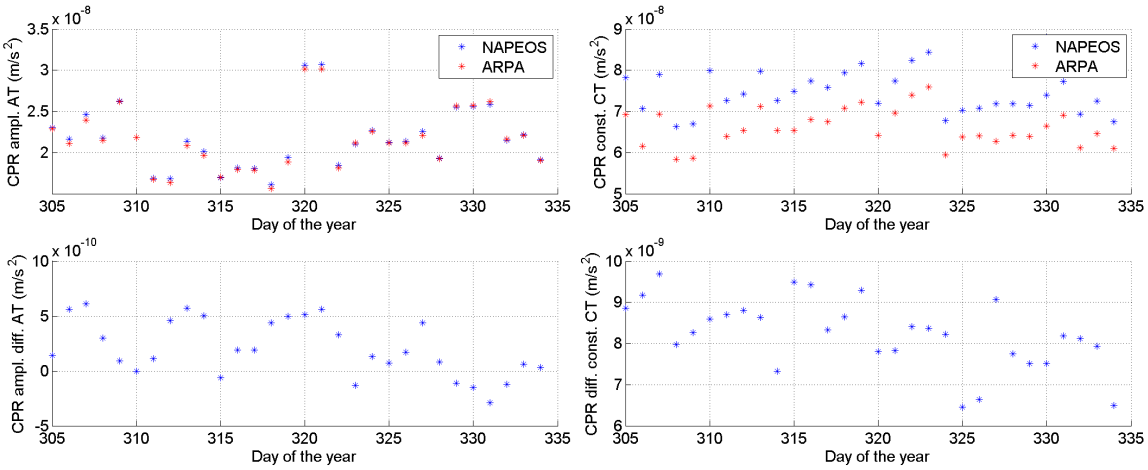

Figure 6.15: Along-track amplitude and cross-track constant CPR's and CPR's difference for the NAPEOS and ARPA ERP IR test cases. A positive difference means a reduction of the values with the ARPA model.

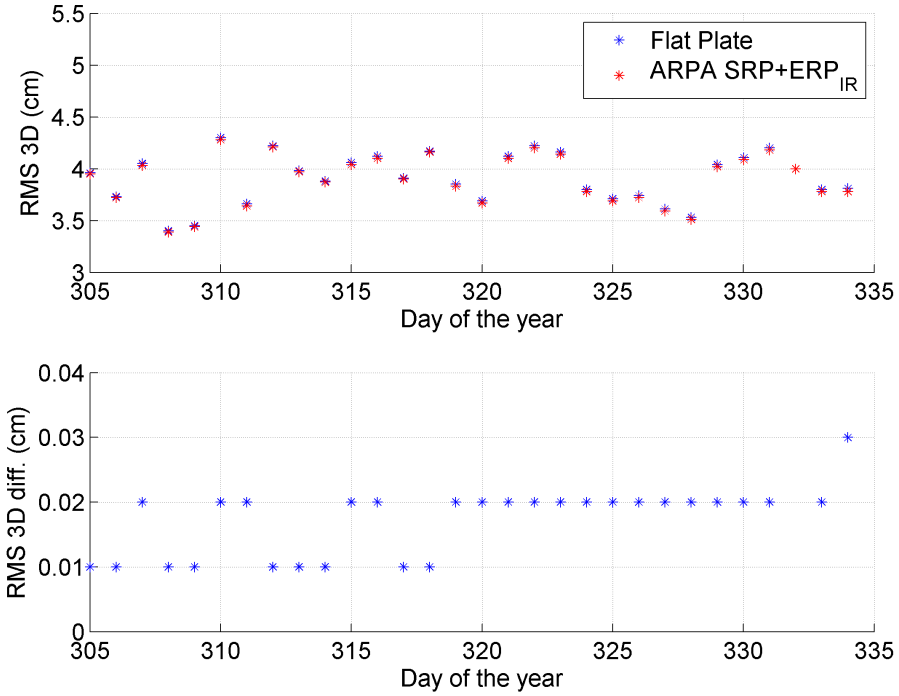

Figure 6.16: Comparison between the reduced-dynamics official PSO solutions and the orbits obtained with the NAPEOS and ARPA ERP IR models. A positive difference means a reduction of the values with the ARPA model.

Figure 6.16 shows the results of the comparison between the reduced-dynamics official PSO solutions and the orbits obtained with the NAPEOS and the ARPA ERP IR models. Both the computed orbits show good consistency with the PSO solutions. Due to the low

Table 6.6: Post-fit RMS for the ARPA ERP albedo and IR test cases, obtained with different ERP radiation maps.

Albedo maps	Post-fit RMS	IR maps	Post-fit RMS
Latitude-dep.	6.372	Latitude-dep.	6.362
ANGARA	6.379	ANGARA	6.421
CERES	6.379	CERES	6.407

Table 6.7: Non-gravitational force models adopted for the GOCE thermal radiation pressure test cases. ARPA TRR model is compared to the solution with no TRR modeling.

Force source	Description	Parameter	Model
SRP	Solar rad. press.	fixed C_R	ARPA
ERP	Albedo rad. press.	fixed $C_{R_{Alb}}$	NAPEOS
	Infrared rad. press.	fixed $C_{R_{IR}}$	NAPEOS
TRR	Thermal re-rad. press.	fixed $C_{R_{TRR}}$	ARPA & none
Emp. acc.	CPR constant along-track	estimated hourly	NAPEOS
	CPR constant cross-track	estimated hourly	NAPEOS
	CPR cosine along-track	estimated hourly	NAPEOS
	CPR cosine cross-track	estimated hourly	NAPEOS
	CPR sine along-track	estimated hourly	NAPEOS
	CPR sine cross-track	estimated hourly	NAPEOS

level of the ERP IR accelerations affecting the satellite dynamics and the absorption of the empirical accelerations, the difference between the ARPA and NAPEOS orbits is small, as for the albedo. The distance of ARPA ERP IR solutions from the PSO solutions is anyway slightly lower for the 70% of the daily arcs.

The previous tests were carried out for all the three Earth radiation maps and the results obtained for the post-fit RMS are shown in Table 6.6. As observable the latitude-dependent maps implemented in NAPEOS lead to better agreement with the GPS observations, as well as slightly lower CPR's. This result is due to the low value of radiation computed with the ANGARA and CERES maps, which, in turn, lead to lower than expected ERP accelerations, as shown in Figures 6.9 and 6.13.

6.3.4 Thermal Re-Radiation Pressure

For this test the ARPA model for the satellite thermal re-radiation pressure was introduced. The solution with the ARPA TRR model was compared to the solution without any TRR modeling, to observe the effects of the thermal emission of the satellite surfaces on the orbit. For this test the non-gravitational dynamical model described in Table 6.7 was set up. Also in this case the solar radiation pressure was set fixed ($C_R = 1.141$) with the ARPA model, and the Earth radiation pressure for the albedo and infrared components was computed with the NAPEOS models. Again, the empirical accelerations in the along-

and cross-track directions were estimated.

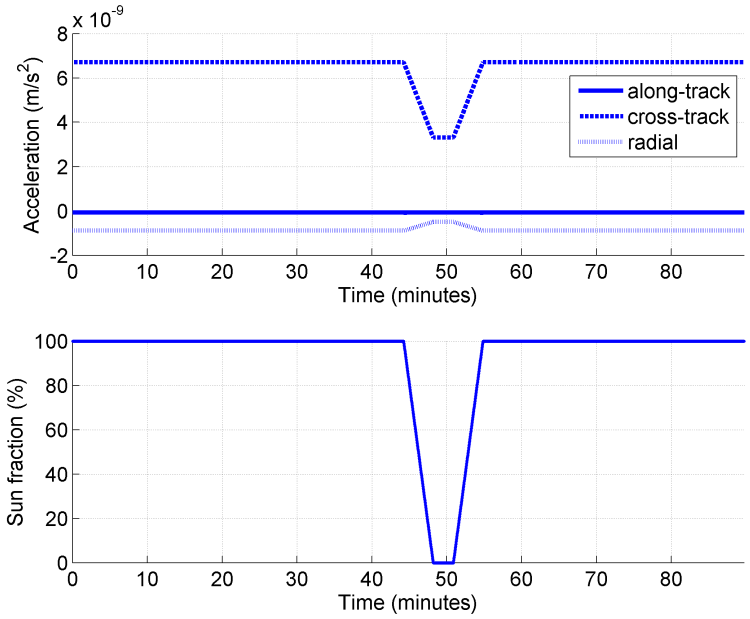

Figure 6.17: Satellite thermal re-radiation pressure acceleration (at the top) obtained with the ARPA model, in the RTN reference frame. At the bottom the percentage fraction of visible Sun.

Figure 6.17 shows the accelerations computed for the TRR with ARPA. As observable the acceleration deriving from the thermal perturbation is a function of the fraction of Sun visible from the satellite location. When the spacecraft is fully exposed to the solar radiation the perturbing acceleration is the one computed for the hot case. When the satellite is instead in full eclipse the perturbation is a direct function of the surface temperature for the cold case. The transition from the hot case to the cold case and viceversa is computed as a function of the Sun fraction, computing the weighted average of the hot and cold case perturbing accelerations. In this way the transitory state is smoothly modeled and no discontinuities are observable in the computed accelerations.

The post-fit RMS is shown in Figure 6.18. As can be observed, the resulting post-fit RMS obtained with the ARPA TRR model is slightly lower than the one obtained without activating the model. The average post-fit RMS, about 6.212 *mm*, is decreased of about 0.015 *mm* for all the 30 daily arcs. The difference which does not appear so significant (a reduction of about 0.2%) is instead important because, as said, the mismodeling in dynamical model is mainly absorbed by the CPR's. The difference introduced with the ARPA TRR model is instead clear from Figure 6.19, where the CPR's in the along- (amplitude term) and cross-track (constant term) are reported. As shown, in the along-track direction the ARPA TRR model is capable of slightly reducing the empirical accelerations, while in the cross-direction the reduction is significant, similarly to the improvement derived from the ARPA SRP model. The decrement is the cross-track direction is again about the 20%, meaning that the ARPA TRR model, introducing the previously unmodeled thermal per-

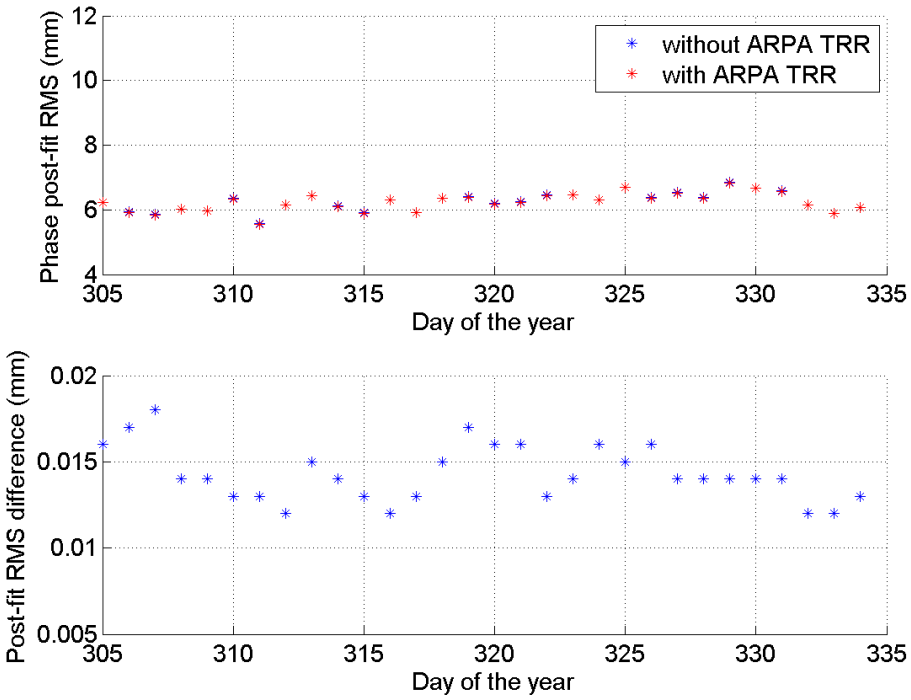

Figure 6.18: Post-fit RMS for the ARPA TRR test cases. Solutions with and without the ARPA TRR model are shown.

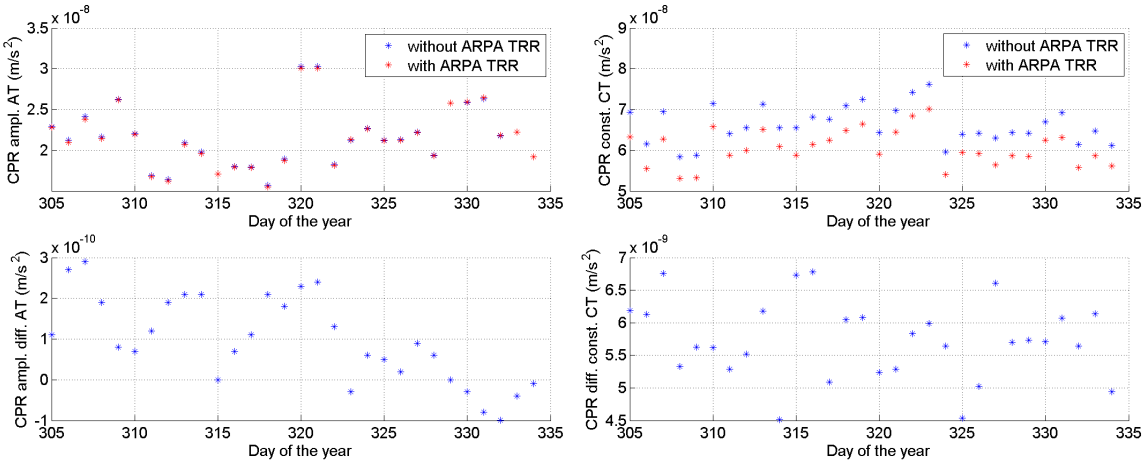

Figure 6.19: Along-track amplitude and cross-track constant CPR's and CPR's difference for the ARPA TRR test cases. A positive difference means a reduction of the values with the ARPA model.

turbation, is improving the solution. The empirical accelerations, which, as said, absorb the majority of the mismodeling, are hence significantly reduced and it can be concluded that ARPA is accurately modeling the TRR perturbation. In addition, the improvement introduced by this new modeling is fast and efficient. Also for the ARPA satellite thermal

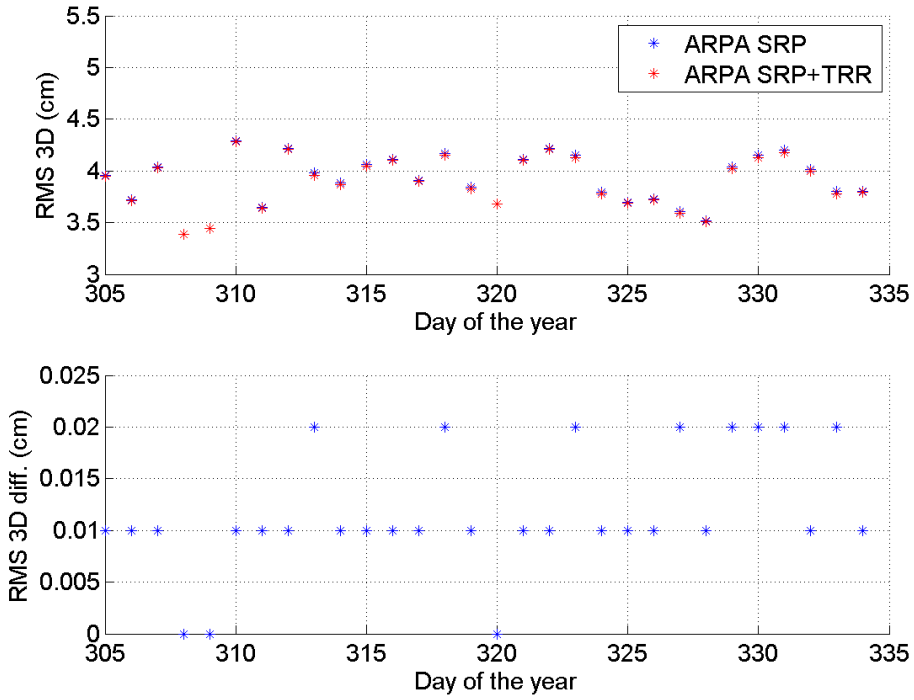

Figure 6.20: Comparison between the reduced-dynamics official PSO solutions and the orbits obtained with and without the ARPA TRR model. A positive difference means a reduction of the values with the ARPA model.

re-radiation, a 20% reduction of the CPR's in the cross-track direction is indeed significant and proves the goodness of the ARPA implemented modeling and technique for the TRR perturbation.

Figure 6.20 shows the results of the comparison between the reduced-dynamics official PSO solutions and the orbits obtained with and without the ARPA TRR models. Both the PSO-NAPEOS and PSO-ARPA orbit distances are at the centimeter level, with an average of about 3.9 cm. Both the computed orbits show good consistency with the PSO solutions. Even if the difference is small, the distance of ARPA TRR solutions from the PSO solutions is slightly lower for 93% of the daily arcs.

Table 6.8: Non-gravitational force models adopted for the GOCE aerodynamics test cases. NAPEOS and ARPA aerodynamic models are compared.

Force source	Description	Parameter	Model
SRP	Solar rad. press.	fixed C_R	ARPA
ERP	Albedo rad. press.	fixed $C_{R_{Alb}}$	NAPEOS
	Infrared rad. press.	fixed $C_{R_{IR}}$	NAPEOS
TRR	Thermal re-rad. press.	fixed $C_{R_{TRR}}$	ARPA
Drag	Aerodynamic drag	estimated C_D	NAPEOS & ARPA
Thrust	Thrust profile	from telemetry	—
Emp. acc.	CPR const. cross-track	estimated hourly	NAPEOS
	CPR cos. along-track	estimated hourly	NAPEOS
	CPR cos. cross-track	estimated hourly	NAPEOS
	CPR sin. along-track	estimated hourly	NAPEOS
	CPR sin. cross-track	estimated hourly	NAPEOS

6.4 Aerodynamic test case

This set of test cases has been adopted to test the databases and implemented routines for what concerns the perturbations on GOCE due to the satellite aerodynamics. For these tests the thrust profile of the satellite was introduced in the dynamics for the POD process, since it is a direct measurement of the atmospheric drag experienced by the spacecraft (due to the drag-free mode). In this way it is possible to compute the satellite aerodynamic forces that are necessary to compensate the thrust. As for the radiative cases, these tests were performed by comparing the new model developed with ARPA and the standard solution adopted by NAPEOS (flat plate). An additional comparison of ARPA with the available ANGARA model for GOCE was computed. Again, for all the tests all the setup in NAPEOS was maintained unchanged and only the aerodynamic model was switched to the required one. Also the number of observations rejected by the data pre-processing (*GnssObs*) and the orbit estimation (*Bahn*) is maintained low (below 1%) in order to obtain comparable solutions.

For the test the model of non-gravitational forces described in Table 6.8 was adopted. The model of forces in this case includes the aerodynamic drag scaling factors estimation. There is to clarify the fact that the C_D estimated with the ARPA and ANGARA models is not properly a drag coefficient, but a scaling factor adopted to adjust and correct the accelerations computed with these models. Hence, when the value is close to the unity it means that the model is accurately modeling the aerodynamic perturbation. 20 C_D's per day were estimated in the process. The thrust profile from the satellite telemetry was included. Again, the empirical accelerations in the along- and cross-track directions were estimated. Note that in this case no constant along-track CPR's were considered since they would interfere with the drag estimation process. The along-track sine and cosine CPR terms were instead kept because of their different period and effects.

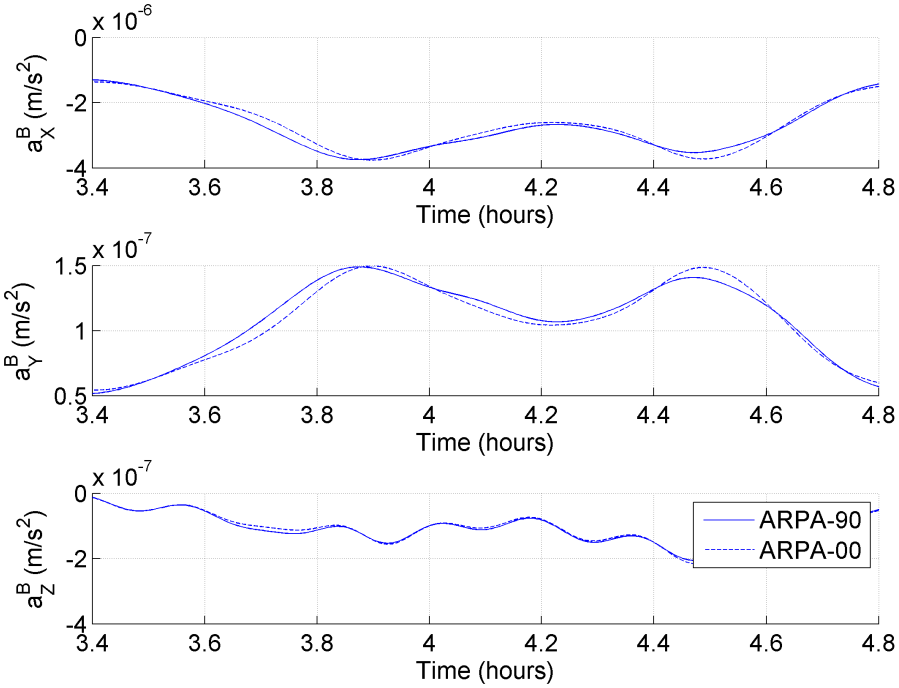

Figure 6.21: Aerodynamic accelerations of GOCE for one orbit, computed with the ARPA model with the MSIS-E-90 (ARPA-90) and NRLMSISE-00 (ARPA-00) atmospheric models, in the body-fixed reference frame.

For these simulations two different atmospheric models were adopted:

- the MSIS-E-90 [40],
- the NRLMSISE-00 [70]),

which provide the required atmospheric properties (density, temperature, mean molecular mass, number density of atomic oxygen) at the satellite location along the orbit.

Figure 6.21 shows the accelerations of GOCE due to the aerodynamics computed with ARPA with the MSIS-E-90 and the NRLMSISE-00 atmospheric models for one orbit. The computed accelerations are similar for both the atmospheric models and, as expected, the acceleration is mainly directed in the along-track direction ($+X$), with which the satellite is aligned. At the time 3.9 hours and 4.5 hours the satellite is crossing the equator, where its altitude is lower and the atmospheric density is higher. At the same positions a significant lateral acceleration is experienced by GOCE in the cross-track direction ($-Y$), due to the transversal winds at the equator (the atmosphere is quasi-corotating with the solid Earth). The lateral acceleration reaches the level of about the 4% of the along-track acceleration.

Figure 6.22 shows the drag acceleration computed with the different models (ARPA, ANGARA and NAPEOS) and the GOCE thrust profile for one orbit. As observable also the thrust level is higher at the equator and decreases at the poles. All the models are capable of accurately modeling the thrust profile along the orbit while they are all slightly

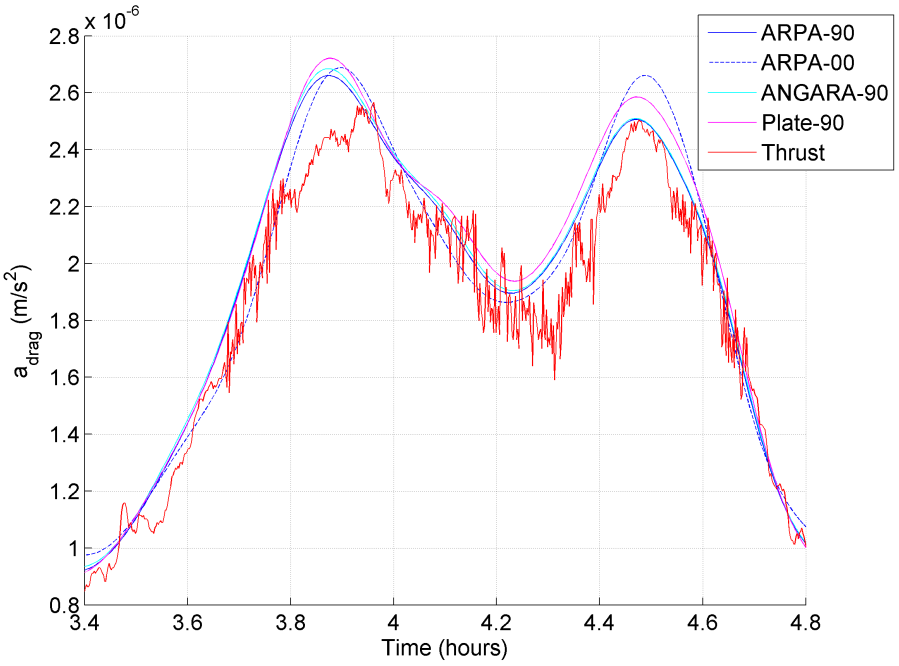

Figure 6.22: Aerodynamic drag computed with different aerodynamic models and atmospheric models for one orbit. GOCE thrust profile as from telemetry is also shown.

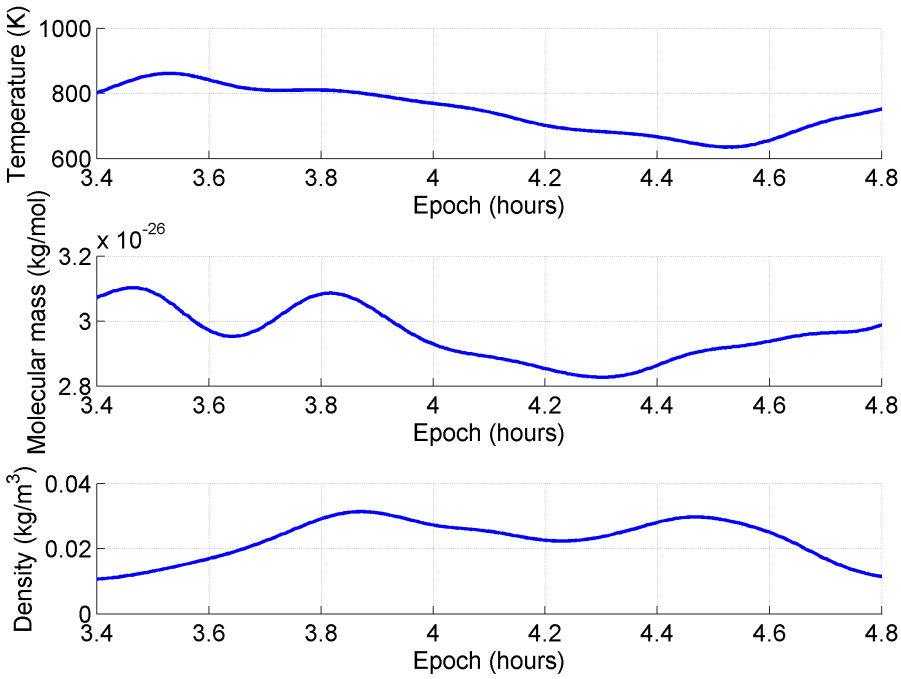

Figure 6.23: Atmospheric temperature, mean molecular mass and density along one orbit of GOCE (from MSIS-E-90).

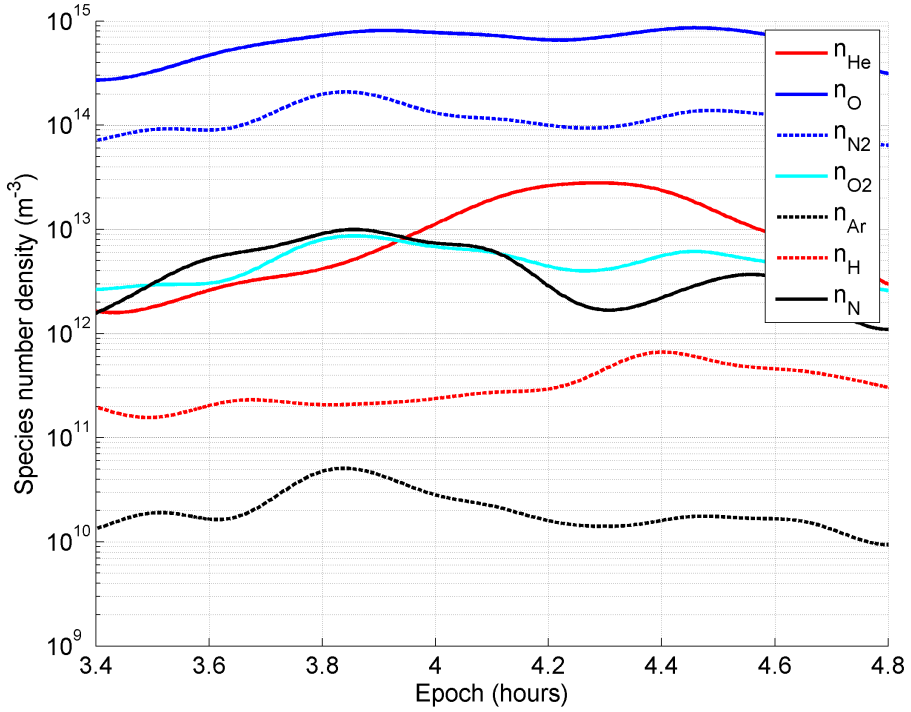

Figure 6.24: Atmospheric species, shown as number densities, along one orbit of GOCE (from MSIS-E-90).

overestimating the deceleration when crossing the equator. This effect is mainly related to the density computed with the atmospheric models. The ARPA aerodynamic model developed for GOCE leads to the best results compared to the other shown models when using the MSIS-E-90 atmospheric model. With this atmospheric model, the atmospheric properties shown in Figure 6.23 and 6.24 were computed for the same orbit shown in the accelerations. Figure 6.23 shows the atmospheric temperature, mean molecular mass and density. As observable, the density profile is similar to the accelerations along the orbit since it is the main parameter that directly determines the atmospheric drag. It is hence higher at the equator and lower at the poles. At the time 4.2 hours the satellite is crossing the north pole with an altitude slightly higher than at the south pole, hence facing higher densities there. Atmospheric temperatures are instead higher at the south pole due to the inclination of the Earth with respect to the solar radiation that heats up the atmosphere. In fact, this orbit is taken from the day 1 November 2009, when the Earth south hemisphere is more exposed to the solar radiation. A similar effect, even though with more oscillations, is observable for the mean molecular mass.

Figure 6.24 shows the atmospheric components as their number densities. At this low altitude of 250 km the atomic oxygen is predominant, about 10 times more concentrated than the nitrogen molecule, and at least 2 orders of magnitude than the other atmospheric components. Due to this high level of atomic oxygen along the entire orbit, the satellite surface lattice is saturated.

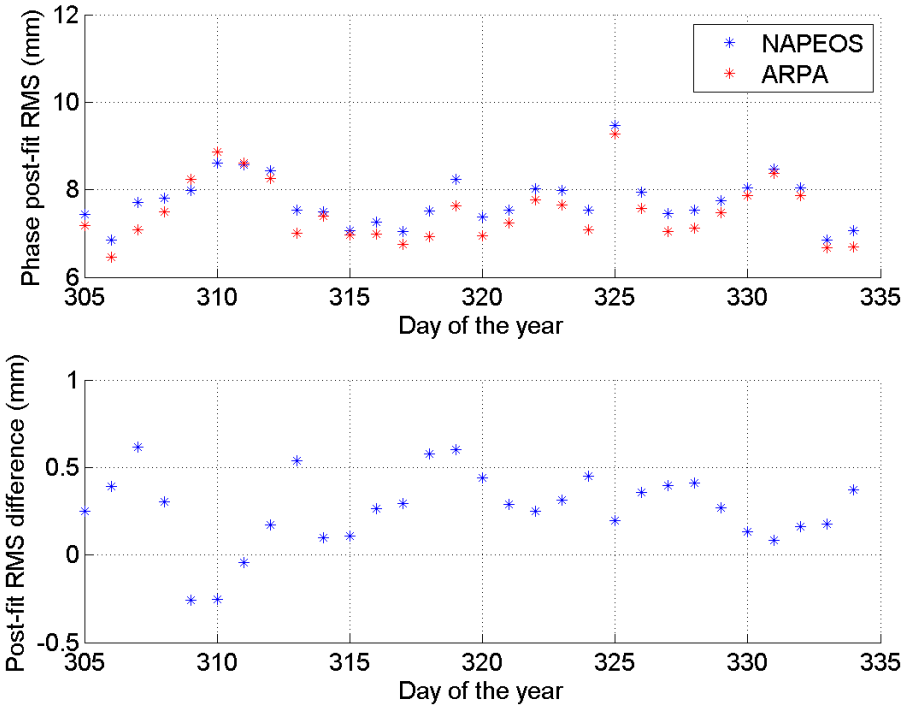

Figure 6.25: Post-fit RMS for the NAPEOS and ARPA aerodynamic test cases, with MSIS-E-90.

The post-fit RMS obtained with the ARPA aerodynamic model when adopting the MSIS-E-90 atmospheric model is shown in Figure 6.25. As can be observed, the resulting post-fit RMS obtained with the ARPA aerodynamic model is lower than the one obtained with the standard NAPEOS model (again the flat plate). The average post-fit RMS, about 7.471 mm, is significantly decreasing for the 90% of the tested days. The average decrement in the post-fit RMS is about 0.316 mm, and for some days it reaches the level of about 0.6 mm. Only for three days the post-fit RMS is higher (about 0.184 mm) with the ARPA model than with the NAPEOS one. The CPR's are maintained at the same level for both the models and the reduction of the post-fit RMS is only due to the accurate modeling of ARPA for the aerodynamic forces.

Figure 6.26 shows the results of the comparison between the reduced-dynamics official PSO solutions and the orbits obtained with the NAPEOS and ARPA aerodynamic models. The PSO-ARPA orbit distance are at the centimeter level, with an average of about 4.28 cm. The orbits computed with ARPA show an average decrement of the distance from the PSO solutions of about 0.42 cm with respect to the distance of the orbits computed with the NAPEOS aerodynamic model. The decrement in the distance from the PSO solutions of about 0.4 cm obtained for the 97% of the daily arcs and the reduction of about 0.3 mm in the post-fit RMS for the 90% of the daily arcs are indeed significant and prove the goodness of the ARPA implemented modeling and technique for the aerodynamic perturbation. These results are also a confirmation that the SESAM model ([73]) is correctly describing the

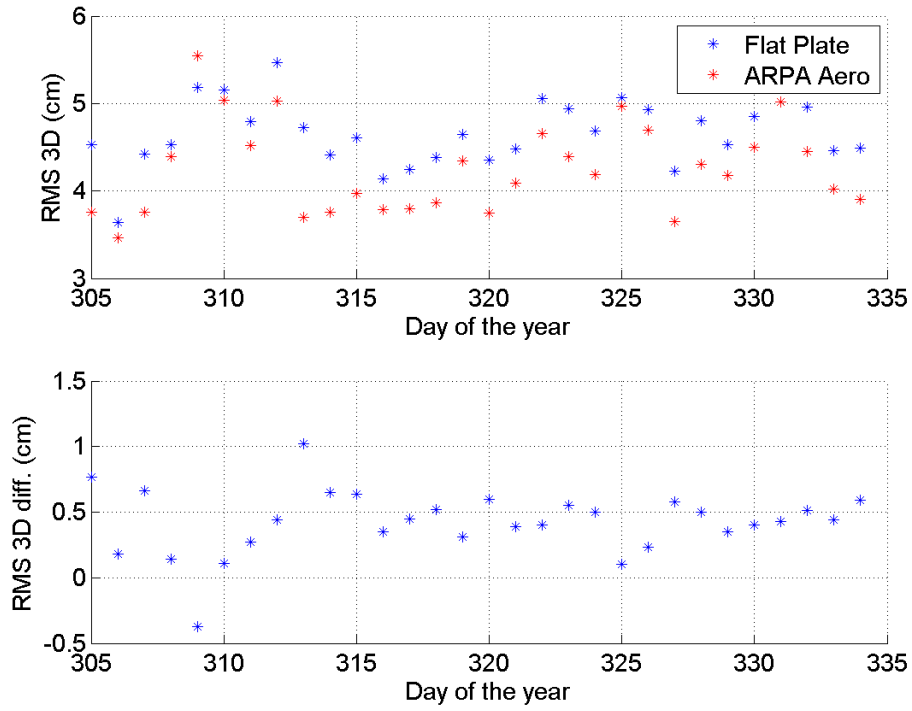

Figure 6.26: Comparison between the reduced-dynamics official PSO solutions and the orbits obtained with the NAPEOS and the ARPA aerodynamic models.

momentum exchange between the atmospheric particles and the satellite surfaces.

The solution obtained with the ARPA aerodynamic model was also compared with the ANGARA aerodynamic model of GOCE adopting the MSIS-E-90 atmospheric model. The results of the post-fit RMS are shown in Figure 6.27 and again ARPA shows an average reduction of the post-fit RMS of about 0.41 mm for all the daily arcs.

Figure 6.28 shows the scaling factors C_D estimated by the POD process for the ARPA and ANGARA aerodynamic models. As previously said, the scaling factors are used to scale the computed accelerations adjusting them to better fit the observations. As can be observed in Figure 6.28 the estimated scaling coefficients are estimated to values that are lower than the unity, this meaning the aerodynamic models, when not corrected by the factors, tend to overestimate the satellite drag. The mean values of the scaling factors are about 0.678 for ARPA and 0.793 for ANGARA with the MSIS-E-90 atmospheric model and 0.6848 for ARPA with the NRLMSISE-00 atmospheric model. This means that the ANGARA is overestimating the accelerations of about the 20%, while ARPA of about the 30%. The explanation of this overestimation is related to the inaccuracies in the aerodynamic coefficients and atmospheric models derivation. It is in fact not possible (for the moment) to be able to derive a perfect description of the aerodynamic coefficients without assuming a particular atmospheric model. It is the same for what concerns the atmospheric model derivation, that has to assume specific aerodynamic coefficients. It is in fact not easy to separate the two components and only the resultant effects (the acceleration induced on

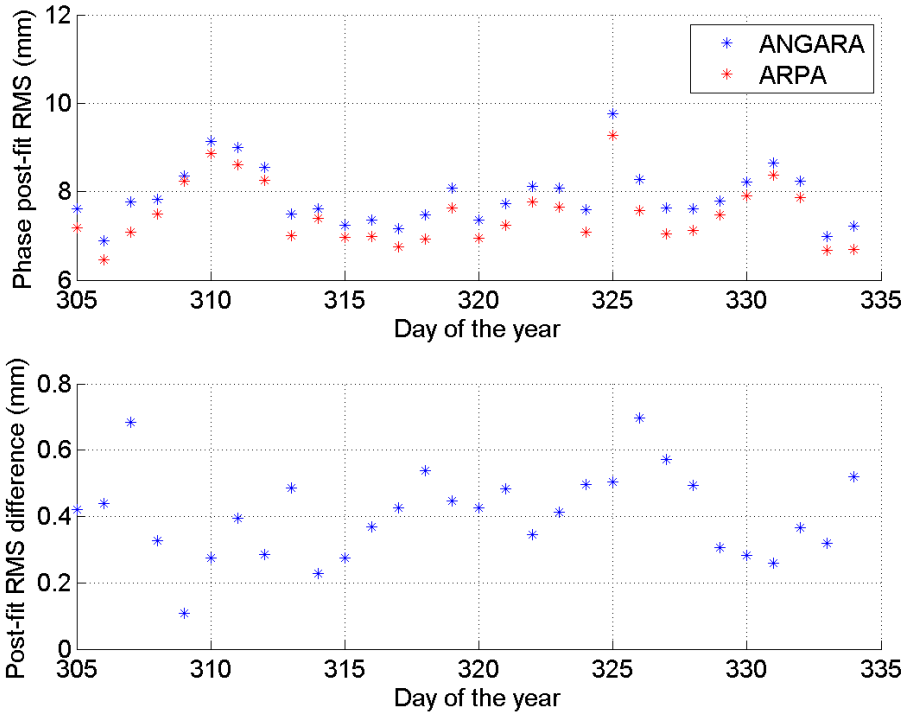

Figure 6.27: Post-fit RMS for the ANGARA and ARPA aerodynamic test cases, with MSIS-E-90.

the spacecraft) are observable. Depending on the solar and geomagnetic conditions, empirical density models (daily averages) can in fact be off by as much as $30 - 40\%$ RMS when considering years worth of data. The model bias could vary almost as much on any given day due to errors in the seasonal variation as represented in the model. Furthermore, the bias difference between any two models could be as big as $10 - 20\%$, sometimes more ([23] and personal communication with Marcin Pilinski).

Figure 6.29 shows the different post-fit RMS computed with the ARPA aerodynamic model with the MSIS-E-90 and the NRLMSISE-00 atmospheric models. The MSIS-E-90 model leads to slightly better results since the post-fit RMS is lower than the one computed with the NRLMSISE-00 model for about 60% of the daily arcs. The average post-fit RMS computed with the MSIS-E-90 model is about 7.596 mm while the one computed with the NRLMSISE-00 model is about 7.631 mm. Even if the difference between these results is small, it can be concluded that for the considered month of data the MSIS-E-90 atmospheric model leads to a better fit of the GPS observations for GOCE and to a better agreement (a difference of 0.04 cm in the distance) with the reduce dynamic PSO solutions.

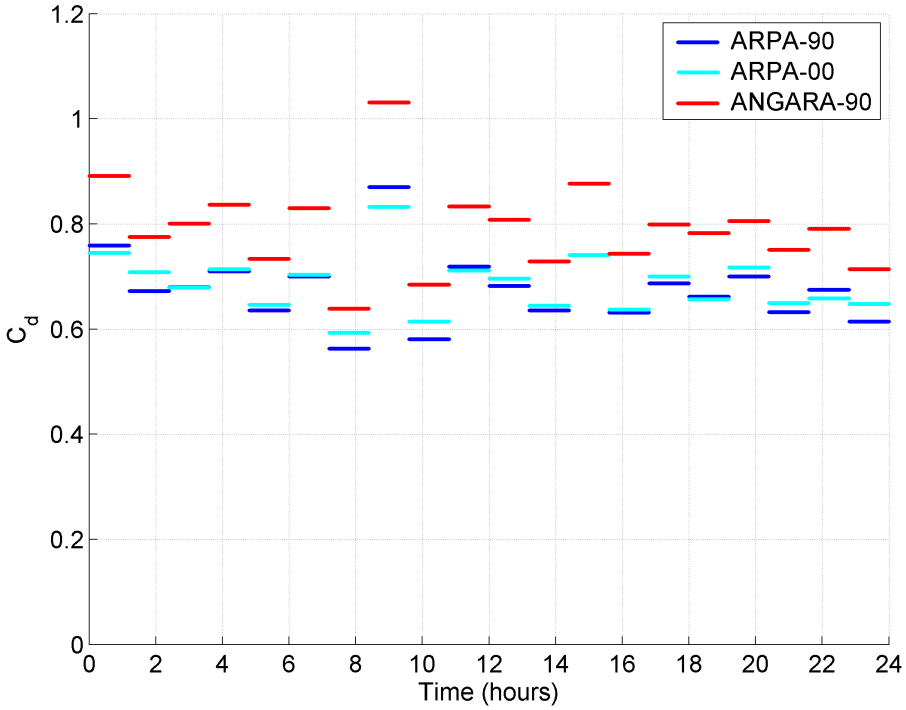

Figure 6.28: Aerodynamic scaling factors for ARPA and ANGARA with different atmospheric models, shown for one daily arc.

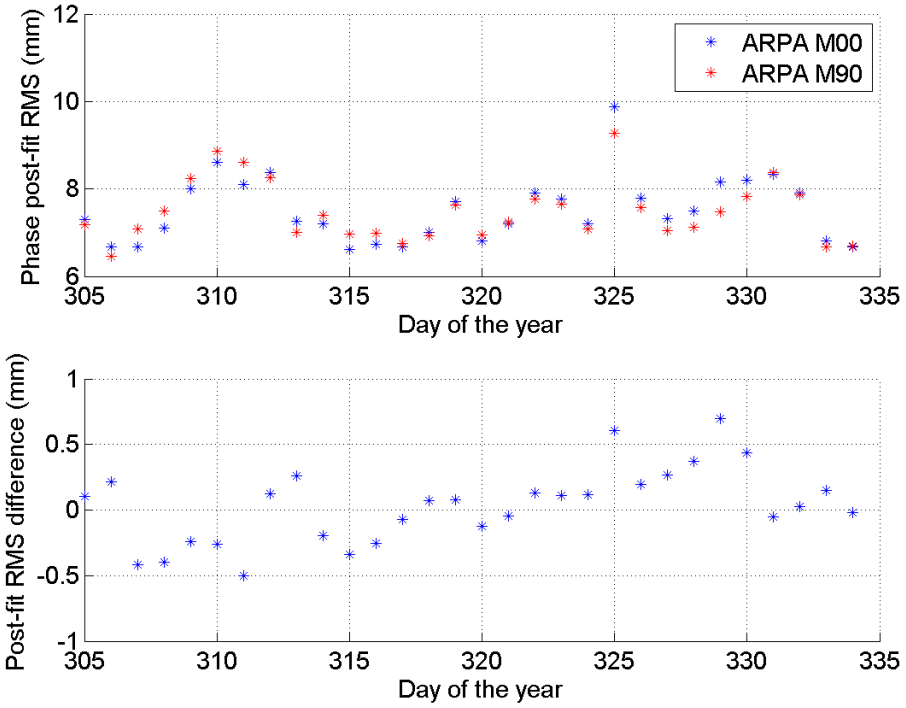

Figure 6.29: Post-fit RMS for the ARPA aerodynamic test cases, with MSIS-E-90 and NRLMSISE-00.

Conclusions and future work

The work of this thesis has dealt with the precise non-gravitational force modeling for the ESA satellite GOCE. This highly detailed modeling has been developed in order to increase the accuracy of the precise orbit determination of the satellite. This work has been carried out at the University of Padova, during the PhD at the Center of studies and activities for space — CISAS – "G. Colombo", as a complementary activity our research group has been involved in. GOCE POD and ocean tide field recovery have been our main objectives in the GOCE-Italy group — an ESA project endorsement funded by the Italian Space Agency (ASI).

In order to be able to observe and estimate the ocean tides parameters from the GOCE orbital perturbations, it has been necessary to accurately model the non-gravitational forces acting on GOCE, so that these contributions are not erroneously absorbed.

To accurately model the non-gravitational perturbations due to the Solar Radiation Pressure (SRP), Earth Radiation Pressure (ERP) for the albedo and infrared components, the satellite Thermal Re-Radiation pressure (TRR), and the aerodynamics, a sophisticated system has been designed and implemented. A raytracing automatic sequence has been set up to simulate the reflections of the photons from Sun and Earth of the surfaces of any satellite (represented with a CAD model). This procedure has been developed to model the geometrical interactions with a high level of accuracy, which is higher than the previously developed models (e.g., cannon-ball and box-wing models) and can be easily adapted to any satellite, considering the particular configuration of its moving parts (e.g., antennas, solar panels). An accurate mesh of pixels of the outer satellite surfaces have been built in order to accurately describe the geometry of the spacecraft for the computation of the TRR and aerodynamics accelerations. The geometric information contained in the raytracing and the surface mesh files are then converted into physical information by means of the ARPA software. ARPA — Aerodynamics and Radiation Pressure Analysis — is the software that was developed for this purpose. This software tool is capable of converting the input files into databases of forces and torques due to SRP, ERP, TRR and aerodynamics, based on the most recent modeling selected from the available literature. In fact, the models implemented in ARPA have been identified after an accurate and elaborated investigation based on available publications and personal communications with experts in the fields. Thanks to this method it has been possible to achieve the presented results in two fields that are significantly different, such as the radiation pressure and the satellite aerodynamics.

ARPA and the raytracing procedure have been designed and developed in order to com-

pute the non-gravitational perturbations on satellites of any shape, weather in Earth-bound orbit, or orbiting another planet, or orbiting another planet, or cruising in interplanetary space.

An accurate analysis of the dependencies of each non-gravitational force component has been carried out in order to normalize the forces, computing radiation pressure and aerodynamic coefficients which can be used by the POD software. This innovative solution has been developed in order to be able to quickly and efficiently reconstruct the in-flight accelerations experienced by a satellite starting from a more general and relatively small database. In this way all the computationally intensive and time consuming realization of the databases in carried out only once, before the actual POD process. The POD process can hence make use of the accurate force models without overloading the system, just scaling the pre-computed coefficients.

With the described procedure and software new ARPA databases for SRP, ERP, TRR and aerodynamics have been developed for GOCE.

The NAPEOS (NAvigation Package for Earth Observation Satellites) software, developed and maintained at ESA/ESOC, was upgraded to make use of the new ARPA inputs and adopted to perform the tests on GOCE. A POD sequence has been set up to carried out the tests.

The tests on GOCE were performed on 30 consecutive daily arcs, starting at the beginning of the GOCE science phase on 1st November 2009. The results for the radiation test cases show a significant reduction of the empirical accelerations, especially in the cross-track direction, of about the 20% for the SRP, 12% for the ERP albedo, 13% for the ERP infrared and 20% for the TRR with respect to the standard NAPEOS force modeling (cannon-ball). For the aerodynamics, an important reduction of the post-fit RMS from 7.6 to 7.3 mm has been observed with the new ARPA model, and a reduction from 4.6 to 4.2 cm of the distance of the orbits computed with ARPA from the official reduced-dynamics GOCE orbits (Precise Science Orbit) has been computed. The obtained results confirm the goodness of the modeling and techniques of ARPA for all the non-gravitational perturbations computed for GOCE.

The current investigation has been adopted to mainly test and validate the developed strategies and, with these, their efficiency and correctness have been proven.

As a future step the ARPA models for GOCE will be adopted to retrieve the ocean tides parameters.

Moreover, since the techniques and methods described in this thesis are applicable to any satellite, new ARPA models will be realized for other spacecrafts, such as satellites from the GNSS constellations and, mainly for the torque components, for interplanetary missions.

Appendix A

ARPA reference system

A.1 Direction of the incoming radiation adopted in ARPA

Figure A.1 shows the Body-fixed Reference Frame (BRF) of GOCE and also shows how the Azimuth Az and Elevation El angles are defined for each vector, simulating the incoming radiation on the spacecraft from the Sun or the Earth or the atmospheric particles aligned with the relative velocity of the spacecraft with respect to the atmosphere.

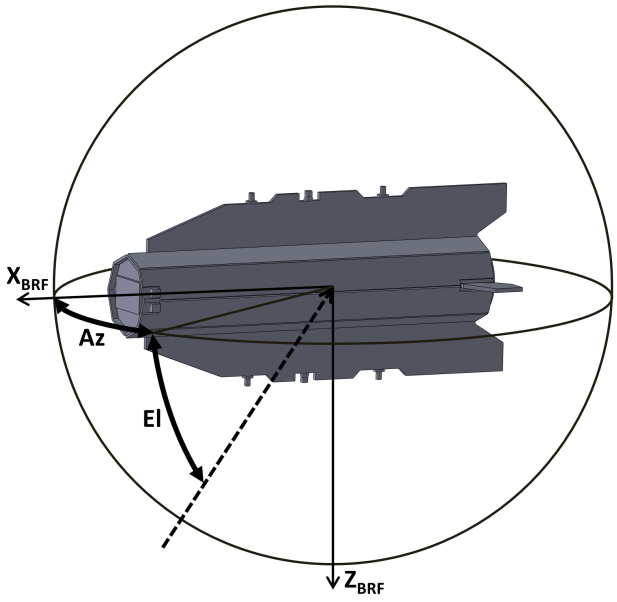

Figure A.1: GOCE reference frame and definition of the direction of the incoming vector (radiation or atmospheric particle) by means of Azimuth Az and Elevation El angles.

A.2 Solar panels degrees of freedom adopted in ARPA

Figure A.2 shows the Degrees Of Freedom (DOF) of the solar panels, as implemented in ARPA, which can be activated if necessary for satellite with steering solar panels. The first DOF ϕ_1 allows the solar panels to rotate around their axis, while the second DOF ϕ_2 allows them to rotate out of their plane.

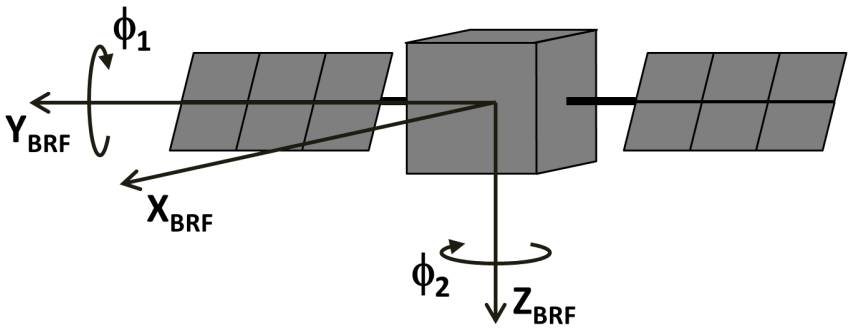

Figure A.2: Degrees of freedom of the solar panels, as implemented in ARPA.

Acknowledgements

First of all I would like to thank my PhD supervisor professor Stefano Casotto for the helpful discussions and valuable suggestions during these years.

I am also thankful to the GOCE-Italy group, especially to professor Ferdinando Sansó, for the opportunity of participating in a challenging scientific project.

Thanks to the European Space Agency and especially to professor Werner Enderle, René Zandbergen and all the Navigation Support Office team in ESOC, for the really great opportunity of collaborating in such an international and friendly environment. My thanks go to Michiel Otten and Tim Springer, who supported (and put up with) me with the upgrade of NAPEOS. Your help has been indeed GREAT! A special thank goes to Claudia Flohrer for the great discussions about reference systems, partial derivatives, estimation theory, beers and German language. Vielen Dank, Claudia, es war sehr wichtig! Thanks also to the GOCE control team, especially to the GOCE SOM Christoph Steiger and the GOCE SOE Carlo Enrico Ghisi, for the great support of technical documentation, and information you provided to me.

I would like to thank Marcin Pilinski and Eelco Doornbos for the great suggestions and indications during both the devolvement and testing phases of this thesis. Thank you very much, for the great discussions and opinions. It really meant a lot to me!!!

I am also EXTREMELY thankful to Max (alias Massimo Bardella), colleague and friend here at the university, without whom I literally wouldn't have been able to learn so many things in such a short time! Max, grazie mille per gli insegnamenti, i suggerimenti e il supporto che mi hai pazientemente dato! I am also thankful to Francesca Panzetta, colleague, friend and efficient collaborator during these years, who was always able to give me good suggestions, and who helped me in writing papers, documents, and with whom I discussed several results. Grazie Fra, soprattutto per i consigli, l'aiuto, e la valutazione estetica delle mie presentazioni!

Thanks to the people in Alpbach and post-Alpbach for the great opportunity to learn, discuss, work (hard) and build such a great team spirit in a short time. It has been really a great opportunity to learn and challenge myself. Go Team Orange, GO!

Thanks to my parents and my brother, who won't probably understand anything of this thesis, but were all the time close to me during the good and the difficult moments. Grazie mille mamma, papá e Matteo per essermi stati vicini e per avermi dato la possibilitá di arrivare fino a qui. Se d'altronde ho raggiunto i miei obiettivi sinora, é sicuramente in gran parte grazie a voi!!!!

Thanks to all my friends of the Brenta Party!! Grazie mille, di cuore, a tutti gli amici del Partito Brenta, del FichClub® e del gruppo scout di Noventa Padovana, per questi magnifici anni trascorsi assieme e per tutte le esperienze e le emozioni condivise insieme!! Grazie davvero!!!

Grazie ai Nasi del Destino, Gherardo e Carlo. Con voi ho condiviso questi anni di universitá, con tutte le esperienze che non sto qui a riassumere. Grazie davvero di tutto, soprattutto per la vostra voglia di star assieme e divertirsi, la vostra ospitalitá e anche di alcuni consigli tecnici!

Grazie a tutti i colleghi del CISAS e soprattutto di Astronomia. Con voi ho condiviso da vicino tutte le esperienze di dottorato nonché innumerevoli pranzi e pause the/caffé.

Grazie alla formidabile e imbattibile squadra del ilMeteo.it. Con voi ho imparato a condividere le esperienze di una squadra, in campo e fuori dal campo!

E infine voglio ringraziare la persona piú importante per me, e che piú mi é stata accanto in questi anni, nonostante la temporanea distanza fisica. Mara, grazie mille per esserci stata sempre e comunque in ogni circostanza, nei momenti felici e nei momenti difficili.
Davvero GRAZIE!!!

Bibliography

[1] S. Adhya. *Thermal re-radiation modelling for the precise prediction and determination of spacecraft orbits.* PhD thesis, Department of Geomatic Engineering, University College London, 2005.

[2] S. Adhya, P. Cross, A. Sibthorpe, and M. Ziebart. Oblate Earth Eclipse State Algorithm for Low-Earth-Orbiting Satellites. *Journal of Spacecraft and Rockets*, 41:157–159, January 2004.

[3] P. G. Antreasian and G. W. Rosborough. Prediction of Radiant Energy Forces on the TOPEX/POSEIDON Spacecraft. *Journal of Spacecraft and Rockets*, 29:81, January 1992.

[4] S. J. Arnold and J. M. Dow. Models for spacecraft acceleration due to earth albedo and infrared radiation. Technical Report OAD WP n. 265, ESA, June 1984.

[5] Y. Bar-Sever and D. Kuang. New Empirically Derived Solar Radiation Pressure Model for Global Positioning System Satellites. *Interplanetary Network Progress Report*, 159:I1, November 2004.

[6] Y.E. Bar-Sever and K.M. Russ. New and improved solar radiation models for gps satellites based on flight data. Final Report Under Task Order Agreement No. RF-182/808 Task Plan 80-4193, Jet Propulsion Laboratory,California Institute of Technology, Pasadena,CA,91125, 1997.

[7] D. Battaglia, C. Gennaro, and A. Berto. Satellite thermal icd. Technical Report GO-IC-AI-0004, issue 05, ThalesAlenia Space, February 2008.

[8] G. Beutler, E. Brockmann, W. Gurtner, U. Hugentobler, L. Mervart, M. Rothacher, and A. Verdun. Extended orbit modeling techniques at the CODE processing center of the international GPS service for geodynamics (IGS): theory and initial results. *Manuscr. Geod.*, 19:367–386, September 1994.

[9] G. A. Bird. Molecular gas dynamics. *NASA STI/Recon Technical Report A*, 76:40225, 1976.

[10] G. A. Bird. Monte carlo simulation of gas flows. *Annual Review of Fluid Mechanics*, 10(1):11–31, 1978.

[11] G. A. Bird. *Molecular Gas Dynamics and the Direct Simulation of Gas Flows*. Oxford science publications. Oxford University Press, Incorporated, 1994.

[12] H. Bock, A. Jäggi, U. Meyer, R. Dach, and G. Beutler. Impact of gps antenna phase center variations on precise orbits of the goce satellite. *Advances in Space Research*, 47:1885–1893, 2011.

[13] H. Bock, A. Jäggi, U. Meyer, P. Visser, J. IJssel, T. Helleputte, Ma. Heinze, and U. Hugentobler. Gps-derived orbits for the goce satellite. *Journal of Geodesy*, 85(11):807–818, 2011.

[14] H. Bock, A. Jäggi, D. Švehla, G. Beutler, U. Hugentobler, and P. N. A. M. Visser. Precise orbit determination for the goce satellite using gps. *Journal of Advances in Space Research*, 39:1638–1647, 2007.

[15] C. Bonacina, A. Cavallini, and L. Mattarolo. *Trasmissione del calore*. CLEUP, 1992.

[16] J.-P. Carrou. *Spaceflight dynamics*. Cépaduès-éd., 1995.

[17] A. Catalogiu and W. Felder. Pfm mechanical and thermal icd. Technical Report GO-IC-ASG-1004, Issue 2b, Astrium GmbH, dec 2006.

[18] G. E. Cook. Drag coefficients of spherical satellites. *Annales de Geophysique*, 22:53–64, 1965.

[19] G. E. Cook. Satellite drag coefficients. *Planetary and Space Science*, 13:929–946, October 1965.

[20] Dassault Systèmes SolidWorks Corporation. Solidworks. [Computer program], 2012. x64 Version, *http://www.solidworks.com*.

[21] ZEMAX Development Corporation. ZEMAX-EE optical design program. [Computer program], 2009. EE Version, *https://www.radiantzemax.com/zemax*.

[22] E. Doornbos. Modeling of non-gravitational forces for ers-2 and envisat. Master's thesis, Delft Institute for Earth-Oriented Space Research, Delft University of Technology, 2001.

[23] E. Doornbos. *Thermospheric Density and Wind Determination from Satellite Dynamics*. PhD thesis, Technische Universiteit Delft, 2011.

[24] E. Doornbos and R. Scharroo. Modelling of Non-gravitational Forces For ERS-2 and ENVISAT. In A. Tzanis, editor, *EGS General Assembly Conference Abstracts*, volume 27 of *EGS General Assembly Conference Abstracts*, page 1305, 2002.

[25] J. M. Dow, R. E. Neilan, and C. Rizos. The international gnss service in a changing landscape of global navigation satellite systems. *Journal of Geodesy*, 83(3-4):191–198, 2009.

[26] M. R. Drinkwater, R. Haagmans, D. Muzi, A. Popescu, R. Floberghagen, M. Kern, and M. Fehringer. The goce gravity mission: Esas first core earth explorer. In *Proceedings of the 3rd international GOCE user workshop*, pages 6–8, 2006.

[27] P. Duque. Aerodynamic forces and moments of free-molecular flow. OAD Working Paper 347, ESA ESOC, Darmstadt, Germany, December 1987.

[28] P. Duque. Environmental forces and moments in free-particle flow:software description and user's guide to program freeflow,. Technical report, GMV, 1989.

[29] H. F. Fliegel, T. E. Gallini, and E. R. Swift. Global positioning system radiation force model for geodetic applications. *Journal of Geophysical Research: Solid Earth*, 97(B1):559–568, 1992.

[30] H.F. Fliegel and T.E. Gallini. Solar force modeling of block IIR Global Positioning System satellites. *Journal of Spacecraft and Rockets*, 33:863–866, November 1996.

[31] C. Förste, S. L. Bruinsma, R. Shako, O. Abrikosov, F. Flechtner, J.-C. Marty, J.-M. Lemoine, C. Dahle, H. Neumeyer, F. Barthelmes, R. Biancale, G. Balmino, and R. König. A new release of EIGEN-6: The latest combined global gravity field model including LAGEOS, GRACE and GOCE data from the collaboration of GFZ Potsdam and GRGS Toulouse. In A. Abbasi and N. Giesen, editors, *EGU General Assembly Conference Abstracts*, volume 14 of *EGU General Assembly Conference Abstracts*, page 2821, April 2012.

[32] Telespazio France. Eoli-sa 9.3.1 - user guide: Interacting with earth observation data. Technical report, Telespazio France, 2013.

[33] R. M. Fredo and M. H. Kaplan. Procedure for Obtaining Aerodynamic Properties of Spacecraft. *Journal of Spacecraft and Rockets*, 18:367, July 1981.

[34] B. Fritsche, M. Ivanov, A. Kashkovsky, G. Koppenwallner, A. Kudryavtsev, U. Voskoboinikov, and G. Zhukova. Radiation pressure forces on complex spacecraft. ESOC contract 11908/96/D/IM, HTG, Germany and ITAM, Russia, Darmstadt, Germany, 1998.

[35] B. Fritsche and H. Klinkrad. Accurate prediction of non-gravitational forces for precise orbit determination - part i: Determination of perturbing forces and torques in an orbital environment. In *AIAA/AAS Astrodynamics Specialist Conference and Exhibit*, August 2004.

[36] B. Fritsche and H. Klinkrad. Accurate prediction of non-gravitational forces for precise orbit determination - part i: Principles of the computation of coefficients of force and torque. In *AIAA/AAS Astrodynamics Specialist Conference and Exhibit*, August 2004.

[37] F. O. Goodman and H. Y. Wachman. Formula for thermal accommodation coefficients. *The Journal of Chemical Physics*, 46(6):2376–2386, 1967.

[38] B. P. Graziano. *Computational Modelling of Aerodynamic Disturbances on Spacecraft within Concurrent Engineering Framework*. PhD thesis, Cranfield University, 2007.

[39] C. A. Gueymard. The suns total and spectral irradiance for solar energy applications and solar radiation models. *Solar energy*, 76(4):423–453, 2004.

[40] A. E. Hedin. Extension of the msis thermosphere model into the middle and lower atmosphere. *Journal of Geophysical Research: Space Physics*, 96(A2):1159–1172, 1991.

[41] F. C. Hurlbut and F. S. Sherman. Application of the nocilla wall reflection model to free-molecule kinetic theory. *Physics of fluids*, 11:486, 1968.

[42] F. C. Hurlbut and F. S. Sherman. Rarefied gas dynamics, *The national commitee for fluid mechanics films*. Video at `http://www.youtube.com/watch?v=T46Wb2d_dV8`, 1968.

[43] D. R. Imbro, M. M. Moe, and K. Moe. On fundamental problems in the deduction of atmospheric densities from satellite drag. *Journal of Geophysical Research*, 80(22):3077–3086, 1975.

[44] Autodesk Incorporation. AutoCAD. [Computer program], 2010. E.49.0.0 Version, *http://www.autodesk.com/products/autodesk-autocad/overview*.

[45] F. P. Incropera and D. P. DeWitt. *Introduction to heat transfer*. Wiley, 1990.

[46] M. N. Izakov. Some problems of investigating the structure of the upper atmosphere and constructing its models. *Space Res*, 5:1191–1213, 1965.

[47] A. Jäggi, R. Dach, O. Montenbruck, U. Hugentobler, H. Bock, and G. Beutler. Phase center modeling for leo gps receiver antennas and its impact on precise orbit determination. *Journal of geodesy*, DOI 10.1007/s00190-009-0333-2(83):1145–1162, 2009.

[48] J. A. Johannessen and M. Aguirre-MArtinex. The four candidate earth explorer core missions, gravity field and steady-state ocean circulation explorer. Technical Report ESA SP- 1233(1), ESA, July 1999.

[49] Z. Kang, B. Tapley, S. Bettadpur, J. Ries, and P. Nagel. Precise orbit determination for {GRACE} using accelerometer data. *Advances in Space Research*, 38(9):2131 – 2136, 2006.

[50] H. Klinkrad, C. Koeck, and P. Renard. Precise satellite skin-force modelling by means of Monte-Carlo ray tracing. *ESA Journal*, 14:409–430, 1990.

[51] H. Klinkrad, G. Koppenwallner, D. Johannsmeier, M. Ivanov, and A. Kashkovsky. Free-molecular and transitional aerodynamics of spacecraft. *Advances in Space Research*, 16(12):33 – 36, 1995. ¡ce:title¿Orbit Determination and Analysis¡/ce:title¿.

[52] P. C. Knocke, J. C. Ries, and B. D. Tapley. Earth radiation pressure effects on satellites. In *AIAA/AAS Astrodynamics Conference*, pages 77–586, August 1988.

[53] G. Kopp and J. L. Lean. A new, lower value of total solar irradiance: Evidence and climate significance. *Geophysical Research Letters*, 38(1), 2011.

[54] G. Koppenwallner. *Freimolekulare Aerodynamik für Satellitenanwendung*. PhD thesis, Dt. Forschungs-u. Versuchsanst. f. Luft-u. Raumfahrt, 1982.

[55] G. Koppenwallner. Free molecular aerodynamics for satellite application. *NASA STI/Recon Technical Report N*, 84:25749, July 1983.

[56] G. Koppenwallner, M. Ivanov, D. Johannsmeier, and A. Kashkovsky. Free molecular and transitional aerodynamics of spacecraft. Technical report, ESA/ESOC contract report, 1994.

[57] G. Koppenwallner, D. Johannsmeier, H. Klinkrad, M. Ivanov, and A. Kashkovsky. A rarefied aerodynamic modelling system for earth satellites (ramses). *Rarefied Gas Dynamics*, 19:1366–1372, 1995.

[58] S. M. Lichten and James S. Border. Strategies for high-precision global positioning system orbit determination. *Journal of Geophysical Research: Solid Earth*, 92(B12):12751–12762, 1987.

[59] F. Lyard, F. Lefevre, T. Letellier, and O. Francis. Modelling the global ocean tides: modern insights from fes2004. *Ocean Dynamics*, 56(5-6):394–415, 2006.

[60] J. A. Marshall, P. G. Antreasian, G. W. Rosborough, and B. H. Putney. Modeling radiation forces acting on satellites for precision orbit determination. In A. Tobias, W. Fehse, A. Getzschmann, and H. G. Backhaus, editors, *Astrodynamics 1991*, pages 73–96, August 1992.

[61] J. A. Marshall and S. B. Luthcke. Modeling radiation forces acting on TOPEX/Poseidon for precision orbit determination. *Journal of Spacecraft and Rockets*, 31:99–105, January 1994.

[62] D. D. McCarthy and G. Petit. Iers conventions (2003). verlag des bundesamts für kartographie und geodäsie. Technical report, DTIC Document, 2004.

[63] P. M. Mehta. Drag coefficient modeling for grace using direct simulation monte carlo. In *AIAA/AAS Astrodynamics Conference*, 2013.

[64] P. M. Mehta. *Thermospheric density and satellite drag modeling*. PhD thesis, Department of Aerospace Engineering, The University of Kansas, 2013.

[65] K. Moe and M. M. Moe. Gas-surface interactions and satellite drag coefficients. *Planetary and Space Science*, 53(8):793 – 801, 2005.

[66] O. Montenbruck and G. Eberhard. *Satellite orbits: models, methods and applications*. Springer, 2000.

[67] N. Munyamba. Derivation of a solar radiation pressure model of the latest glonass spacecraft. Master's thesis, University College London,Department of Civil, Environmental and Geomatic EngineeringEngineering, London, UK, 2010.

[68] S. Nocilla. The Surface Re-Emission Law in Free Molecule Flow. In J. A. Laurmann, editor, *Rarefied Gas Dynamics, Volume 1*, page 327, 1963.

[69] F. Panzetta. *Determination of the ocean tide model from LEO satellite orbital perturbation analysis*. PhD thesis, CISAS, Università degli Studi di Padova, 2005.

[70] J. M. Picone, A. E. Hedin, D. P. Drob, and A. C. Aikin. Nrlmsise-00 empirical model of the atmosphere: Statistical comparisons and scientific issues. *Journal of Geophysical Research: Space Physics*, 107(A12):SIA 15–1–SIA 15–16, 2002.

[71] M. D. Pilinski, B. M. Argrow, and S. E. Palo. Semiempirical model for satellite energy-accommodation coefficients. *Journal of Spacecraft and Rockets*, 47(6):951–956, 2010.

[72] M. D. Pilinski, B. M. Argrow, and S. E. Palo. Drag coefficients of satellites with concave geometries: Comparing models and observations. *Journal of Spacecraft and Rockets*, 48(2):312–325, 2011.

[73] M. D. Pilinski, B. M. Argrow, S. E. Palo, and B. R. Bowman. Semi-empirical satellite accommodation model for spherical and randomly tumbling objects. *Journal of Spacecraft and Rockets*, 50(3):556–571, 2013.

[74] W.W. Porter. Solar force-torque model for the gps space vehicle system. Opt. Model Rept. TOR 76 MA641, enclosure 2 (18 February 1976), Rockwell International, Rockwell Int.,Seal Beach, CA, 1976. (Reissued 1983.).

[75] A. Quarteroni, R. Sacco, and F. Saleri. *Numerical Mathematics*. Springer, 2007.

[76] B. Rievers and C. Lämmerzahl. New precise method for accurate modeling of thermal recoil forces. In S. A. Klioner, P. K. Seidelmann, and M. H. Soffel, editors, *IAU Symposium*, volume 261 of *IAU Symposium*, pages 426–428, January 2010.

[77] B. Rievers and C. Lämmerzahl. High precision thermal modeling of complex systems with application to the flyby and pioneer anomaly. *Annalen der Physik*, 523(6):439–449, 2011.

[78] B. Rievers, C. Lämmerzahl, and H. Dittus. Modeling of thermal perturbations using raytracing method withpreliminary results for a test case model of the pioneer 10/11 radioisotopic thermal generators. *Space Science Reviews*, 151(1-3):123–133, 2010.

[79] B. Rievers, C. Lämmerzahl, L. Meike, B. Stefanie, and H. Dittus. New powerful thermal modelling for high-precision gravity missions with application to pioneer 10/11. *New Journal of Physics*, 11(11):113032, 2009.

[80] H.J. Rim and B.E. Schutz. Precision orbit determination (pod). *Algorithm Theoretical Basis Document, Center for Space Research, The University of Texas at Austin, Austin, Tex, USA*, 2002.

[81] C. J. Rodriguez-Solano. Impact of albedo modelling on GPS orbits. Master's thesis, Technische Universität München, Munich, Germany, 2009.

[82] C. J. Rodriguez-Solano, U. Hugentobler, and P. Steigenberger. Adjustable box-wing model for solar radiation pressure impacting GPS satellites. *Advances in Space Research*, 49:1113–1128, April 2012.

[83] M. Rothacher, G. Beutler, and L. Mervart. The perturbation of the orbital elements of gps satellites through direct radiation pressure and y-bias. *Paper presented at the 1995 IGS Workshop, Potsdam, Germany*, pages 1–15, May 15-17, 1995.

[84] D. Sampietro and M. Reguzzoni. Exploitation of the First Release of GOCE Data for Local Moho and Geoid Estimation: the Example of the Alpine Area. *AGU Fall Meeting Abstracts*, page A807, December 2010.

[85] S. A. Schaaf and P. L. Chambré. *Flow of rarefied gases*. Princeton University Press Princeton, 1961.

[86] L. H. Sentman. Free molecule flow theory and its application to the determination of aerodynamic forces. Technical report, DTIC Document, 1961.

[87] A. Sibthorpe. *Precision non-conservative force modelling for low Earth orbiting spacecraft*. PhD thesis, Department of Geomatic Engineering, University College London, 2006.

[88] T. Springer. Napeos mathematical models and algorithms. Technical report, DOPS-SYS-TN-0100-OPS-GN, 2009.

[89] T. A. Springer, G. Beutler, and M. Rothacher. Improving the orbit estimates of gps satellites. *Journal of Geodesy*, 73(3):147–157, 1999.

[90] T. A. Springer, G. Beutler, and M. Rothacher. A new solar radiation pressure model for gps. *Advances in Space Research*, 23(4):673–676, 1999.

[91] J. Stark. Aerodynamic modelling of spacecraft for precise orbit determination. In *Proceedings of the Second International Symposium on Spacecraft Flight Dynamics*, volume ESA SP-255, pages 239–246, Darmstadt, Germany, October 1986.

[92] J. A. Storch. Aerodynamic disturbances on spacecraft in free-molecular flow. Aerospace report TR-2003(3397)-1, The Aerospace Corporation, El Segundo, California, October 2002.

[93] M. F. Storz, B. R. Bowman, and J. I. Branson. High accuracy satellite drag model (hasdm). In *AIAA/AAS Astrodynamics Specialist Conference and Exhibit*, volume AAS 2002-4886, Monterey, California, August 2002. American Astronautical Society (AAS) and American Institute of Aeronautics and Astronautics (AIAA).

[94] M. F. Storz, B. R. Bowman, J. I. Branson, S. J. Casali, and W. K. Tobiska. High accuracy satellite drag model (hasdm). *Advances in Space Research*, 36(12):2497 – 2505, 2005. ¡ce:title¿Space Weather¡/ce:title¿.

[95] E. K. Sutton. *Thermosphere Densities and Winds from CHAMP and GRACE Satellite accelerometer data*. PhD thesis, Department of Aerospace Engineering Sciences, University of Colorado at Boulder, 2008.

[96] B. D. Tapley, J. C. Ries, G. W. Davis, R. J. Eanes, B. E. Schutz, C. K. Shum, M. M. Watkins, J. A. Marshall, R. S. Nerem, B. H. Putney, S. M. Klosko, S. B. Luthcke, D. Pavlis, R. G. Williamson, and N. P. Zelensky. Precision orbit determination for topex/poseidon. *Journal of Geophysical Research: Oceans*, 99(C12):24383–24404, 1994.

[97] B.D. Tapley, B.E. Schutz, and G.H. Born. *Statistical Orbit Determination*. Elsevier, 2004.

[98] D. A Vallado and D. Finkleman. A critical assessment of satellite drag and atmospheric density modeling. In *Astrodynamics specialist conference and exhibit*, pages 18–21, 2008.

[99] P. Visser, J. van den IJssel, T. van Helleputte, H. Bock, A. Jäggi, G. Beutler, and M. Heinze. Rapid and precise orbit determination for the goce satellite. In *June-2010 in the ESA Living Planet Symposium in Bergen, Norway*, 2010.

[100] P. N. A. M. Visser and J. van den IJssel. Gps-based precise orbit determination of the very low earth-orbiting gravity mission goce. *Journal of Geodesy*, 74(7-8):590–602, 2000.

[101] P. N. A. M. Visser, J. van den IJssel, T. van Helleputte, H. Bock, A. Jäggi, G. Beutler, D. Švehla, U. Hugentobler, and M. Heinze. Orbit determination for the goce satellite. *Advances in Space Research*, 43(5):760–768, 2009.

[102] B. A. Wielicki, B. R. Barkstrom, E. F. Harrison, R. B. Lee, III, G. L. Smith, and J. E. Cooper. Clouds and the Earth's Radiant Energy System (CERES): An Earth Observing System Experiment. *Bulletin of the American Meteorological Society*, 77:853–868, May 1996.

[103] R. C. Willson and H. S. Hudson. Solar luminosity variations in solar cycle 21. *Nature*, 332:810–812, April 1988.

[104] L. Wimer, A. Cataloglu, K. Eckert, K. Kempkens, and H.-K. Stecker. Thermal analysis report. Technical Report GO-RP-ASG-0015, EADS Astrium, May 2005.

[105] L. Wimer, A. Cataloglu, K. Eckert, U. Muedsam, H.-K. Stecker, and A. Woelker. Thermal mathematical model description. Technical Report GO-RP-ASG-0055, EADS Astrium, December 2004.

[106] M. Ziebart. Generalized analytical solar radiation pressure modeling algorithm for spacecraft of complex shape. *Journal of spacecraft and rockets*, 41(5):840–848, 2004.

[107] M. Ziebart, S. Adhya, A. Sibthorpe, S. Edwards, and P. Cross. Combined radiation pressure and thermal modelling of complex satellites: Algorithms and on-orbit tests. *Advances in Space Research*, 36:424–430, 2005.

[108] M. Ziebart and P. Dare. Analytical solar radiation pressure modelling for glonass using a pixel array. *Journal of Geodesy*, 75(11):587–599, 2001.